

COLLISIONAL-RADIATIVE MODELLING OF NEUTRAL
BEAM ATTENUATION AND EMISSION

A THESIS SUBMITTED TO
THE DEPARTMENT OF PHYSICS AND APPLIED PHYSICS
OF THE UNIVERSITY OF STRATHCLYDE
FOR THE DEGREE OF
DOCTOR OF PHILOSOPHY

by
Harvey Anderson
February 1999

© Copyright 1999

The copyright of this thesis belongs to the author under the terms of the United Kingdom Copyright Acts as qualified by University of Strathclyde Regulation 3.49. Due acknowledgement must always be made of the use of any material contained in, or derived from, this thesis.

Abstract

In addition to heating tokamak plasmas, neutral beam injection can also be exploited as a quantitative diagnostic to investigate the concentration of impurities in the plasmas via charge exchange spectroscopy. For this use, a detailed knowledge of the beam attenuation or alternatively the neutral beam density in the plasma is required. There are two methods which may be employed to determine the neutral beam density. The first approach involves modelling the rate at which the beam neutrals are ionised as they traverse the plasma. The second and in principle more accurate method, involves the direct measurement of the intensity of the spectral lines emitted from the excited beam neutrals. Then with the use of atomic modelling the neutral beam density can be recovered. This is the basis of beam emission spectroscopy.

The work in this thesis, which addresses the issue of modelling and measuring the neutral beam density, can be separated into two distinct parts. The first concerns the deduction of the neutral deuterium beam density at JET Joint Undertaking using both the theoretical and experimental approach. The second part of this thesis involves developing a Bundled-nISL collisional-radiative model to predict the attenuation and emission associated with a fast neutral helium beam. The model is then used to explore the attenuation and the behaviour of the excited state population structure of the beam atoms as a function of typical plasma parameters.

Experimental aspects associated with beam emission spectroscopy at JET are summarised and a detailed description of the atomic modelling required to support the diagnostic exploitation of fast neutral deuterium and helium beams is given. The modelling codes used and developed during the course of this work form part of the Atomic Data and Analysis Structure, ADAS.

Acknowledgements

During the course of this work I have sought the help and advice from many and it is at this point I would like to take the opportunity to thank them.

Firstly, I would like to thank my supervisor Prof. Hugh Summers. I am grateful for all the advice and support I have received over the last three years. I would also like to thank Dr. David Brooks for his help and advice concerning IDL, physics and life in general. Also thanks to Stuart Loch and Gordon Fischbacher for making our office at Strathclyde a venue for interesting discussions.

The experimental aspects of this thesis were conducted at JET Joint Undertaking. I would like to thank Dr. Paul Thomas and members of experimental division II for their hospitality and assistance. In particular, I would like to thank my JET supervisor Dr Manfred von Hellermann. I would also like to thank Drs Andy Meigs, Ralf Konig, Zlaus-Dieter Zastrow, Martin O'Mullane and Lorne Horton. A special thanks also goes to Kate Bell, Clive Flewin and Hui Chen.

On a personal note, I am deeply grateful to Margaret Harrison for her continual source of encouragement. This thesis would definitely not have been completed without her.

Contents

1. Introduction	
1.1. Active and passive spectroscopy	1
1.1.1. Passive spectroscopy	2
1.1.2. Active spectroscopy	4
1.2. Aim of this work	9
1.3. Atomic Data and Analysis Structure	10
1.4. Format of thesis	12
2. Atomic modelling relevant to neutral beam driven diagnostics	
2.1. Introduction	13
2.2. Physical conditions and separation of time scale	13
2.2.1. Thermodynamic equilibrium	13
2.2.2. Local thermodynamic equilibrium	15
2.2.3. Statistical balance equation	17
2.2.4. Ranking of atomic lifetimes	18
2.3. Atomic processes associated with a deuterium beam	20
2.4. Atomic processes associated with a helium beam	24
2.5. Approaches to modelling	31
2.5.1. Coronal equilibrium model	33
2.5.2. Collisional-radiative model	34
2.6. Previous theoretical studies	39
2.6.1. Modelling a neutral deuterium beam	39
2.6.2. Modelling a neutral helium beam	41
3. Collisional-radiative models for neutral beam attenuation and emission	
3.1. Introduction	43
3.2. The bundled-nS model for a deuterium beam	43
3.2.1. Radiative processes	46
3.2.2. Collisional processes	47
3.2.3. Beam-thermal rate coefficients	50
3.2.4. Fundamental atomic data	51
3.2.5. Method of solution	52
3.3. The bundled-nLSL model for a helium beam	55
3.3.1. Radiative processes	57
3.3.2. Collisional processes	58
3.3.3. Fundamental atomic data	59
3.3.4. Method of solution	59
3.4. Computational implementation and validation	61
3.4.1. Implementation of the models within ADAS	61

3.4.2.	Validation of ADAS310, the bundled-nS model	70
3.4.3.	Validation of ADAS311, the bundled-nISL model	72
3.5.	Summary	73
4.	Parameter dependencies and application of the derived atomic data relevant to neutral deuterium beam attenuation and emission	
4.1.	Introduction	74
4.2.	Effective collisional-radiative ionisation coefficients	74
4.2.1.	Density dependence	75
4.2.2.	Neutral beam energy dependence	77
4.2.3.	Temperature dependence	79
4.2.4.	Nuclear charge dependence	81
4.2.5.	The importance of impurities	82
4.2.6.	Influence of the fundamental low level data	86
4.2.7.	Conclusion	92
4.3.	Effective Balmer-alpha emission coefficients	94
4.3.1.	Density dependence	95
4.3.2.	Neutral beam energy dependence	97
4.3.3.	Temperature dependence	98
4.3.4.	Nuclear charge dependence	100
4.3.5.	The importance of impurities	101
4.3.6.	Influence of the fundamental low level data	105
4.3.7.	Conclusion	109
4.4.	Application to experimental programs	111
4.4.1.	Introduction	111
4.4.2.	Production and archiving the derived data	112
4.4.3.	Linear interpolation scheme	113
4.4.4.	Linear combination scheme	114
4.4.5.	Accuracy of the linear interpolation and combination scheme	115
4.4.5.1.	Effective beam stopping coefficients	115
4.4.5.2.	Effective beam emission coefficients	119
4.4.6.	Conclusion	122
5.	Beam emission spectroscopy at JET	
5.1.	Historical overview	123
5.2.	The JET beam emission spectroscopy diagnostic	124
5.2.1.	Diagnostic apparatus	124
5.2.2.	Observed beam emission spectrum	126
5.2.3.	Experimental analysis	128
5.2.3.1.	Method and objectives	128
5.2.3.2.	Motional Stark effect	129
5.2.3.3.	Spectral analysis	131
5.3.	The charge exchange analysis package	133
5.3.1.	The role of the charge exchange analysis package	133
5.3.2.	Iterative path to absolute impurity concentrations	134
5.3.3.	Evaluation of the neutral beam density	135
5.3.3.1.	Numerical attenuation calculation	136
5.3.3.2.	Spectroscopic measurement	137
5.4.	Examination of the analysis procedure	138

5.4.1.Overview	138
5.4.2.The spectral analysis	138
5.4.3.The CHEAP analysis.....	141
5.4.4.Review of the fundamental and derived atomic data	141
5.4.5.Conclusion.....	145
5.5. Results	146
5.5.1.Single beam bank pulses	146
5.5.2 Double beam bank pulses	148
5.6. Conclusion.....	151
6.Predictive studies of helium beam attenuation and emission	
6.1. Introduction	152
6.2. Review of the collisional-radiative coupling coefficients	153
6.3. Collisional-radiative cross coupling coefficients	155
6.3.1.Non spin changing transitions	157
6.3.2.Spin changing transitions	163
6.3.3.Collisional-radiative ionisation coefficients.....	169
6.4. Quasi-static excited population structure	171
6.4.1.Neutral beam energy dependence.....	171
6.4.2.Density dependence.....	174
6.4.3.Temperature dependence.....	176
6.4.4.Comparison of the role of the metastable levels	179
6.4.5.The influence of impurities	184
6.5. Evolution of the metastable populations under JET conditions.....	186
6.5.1.Method of calculation.....	186
6.5.2.Metastable population : Quasi-static Vs Spatial solution.....	189
6.5.3.Attenuation of a neutral helium beam	194
6.5.4.Additional Physics of helium beam attenuation.....	204
6.5.4.1.Influence of the local temperature	204
6.5.4.2.Influence of the local electron density	206
6.6. Conclusion.....	208
7. Thesis Summary and discussion	211
References.....	214
Appendix A.....	218

1.0 Introduction

The spectroscopic measurement and monitoring of impurity radiation in tokamak plasmas has not only led to key advances in the diagnosis of fusion plasmas, but has also contributed to our understanding of the behaviour of atomic processes and populations in a wide range of novel environments.

A typical tokamak plasma consists mainly of electrons and deuterons together with a small concentration of impurities[1,2]. The presence of such impurities gives cause for concern. As tokamak plasmas are heated to high temperatures and confined for times required to meet the Lawson criteria[3], the plasma impurities radiate energy through the emission of spectrum lines and bremsstrahlung radiation, modifying the plasma resistivity as well as their own sources from the vessel walls and the divertor target plates. Thus they produce many effects, often unwanted, which require a detailed knowledge of impurity concentration for their evaluation.

The current method of attempting to control plasma impurities is by employing divertor configurations to channel the scrape off layer plasma to remote target plates. The divertor essentially acts as an exhaust system to assist with the removal of impurities from the bulk plasma[4] as well as inhibiting removed impurities returning to the confined plasma. These environments add to the demand for the development of advanced spectroscopic methods which can measure impurity ions with greater accuracy.

1.1 Active and passive spectroscopy

The application of spectroscopy to monitor plasma impurities can be categorised as either passive or active. Passive spectroscopy involves exploiting the natural emission from impurity ions or atoms in the thermal plasma, where as active spectroscopy involves perturbing by external means the ions or atoms contained in the plasma so as to enhance or alter their emission. The latter is potentially the more accurate diagnostic procedure. Spectroscopy is not only confined to the study of impurity concentrations in fusion plasmas, but important quantities such as the

plasma temperature and the electron density are also of interest. In the following sections we show examples of both active and passive spectroscopic methods

1.1.1 Passive spectroscopy

Typical quantities which may be measured using passive spectroscopy include the electron density and electron temperature from spectral line ratios, the effective ion charge of the plasma as well as the impurity concentration and impurity fluxes from absolute intensities and ion temperatures from line widths.

If we first consider the use of spectral line ratios, a common method involves exploiting the emission due to dielectronic satellite lines associated with plasma impurity ions[1,5], see figure 1.1.

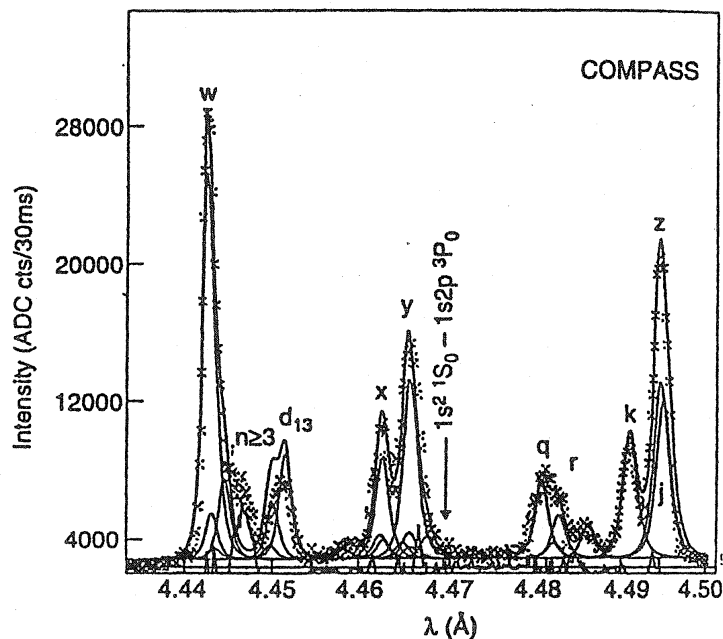


Figure 1.1 Spectral emission due to dielectronic satellite lines of He-like Cl XVI from the COMPASS experiment. The electron temperature is obtained from the ratio of the lines w and k. The diagram was taken from [5] where a detailed discussion can be found.

The satellite lines arise due to radiative stabilisation following resonance capture in the process of dielectronic recombination. As discussed by Coffey et. al.[5], the electron temperature can be obtained from the ratio of the lines denoted by the labels w and k. Also from the width of the w line the associated ion temperature can be

inferred. The widths of passive emission lines can also be used to measure the electron density via Stark broadening. A recent example reported by Terry et.al.[6] and later by Meigs[7], involves utilising the high-n Balmer series, see figure 1.2.

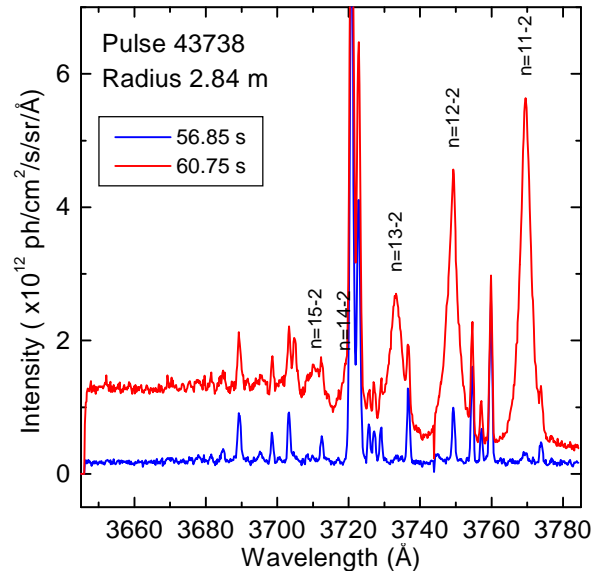


Figure 1.2 Spectrum of the high n-Balmer series for deuterium, courtesy of Dr A. G. Meigs[7]. The Stark widths of the high-n Balmer lines can be used to infer the electron density. The average electron density for low recombination (56.95 s) is approximately $2.3 \times 10^{19} \text{ m}^{-3}$ and $3.5 \times 10^{19} \text{ m}^{-3}$ at high recombination (60.75 s).

The high-n Balmer series arises due to the dominant role of recombination in low temperature and high electron density environments.

Focusing on the passive measurements associated with impurity ions. The excitation and ionisation state of emitting impurities is almost entirely electron impact driven. Also the interpretation is complicated by the non-localised nature of the emission. Figure 1.3 shows a BeII feature typifying the experimental data used for analysis of influx. More complicated inferences such as the recycling of neutral hydrogen diffusing into the edge of the plasma has also been attempted. This is achieved by exploiting the emission from impurity ions themselves following the capture of an electron via thermal charge exchange[1,8],



Thermal charge exchange usually occurs at the edge of the plasma where the conditions are such that hydrogen isotopes can act as donors to partially ionised impurity ions[8]. The thermal charge exchange emission from CVI and CIII impurity ions is also shown in figure 1.3.

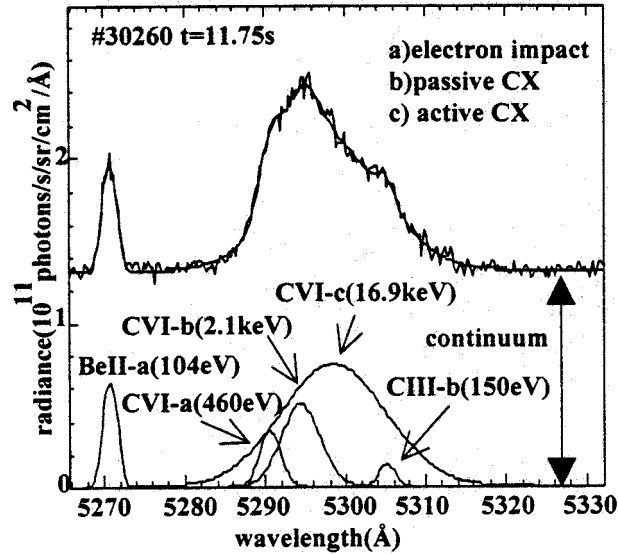


Figure 1.3 Thermal charge exchange spectrum showing the emission from CVI(n=8-7) and CIII(n=7-5) impurity ions. Also shown is the contribution to the spectrum due to a) impact excitation, and c) active charge exchange emission. The diagram was taken from [8].

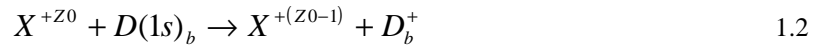
Finally, the effective ion charge of the plasma, which is a measure of the total impurity content of the plasma, can be obtained from passive measurements of the bremsstrahlung radiation[9].

1.1.2 Active spectroscopy

Active spectroscopy as mentioned earlier, is not only more accurate but can be employed to measure a range of parameters which are not readily accessible using passive spectroscopy. Techniques such as pellet injection, gas puffing and Laser ablation[10] can all be used to study the impurity transport of the plasma. The active introduction of trace impurities into the plasma is not only confined to the study of

transport parameters, quantities such as the electron density and temperature can be measured using line ratio techniques during gas puffing experiments[11]. However the most fruitful active diagnostic method arises from the injection of neutral atomic beams into the plasma.

Neutral beam injection can be employed to investigate the edge as well as the core of the plasma. As an edge diagnostic, slow neutral helium[12,13] and lithium beams[14] are often employed to measure the edge electron density and temperature, while fast neutral helium and deuterium beams, which penetrate into the core of the plasma, can be used to measure a wide range of parameters[15,16,17]. Confining ourselves to fast beams, neutral deuterium beams can be exploited as diagnostic probes to measure the concentration and temperature for a wide range of impurity ions using active charge exchange spectroscopy[18]. Active charge exchange involves measuring the emission from impurity ions following the capture of an electron from the beam atoms,



The impurity ion density can then be recovered from the recorded charge exchange emission using the relation,

$$n_{z_0} = \frac{4\pi \int \Phi_{CX}(\lambda) d\lambda}{q_{cx} \int n_b ds} \quad 1.3$$

where Φ_{CX} is the charge exchange emission flux, q_{cx} is the effective emission coefficient[19] and $\int n_b ds$ is the line integrated beam density. The ion temperature can be obtained from the width of the Doppler broadened emission line in the usual manner. We show in figure 1.4 an example of a deuterium beam active charge exchange spectrum.

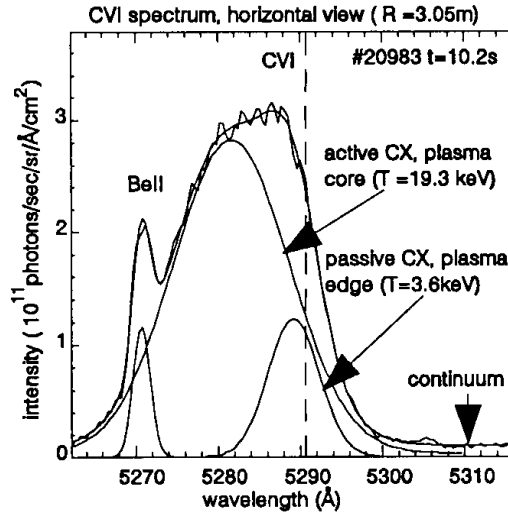


Figure 1.4 Deuterium beam active charge exchange spectrum for CVI at 5290 Å (T=19.3 keV), also shown is the passive emission spectrum. This diagram was taken from [16] where a full description of the spectrum is given. The CVI concentration is obtained from measuring the total charge exchange flux. The temperature is obtained from the width of the Doppler broadened line.

Active charge exchange spectroscopy provides an accurate and localised measurement of the plasma impurity densities. However the accuracy at which the impurity concentration can be measured is governed by the accuracy at which the neutral beam density is known.

The most common approach to determine the neutral beam density is to employ a simple attenuation calculation which takes into consideration the atomic processes which contribute to ionising the beam atoms[16]. However it is now possible, in principle anyway, to accurately measure the neutral beam density using Balmer-alpha beam emission spectroscopy[20]. As the neutral deuterium beam atoms penetrate into the plasma, before they are ionised they become temporarily excited and as they relax their emission contains information regarding the population of the n=3 shell of the beam atoms. The neutral beam density can then be recovered from the beam emission spectrum using the relation,

$$n_b = \frac{1}{n_e} \left(\frac{\Phi_{D-\alpha}}{q_{D-\alpha}} \right) \quad 1.4$$

where $\Phi_{D-\alpha}$ is the total flux of the beam emission spectrum, n_e is the electron density and $q_{D-\alpha}$ is the theoretical Balmer-alpha effective emission coefficient. In working plasmas the situation is complicated. The beam atoms experience an electric field within their own frame of reference as a result of moving with a velocity through the confining magnetic field of the tokamak. The influence of the electric field is to remove the degeneracy associated with the energy levels of the beam atoms. This gives rise to a Stark resolved energy level structure and the beam emission spectrum is observed as a series of Stark components, see figure 1.5.

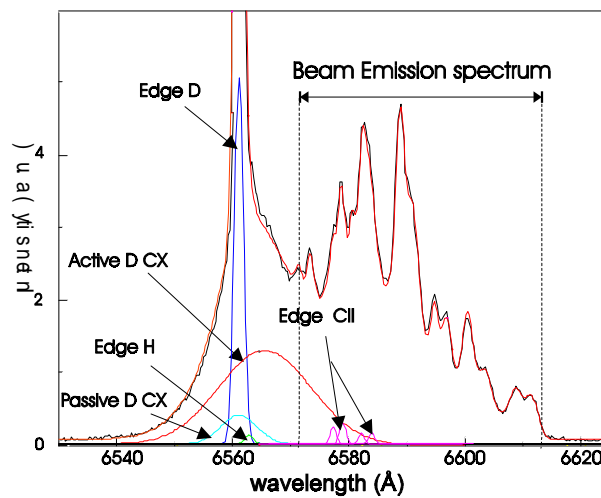


Figure 1.5 Beam emission spectrum for a high power double beam bank pulse from the JET experiment. The beam emission spectrum is a complicated array of Stark components which overlap each other. Also shown are the active and passive charge exchange signals which are in the spectral vicinity of the beam emission spectrum.

Turning our attention to the use of fast helium beams. A neutral helium beam can be used to measure the impurity concentrations and their associated temperatures in the same manner as with a fast neutral deuterium beam. We show in figure 1.6 an example of a helium beam active charge exchange spectrum.

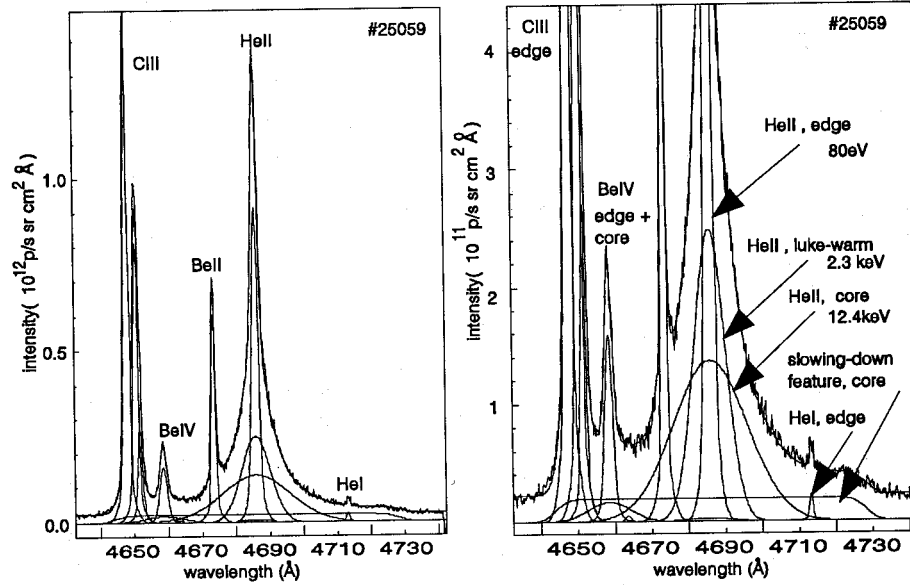


Figure 1.6 Helium beam active charge exchange spectrum. The figure on the left gives a general overview of the features contained within the observed spectral region. The figure on the right is an expanded figure showing thermal and non-thermal components. These figures were taken from [16] where more information can be found.

There are however significant benefits of using a neutral helium beam rather than a fast deuterium beam as a diagnostic probe. The most practical benefit involves reducing the generation of neutrons during plasma operation. A fast neutral deuterium beam contributes to producing neutrons via the beam-beam and beam-plasma interaction[21]. These unwanted neutrons contribute to activating the experimental vessel as well as complicating the analysis of the neutron flux signals from the bulk plasma. Using a neutral helium beam (^3He) removes this problem since the contribution to the neutron production due to the beam-beam and beam-plasma interaction is very small.

There are also diagnostic benefits, the most obvious concerns the detection of alpha particles via the resonant process of double charge exchange[22]. More interestingly though, is the new diagnostic capabilities which may arise due to the presence of metastable levels in the beam atoms. If the $\text{He}(2^3\text{S})$ metastable is significantly populated it may act as a charge exchange donor. Preferential charge exchange between the ground state and the $\text{He}(2^3\text{S})$ with different plasma impurity ions may be possible. This would lead to a more flexible charge exchange diagnostic.

It should be noted though that the use of a fast neutral helium beam is very much still in its infancy. There are many issues which require some investigation. For example, what happens to the metastable population as the beam traverses the plasma?, what is the behaviour of the excited state population structure?, and do the metastables levels contribute significantly to the beam attenuation?. The application of beam emission spectroscopy with a neutral helium beam also requires some attention. It is expected that the lines associated with the $n=3$ to 2 shell for both spin systems can be of immediate diagnostic use[23]. A more interesting aspect concerns the excited levels of the beam atoms where the Lorentz electric field results in the formation of forbidden lines. These lines may be of use to infer the internal magnetic field of the plasma[24]. However extensive spectroscopic observations are still required to explore the diagnostic potential of the helium beam emission spectrum.

1.2 Aim of this work

There are two main topics which we address in this work. The first involves measuring the neutral deuterium beam density at JET Joint Undertaking[25] via beam emission spectroscopy. The primary aim is to be able deduce the neutral beam density for high power double beam bank pulses on a reliable basis. Continuing along this theme we also consider the evaluation of the neutral beam density using a numerical attenuation calculation. To achieve the former and latter we employ a bundled- nS collisional-radiative model to evaluate effective stopping and Balmer-alpha emission coefficients. We also aim to show the parameter dependencies of these coefficients and the underlying role of the atomic processes which contribute to the attenuation and population redistribution of the neutral deuterium beam atoms. A comparison is then made between the numerical attenuation calculation and the results obtained from the spectroscopic measurements.

The second topic which is of concern involves modelling the attenuation and the excited state population structure of a fast neutral helium beam. To address some of the uncertainties with regards to a fast helium beam we have developed a bundled- nSL collisional-radiative model. This model is employed to investigate the behaviour of the excited state population structure, the evolution of the metastable

populations and the beam attenuation. Effective cross coupling coefficients are also calculated and their parameter dependencies are explored.

During the course of this work, computational tools designed to archive and study the global behaviour of the derived atomic data for both neutral deuterium and helium beams have also been developed. These programs, together with the bundled-nSL model, have been written for general use within the Atomic Data and Analysis Structure package, ADAS.

1.3 Atomic Data and Analysis Structure

The Atomic Data and Analysis Structure package[26] is a collection of programs and databases which have been designed to assist with the modelling and analysis of spectral observations from fusion and astrophysical plasmas. There are three main components of the ADAS system. These include a suite of interactive programs, a collection of fundamental and derived atomic databases and a library of FORTRAN routines. If we first consider the interactive programs. The ADAS package consists of seven different series of modelling codes, each of which addresses different areas of atomic physics. In any given series there are a number of individual programs. Each of the programs are driven by an IDL interface while the main calculation is done using a FORTRAN routine which is ‘spawned’ from the IDL. The main interface of ADAS can be seen in figure 1.7.

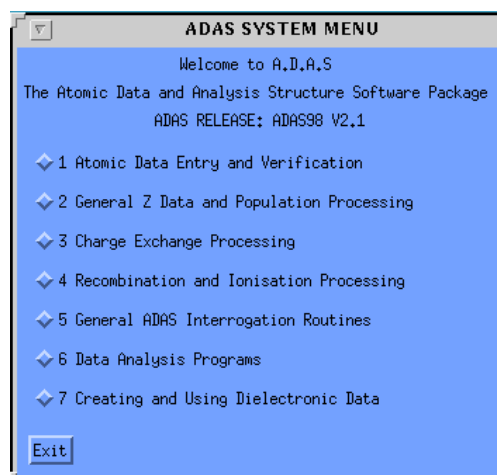


Figure 1.7 Snap shot of the main IDL interface of the Atomic Data Analysis Structure Package.

The processing screen contains an array of toggle buttons which correspond to each of the series of modelling codes. If the user activates a button, the menu corresponding to the list of programs for that particular series will appear. As an example we show in figure 1.8 the menu for the series three programs.

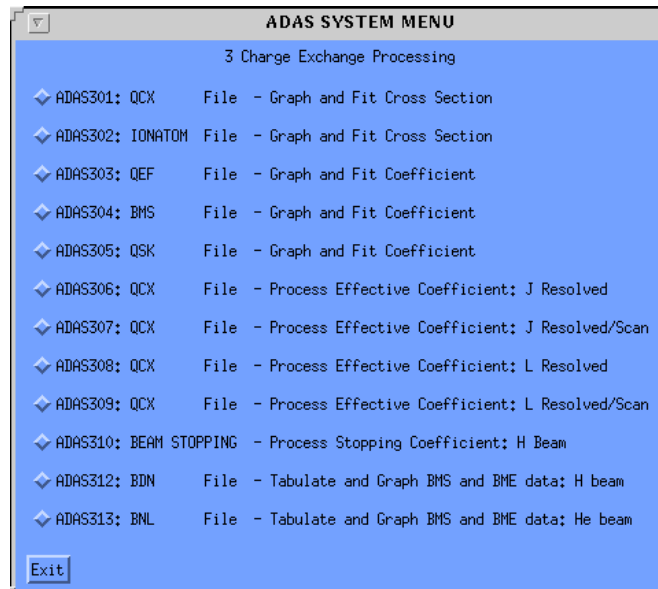


Figure 1.8 Snap shot of the series three menu system.

If the user then activates any of the toggle buttons a series of interactive panels will guide the user through the calculation of interest.

Focusing on the derived and fundamental atomic databases of ADAS. There are a total of twenty six databases, each of which are archived according to an ADAS data format prescription[26]. To distinguish each database they are individually assigned an ADAS data format number e.g. adf21. The fundamental atomic databases are based on extensive compilations of the best available experimental and theoretical data, while the derived atomic databases contain the output from the modelling codes of ADAS and are conveniently stored in a format to be of direct use to experiment.

The last component of the ADAS system is the library of FORTRAN routines[27]. These routines are designed to allow the user to access the fundamental and derived atomic databases for their own application. Also there are routines which evaluate quantities which may also be of interest for individual applications.

1.4 Format of thesis

We begin in chapter 2.0 by describing the physical conditions of tokamak plasmas and the atomic processes which contribute to the attenuation and the excited state population structure of neutral deuterium and helium beam atoms. We also discuss in detail the collisional-radiative approach of modelling beam attenuation and emission, which is the method adopted in this work. A brief literature review of previous work is also given.

Chapter 3.0 outlines the application of collisional-radiative theory in the form of the bundled-nS deuterium beam model and the more elaborate bundled-nlSL helium beam model. The computation implementation of each of these models are discussed within the context of ADAS and an account of their operation and validation is also given.

A detailed study of the parameters dependencies of the effective stopping and Balmer-alpha emission coefficients for a deuterium beam is the subject of Chapter 4.0. In this chapter we also discuss the archiving and the rapid assembly of the effective coefficients for experimental analysis. This chapter serves as a preamble to chapter 5.0 which details the application of the bundled-nS model in an attempt to exploit the beam emission signature at JET Joint Undertaking. The spectroscopic deduction of the neutral beam density using the beam emission flux and the Balmer-alpha emission coefficients is the topic of interest here. The evaluation of the neutral beam density using the theoretical beam stopping coefficients is also of concern.

In chapter 6.0, using the bundled-nlSL model we investigate the parameter dependencies of the collisional-radiative coefficients and the equilibrium excited state populations. We also investigate the implications of neglecting the metastable nature of the He(2^1S) and He(2^3S) levels while evaluating their population. A study of the attenuation of a fast neutral helium beam, while altering the initial metastable content on entry to the plasma, is also undertaken. A summary and discussion regarding the contents of the thesis is then given in Chapter 7.0.

2.0 Atomic modelling relevant to neutral beam driven diagnostic

2.1 Introduction

To fully exploit the diagnostic potential of injecting neutral atomic beams into tokamak plasmas, a detailed knowledge of the attenuation and the excited state population structure of the neutral beam atoms is required. To obtain such information requires quite elaborate statistical models which include detailed descriptions of the atomic processes which contribute to exciting and ionising the penetrating beams. The pathways through the complexity depends on the conditions of the plasma, the ranking of atomic and plasma lifetimes and the actual beam atoms themselves.

In this chapter we discuss the broad assumptions which are employed to enable us to model the attenuation and excited state population structure of neutral deuterium and helium beam atoms. We then summarise the particular primary and secondary atomic processes which are involved for each beam species. We illustrate in detail the behaviour of each process as a function of energy since this allows one to quantitatively assess the varying and relative influence of each atomic process. Finally, we explain the choice of statistical models which we employ and give a historical review of previous modelling approaches by others.

2.2 Physical conditions and separation of time scales

2.2.1 Thermodynamic equilibrium

For a plasma which has reached thermodynamic equilibrium, the distribution of the plasma particles on an atomic level can be described using equilibrium statistical mechanics. The radiation field in such a plasma is free of any spectral lines and is that of a blackbody. The radiation field is Plankian with an energy density,

$$U(\nu) = \frac{8\pi h \nu^3 d\nu / c^3}{\exp(h\nu / k_B T_r) - 1} \quad 2.1$$

where k_B is boltzmann's constant, ν is the frequency of the photons and T_r is the temperature of the radiation field which is equal to both the electron and ion temperature.

The velocity distribution and the excited state population structure of the plasma constituents can be described by Maxwell-Boltzmann statistics. For a particle of mass m and temperature T the speed distribution is Maxwellian,

$$f(v) = 4\pi v^2 \left(\frac{m}{2\pi k_B T} \right)^{\frac{3}{2}} \exp\left(-\frac{mv^2}{2k_B T} \right) \quad 2.2$$

where v is the particle velocity.

The excited state population distribution of a single atom or ion contained in the plasma is given by Boltzmann's equation which relates the population of two levels, N_i and N_j , their statistical weights and their excitation energies as,

$$\frac{N_i}{N_j} = \frac{w_i}{w_j} \exp\left(-\frac{(E_i - E_j)}{k_B T} \right) \quad 2.3$$

When the population distribution of more than one ionisation stage of a particular species are compared, we can extend Boltzmann's equation to describe the excited state population of one ionisation stage relative to the ground state of the next ionisation stage. This is called the Saha-Boltzmann equation which is given as,

$$N_i = n_e n_+ 8 \left(\frac{\pi a_0^2 I_H}{k T_e} \right)^{\frac{3}{2}} \frac{w_i}{2w_+} \exp\left(\frac{I_i}{k T} \right) \quad 2.4$$

where N_i and w_i are respectively the population and statistical weight of the level i . The quantity n_+ is the population of the ground state of the next ionisation stage, w_+ is the corresponding statistical weight and n_e is the free electron number density.

There is yet another useful property associated with plasmas which are in thermodynamic equilibrium. That is the principle of detailed balance. The distribution of energy amongst the electrons and ions has reached equilibrium at a particular temperature, therefore the rate at which atomic processes contribute to

populating or depopulating excited levels of ions or atoms contained in the plasma will be balanced by the rate of the corresponding reverse processes. In such circumstances we describe the forward atomic processes to be in detailed balance with the reverse processes. For example, spontaneous and stimulated emission would be in detailed balance with photo-excitation. This principle can be used to arrive at relationships which connect the coefficients used to describe the rate at which the forward and reverse reaction of a particular atomic process occurs. If we consider electron impact excitation for which the corresponding reverse reaction is electron impact de-excitation, it can be shown using equation 2.3 that the rate coefficients for the forward ($q_{i \rightarrow j}$) and the reverse ($q_{j \rightarrow i}$) reaction satisfies the relationship,

$$q_{i \rightarrow j} = q_{j \rightarrow i} \frac{w_i}{w_j} \exp\left(-\frac{(E_i - E_j)}{k_B T_e}\right) \quad 2.5$$

where T_e is the electron temperature. Therefore the rate coefficient for electron impact de-excitation can be obtained from the rate coefficient for electron impact excitation and vice versa.

2.2.2 Local thermodynamic equilibrium

Tokamak plasmas however are far from thermodynamic equilibrium. This is primarily due to the fact that radiation can easily escape from the plasma. Under normal operating conditions tokamak plasmas are optically thin to their own radiation. Due to the magnetically confined particles though the plasma does approach conditions which are near to thermodynamic equilibrium. Elastic collisions between electrons and between protons and between electrons and protons are efficient to establish Maxwellian velocity distributions. Excited levels of atoms and ions in the plasma which are populated and depopulated by electron and proton collisions approach values that would have been obtained as if the plasma was in thermodynamic equilibrium. This condition is called local thermodynamic equilibrium, LTE. For excited levels which are in LTE, Maxwell-Boltzmann statistics are valid.

The formation of LTE conditions in a plasma is governed by the rate at which the plasma constituents take up Maxwellian distributions. For free particle distributions as discussed by Spitzer[28], this is characterised by so-called slowing down times. The slowing down time describes the rate at which the kinetic energy distribution between two elastic collision partners approaches that of a Maxwellian. In the tokamak plasma we are concerned with electron-electron, proton-proton and electron-proton relaxation. The electron-proton slowing down time is usually referred to as the equilibration time. The slowing down time associated with electron-electron collisions (τ_{e-e}) is given by Spitzer (see page 133),

$$\tau_{e-e} = 0.266 \frac{T_e^{3/2}}{n_e \ln \Lambda} \quad 2.6$$

where T_e and n_e are respectively in units of $^{\circ}\text{K}$ and cm^{-3} . The quantity $\ln \Lambda$ is the Coulomb logarithm for which tabulated values are also given by Spitzer. Similar formulae give the slowing down time for proton-proton collisions (τ_{p-p}) and the equilibration time between electrons and protons (τ_{eq}) and these are related by,

$$\tau_{p-p} \approx \left(\frac{m_p}{m_e} \right)^{1/2} \tau_{e-e} \quad \tau_{p-p} \approx 43 \tau_{e-e} \quad 2.7$$

$$\tau_{eq} \approx \frac{m_p}{m_e} \tau_{e-e} \quad \tau_{eq} \approx 1836 \tau_{e-e} \quad 2.8$$

In the context of the present work it is instructive to compare the slowing down and equilibration times to the energy confinement time of the JET tokamak plasma. This will enable us to assess if the free particle Maxwellians are achieved in a tokamak plasma and the degree to which Maxwell-Boltzmann statistics can be applied to highly excited ion populations. In table 2.1 we show the slowing down and equilibration times for a plasma with a temperature of 2.0×10^3 eV as a function of electron density.

$N_e (cm^{-3})$	1.0×10^{13}	3.0×10^{13}	5.0×10^{13}	7.0×10^{13}	1.0×10^{14}
$\tau_{e-e} (s)$	$\sim 2.1 \times 10^{-4}$	$\sim 7.0 \times 10^{-5}$	$\sim 4.2 \times 10^{-5}$	$\sim 3.0 \times 10^{-5}$	$\sim 2.1 \times 10^{-5}$
$\tau_{p-p} (s)$	$\sim 9.0 \times 10^{-3}$	$\sim 3.0 \times 10^{-3}$	$\sim 1.8 \times 10^{-3}$	$\sim 1.2 \times 10^{-3}$	$\sim 9.0 \times 10^{-4}$
$\tau_{e-p} (s)$	~ 0.3	~ 0.1	~ 0.07	~ 0.05	~ 0.03

Table 2.1 Slowing down and equilibration times. The temperature was 2.0×10^3 eV and the Coulomb logarithm was taken to be approximately 14.

The confinement time of the JET tokamak plasma is approximately 1.0 second, therefore from table 2.1 it can be seen that the formation of free particle Maxwellians can easily be achieved. It should be noted though that excited levels of ions and atoms which are primarily populated and depopulated by radiative processes do not satisfy the criteria for LTE. This occurs for low lying excited levels where collisional redistribution is less effective. This condition is described as non local thermodynamic equilibrium, non-LTE. In non-LTE environments Maxwell-Boltzmann statistics can not be used to describe the excited state population structure of plasma ions and atoms and an alternative method is sought.

2.2.3 Statistical balance equations

A general approach used to obtain the population of non-LTE and LTE levels is by solution of the statistical balance equations. The statistical balance equations represent the rate at which the excited levels of an atom or an ion are populated and depopulated. In the present work, where we are interested in modelling the excited population structure of neutral beam atoms, the statistical balance equations are,

$$\frac{dN_i}{dt} + v_b \frac{dN_i}{dx} = \left(\text{Populating} \rightarrow N_i \right) - \left(\text{Depopulating} \leftarrow N_i \right) \quad 2.9$$

for $i=1, 2, 3...$

where v_b is the beam velocity and dx is along the beam path. The terms in the brackets on the right hand side represent the rate at which the atomic processes contribute to populating and depopulating each of the excited levels of the beam

atoms, whilst the terms on the left hand side include a spatial and time dependent derivative. The spatial derivative represents the rate at which the populations change due to alterations in the local environment as the beam atoms continue into the plasma. The time derivative accounts for a change in the population due to a variation in the source of the beam atoms. The neutral beams which are of interest in this thesis however are considered to be steady state sources and the time derivative of equation 2.9 can be set to zero i.e. $dN_i/dt = 0$. The solution of the above equations yield the population density of each level, N_i , and as discussed later, further manipulation of the equations enables one to describe the attenuation of the beam atoms.

2.2.4 Ranking of atomic lifetimes

The method of solving the statistical balance equations is now the point of interest. To determine the most convenient method of solution one has to compare the time scales on which the local plasma conditions change relative to the lifetimes associated with the excited levels of the neutral beam atoms. The local plasma conditions include the electron and ion density as well as their associated temperatures. If the atomic lifetimes are short in comparison to the time scales on which the local conditions change, the excited states of the beam neutrals can relax and achieve a steady-state equilibrium population. In such circumstances we can reduce the statistical balance equations to a simple system of linear equations i.e. $v_b dN_i/dx = 0$. We call this the quasi-static equilibrium solution. If however the local conditions change more rapidly which prevents the excited states to relax, a spatially dependent solution of the statistical balance equations is necessary.

The atomic lifetimes associated with the excited levels of an atom can vary enormously. However it is possible to separate the excited levels into three distinct categories according to their lifetime[29]. These are autoionising, ordinary and metastable levels. The lifetime of these levels respectively satisfy the inequality,

$$\tau_a \ll \tau_o \ll \tau_m \tag{2.10}$$

where τ_a is $\sim 10^{-12}$ s, τ_o is equal to the reciprocal of the associated transition probability and $\tau_m \sim 10/z_0^4$. To quantitatively assess the time scales on which the local conditions of the plasma change involves evaluating scaled lengths for both the electron and ion density and their respective temperatures[30]. The scaled lengths represent the spatial distance over which the beam atoms can travel before the former and latter parameters begin to change substantially. As an example the scaled length for the electron density is defined as,

$$\ell_{n_e} = \left[\frac{1}{n_e} \frac{dn_e}{dx} \right]^{-1} \quad 2.11$$

It is more convenient though to convert the scaled length into an apparent lifetime using the relation,

$$\tau_{n_e} = \frac{\ell_{n_e}}{v_b} \quad 2.12$$

The lifetime gives the time scale on which the electron density changes and can be used to compare with the atomic lifetime of the beam atoms. The time scales on which the remaining plasma parameters change are also obtained in a similar manner. In the present work though, to a good approximation, the time scales on which the local plasma conditions alter (τ_d) is comparable to the lifetime of the metastable levels. Therefore we can then extend the ranking of the lifetimes,

$$\tau_a \ll \tau_o \ll \tau_m \approx \tau_d \quad 2.13$$

In the case of modelling the excited population structure of neutral deuterium beam atoms, from the ranking of atomic lifetimes the excited states will reach an equilibrium population. To obtain the excited state population structure the statistical balance equations, excluding the ground state, can be reduced to a system of linear equations i.e. $\sum v_b dN_i/dx = 0$, see section 3.2.

Modelling the excited state population structure of a neutral helium beam is some what different. The presence of two excited metastable levels ($\text{He}(2s \ ^1S)$, $\text{He}(2s \ ^3S)$) complicates the modelling. In any case the excited states, excluding the

two metastable levels, will approach an equilibrium population. The statistical balance equations can be reduced to a system of linear equations with the exception of the ground and the two metastable levels i.e. $\sum v_b dN_i/dx = 0$, see section 3.3. It should be noted that it is also important to be able to calculate the population of the non-equilibrium metastable levels. This can be achieved via a spatially dependent solution of the statistical balance equations, see chapter 6.0.

2.3 Atomic processes associated with a neutral deuterium beam

The penetration of a neutral deuterium beam into a plasma is governed by the behaviour of the primary and secondary atomic processes which contribute to stripping the electrons from the neutral beam atoms. The primary atomic processes we consider first are for a pure D^+ plasma and are those which directly deplete the ground state, namely direct charge exchange as well as electron and ion impact ionisation. In figure 2.1 we show the fundamental cross sections for each process.

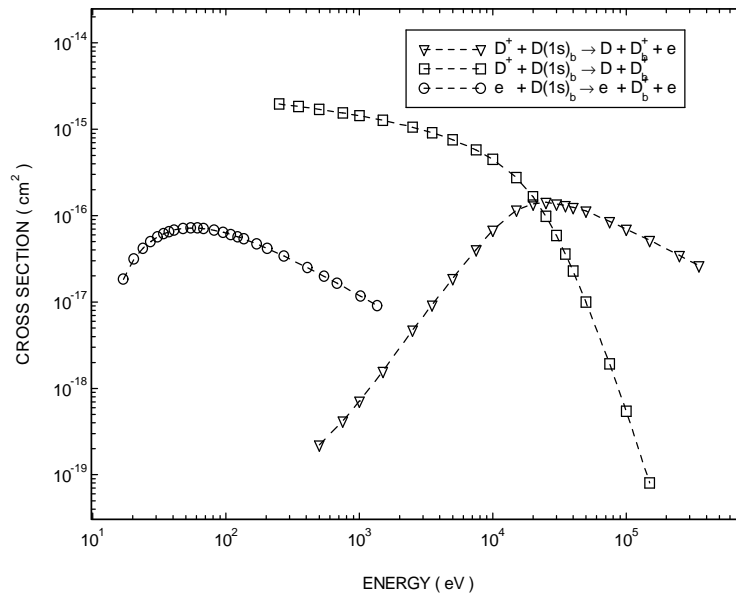


Figure 2.1 Cross sections for the direct atomic process associated with deuterium beam atoms.

As can be observed the contribution from each atomic process is determined by the relative collision energy. Charge exchange dominates until around 20 keV where the influence of ion impact ionisation becomes important. We emphasise that figure 2.1 shows the fundamental cross sections and not the rate coefficients, therefore the

contribution due to electrons appears to be very small. It should be noted that the electrons are moving with a velocity which is approximately 60 times faster than the D^+ ions and the resultant rate coefficient will be significant. Nevertheless charge exchange marginally remains the dominant process at the low energies.

The secondary atomic processes, which influence the ionisation of a penetrating deuterium beam, can be subdivided into two categories. The first category concerns bound-bound processes which excite the beam atoms and then contribute to the collisional and radiative redistribution amongst their excited states. The second category are the bound-free collisional processes which deplete the excited state populations. In the present context however we restrict ourselves to discussing the behaviour of the bound-bound and bound-free collisional processes, since under optically thin plasma conditions the only significant radiative process is that of spontaneous emission.

Collisional excitation and redistribution amongst the excited states are driven by electron and ion impact from the ground and neighbouring excited states. In the plasma, these processes are also accompanied by their corresponding reverse reactions, that is electron and ion impact de-excitation. In figure 2.2 we contrast the behaviour of the excitation cross sections for collisions with ions (D^+) and electrons. As can be observed, electron impact excitation is dominant at the lower energies. As the energy is increased, the contribution due to electron impact excitation becomes negligible as ion impact excitation becomes important.

The dominant bound-free processes responsible for ionising the excited state populations include ion impact ionisation and charge exchange. In figure 2.3 we contrast the behaviour of each process as a function of energy for different principal quantum shells. Also shown is the behaviour of electron impact ionisation from the $n=2$ and $n=3$ shell.

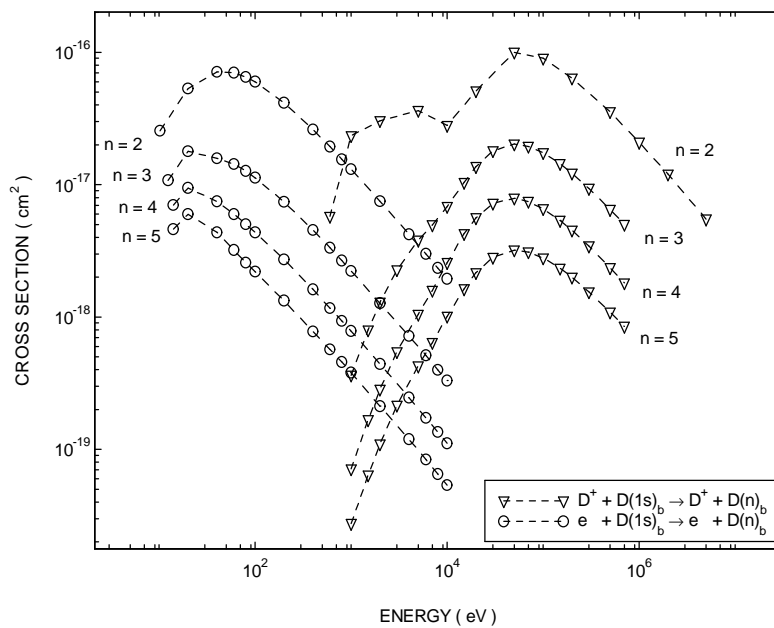


Figure 2.2 Cross sections for electron and ion impact excitation from the ground state to the $n = 2$, 3, 4 and $n=5$ shell.

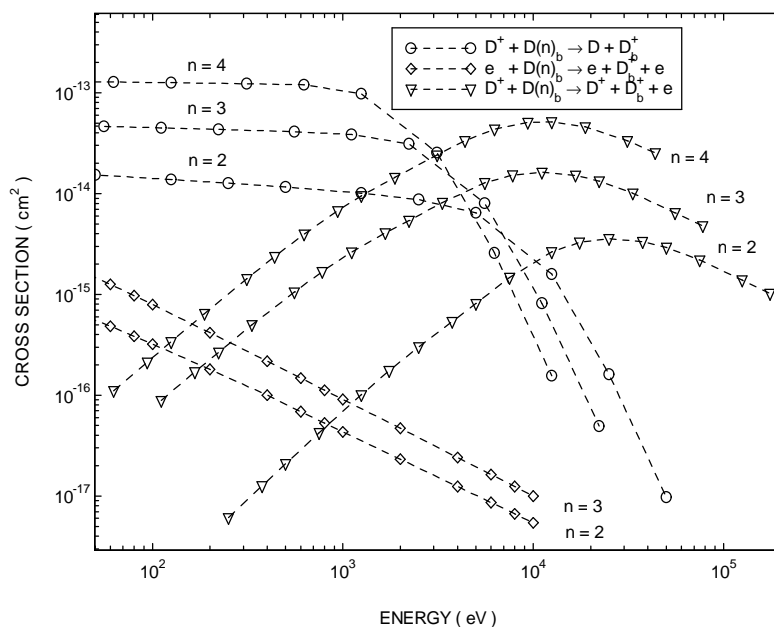


Figure 2.3 Impact ionisation and charge exchange cross sections associated with the $n=2$, 3 and $n=4$ shell.

As shown in figure 2.3, the contribution due to electron impact ionisation appears to be small due to the presence of charge exchange which is dominant up to 3.0 keV,

see earlier. We note the magnitude of the charge exchange and ion impact ionisation cross sections which increase with the principal quantum number (c.f. figure 2.1).

In tokamak plasmas the atomic processes associated with impurity ions should also be given some consideration, due to their unavoidable presence they can also contribute to stripping the electron from the neutral beam atoms. In figure 2.4 we show the cross sections for direct charge exchange and ion impact ionisation of the beam atoms due to collisions with a select range of fully stripped ions which are common plasma impurities.

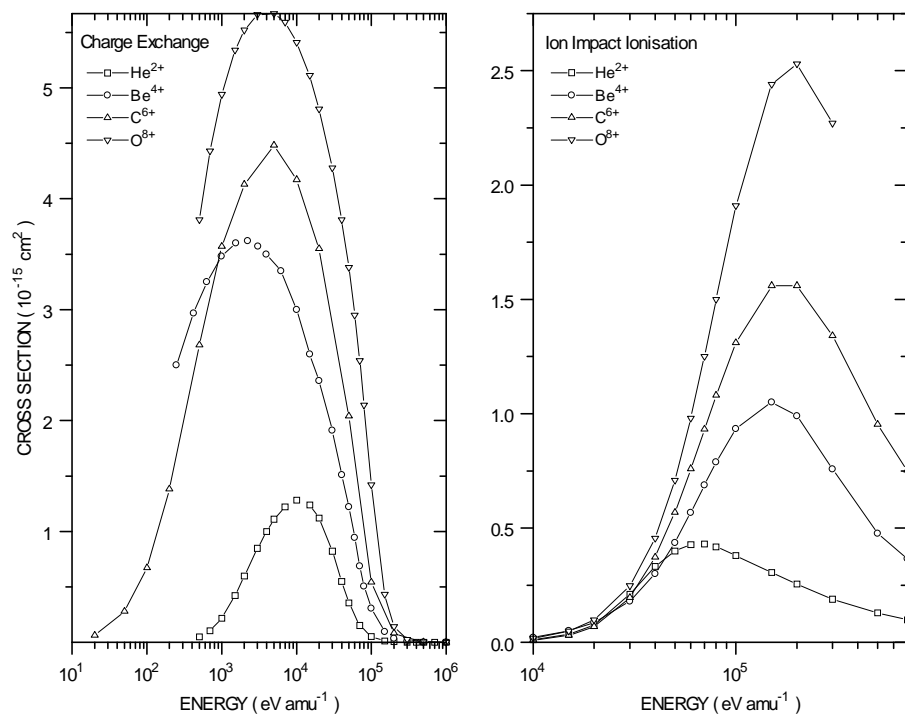


Figure 2.4 Cross sections for direct charge exchange and ion impact ionisation of the deuterium beam atoms for a selected range of fully stripped plasma impurity ions. The figure to the left exhibits the charge exchange cross sections while the figure to the right shows the behaviour of ion impact ionisation cross sections.

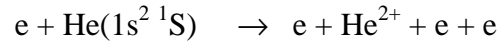
It can be observed from both figures, that the magnitude of the cross sections which describe each process increase with nuclear charge. Similar observations can be made for the remaining atomic processes associated with each of the impurity ions. These include ion impact excitation as well as charge exchange and ion impact ionisation from the excited states of the beam neutrals. The concentration of each impurity ion

in a tokamak plasma is small ($< 5\%$), however due to their large cross sections their influence on stripping the electrons from the beam atoms is comparable to that of the D^+ ions which is the main constituents of the plasma ($> 90\%$).

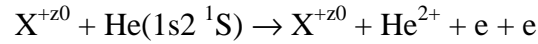
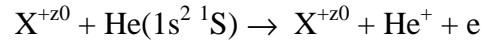
2.4 Atomic processes associated with a neutral helium beam

The penetration of a neutral helium beam into a tokamak plasma can similarly be characterised by the primary and secondary atomic processes which contribute to stripping the electrons from the neutral beam atoms. Due to the presence of two bound electrons associated with the beam atoms, both of which may be active, the variety and complexity of the primary and secondary processes increases substantially over that for a deuterium beam. The main processes are as follows,

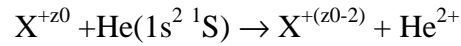
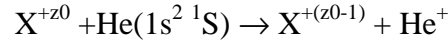
- (i) Single and double electron impact ionisation



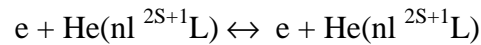
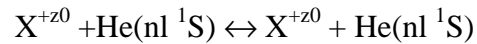
- (ii) Single and double ion impact ionisation



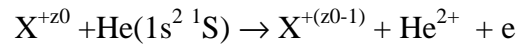
- (iii) Single and double charge exchange



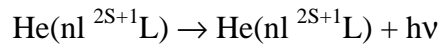
- (iv) Ion and electron impact excitation / de-excitation



- (v) Transfer double ionisation



- (vi) Spontaneous emission



The primary atomic processes which are responsible for directly stripping the electrons from the neutral helium beam atoms include single and double impact

ionisation, single and double charge exchange as well as single transfer ionisation. In figure 2.5 we show the cross sections which describe the behaviour of each of these processes.

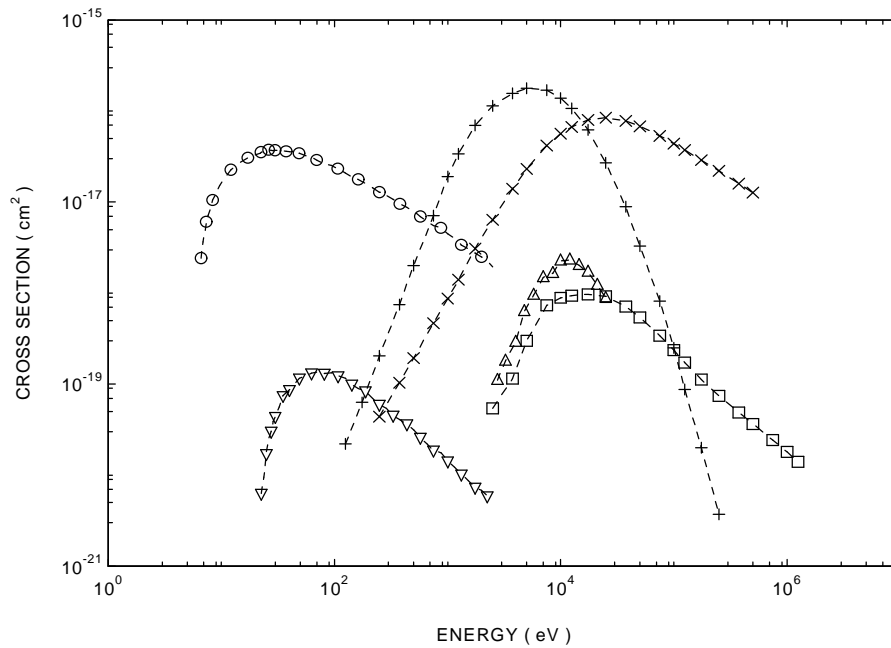


Figure 2.5 Cross sections for the primary atomic processes which contribute to stripping the electrons from the He($1s^2 \ ^1S$) ground state of the beam atoms. ○ : Single electron impact ionisation, ∇ : Double electron impact ionisation, + : Single charge exchange, × : Single ion impact ionisation, Δ : Transfer double ionisation, : Double ion impact ionisation .

As can be observed the role of single electron impact ionisation dominates at the lower energies. At ~ 750 eV single charge exchange becomes important and a competition between single ion impact ionisation commences. The competition continues until around ~ 17.5 keV where single ion impact ionisation becomes substantial.

In the same manner as discussed in section 2.3 for a deuterium beam, the secondary atomic processes which contribute to exciting and ionising a penetrating helium beam can be categorised into two sections. The first category concerns bound-bound processes whilst the second includes bound-free. We confine ourselves here to describing only the behaviour of bound-bound and bound-free collisional processes.

Collisional redistribution amongst the excited states of the beam atoms is primarily due to electron and ion impact excitation from the He($1s^2 \ ^1S$) ground and

neighbouring excited states. In the plasma, these processes are also accompanied by their corresponding reverse reactions. That is electron and ion impact de-excitation. Electrons can populate both the singlet and triplet excited states whilst ions can only populate the excited singlet states. This is due to the fact that for a spin changing transition to occur an exchange reaction between like particles is required. We show in figure 2.6 the behaviour of electron and ion (D^+) impact excitation from the $He(1s^2\ ^1S)$ ground state to various excited singlet levels.

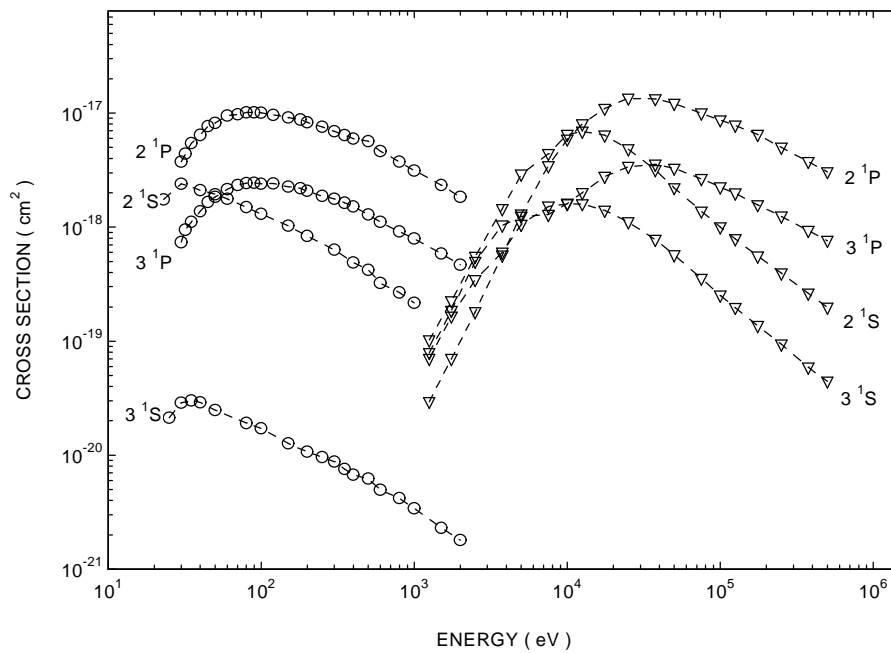


Figure 2.6 Cross sections for electron and ion impact excitation from the $He(1s^2\ ^1S)$ ground state to various excited singlet levels . O : Electron impact excitation, ∇ : Ion (D^+) impact excitation .

Electron impact excitation, as mentioned before, can also contribute to populating the triplet excited levels. This can occur through direct excitation from the ground state of the beam atoms or via excited state transitions from the singlet to triplet spin system. In figure 2.7 we show the behaviour of electron impact excitation from the ground to various excited triplet states. Also shown is the electron impact excitation cross sections from the $He(2s\ ^3S)$ metastable level to neighbouring excited levels.

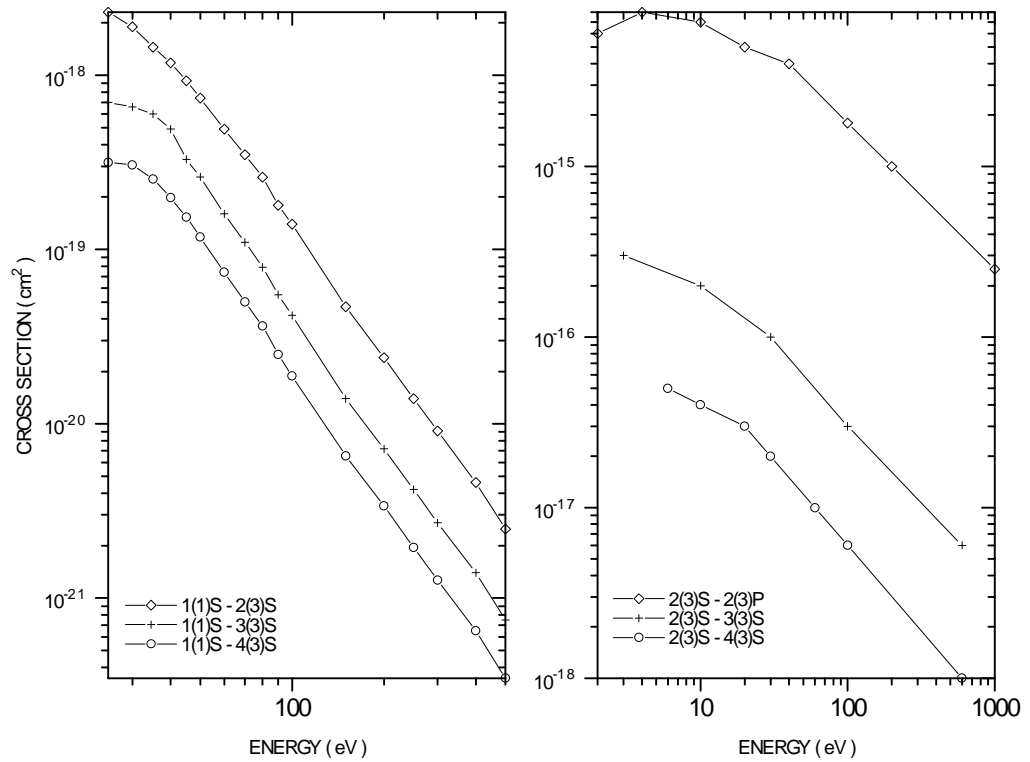


Figure 2.7 Cross sections for electron impact excitation. The figure to the left illustrates the behaviour of excitation from He($1s^2 \ ^1S$) to excited triplet levels. The figure to the right contains excitation cross sections for transitions from the He($2s \ ^3S$) metastable to neighbouring excited levels.

Due to the presence of metastable levels in helium i.e. He($2s \ ^1S$) and He($2s \ ^3S$), we should also focus our attention on the atomic processes associated with these levels. The motivation being that the metastable population may become significant as the beam penetrates into the plasma. Therefore the associated atomic processes will contribute substantially to stripping the electrons from the beam atoms. In figure 2.8 we show the behaviour of the primary atomic processes which contribute to stripping the electrons from the He($2s \ ^3S$) metastable level.

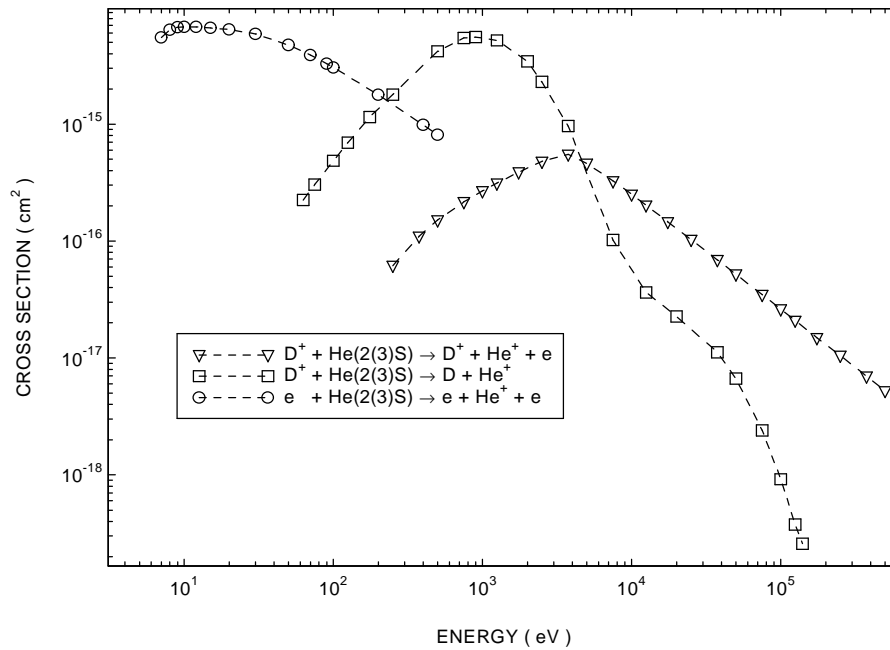


Figure 2.8 Cross sections for the atomic processes which contribute to stripping the electrons from the He($2s\ ^3S$) metastable level.

As can be seen, electron impact ionisation dominates until ~ 200 eV where the contribution due to charge exchange becomes substantial. In the usual manner ion impact ionisation competes with charge exchange. It is of interest to compare the behaviour of the atomic processes shown in figure 2.8 with the corresponding processes associated with the He($1s^2\ ^1S$) ground state, see figure 2.5. The cross sections involving the He($2s\ ^3S$) level are larger than that associated with the ground state. It can also be observed that the charge exchange cross section associated with the triplet metastable begins to dominate at ~ 200 eV and continues to do so until ~ 5.0 keV. In the case of the ground state the dominant behaviour of the charge exchange process occurs from ~ 750 eV to ~ 17.5 keV.

The influence of impurities contained in the plasma should also be taken into consideration since they will contribute to stripping the electrons from the helium beam atoms. In figure 2.9 we illustrate the behaviour of single and double charge exchange associated with the ground state of the beam atoms for a selected range of fully stripped ions which are common plasma impurities.

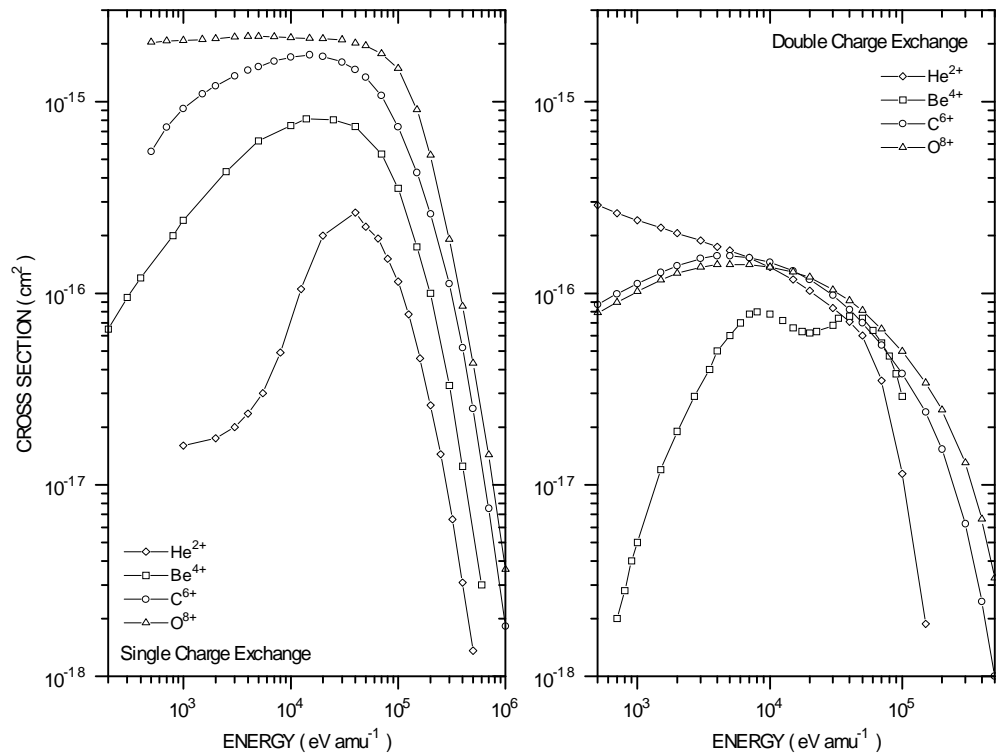


Figure 2.9 Single and double charge exchange cross sections associated with the $\text{He}(1s^2 \ ^1S)$ ground state. The figure to the left illustrates the cross sections for single charge exchange for a selected range of fully stripped ions which are common plasma impurities. The figure to the right shows the cross sections for double charge exchange.

As illustrated in the figure above, single charge exchange exceeds double charge exchange for all the ions with the exception of fully stripped helium. Below ~ 10 keV amu^{-1} double charge exchange dominates single charge exchange for helium. Double charge exchange between fully stripped helium and neutral helium atoms is a symmetrical resonant process and as a consequence has a large cross section[31]. In figure 2.10, we illustrate the behaviour of single and double ion impact ionisation for a similar variety of fully stripped plasma impurity ions.

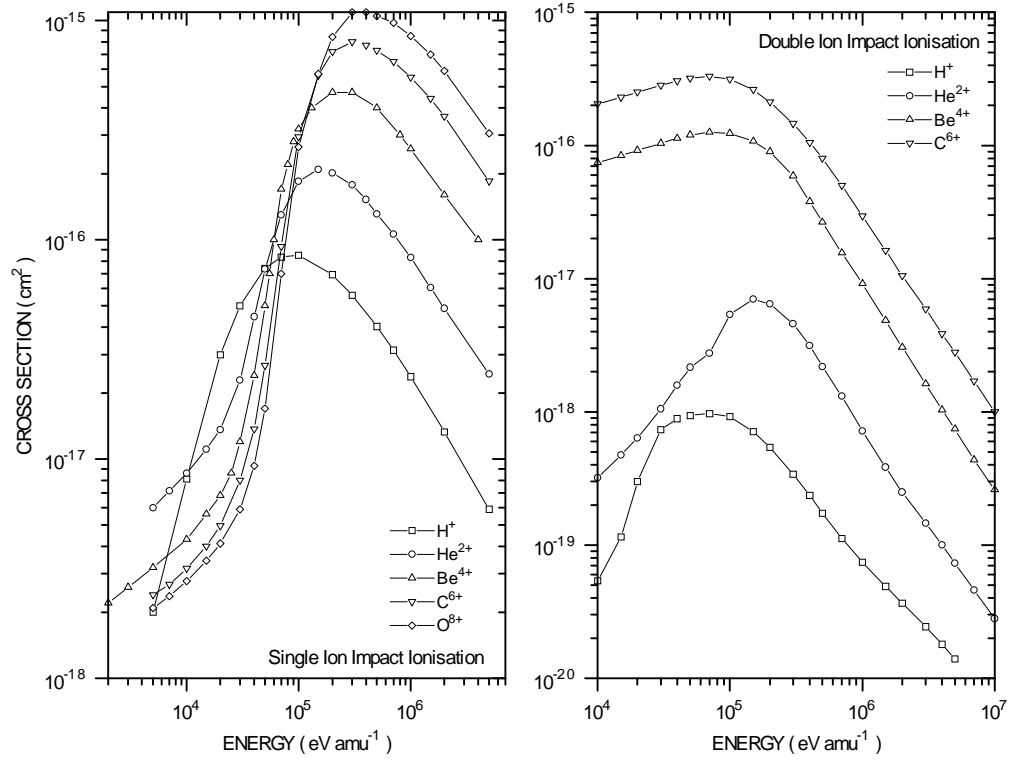


Figure 2.10 Cross sections for single and double ion impact ionisation from the $\text{He}(1s^2 \ ^1S)$ ground state of the beam atoms. The figure to the left shows the cross sections for single ion impact ionisation for a variety of fully stripped ions which are common plasma impurities. Also shown in the figure for comparison is the cross section describing single ion impact ionisation due to H^+ . The figure to the right illustrate the cross sections for double ion impact ionisation for a similar range of plasma impurities.

We must also take into consideration the contribution due to the plasma impurity ions at stripping electrons from the metastable levels of the beam atoms. In figure 2.11 we show the cross sections for charge exchange and ion impact ionisation from the $\text{He}(2s \ ^3S)$ metastable for a selected range of fully stripped plasma impurities.

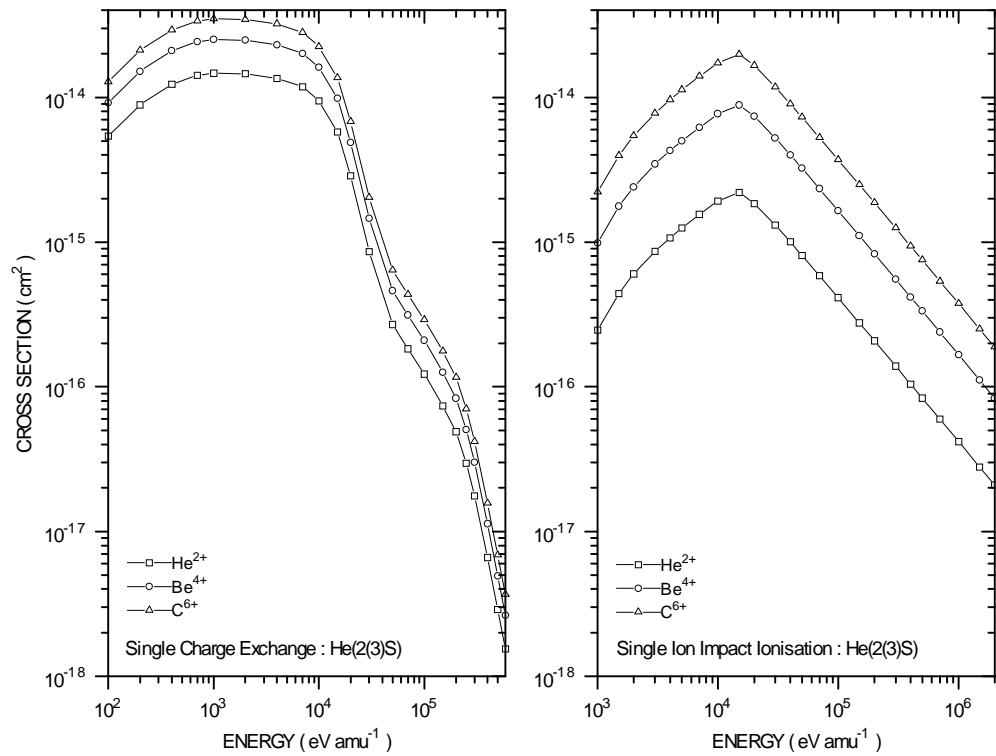


Figure 2.11 Charge exchange and ion impact ionisation from He($2s\ ^3S$) metastable level. The figure to the left illustrates the cross sections for single charge exchange for various fully stripped plasma impurity ions. The figure to the right exhibits the cross sections for ion impact ionisation .

It is of interest to compare the charge exchange cross sections shown above with the cross sections associated with the ground state of the beam atoms, see figure 2.9. It can be observed that the cross sections associated with the He($2s\ ^3S$) level are substantially larger than the cross sections associated with the ground state.

2.5 Approaches to modelling

When fast neutral beam atoms are injected into a tokamak plasma, the impurity ion impact atomic processes which excite and ionise the beam neutrals are the most important and so the population structure is primarily governed by the ion density. There are three different ‘pictures’ of the population structure which apply to the particular regimes of the ion density. These are schematically shown in figure 2.12

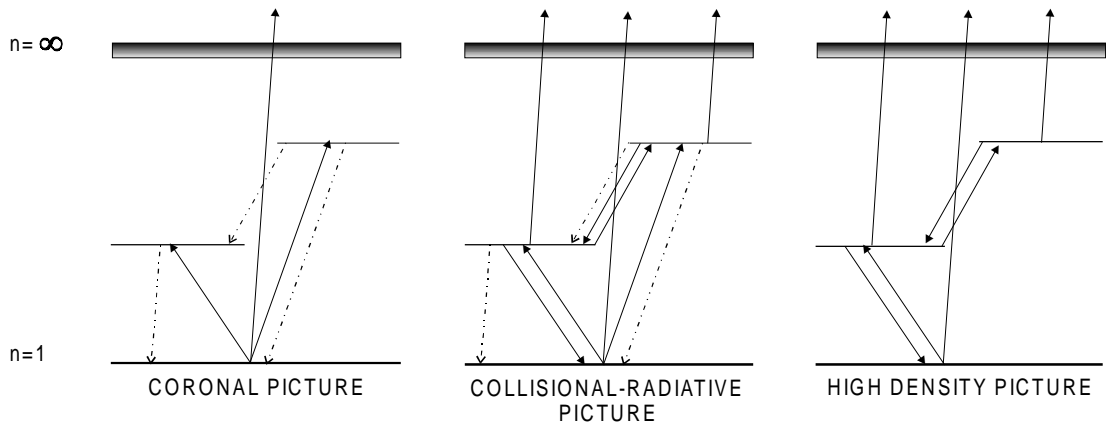


Figure 2.12 Schematic energy level structure of an arbitrary beam atom. The dashed and solid lines represent the radiative and collisional processes respectively. Working from left to right. Firstly the coronal picture, the beam atoms can only be ionised by direct collisional ionisation from the ground state. Next is the collisional-radiative picture where the beam atoms can be ionised by direct and stepwise atomic processes. Finally, the high density picture which describes the regime where the collisional processes completely dominate the radiative processes. Ionisation is due to direct and stepwise collisional processes, excitation also contributes to ionisation.

The first ‘picture’ applies to a low density plasma ($< 1.0 \times 10^{11} \text{ cm}^{-3}$ for pure D^+ plasma) where the conditions are such that the beam atoms can only be ionised by collisional ionisation (which may include charge transfer) from their ground state. There is no significant contribution to ionisation from the excited states. This is due to the fact that in this regime the excited populations are low relative to the ground population. The excited levels are populated by electron and ion impact excitation from the ground but rapidly depopulate by radiative decay before any further excitation or ionisation can occur. This is described as the coronal picture.

As the ion density of the plasma increases ($\sim 1.0 \times 10^{13} \text{ cm}^{-3}$ for a pure D^+ plasma), the influence of the collisional processes increases so that a competition with the radiative processes commences. The beam atom population structure is now determined by a wide range of collisional and radiative processes associated with their ground and excited states. The beam neutrals can now be ionised by direct and stepwise atomic processes. This is called the collisional-radiative picture.

The last ‘picture’ which is of interest occurs when the ion density of the plasma is increased substantially ($\sim 1.0 \times 10^{18} \text{ cm}^{-3}$ for a pure D^+ plasma), so that

collisional processes completely dominate the radiative processes. The contribution to the ionisation of the beam atoms is due to direct and stepwise collisional atomic processes associated with the ground and excited states. The excited state populations diminish. This is called the high density picture. In such a regime the condition of local thermodynamic equilibrium is achieved both for high and low lying levels.

2.5.1 Coronal equilibrium model

The coronal picture gives the simplest approach to obtain the excited state population structure of the beam atoms, as well as the rate at which they are being ionised. In this case, for the ionisation loss from the ground state there is no need to consider the contribution from the excited states. If we consider a simple case where the beam atoms have no metastables and the plasma is free of impurities, the statistical balance equations for the excited levels ($i > 1$) are of the form,

$$v_b \frac{dN_i}{dx} = \left(N_1 n_e q_{1 \rightarrow i}^e + N_1 n_p q_{1 \rightarrow i}^p + \sum_{j>i} N_j A_{j \rightarrow i} \right) - \left(\sum_{j<i} N_i A_{i \rightarrow j} \right) \quad 2.14$$

for $i = 2, 3, \dots$

where N_1 corresponds to the population of the ground state, $q_{1 \rightarrow i}^e$ and $q_{1 \rightarrow i}^p$ are the collisional excitation rates to level i due to electrons and protons respectively. The quantity $A_{i \rightarrow j}$ is the transition probability from the level i to level j . The population structure can be obtained by assuming the excited levels have relaxed and reached equilibrium relative to the instantaneous ground population. Therefore $v_b dN_i/dx = 0$ and equation 2.14 reduces to a set of linear equations which yield the excited populations relative to the ground state population N_1 by downward recursion. The corresponding statistical balance equation for the ground state is given as,

$$v_b \frac{dN_1}{dx} = \left[\sum_{j>1} N_j A_{j \rightarrow 1} \right] - \left[\sum_{j>1} (n_e q_{1 \rightarrow j}^e + n_p q_{1 \rightarrow j}^p) N_1 + (n_e q_{1 \rightarrow \infty}^e + n_p q_{1 \rightarrow \infty}^p + n_p q_{1 \rightarrow \infty}^{CX}) N_1 \right] \quad 2.15$$

where $q_{1 \rightarrow \infty}^e$, $q_{1 \rightarrow \infty}^p$ and $q_{1 \rightarrow \infty}^{cx}$ are the respective contributions due to direct electron and proton impact ionisation as well as charge exchange. If we then substitute equation 2.14, under the assumption that the excited states have reached equilibrium, into equation 2.15 we arrive at,

$$v_b \frac{dN_1}{dx} = -\left(n_e q_{1 \rightarrow \infty}^e + n_p q_{1 \rightarrow \infty}^p + n_p q_{1 \rightarrow \infty}^{cx}\right) N_1 \quad 2.16$$

Assuming that the majority of the beam atoms are initially in their ground state, this equation can then be used to model the attenuation of the beam. It is more convenient though to describe the attenuation of the beam in terms of an effective stopping cross section which is defined as,

$$\sigma_s = \left[q_{1 \rightarrow \infty}^e + \frac{n_p}{n_e} \left(q_{1 \rightarrow \infty}^p + q_{1 \rightarrow \infty}^{cx} \right) \right] \frac{1}{v_b} \quad 2.17$$

where σ_s is the effective beam stopping coefficient. The effective stopping coefficient can then be used to evaluate the beam attenuation at any given point along the beam using the following relation,

$$n_b = n_0 \exp\left(-\int n_e \sigma_s dl\right) \quad 2.18$$

where n_0 is the initial beam density on entry to the plasma and dl is along the path taken by the neutral beam. It should be noted however that equation 2.18 is only valid provided the beam atoms of interest does not contain any long lived metastable levels.

2.5.2 Collisional-radiative model

The simple coronal picture however is only applicable for low density plasmas where the radiative processes occur on time scales faster than the collisional processes. In tokamak plasmas the ion densities are sufficiently high and encourage the collisional

processes to compete with the radiative processes. The excited states of the beam atoms are populated and depopulated by both collisional and radiative processes. This is the so called collisional-radiative picture. The statistical balance equations for an arbitrary beam atom are,

$$\begin{aligned}
v_b \frac{dN_i}{dx} = & \sum_{i' > i} (A_{i' \rightarrow i} + n_e q_{i' \rightarrow i}^e + n_p q_{i' \rightarrow i}^p) N_{i'} + \sum_{i'' < i} (n_e q_{i \rightarrow i''}^e + n_p q_{i \rightarrow i''}^p) N_{i''} + \\
& \left(\alpha_i^{RR} + \alpha_i^{DR} + \frac{n_b}{n_e} \alpha_i^{CX} + \alpha_i^{(3)} n_e \right) n_+ n_e - \sum_{i' < i} (A_{i \rightarrow i'} + n_e q_{i \rightarrow i'}^e + n_p q_{i \rightarrow i'}^p) N_{i'} \\
& - \sum_{i > i'} (n_e q_{i \rightarrow i'}^e + n_p q_{i \rightarrow i'}^p) N_{i'} - (n_e q_{i \rightarrow \infty}^e + n_p q_{i \rightarrow \infty}^p + n_p q_{i \rightarrow \infty}^{CX}) N_i
\end{aligned} \quad 2.19$$

for $i = 1, 2, 3, \dots$

where $i'' < i < i'$ and $q_{i \rightarrow i'}$ is the excitation rate from state i to i' by electrons and protons according to the superscript. The corresponding de-excitation rate is given as $q_{i' \rightarrow i}$ and $A_{i' \rightarrow i}$ is the spontaneous emission coefficient for the radiative transition from level i' to i . Impact ionisation is represented by $q_{i \rightarrow \infty}$ where the superscript indicates whether it is by electrons or protons and the rate coefficient for charge exchange from state i is given as $q_{i \rightarrow \infty}^{CX}$. The quantities α^{RR} , α^{DR} and $\alpha^{(3)}$ are respectively the contributions due to radiative, dielectronic and three-body recombination. The quantity α^{CX} is the contribution due to charge exchange where the beam atoms themselves are the donors. It should be noted though that since the beam atoms are in a strictly ionising environment the latter and former recombining processes only become of interest when the neutral beam atoms are moving with such a slow velocity that they can be considered stationary. In which case the statistical balance equations describe the conditions of a thermal plasma rather than a point in the plasma which is traversed by a neutral beam.

The statistical balance equations in equation 2.19 form the basis of what is formally known as collisional-radiative modelling and is the method adopted in this work. Collisional-radiative modelling, as originally developed by Bates et. al.[32], involves solving the statistical balance equations while taking into consideration the influence of stepwise atomic processes. Quantities such as the excited population

structure and collisional-radiative coefficients are of interest. The collisional-radiative coefficients include effective cross coupling, ionisation and recombination coefficients.

To recast the statistical balance equations into the framework of generalised collisional-radiative theory a common starting point is to write equation 2.19 using matrix notation,

$$v_b \frac{dN_i}{dx} = n_e n_+ r_i - \sum_j C_{ij} N_j \quad 2.20$$

for $i = 1, 2, 3, \dots$

where C_{ij} ($C_{ij} \equiv C_{j \rightarrow i}$) is the collisional-radiative matrix for which the matrix elements are defined as follows.

$$C_{ij} = \begin{cases} A_{j \rightarrow i} + n_e q_{j \rightarrow i}^e + n_p q_{j \rightarrow i}^p & j > i \\ n_e q_{j \rightarrow i}^e + n_p q_{j \rightarrow i}^p & j < i \end{cases} \quad 2.21$$

and,

$$C_{ii} = - \sum_{j < i} \left(A_{i \rightarrow j} + n_e q_{i \rightarrow j}^e + n_p q_{i \rightarrow j}^p \right) - \sum_{j > i} \left(n_e q_{i \rightarrow j}^e + n_p q_{i \rightarrow j}^p \right) - n_e q_{i \rightarrow \infty}^e - n_p q_{i \rightarrow \infty}^p - n_p q_{i \rightarrow \infty}^{CX} \quad 2.22$$

The variable r_i is the composite recombination coefficient and is defined as,

$$r_i = \alpha_i^{RR} + \alpha_i^{DR} + \frac{n_b}{n_e} \alpha_i^{CX} + \alpha_i^{(3)} n_e \quad 2.23$$

Following the work of Spence[19], if we generalise and assume that the beam atoms of interest have m ‘non-equilibrium’ levels (that is levels whose populations are not locally relaxed), we can separate the ordinary excited levels which have reached local equilibrium from the non-equilibrium levels. Letting N_j^{eq} denote the equilibrium excited level populations then,

$$v_b \frac{dN_\rho}{dx} = n_e n_+ r_\rho - \sum_j C_{\rho j} N_j \quad 1 \leq \rho \leq m \quad 2.24$$

$$v_b \frac{dN_i}{dx} = 0 = n_e n_+ r_i - \sum_j C_{ij} N_j^{eq} \quad i > m \quad 2.25$$

where equation 2.24 describes the population of the non-equilibrium levels which are denoted by the Greek subscript ρ . The ground state is of course such a non-equilibrium level. Generally the ground state and metastable states are the non-equilibrium levels for beams in fusion plasmas. Equation 2.25 describes the behaviour of the excited levels which have reached equilibrium. Separating the non-equilibrium and equilibrium populations in 2.24 and 2.25 gives,

$$v_b \frac{dN_\rho}{dx} = n_e n_+ r_\rho - \sum_{j>m} C_{\rho j} N_j^{eq} - \sum_{\sigma=1}^m C_{\rho\sigma} N_\sigma \quad 2.26$$

$$0 = n_e n_+ r_i - \sum_{j>m} C_{ij} N_j^{eq} - \sum_{\sigma=1}^m C_{i\sigma} N_\sigma \quad 2.27$$

Therefore the equilibrium population can be obtained by multiplying equation 2.27 by the inverse of C_{ij} ,

$$N_j^{eq} = n_e n_+ \sum_{i>m} C_{ji}^{-1} r_i - \sum_{i>m} \sum_{\sigma=1}^m C_{ji}^{-1} C_{i\sigma} N_\sigma \quad j > m \quad 2.28$$

If we now substitute this equation back into equation 2.26 we arrive at,

$$v_b \frac{dN_\rho}{dx} = n_e n_+ \left[r_\rho - \sum_{j>m} \sum_{i>m} C_{\rho j} C_{ji}^{-1} r_i \right] - \sum_{\sigma=1}^m \left[C_{\rho\sigma} - \sum_{j>m} \sum_{i>m} C_{\rho j} C_{ji}^{-1} C_{i\sigma} \right] N_\sigma \quad 2.29$$

Which is more commonly written in terms of the time derivative as,

$$\frac{dN_\rho}{dt} = n_e n_+ \alpha_\rho - n_e \sum_{\sigma=1}^m S_{\rho\sigma} N_\sigma \quad 2.30$$

where $S_{\rho\sigma}$ is the cross coupling coefficient for the non-diagonal elements while the diagonal elements include the effective ionisation coefficient,

$$S_{\rho\sigma} = \left(C_{\rho\sigma} - \sum_{j>m} \sum_{i>m} C_{\rho j} C_{ji}^{-1} C_{i\sigma} \right) \frac{1}{n_e} \quad 2.31$$

and α_ρ is the collisional-radiative recombination coefficient,

$$\alpha_\rho = r_\rho - \sum_{j>m} \sum_{i>m} C_{\rho j} C_{ji}^{-1} r_i \quad 2.32$$

The rate at which electrons recombine from the continuum onto a non-equilibrium level ρ is given by the recombination coefficient α_ρ . The cross coupling coefficients describe the rate at which the non-equilibrium levels, including the ground state, are populated and depopulated within a collisional-radiative frame work. The cross coupling coefficients can also be used to obtained the collisional-radiative ionisation coefficients. These coefficients represent the rate at which the non-equilibrium levels of the beam atoms are ionised and are obtained using the following expression,

$$S_\rho = S_{\rho\rho} - \sum_{\sigma=1}^{\rho-1} S_{\rho\sigma} - \sum_{\sigma=\rho+1}^m S_{\rho\sigma} \quad 2.33$$

In the case of a deuterium beam, the only non-equilibrium level is the ground state. The $2s \ ^2S$ level is not a non-equilibrium level since there is strong $2s \ ^2S \rightarrow 2p \ ^2P$ collisional and field mixing. There are no cross coupling coefficients, only the single collisional-radiative ionisation coefficient. On the assumption that only the ground state of the beam atoms is significantly populated, this coefficient can be used to describe the rate at which the beam atoms are ionised and is commonly referred to as the effective beam stopping coefficient. It is converted into an effective beam stopping cross section by dividing through with the beam velocity. Using equation 2.18 the attenuation of a neutral deuterium beam can be calculated. The equilibrium populations of the excited states are simply evaluated relative to the ground state are equation 2.28.

For a neutral helium beam, there are three non-equilibrium levels. The ground state and the two metastable levels ($\text{He}(2 \ ^1S)$ and $\text{He}(2 \ ^3S)$). There is a total of nine

cross coupling coefficients and three effective ionisation coefficients. The Greek subscripts of equation 2.31 indicate the initial and final states associated with each coefficient. The diagonal elements represent the total population loss rate from the specified non-equilibrium level. This total loss rate includes the loss rate to the continuum as well as to the other remaining non-equilibrium levels, whilst the effective ionisation coefficients describe the rate at which electrons are lost from each of the non-equilibrium levels to the continuum. To model the attenuation of the beam we can no longer employ the simple expression of equation 2.18, a spatially dependent solution of the following set of equations is required.

$$\begin{aligned}
v_b \frac{dN_{1^1S}}{dx} &= n_e S_{1^1S} N_{1^1S} - n_e S_{2^1S \rightarrow 1^1S} N_{2^1S} - n_e S_{2^3S \rightarrow 1^1S} N_{2^3S} \\
v_b \frac{dN_{2^1S}}{dx} &= -n_e S_{1^1S \rightarrow 2^1S} N_{1^1S} + n_e S_{2^1S} N_{2^1S} - n_e S_{2^3S \rightarrow 2^1S} N_{2^3S} \\
v_b \frac{dN_{2^3S}}{dx} &= -n_e S_{1^1S \rightarrow 2^3S} N_{1^1S} - n_e S_{2^1S \rightarrow 2^3S} N_{2^1S} + n_e S_{2^3S} N_{2^3S}
\end{aligned} \tag{2.34}$$

where $N_{n \ 2S+1 \ L}$ is the population of the level specified by the quantum numbers n , S and L . The contribution to the equilibrium population of each excited state from each non-equilibrium level is calculated using equation 2.28.

2.6 Previous theoretical studies

2.6.1 Modelling neutral deuterium beam

The first attempt at modelling the attenuation of a neutral deuterium beam, as it entered into a tokamak plasma, was reported by Riviere[33] in 1971. Riviere employed a simple coronal type model to investigate the penetration depth of a beam as a function of typical plasma parameters. The approach of using a simple coronal type model was continued by many others[21, 34], even after the work of Boley et. al.[35]. Boley et. al. demonstrated that a collisional-radiative description was necessary to include all the atomic processes which contribute to ionising the beam

neutrals. A series of coupled differential equations, which spanned from the ground state to the Lorentz ionisation limit associated with the beam atoms, was employed to model the effective ionisation of the beam neutrals and hence the beam attenuation.

Although a lot of information regarding the beam attenuation was now available, little was known about the behaviour of the excited state population structure until the work of Summers[36] and the later efforts of Spence[19] at JET Joint Undertaking. Using a code which was originally based on the earlier work of Burgess and Summers[37], a detailed description of the excited population structure of the beam atoms was now readily available. Interest in the excited population structure of the beam atoms grew and was later modelled by Korotkov[38]. Using the method described by Boley et. al., Korotkov investigated both the excited population structure and the attenuation of neutral deuterium beam atoms. The excited state populations were calculated in what we describe as the bundled-n approximation. In which the population of each principal quantum shell are evaluated.

Due to the increased availability of high quality atomic data, the attenuation calculations of Korotkov were later revised by Janev et. al[39]. Janev et. al. conducted a more elaborate study of the beam attenuation and presented analytical fits to the effective beam stopping cross sections.

The present work develops from the original JET collisional-radiative model where we assemble a series of statistical balance equations in the bundled-nS approximation. The method of solution is complete and enables one to conduct a detailed study of the effective stopping coefficients as well as the excited state population structure. The code systematically accesses the most recent fundamental atomic data and employs a wide variety of formulae to generate the cross sections for transitions where there is no fundamental data available. We do not present our data in terms of analytical fits. ADAS as a matter of policy archives exact numerical data. The analytical fits of Janev et. al. are unsound in the low and high density asymptotic limits of the effective beam stopping cross sections. As an example we show in figure 2.13, a comparison between the results obtained in this work and the analytical fits of Janev et. al. as a function of beam energy

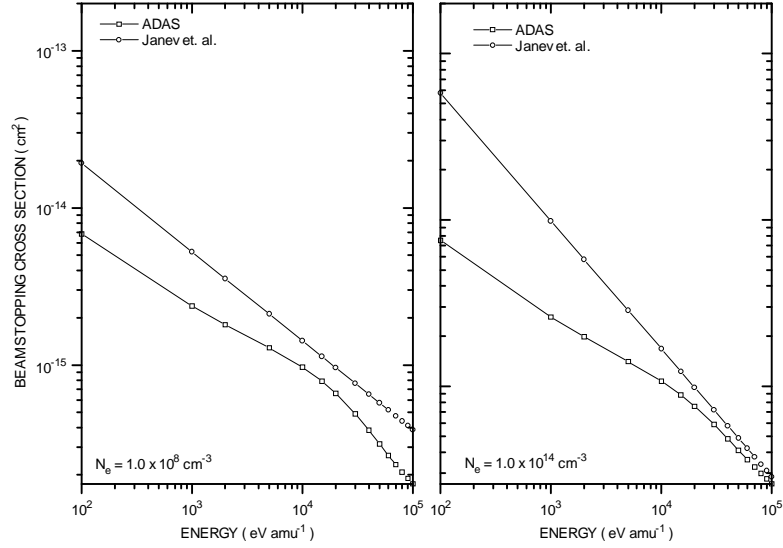


Figure 2.13 Beam stopping cross sections Vs energy for a pure H^+ plasma. Comparison between the analytical fits of Janev et. al.[39] and the results obtained from this work. The densities where selected to illustrate the difference at the coronal limit ($1.0 \times 10^8 \text{ cm}^{-3}$) and near the high density regime ($1.0 \times 10^{14} \text{ cm}^{-3}$).

2.6.2 Modelling a neutral helium beam

The application of a neutral helium beam as an edge or as a core diagnostic needs slightly different modelling approaches. As an edge diagnostic, a slow beam is employed to penetrate into the periphery of the plasma where the conditions are usually such that a spatially dependent solution of the statistical balance equations is required[12, 13]. For a fast neutral helium beam as a core diagnostic, the excited levels, with the exception of the metastables, have reached local equilibrium. There had been various attempts to model the attenuation and excited population structure of fast neutral helium beams[38,40]. However, the most significant contribution was due to the later work of Korotkov[41]. Using a series of coupled equations, Korotkov investigated the behaviour of the excited population structure and the beam attenuation under the assumption that the metastable levels had relaxed and reached equilibrium. The excited populations were calculated in what we describe as the bundled-nlSL approximation. The bundled-nlSL approximation involves evaluating

the population for each of the angular sub-states for the low lying levels, while the population of the higher levels are calculated in a bundled-nS approximation.

An attempt to include the influence of the non-equilibrium metastable levels on the population structure and attenuation was undertaken by a combined effort of Korotkov and Janev[42]. In addition to using improved fundamental data, Korotkov et. al., introduced an approximate method to describe the influence of the non-equilibrium levels.

In this work we model the attenuation and population structure of a neutral helium beam by assembling the complete set of coupled equations in the bundled-nSL approximation. The method of solution here however is more general and complete since we do not assume that the metastable level populations have relaxed. In these circumstances, the attenuation of the beam is no longer characterised by a single stopping coefficient. Rather it is described by a coupled set of three equations linked by collisional-radiative cross coupling coefficients. These cross coupling coefficients are also calculated in the full bundled-nSL model. We give considerable attention to using the most recent fundamental data and as for deuterium employ a variety of approximate methods to generate cross sections for transitions where there is no fundamental data available.

3.0 Collisional-radiative models for beam attenuation and emission

3.1 Introduction

In this chapter we discuss the formulation and computational implementation of the bundled-nS deuterium beam model within the context of ADAS. The bundled-nSL helium beam model is also presented in a similar manner. It should be noted that the bundled-nS model was originally written in FORTRAN by Burgess and Summers[37] and was later modified by Spence[19]. In this work our main contribution to the bundled-nS model has been the optimising and validation of the program. Then we deployed it to model the attenuation and emission associated with the neutral deuterium beams at JET, see chapter 5.0. The bundled-nSL model was extensively developed during the course of this work for application to helium beams, although the code had its origin in an existing program designed to model the excited population structure of atoms in an astrophysical plasma[43]. The bundled-nSL is also written in FORTRAN. We have also developed interactive programs which interrogate and archive the output from each of these collisional-radiative models. The details of these programs are also discussed in this chapter.

3.2 The bundled-nS model for a deuterium beam

The bundled-nS model evaluates the excited population structure of neutral deuterium. The model is a very many n-shell treatment, in which the populations of a representative set of principal quantum shells are calculated since matrix condensation techniques are used to render the problem tractable[37]. Due to the near energy degeneracy of the l-substates of deuterium, the bundled-nS approximation, in even low density tokamak plasmas, suffices. Even in circumstances, where the degeneracy is partially removed (for example by the motional Stark perturbation), to a good approximation the population of the sub-states for a given n are statistical at tokamak densities. Our model is general in that the deuterium atoms can either be in thermal plasma, which may possibly be traversed by a neutral beam, or be the main constituents of a beam. In the case of deuterium atoms in a thermal plasma, the excited population structure and collisional-radiative recombination and ionisation coefficients are evaluated. In the present work we are concerned with deuterium

atoms in a beam, therefore the quantities of interest include only the excited population structure and the collisional-radiative ionisation coefficients. The effective ionisation coefficient, as mentioned earlier, represents the rate at which the beam atoms are ionised as the beam traverses the plasma and is commonly referred to as the effective beam stopping coefficient.

The statistical balance equations of the bundled-nS model include all the processes which contribute to populating and depopulating each principal quantum shell. These take the form shown below.

$$\begin{aligned}
v_b \frac{dN_i}{dx} = & \sum_{i' > i} \left(A_{i' \rightarrow i} + U(\nu) B_{i' \rightarrow i} + n_e q_{i' \rightarrow i}^e + n_p q_{i' \rightarrow i}^p + n^{(imp)} q_{i' \rightarrow i}^{(imp)} \right) N_{i'} + \\
& \sum_{i'' < i} \left(U(\nu) B_{i'' \rightarrow i} + n_e q_{i'' \rightarrow i}^e + n_p q_{i'' \rightarrow i}^p + n^{(imp)} q_{i'' \rightarrow i}^{(imp)} \right) N_{i''} + \\
& \left(\alpha_i^{RR} + \frac{n_b}{n_e} \alpha_i^{CX} + \int U(\nu) B_{k \rightarrow i} dk + \alpha_i^{(3)} n_e \right) n_e n_+ - \\
& \sum_{i' < i} \left(A_{i \rightarrow i'} + U(\nu) B_{i \rightarrow i'} + n_e q_{i \rightarrow i'}^e + n_p q_{i \rightarrow i'}^p + n^{(imp)} q_{i \rightarrow i'}^{(imp)} \right) N_i - \\
& \sum_{i' > i} \left(U(\nu) B_{i \rightarrow i'} + n_e q_{i \rightarrow i'}^e + n_p q_{i \rightarrow i'}^p + n^{(imp)} q_{i \rightarrow i'}^{(imp)} \right) N_i - \\
& \left(n_e q_{i \rightarrow \infty}^e + n_p q_{i \rightarrow \infty}^p + n_p q_{i \rightarrow \infty}^p + n^{(imp)} q_{i \rightarrow \infty}^{(imp)} + \int U(\nu) B_{i \rightarrow k} dk \right) N_i
\end{aligned} \tag{3.1}$$

for $i = 1, 2, 3, \dots$

Note the presence of a radiation field. This is viewed here as a possible external radiation field penetrating the plasma. Although the external radiation field on the population structure is treated correctly in atomic terms it is actually for the present beam studies an artificial device for population modification. This is discussed in section 3.2.5. There is no actual external radiation field present in our JET studies. $U(\nu)B_{i \rightarrow i'}$ corresponds to the contribution due to photo-excitation ($i' > i$) and stimulated emission ($i' < i$). The quantity $\int U(\nu)B_{k \rightarrow i} dk$ is the contribution due to stimulated recombination and $\int U(\nu)B_{i \rightarrow k} dk$ is the photo ionisation rate. The influence of plasma impurities are also included in the statistical balance equations. The protons¹ contained in the plasma are treated as special plasma species while the

¹ We use the term 'protons' to refer to any of the isotopes of fully stripped hydrogen.

remaining ions are treated as ‘impurities’. The symbol $n^{(imp)}$ represents the total effective impurity density. In general several impurity species may be involved in collisionally inducing transitions. If we let the set of impurity charges and fractions be $\{z_{0i}^{(imp)}, f_i^{(imp)}; i=1,..I\}$. Then the total effective impurity density and the effective charge Z_{eff} , as evaluated by the bundled-nS model is,

$$n^{(imp)} = (n_e - n_p) / \left(\sum_{i=1}^I z_{0i}^{(imp)} f_i^{(imp)} \right) \quad 3.2$$

$$Z_{eff} = \left(n_p + n^{(imp)} \sum_{i=1}^I (z_{0i}^{(imp)})^2 f_i^{(imp)} \right) / n_e \quad 3.3$$

and the number density of each individual impurity ion is simply,

$$n_i^{(imp)} = n^{(imp)} f_i^{(imp)} \quad 3.4$$

In the case of a single impurity, which is frequently used as an effective impurity, it is convenient to alter the definition. The effective charge for a single impurity and its number density is now evaluated as,

$$z_0^{(imp)} = (Z_{eff} n_e - n_p) / (n_e - n_p) \quad 3.5$$

$$n^{(imp)} = (n_e - n_p) / z_0^{(imp)} \quad 3.6$$

The bundled-nS model employs a wide range of approximate methods to evaluate the rate coefficients associated with the atomic processes which are included in the statistical balance equations. For convenience it is assumed that the electron and ion temperature are identical. We should point out that the beam atoms are in a purely ionising regime, therefore it is unnecessary to include recombining processes such as radiative recombination (α^{RR}) and charge exchange (α^{CX}). These processes have only been included due to the general nature of the model. The program also accesses a collection of databases which contain more refined atomic data which is used to substitute the approximate methods where ever possible.

In the following sub-sections we briefly summarise the approximate methods and indicate the extent to which fundamental atomic data is used. A detailed account of the former is given by Spence[19]. We also outline the method which is adopted to solve the statistical balance equations.

3.2.1 Radiative atomic processes

We begin by first considering the spontaneous emission coefficient, which describes the rate at which an electron naturally decays from the upper level n to the lower level n' , this is calculated using the expression,

$$A_{n \rightarrow n'} = \left(\frac{16\alpha^4 c}{3\sqrt{3}\pi a_0} \right) \frac{z_0^4 g_{n,n'}^I}{n^3 n' (n^2 - n'^2)} \quad 3.7$$

where $g_{n,n'}^I$ is the bound-bound Gaunt factor[37], α is the fine structure constant, a_0 is the first Bohr orbit radius and z_0 is the nuclear charge of the beam atom. The spontaneous emission coefficient is then used to obtain expressions for the stimulated emission and photo-excitation coefficient. The Einstein B-values can be obtained using the following relations,

$$B_{n \rightarrow n'} = A_{n \rightarrow n'} \left/ \frac{8\pi}{c^3} h\nu^3 \right. \quad B_{n' \rightarrow n} = \frac{n^2}{n'^2} B_{n \rightarrow n'} \quad 3.8$$

Therefore the stimulated emission coefficient is,

$$U(\nu)B_{n \rightarrow n'} = \left(\frac{16\alpha^4 c}{3\sqrt{3}\pi a_0} \right) \frac{W z_0^4 g_{n,n'}^I}{n^3 n' (n^2 - n'^2)} \left[\exp\left(\frac{h\nu}{kT_r}\right) - 1 \right]^{-1} \quad 3.9$$

and the photo-excitation coefficient,

$$U(\nu)B_{n' \rightarrow n} = \left(\frac{16\alpha^4 c}{3\sqrt{3}\pi a_0} \right) \frac{W z_0^4 g_{n,n'}^I}{n n'^3 (n^2 - n'^2)} \left[\exp\left(\frac{h\nu}{kT_r}\right) - 1 \right]^{-1} \quad 3.10$$

where $U(\nu)$ is the energy density, T_r is the temperature of the radiation field and W is a dilution factor. The radiative recombination coefficient is evaluated using the following equation,

$$\alpha_n^r = 8 \left(\frac{\pi a_0^2 I_H}{k T_e} \right)^{3/2} \left(\frac{8 \alpha^4 c}{3 \sqrt{3} \pi a_0} \right) \frac{z_0^4}{n^3} \exp\left(I_n / k T_e \right) \int_{I_n / k T_e}^{\infty} \frac{g_{n,n}^{II} \exp(-x)}{x} dx \quad 3.11$$

where $g_{n,n}^{II}$ is the bound-free Gaunt factor[37] and $x = h\nu/kT_r$. The atomic process of photo-ionisation is now of interest . This coefficient is evaluated using the following expression,

$$\int U(\nu) B_{n \rightarrow \kappa} = \left(\frac{8 \alpha^4 c}{3 \sqrt{3} \pi a_0} \right) \frac{W z_0^4}{n^5} \int_{I_n / k T_r}^{\infty} \frac{g_{n,n}^{II}}{x [\exp(x) - 1]} dx \quad 3.12$$

and finally, the stimulated radiative recombination is given as,

$$\int U(\nu) B_{\kappa \rightarrow n} d\kappa = \frac{2^6}{3 \sqrt{3}} \left(\frac{\pi^{1/2} a_0^2 \alpha^4 c I_H^{3/2}}{k^{3/2} T_e^{3/2}} \right) \frac{W z_0^4}{n^3} \exp\left(I_n / k T_e \right) \int_{I_n / k T_r}^{\infty} \frac{g_{n,n}^{II} \exp(-T_r x / T_e)}{x [\exp(x) - 1]} dx \quad 3.13$$

3.2.2 Collisional atomic processes

There are three methods which the bundled-nS model can use to evaluate electron impact excitation rates. These include the method of Van Regemorter[44], the impact parameter approximation[37] and the prescription by Percival and Richards[45]. The method of Van Regemorter involves describing the electron excitation rate coefficients with effective P-factors. The electron impact excitation is then given as,

$$q_{n' \rightarrow n} = \frac{2^8}{3} \left(\frac{2 \sqrt{\pi} \alpha c a_0^2}{3} \right) \frac{n^5 n'^3}{(n^2 - n'^2)^4} \frac{g_{n,n'}^I}{z_0^2} \left(\frac{I_H}{k T_e} \right)^{3/2} \exp\left(-\frac{\Delta E_{n,n'}}{k T_e} \right) P\left(\frac{\Delta E_{n,n'}}{k T} \right) \quad 3.14$$

where $P(\Delta E_{n,n'}/kT_e)$ is the Van Regemorter P-factor and $\Delta E_{n,n'}$ is the transition energy between the levels n and n' . The corresponding de-excitation rate is then give as,

$$q_{n \rightarrow n'} = \frac{2^8}{3} \left(\frac{2\sqrt{\pi}\alpha c a_0^2}{3} \right) \frac{n^5 n'^3}{(n^2 - n'^2)^4} \frac{g_{n,n'}}{z_0^2} \left(\frac{I_H}{kT_e} \right)^{3/2} P \left(\frac{\Delta E_{n,n'}}{kT_e} \right) \quad 3.15$$

The basic expression to obtain the electron impact excitation cross-sections using the impact parameter method is,

$$\sigma_{n' \rightarrow n} = 2\pi \int_0^{\infty} P_{n' \rightarrow n} b db \quad 3.16$$

where b is the impact parameter and $P_{n' \rightarrow n}$ is the probability of the target electron being excited from the level n' , to the upper level n . As discussed in detail by Burgess and Summers[37], the probability $P_{n' \rightarrow n}$, can be evaluated using time dependent perturbation theory. However perturbation theory is only valid for weak coupling i.e. at large impact parameters. Therefore Burgess and Summers have derived expression according to whether the impact parameter is large enough to be considered for weak coupling or small enough for strong coupling. To avoid digressing we simply quote their results. In the case of weak coupling the excitation cross section is,

$$\sigma_{n' \rightarrow n} = \frac{I_H}{W_n} \left[8 \left(\frac{I_H}{\Delta E_{n,n'}} f_{n \rightarrow n'} \right) Y(\xi, \delta_0) \right] \pi a_0^2 \quad 3.17$$

and for strong coupling the excitation cross section described,

$$\sigma_{n' \rightarrow n} = \frac{I_H}{W_n} \left[8 \left(\frac{I_H}{\Delta E_{n,n'}} f_{n \rightarrow n'} \right) Y(\xi, \delta_1) + \frac{z}{a_0} R_1^c + 0.5 k_n k_{n'} (R_1^c)^2 \right] \pi a_0^2 \quad 3.18$$

A detailed description of each equation can be found in the [37]. Finally, the prescription of Percival and Richards[45], which is based on a combination of semi-classical methods and experimental data, yields the following expression,

$$\sigma_{n' \rightarrow n} = \frac{n^4 I_H \pi \alpha_0^2}{z_0^2 E} (ADL + FGH) \quad 3.19$$

the details of which can be found in [45]. The corresponding collisional de-excitation cross sections for both the impact parameter and the latter method are calculated using the principle of detailed balance.

If we now consider electron impact ionisation. There is only one approximate method which is available for use in the bundled-nS model. This is the Exchange Classical Impact Parameter (ECIP) method of Burgess[46]. The electron impact ionisation rate from the level denoted by the principal quantum number n is given as,

$$q_{n \rightarrow \infty} = (8\sqrt{\pi} \alpha c a_0^2) \left(\frac{I_H}{kT_e} \right)^{1/2} \frac{n^2}{z_0^2} \exp\left(-\frac{I_n}{kT_e} \right) \int_0^{\infty} G \exp(-\xi) d\xi \quad 3.20$$

where $\xi = (W_n - I_n) / kT_e$ and G is defined as,

$$G = \left[\left(\frac{W_n/I_n - 1}{W_n/I_n + 1} \right) - \frac{W_n/I_n}{(W_n/I_n + 1)^2} \ln\left(\frac{W_n}{I_n} \right) + \frac{1}{4} I^{IP}(W_n) \right] \quad 3.21$$

W_n is the initial energy of the incident electron and I^{IP} is the contribution due to impact parameter[37]. This expression is then used to obtain the three body recombination rate coefficient,

$$\alpha_n^{(3)} = 2^6 \pi^2 (\alpha c a_0^5) \left(\frac{I_H}{kT_e} \right)^2 \frac{n^4}{z_0^2} \int_0^{\infty} G \exp(-\xi) d\xi \quad 3.22$$

We now consider the methods which are employed to evaluate the ion impact excitation cross-sections. There are three different methods which are available for use. These include the impact parameter method[37], the semi-empirical formula of Lodge et. al.[47], and the two state approximation of Vainshtein et. al.[48]. The impact parameter method involves similar expressions to equations 3.17 and 3.18. A detailed description is given by Burgess and Summers[37]. The semi-empirical formula of Lodge et. al is based on a combination of semi-classical methods and experimental data. The resultant formula, for which the details can be found in [47] is,

$$\sigma_{n' \rightarrow n} = \frac{n^4 \pi a_0^2}{\epsilon} (ADL + FGH) \quad 3.23$$

The two state approximation of Vainshtein et. al.[48] describes the behaviour of ion impact excitation with the following equation,

$$\sigma_{n' \rightarrow n} = 2\pi \left(\frac{\lambda}{v} \right) \exp(-2\sqrt{2\beta}) I(\beta) \quad 3.24$$

where $I(\beta)$ is calculated from a definite integral and λ is related to the oscillator strength[48]. The corresponding de-excitation cross sections for each method are also obtained using the principle of detailed balance. The last approximate method concerns ion impact ionisation. The bundled-nS model employs the binary encounter formula of Percival and Richards[49].

3.2.3 Beam thermal rate coefficients

The approximate methods employed by the bundled-nS model, with the exception of the method of Van Regemorter, evaluates the cross sections which described the behaviour of the collisional processes. However to assemble the statistical balance equations we must convert the cross sections into beam-thermal rate coefficients.

The collision between two particles in a thermal plasma is characterised by their relative velocity. The associated rate coefficient is defined as,

$$\langle v_r \sigma(v_r) \rangle = \int_{v_{\min}}^{\infty} \int_{v_{\min}}^{\infty} v_r f(v_p) f(v_t) \sigma(v_r) dv_p dv_t \quad 3.25$$

where v_r is the relative velocity between the target and the projectile. The quantities $f(v_t)$ and $f(v_p)$ are the corresponding velocity distributions for each particle. In the present work the projectiles are the beam atoms, which have a known velocity, and the target particles are the thermal ions contained in the plasma. Therefore the rate coefficient for the collision between the beam neutrals and target ions is,

$$\langle v_r \sigma \rangle = \int_{v_{\min}}^{\infty} v_r \sigma(v_r) f(v_t) dv_t \quad 3.26$$

The relative velocity is defined as $v_r = |v_p - v_t|$, which is expressed as,

$$v_r = |v_p - v_t| = \sqrt{v_p^2 + v_t^2 + 2v_p v_t \cos \vartheta} \quad 3.27$$

where ϑ is defined as the angle between the projectile and the target. The beam-thermal rate coefficient as evaluated in the bundled-nS model is then defined as,

$$\langle v_r \sigma(v_r) \rangle = \frac{1}{2} \int_0^{\pi} \int_{v_{\min}}^{\infty} v_r \sigma(v_r) f(v_t) \sin \vartheta dv_t d\vartheta \quad 3.28$$

It is of interest to point out that electrons in the plasma are moving with velocities much greater than that of the beam atoms. Therefore the rate coefficients associated with electron collisions are effectively independent of the beam velocity.

3.2.4 Fundamental atomic data

The supplementary data which is utilised by the bundled-nS model is now considered. There are three main databases which contain electron impact excitation, electron impact ionisation and ion-atom collision data respectively. If we first concern ourselves with electron impact excitation database. This database contains electron impact excitation coefficients which are stored in the form of effective

collision strengths[29]. The effective collision strengths are tabulated for transitions up to the n=5 shell. This data is periodically updated and is a combination of both theoretical and experimental data. During the course of this work the contents of the database was based on the calculations of Sampson and co-workers [50,51,52] and the data of Callaway[53]. This database also contains a compilation of spontaneous emission coefficients, the details of which can be found in [54]. Turning our attention to the electron impact ionisation database. This database contains Maxwell averaged rate coefficients which are periodically updated. The contents of the database during this work was based on the data reported by Bell et. al.[55]. The last database of concern, which is the largest by far, contains a wide range of ion-atom collision data. The database contains cross sections for charge exchange and ion impact ionisation from the ground and excited states up to the n=5 shell. Ion impact excitation data up to the n=5 shell is also included. The data is stored in the format of raw cross sections and encompasses the reactions mentioned for all the impurity species up to the first period. A detailed review of this database can be found in appendix A.

3.2.5 Method of solution

Due to the generalised nature of the bundled-nS model, rather than simply solving for the excited populations, an alternative approach is adopted. There are three basic driving mechanisms which are responsible for populating the excited levels of deuterium. These include charge exchange recombination, excitation from the ground state and recombination of free electrons. The model solves the statistical balance equations for each of the individual contributions associated with every principal quantum shell of interest. To obtain the individual contributions we start from the statistical balance equation written in matrix notation,

$$v_b \frac{dN_i}{dx} = n_e n_+ r_i - \sum_j C_{ij} N_j \quad 3.29$$

If we now re-write this expression in the form,

$$v_b \frac{dN_i}{dx} = n_e n_+ \mathfrak{R}_i + n_b n_+ \alpha_i^{CX} - \sum_j C_{ij} N_j \quad 3.30$$

where \mathfrak{R}_i is defined as,

$$\mathfrak{R}_i = \alpha_i^{RR} + n_e \alpha_i^{(3)} + \int U(v) B_{\kappa \rightarrow i} d\kappa \quad 3.31$$

We can now re-write expression 3.30 in terms of the quasi-static and non-equilibrium levels using the notation of chapter 2.0,

$$v_b \frac{dN_i}{dx} = n_e n_+ \mathfrak{R}_i + n_b n_+ \alpha_i^{CX} - \sum_{j>m} C_{ij} N_j^{eq} - \sum_{\sigma=1}^m C_{i\sigma} N_\sigma \quad 3.32$$

The expression for the equilibrium populations is,

$$N_j^{eq} = n_e n_+ R_j + n_b n_+ G_j + \sum_{\sigma=1}^m E^\sigma N_\sigma \quad 3.33$$

which distinguishes the different driving mechanisms,

$$R_j = \sum_{i>m} C_{ji}^{-1} \mathfrak{R}_i \quad 3.34$$

$$G_j = \sum_{i>m} C_{ji}^{-1} \alpha_i^{CX} \quad 3.35$$

$$E^\sigma = - \sum_{i>m} C_{ji}^{-1} C_{i\sigma} \quad 3.36$$

R_j , G_j , and E^σ are respectively the contributions which populate the excited levels of the beam atoms due to recombination, charge exchange and excitation from the non-equilibrium levels. For deuterium the number of non-equilibrium levels is one, therefore equation 3.33 now reads as,

$$N_j^{eq} = n_e n_+ R_j + n_b n_+ G_j + E^1 N_1 \quad 3.37$$

Rather than solving this equation directly it is more convenient to solve for the ‘ b_n -factors’ which are defined using the modified Saha-Boltzmann equation,

$$N_n = n_e n_+ 8 \left(\frac{\pi a_0^2 I_H}{kT_e} \right)^{3/2} n^2 \exp\left(\frac{I_n}{kT_e} \right) b_n \quad 3.38$$

The b_n factors describe the deviation from thermodynamic equilibrium at which they should be equal to a value of one. If we substitute the modified Saha-Boltzmann equation into equation 3.37 we arrive at,

$$b_n = F_{(n)}^1 \left(\frac{N_1}{n_+} \right) + F_{(n)}^2 + F_{(n)}^3 \left(\frac{n_b}{n_e} \right) \quad 3.39$$

where $F_{(n)}^1$, $F_{(n)}^2$ and $F_{(n)}^3$ are respectively the contributions which populate the level n due to excitation from the ground, recombination and charge exchange. The quantity n_b is the beam density and N_1 is the population of the ground state of the beam neutrals. In the present context our interest is with the $F_{(n)}^1$ quantity, since this gives the contribution which populates the excited levels of the beam atoms from their ground state.

We have a computational algorithm for distinguishing these contributions, we first fix the beam density to zero, this sets the contribution due to charge exchange to zero. We then apply a synthetic radiation field which depopulates the ground state due to the inclusion of photo-ionisation in the statistical balance equations. The $F_{(n)}^2$ recombination contribution can be calculated in isolation. If we then switch off the radiation field and keep the beam density as zero we can then evaluate the $F_{(n)}^1$ contribution. Finally, if the radiation field is set to zero and the beam density is not equally to zero the $F_{(n)}^3$ contribution can be calculated.

The quantities which are tabulated as output from the model include the b_n , $F_{(n)}^1$, $F_{(n)}^2$ and $F_{(n)}^3$ components. The solution of the Saha-Boltzmann equation in the form the $N_n/b_n \times n_+$ is also tabulated along with the effective beam stopping coefficients. Therefore the excited state population relative to the ground state can be obtained from the output since,

$$\frac{N_n}{N_1} = F_{(n)}^1 \left(\frac{N_n}{b_n n_+} \right) \quad 3.40$$

which allows us to define the effective beam emission coefficient for the transition $n \rightarrow n'$ as,

$$q_{n \rightarrow n'}^{BES} = \frac{A_{n \rightarrow n'}}{n_e} F_{(n)}^I \left(\frac{N_n}{b_n n_+} \right) \quad 3.41$$

where $A_{n \rightarrow n'}$ is the transition probability. The effective beam emission coefficient is the number of photons emitted per unit volume per second. The beam emission coefficient is employed to recover the neutral beam density from the D_α emission from the excited beam atoms in experimental analysis, see chapter 5.0.

3.3 The bundled-nISL model for a helium beam

The bundled-nISL model has been designed to operate in a similar manner to the bundled-nS model. The bundled-nISL models calculates the excited population structure of helium atoms either in a optically thin thermal plasma or in a mono-energetic beam penetrating into a plasma. It is an nl-spin resolved model which calculates the populations of the l-substates from the ground state up to an arbitrary principal quantum number, above which a bundled-nS treatment is then adopted, see figure 3.1.

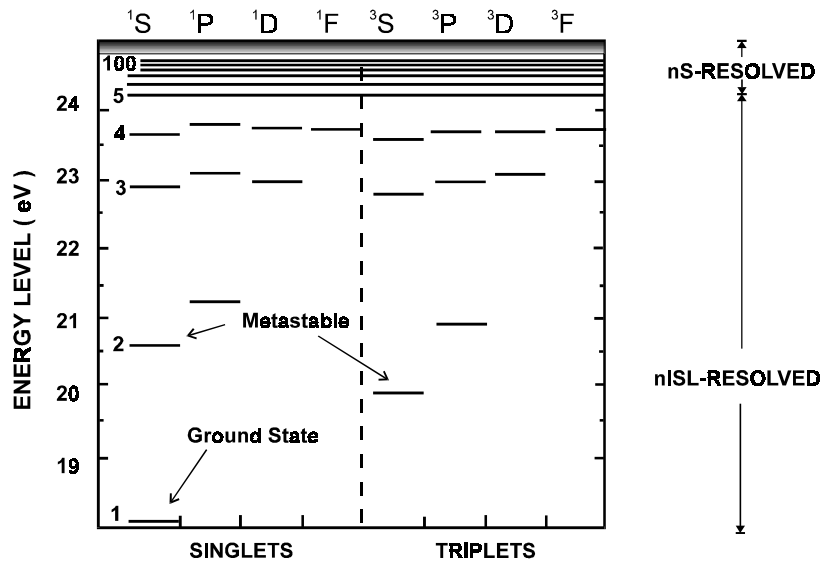


Figure 3.1 Schematic illustration of the bundled-nISL model. The low levels are calculated in an nl-resolved picture up to an arbitrary principal quantum shell, above which a bundled-nS treatment is adopted.

The switching of principal quantum numbers is such that for it and higher principal quantum shells l-redistribution is effectively complete. The ground state and the He(2 ¹S) and He(2 ³S) metastables are treated as non-equilibrium levels. Therefore the equilibrium populations of the excited states are calculated relative to each non-equilibrium level. The statistical balance equations are similar to those of the bundled-nS model but contain additional processes which were not applicable in the nS-resolved picture. These include spin changing electron collisions and collisional transitions between degenerate levels. The statistical balance equations written in matrix notation are as before,

$$v_b \frac{dN_i}{dx} = n_e n_+ \mathfrak{S}_i - \sum_j \mathcal{C}_{ij} N_j \quad 3.42$$

for $i = 1, 2, 3, \dots$

However \mathfrak{S}_i now includes recombining terms to both the singlet and the triplet excited levels and the collisional-radiative matrix is of the form,

$$\mathcal{C}_{ij} = \left[\begin{array}{c|c} \textit{Singlets} & T \rightarrow S \\ \hline S \rightarrow T & \textit{Triplets} \end{array} \right] \quad 3.43$$

where the top left hand partition concerns the atomic rates associated with the pure singlet spin system. The top right hand partition includes the atomic rates which describe the collisionally induced transitions from the triplet to singlet spin system (electron exchange collisions). The bottom right hand partition includes the atomic rates for a pure triplet spin system and the associated left hand partition contains the spin changing contribution from the singlet to the triplet spin system. The diagonal elements of the collisional-radiative matrix describes the total loss rate from each level as previously.

The approximate methods used to evaluate the cross-sections and rate coefficients in the bundled-nS model are relevant for hydrogenic and non-hydrogenic

ions in the bundled-nlSL model but require a specification of how they are to be fractionated over l-substates. In the following sub-sections we summarise the differences in the way they have been implemented. We also discuss the approximate methods employed for the atomic processes which were not applicable to the bundled-nS model. The bundled-nlSL model also accesses several databases in the same manner as the bundled-nS model, and we detail which fundamental atomic data is used. Finally, we outline the method of solving the statistical balance equations when there are three non-equilibrium levels.

3.3.1 Radiative processes

As mentioned earlier, the approximate methods employed in the bundled-nS model can be used for hydrogenic and non-hydrogenic ions in the bundled-nlSL model. Where appropriate however exact energy levels and statistical weights for helium are adopted. Exact energy levels for the low levels in the bundled-nlSL model are expanded over the complete manifold of levels using the quantum defect method for each spin system. That is the quantum defect is calculated using a series expansion.

$$\mu = a_1 + a_2 E_1 + a_3 E_2^2 + a_4 E_3^3 \quad 3.44$$

where the energy levels E_1 , E_2 and E_3 are the exact values which are entered as input. This is repeated for the s, p, and d l-series and for both spin systems with the energy levels then calculated from,

$$E_{nl} = \frac{z_0^2 I_H}{(n - \mu)^2} \quad 3.45$$

Higher l-series have negligible quantum defects. The statistical weights depend on whether we are concerned with levels which are part of the low level nlSL-resolved treatment or the high level bundled-nS picture. If we define n_2 as the arbitrary principal quantum shell which separates the nlSL and nS resolved treatment. The statistical weights are defined as,

$$n < n_2 \quad i \equiv nlSL \quad w_i = (2L + 1)(2S + 1) \quad 3.46$$

$$n > n_2 \quad i \equiv nS \quad w_i = n^2 (2L_p + 1)(2S_p + 1) \quad 3.47$$

where L_p and S_p are the total angular and spin quantum numbers associated with the parent ion. We also require nl-resolved bound-bound and bound-free Gaunt factors to evaluate quantities such as the spontaneous emission and the radiative recombination coefficient. The expressions used to evaluate these factors are of considerable complexity and a detailed account can be found in the work of Summers[43].

3.3.2 Collisional processes

The expressions which were used for the bundled-nS model form a starting point for the bundled-nlSL model. However there are several additional processes which have to be taken into account which were not applicable in the nS-resolved picture. These processes include ion and electron collisions between degenerate levels and electron driven spin changing collisions. The approximate methods to evaluate the rate coefficients for each of these processes is discussed in detail by Summers[43]. We simply quote the results here. For degenerate collisions due to electrons and ions, the rate coefficient is given as,

$$q_{nlSL \rightarrow n'l'SL'} = \sqrt{\pi} \alpha c a_0^2 \left(\frac{I_H}{kT_e} \right)^{\frac{1}{2}} \left(\frac{m}{m_e} \right)^{\frac{1}{2}} \frac{1}{z_1^2} D_{nlSL \rightarrow n'l'SL'} \left\{ 26.57 + \log \left(\frac{z_1^2 T m_e}{D_{nl} m} \right) + \log R_c^2 \right\}$$

where m and T are respectively the mass and temperature of the colliding particle. The quantity R_c^2 is described as a cut-off to ensure the collision cross sections have finite values. The expression for spin changing transitions between each spin system is,

$$q_{nlSL \rightarrow n'l'S'L'} = \frac{5}{12} \frac{(2L' + 1)(2S' + 1)}{(2L_p + 1)(2S_p + 1)} |\eta_{n'l'}^{nl}|^2 q(\epsilon_1 \rightarrow \epsilon_2) \quad S \neq S' \quad 3.48$$

where $\eta_{n'l'}^{nl}$ is an overlap fractional function. A detailed account of each expression can also be found in the work of Spence[19].

3.3.3 Fundamental atomic data

The supplementary data is stored in a similar format to the data used for the bundled-nS model. There are three databases which contain electron impact excitation, electron impact ionisation and ion-atom collision data respectively. If we first consider the electron impact excitation database. This database contains excitation rates which have been stored in the form of effective collision strengths for dipole and non-dipole transitions between all the resolved levels up to the n=4 shell. The contents of the database is primarily from the compilation of de Heer[56] but includes the work of many others[54]. Also included in this database is a compilation of spontaneous emission coefficients, the details of which can also be found in [54]. Focusing on the electron impact ionisation database. This database contains Maxwell averaged electron impact ionisation rates associated with the ground state and the He(2 ¹S) and He(2 ³S) metastables. This data is based on the work of Bell et. al.[55] and Fujimoto[57]. The ion-atom database, which is the largest database, contains cross-sections for charge exchange, ion impact excitation and ionisation from the ground and excited states of the singlet and triplet spin system. For this work the data used was based on a compilation by Summers[54].

3.3.4 Method of solution

In the same manner as the bundled-nS model, the bundled-nISL model solves for the effective contributions. As shown earlier in section 3.2.5, the quasi-static populations can be obtained using the expression,

$$N_j^{eq} = n_e n_+ R_j + n_b n_+ G_j + \sum_{\sigma=1}^m E^\sigma N_\sigma \quad 3.49$$

where in this case the number of non-equilibrium levels is three. Using the modified Saha-Boltzmann equation which is now written as,

$$N_i = n_e n_+ 8 \left(\frac{\pi a_0^2 I_H}{kT_e} \right)^{3/2} \frac{w_i}{2w_+} \exp\left(-\frac{I_i}{kT_e}\right) b_i \quad 3.50$$

where w_+ is the statistical weight of the parent ion,

$$w_+ = (2L_p + 1)(2S_p + 1) \quad 3.51$$

Equation 3.49 can be re-written in terms of the b_{nl}^{2S+1L} factors,

$$b_{nl}^{2S+1L} = FI_{(nlS)} \left(\frac{N_{1^1S}}{n_+} \right) + FII_{(nlS)} \left(\frac{N_{2^1S}}{n_+} \right) + FIII_{(nlS)} \left(\frac{N_{2^3S}}{n_+} \right) + F^2_{(nlS)} \quad 3.52$$

The quantities $FI_{(nlS)}$, $FII_{(nlS)}$ and $FIII_{(nlS)}$ separate the effective excitation contributions which populate the excited levels by driving from the ground state and the He(2^1S) and He(2^3S) metastables respectively. The contribution to populating the excited levels due to recombination from the continuum is $F^2_{(nlS)}$. It should be noted that the charge exchange $F^3_{(nlS)}$ contribution had been omitted from equation 3.52, since we have not incorporated charge exchange data for the thermal plasma atom case. The solution of equation 3.52 is achieved by a combination of switching on and off a synthetic radiation field in a similar manner as in the bundled-nS model.

The tabulated output from the model contains the excitation contributions (FI , FII , $FIII$) and the solution of the Saha-Boltzmann equation in the form $N_{nl}^{2S+1L} / b_{nl}^{2S+1L} \times n_+$. Also included are the effective cross coupling coefficients which are calculated using the expression discussed in chapter 2.0,

$$S_{\rho\sigma} = C_{\rho\sigma} - \sum_{j>m} \sum_{i>m} C_{\rho j} C_{ji}^{-1} C_{i\sigma} \quad 3.53$$

The equilibrium populations relative to the ground state and each metastable are then obtained from the tabulated output using the following relations.

$$\frac{N_{nl}^{2S+1L}}{N_{1^1S}} = FI_{(nlS)} \left(\frac{N_{nl}^{2S+1L}}{b_{nl}^{2S+1L} n_+} \right) \quad 3.54$$

$$\frac{N_{nl}^{2S+1L}}{N_{2^1S}} = FII_{(nlS)} \left(\frac{N_{nl}^{2S+1L}}{b_{nl}^{2S+1L} n_+} \right) \quad 3.55$$

$$\frac{N_{nl}^{2S+1L}}{N_{2^3S}} = FIII_{(nlS)} \left(\frac{N_{nl}^{2S+1L}}{b_{nl}^{2S+1L} n_+} \right) \quad 3.56$$

The effective beam emission coefficients relative to each metastable can then be defined in a similar manner as in section 3.2.5 .

3.4 Computational implementation and validation

3.4.1 Implementation of the models within ADAS

The bundled-nS model has been implemented into the ADAS system as ADAS310. We summarise the main features of ADAS310 here and further details can be found in [26]. As with all ADAS programs, there are three main IDL compound widgets which serve as the user interface. The input, the main processing and the output screen. We focus our attention here on the main processing screen of ADAS310, see figure 3.2.

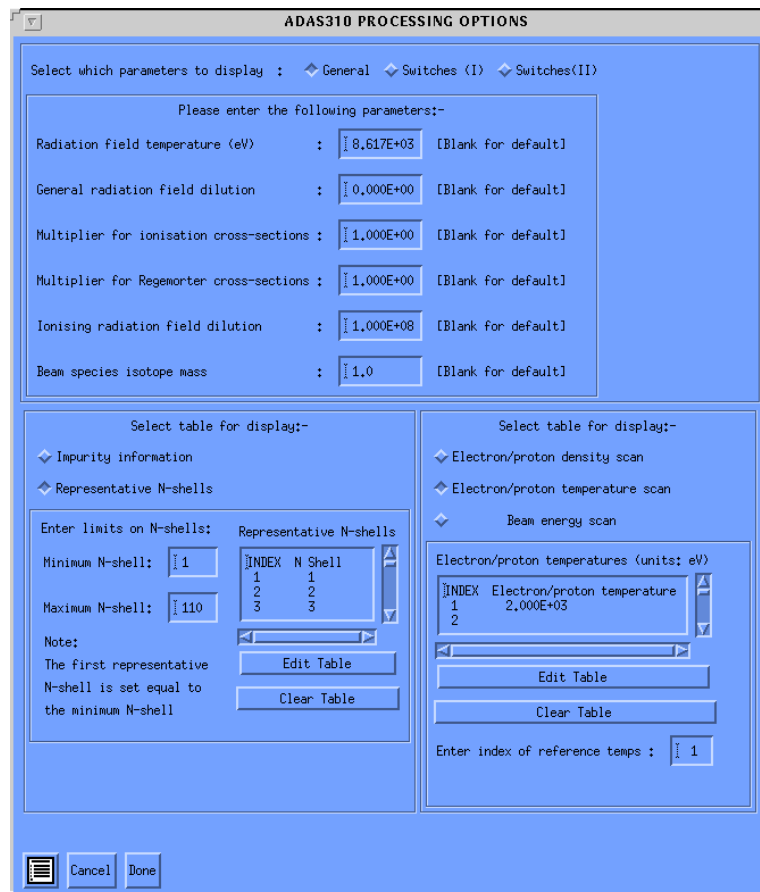


Figure 3.2 Snapshot of the main processing screen of ADAS310.

The processing screen consists of several panels which allow the user to select and enter the required input parameters. The bottom left hand panel concerns the selection of plasma impurity ions and the range of principal quantum shells for which the excited state population is to be evaluated. The panel on the bottom right allows the user to enter the required temperature, density and neutral beam energy range. The panel at the top is of most interest, since it is in this area where the user can select the different approximate methods to evaluate the rate coefficients for the atomic processes included in the statistical balance equations. As can be seen in the top panel of figure 3.2, there are a series of toggle buttons. If the user activates the button which is labelled 'Switch I', an additional panel will appear, see figure 3.3.

Figure 3.3 Snap shot of the panel which appears when the button labelled 'Switch I' is activated.

This panel allows the user to select the method for evaluating the electron impact excitation cross sections and hence the rate coefficients. The panel also contains the switch which allows the user to access the collection of fundamental atomic databases. If this switch is activated the data contained in each database is extracted and is used to replace the values obtained from the approximate methods. In the context of ADAS, each of the databases are stored in their own specific ADAS data file format (adf). The database containing electron impact excitation rates is archived in the file format known as adf04. The electron impact ionisation data is archived according to the prescription of the file format adf07, while the ion-atom

database is stored in the file format of adf02. A detail description of each of the file formats can also be found in [26].

If the user now activates the button labelled ‘switch II’, a second panel will appear, see figure 3.4.

The screenshot shows a software interface with a blue background. At the top, it says 'Select which parameters to display :'. Below this are three expandable menu items: 'General', 'Switches (I)', and 'Switches(II)'. The 'Switches(II)' menu is currently expanded, showing a sub-panel with the title 'Please enter the following parameter switches:-'. This sub-panel contains four rows of controls:

- 'Activate ion impact cross-sections' with a 'NO' button.
- 'Delta N range for ion impact cross-sections' with a text input field containing the number '2'.
- 'Use Lodge ion impact cross-sections' with a 'YES' button and a note in brackets: '[NO defaults to Vainshtein X-sections]'. The 'YES' button is highlighted.
- 'Use beam energy in forming ion cross-sections' with a 'YES' button.

Figure 3.4 Snapshot of the panel which appears when the button labelled ‘Switch II’ is activated.

This panel allows the user to choose between the different approximate methods which are employed to evaluate ion impact excitation cross-sections. The panel also contains switches which allow the user to turn off the ion collisions as well as to form the ion-atom rate coefficients without taking into account the beam velocity. The latter being equivalent to switching the beam off and modelling the excited state population structure of deuterium in a thermal plasma.

After the user has finalised their selection, ADAS310 then loops around the specified range of temperatures, densities and neutral beam energies. In each case assembling the statistical balance equations and solving for the equilibrium populations and effective beam stopping coefficients. The main output, which is in the ADAS adf26 type format, contains tables of the F 's, b_n 's and the effective beam stopping coefficients. We show in table 3.1 the typical output from ADAS310 for a relatively simple case.

TABLE FOR ION PRINCIPAL QUANTUM SHELL POPULATIONS IN THERMAL PLASMA						
		Z0 = 1.00E+00	Z1 = 1.00E+00			
TRAD = 1.00E+08 K		TE = 2.32E+07 K		TP = 2.32E+07 K		
W = 0.00E+00		NE = 1.00E+12 CM-3		NP = 1.00E+12 CM-3		
EH = 5.00E+03 EV/AMU		NH = 1.00E+07 CM-3		NH/NE = 1.00E-05 FLUX = 9.78E+14 CM-2 SEC-1		
CX OFF : N1/N+ = 1.16108E-09 RECOMB COEFF = 1.42279E-16 CM+3 SEC-1 IONIZ COEFF = 1.22541E-07 CM+3 SEC-1						
CX ON : N1/N+ = 4.76864E-05 RECOMB COEFF = 5.84353E-12 CM+3 SEC-1 IONIZ COEFF = 1.22541E-07 CM+3 SEC-1						
I	N	F1	F2	F3	B(CHECK)	B(ACTUAL) NN/(BN*N+)
1	1	0.00000E+00	3.11171E+05	1.27797E+15	1.27804E+10	1.27804E+10 3.73131E-15
2	2	3.60194E+09	3.49143E+00	7.13883E+10	8.85650E+05	8.85650E+05 1.48493E-14
3	3	1.27748E+09	2.34706E+00	4.34908E+10	4.95829E+05	4.95829E+05 3.33793E-14
4	4	5.08493E+08	1.60159E+00	5.95132E+09	8.37630E+04	8.37630E+04 5.93213E-14
5	5	1.36343E+08	1.17348E+00	8.63307E+08	1.51359E+04	1.51359E+04 9.26753E-14
6	6	3.94663E+07	1.05453E+00	1.63609E+08	3.51915E+03	3.51915E+03 1.33441E-13
7	7	1.40732E+07	1.01994E+00	4.03570E+07	1.07569E+03	1.07569E+03 1.81619E-13
8	8	5.82632E+06	1.00836E+00	1.22062E+07	4.00906E+02	4.00906E+02 2.37209E-13
9	9	2.80157E+06	1.00404E+00	4.43355E+06	1.78936E+02	1.78936E+02 3.00211E-13
10	10	1.61959E+06	1.00234E+00	1.97951E+06	9.80297E+01	9.80297E+01 3.70626E-13
11	11	1.23372E+06	1.00178E+00	1.21778E+06	7.20110E+01	7.20110E+01 4.48452E-13
12	12	8.60349E+05	1.00124E+00	7.15872E+05	4.91869E+01	4.91869E+01 5.33690E-13
13	15	2.76860E+05	1.00040E+00	1.61784E+05	1.58207E+01	1.58207E+01 8.33876E-13
14	20	5.23029E+04	1.00007E+00	2.37014E+04	3.73122E+00	3.73122E+00 1.48243E-12
15	30	6.82995E+03	1.00001E+00	2.84341E+03	1.35414E+00	1.35414E+00 3.33543E-12
16	40	1.54437E+03	1.00000E+00	6.25293E+02	1.07990E+00	1.07990E+00 5.92963E-12
17	50	4.75304E+02	1.00000E+00	1.89911E+02	1.02457E+00	1.02457E+00 9.26503E-12
18	60	1.75921E+02	1.00000E+00	6.97467E+01	1.00909E+00	1.00909E+00 1.33416E-11
19	70	7.19489E+01	1.00000E+00	2.83621E+01	1.00371E+00	1.00371E+00 1.81594E-11
20	80	2.98631E+01	1.00000E+00	1.16986E+01	1.00154E+00	1.00154E+00 2.37184E-11
21	90	1.07568E+01	1.00000E+00	4.16035E+00	1.00055E+00	1.00055E+00 3.00186E-11
22	100	1.27021E+00	1.00000E+00	4.26867E-01	1.00006E+00	1.00006E+00 3.70601E-11
BN = F1*(N1/N+) + F2 + F3*(NH/NE)						
N1 = POPULATION OF GROUND STATE OF ION						
N+ = POPULATION OF GROUND STATE OF NEXT IONISATION STAGE						
NN = POPULATION OF PRINCIPAL QUANTUM SHELL N OF ION						
BN = SAHA-BOLTZMANN FACTOR FOR PRINCIPAL QUANTUM SHELL N						
EH = NEUTRAL HYDROGEN BEAM ENERGY						
W = RADIATION DILUTION FACTOR						
Z0 = NUCLEAR CHARGE						
Z1 = ION CHARGE+1						
NIP = 0 INTD = 3 IPRS = 1 ILOW = 1 IONIP = 1 NIONIP = 2 ILPRS = 1 IVDISP = 1						
ZEFF = 1.0 TS = 1.00D+08 W = 0.00D+00 CION = 1.0 CPY = 1.0 W1 = 1.00D+08 ZIMP = .0(0.00D+00)						
1						

Table 3.1 Typical output from ADAS310 for a pure D⁺ plasma. The output from ADAS310 is archived according to the file format of adf26. A summary of the input parameters is specified at the bottom of the tabulated output.

It is common practice to generate effective stopping and emission coefficients for a wide range of plasma parameters. The plasma parameters being the temperature, density and neutral beam energy. The typical output from ADAS310 for a single impurity species is approximately 3.5 Mb and consists of a series of tables as shown in table 3.1. We then have to extract the effective stopping and emission coefficients and store them in a suitable format. To automate this process, during the course of this work we have developed an interactive program which is employed to

interrogate the adf26 type files. The program offers the user the choice of whether to extract effective stopping or effective emission coefficients for an arbitrary transition from the adf26 type file. This program is known as ADAS312 and we summarise the main features here, a more detailed description can be found in [58]. We show in figure 3.5 the main processing screen of ADAS312.

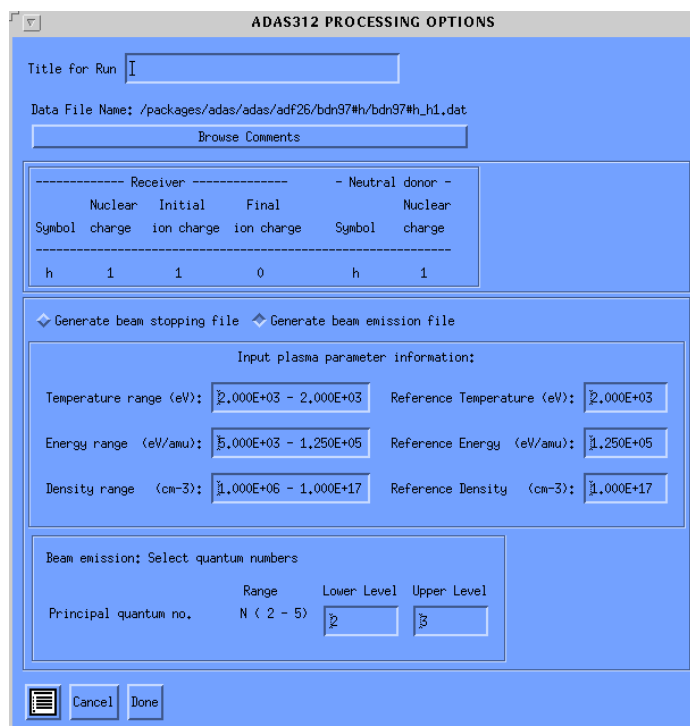


Figure 3.5 Snap shot of the main processing screen of ADAS312.

The processing screen consist of several panels. The panel in the middle displays the parameter range over which the contents of the adf26 type file has been evaluated. It is also within this panel that the user selects whether effective stopping or emission coefficients are to be extracted from the adf26 type file. If the user activates the beam emission button, the panel at the bottom is sensitised. This panel allows the user to enter the upper and lower principal quantum number for the transition corresponding to the effective beam emission coefficient which is required. If the user activates the beam stopping button, the bottom panel is de-sensitised which prevents the user entering any information. Once the user has finalised their selection and activated the button labelled ‘Done’, the user is presented with the output screen. This screen offers several choices, the user can choose to save the extracted data to file or to

view the data as a surface plot or even both. If we consider the scenario where both of the options have been selected. The user is then presented with a graphical screen which contains a surface plot of the selected data, see figure 3.6.

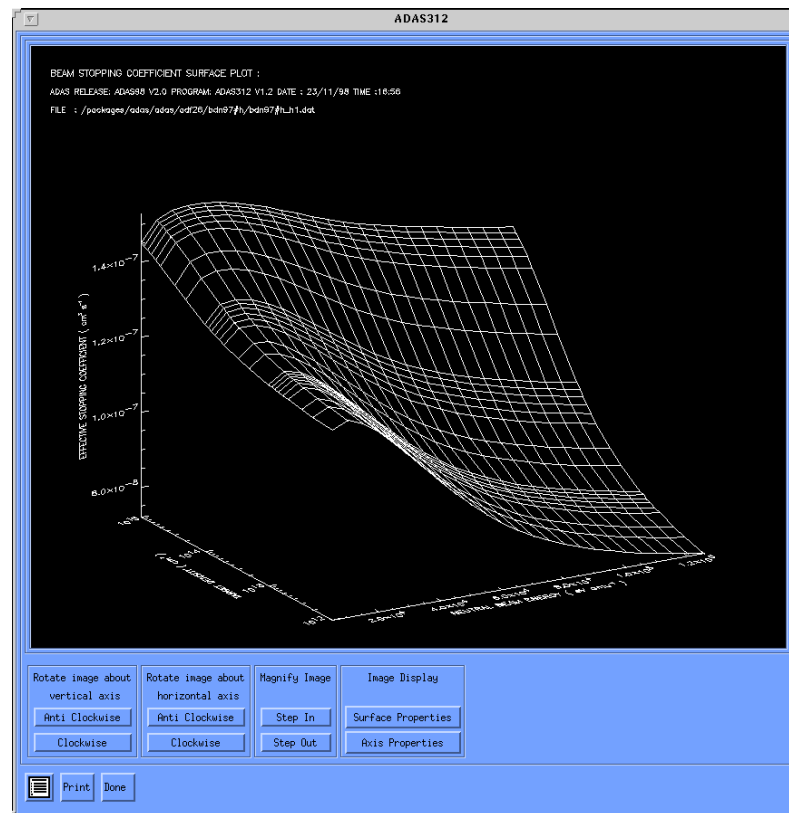


Figure 3.6 Snapshot of the graphical screen of ADAS312.

The graphical screen allows the user to interactively inspect the data by being able to zoom in or out or by rotating the surface plot through various angles. If the user activates the ‘print’ button the contents of the graphics window will then be written to an appropriate graphics file. Once the user returns back to the output screen by activating the ‘done’ button, the selected data is then written to file. The effective stopping and emission coefficients are respectively archived according to the specifications of the ADAS adf21 and adf22 type files. We show in table 3.2 an example of an adf21 type file which contains effective stopping coefficients for a pure D^+ plasma.

```

1 /SCREF=1.081E-07 /SPEC=H /DATE=09/04/98 /CODE=ADAS312
-----
25 25 /TREF=2.000E+03
-----
5.000E+03 1.000E+04 1.500E+04 2.000E+04 2.500E+04 3.000E+04 3.500E+04 4.000E+04
4.500E+04 5.000E+04 5.500E+04 6.000E+04 6.500E+04 7.000E+04 7.500E+04 8.000E+04
8.500E+04 9.000E+04 9.500E+04 1.000E+05 1.050E+05 1.100E+05 1.150E+05 1.200E+05
1.250E+05
1.000E+12 2.000E+12 3.000E+12 5.000E+12 6.000E+12 7.000E+12 8.000E+12 9.000E+12
1.000E+13 2.000E+13 3.000E+13 5.000E+13 6.000E+13 7.000E+13 8.000E+13 9.000E+13
1.000E+14 2.000E+14 3.000E+14 5.000E+14 6.000E+14 7.000E+14 8.000E+14 9.000E+14
1.000E+15
-----
1.225E-07 1.246E-07 1.229E-07 1.198E-07 1.160E-07 1.120E-07 1.079E-07 1.038E-07
9.981E-08 9.607E-08 9.272E-08 8.966E-08 8.704E-08 8.473E-08 8.274E-08 8.104E-08
7.953E-08 7.823E-08 7.706E-08 7.601E-08 7.506E-08 7.418E-08 7.338E-08 7.264E-08
7.195E-08
. . . . .
. . . . .
. . . . .
. . . . .
1.450E-07 1.505E-07 1.523E-07 1.529E-07 1.528E-07 1.523E-07 1.514E-07 1.502E-07
1.488E-07 1.472E-07 1.456E-07 1.439E-07 1.425E-07 1.411E-07 1.399E-07 1.388E-07
1.378E-07 1.369E-07 1.361E-07 1.353E-07 1.345E-07 1.337E-07 1.330E-07 1.323E-07
1.316E-07
-----
20 /EREF=6.500E+04 /NREF=6.000E+13
-----
1.000E+02 2.000E+02 3.000E+02 5.000E+02 6.000E+02 7.000E+02 8.000E+02 8.966E+02
1.000E+03 2.000E+03 3.000E+03 5.000E+03 6.000E+03 7.000E+03 8.000E+03 8.966E+03
1.000E+04 2.000E+04 3.000E+04 5.000E+04
-----
1.302E-07 1.294E-07 1.268E-07 1.222E-07 1.203E-07 1.187E-07 1.173E-07 1.161E-07
1.150E-07 1.081E-07 1.045E-07 1.003E-07 9.883E-08 9.763E-08 9.659E-08 9.570E-08
9.484E-08 8.903E-08 8.517E-08 7.971E-08
-----
C
C
C ADAS FILE TYPE : ADF21
C SOURCE FILE : /packages/adas/adas/adf26/bdn97#h/bdn97#h_h1.dat
C
C USER ID : anderson
C
-----

```

Table 3.2 Example of an adf21 type file which contains effective stopping coefficients for a pure D⁺ plasma.

The format of the adf22 type files are identical to the structure shown in table 3.2 but contain effective emission coefficients. In both of the file formats, the effective coefficients are stored as a one and two dimensional grids tuned for rapid experimental analysis, see chapter 4.0.

The bundled-nlSL model is intended to be placed into the ADAS system as ADAS311 in the near future. At the moment it is an off line program which is driven by an ASCII file containing all the relevant input parameters. The output file from the program, which is also classified as an ADAS adf26 type file, contains the F's and

the b-factors for both the singlet and triplet spin system. The collisional-radiative cross coupling coefficients are also included. We show in table 3.3 the typical output from ADAS311.

EFFECTIVE CONTRIBUTION TABLE FOR ION PRINCIPAL QUANTUM SHELL POPULATIONS IN THERMAL PLASMA											
HELIUM		Z0 = 2.00E+00	Z1 = 1.00E+00								
TRAD = 1.00E+08 K		TE = 1.16E+06 K		TP = 1.16E+06 K							
W = 0.00E+00		NE = 1.00E+05 CM-3		NP = 1.00E+00 CM-3							
EH = 1.00E+00 EV/AMU		NH = 1.00E+07 CM-3		NH/NE = 1.00E+02		FLUX = 1.38E+13 CM-2 SEC-1					
COLLISIONAL DIELECTRONIC RATES											
EFFECTIVE IONISATION AND CROSS COUPLING RATES											
IG	I	ALF	1		2		31				
1	1	2.1711471E-13	2.1383283E-08	-1.8729842E-06	-2.7239829E-09						
2	2	7.9081675E-15	-8.5961126E-10	2.0900639E-06	-6.5498303E-10						
3	31	6.4304632E-13	-5.0658281E-10	-1.9117015E-08	2.0775860E-07						
LEVELS OF MULTIPLICITY 1											
0	IR	N	L	LT	F1(I)	F1(II)	F1(III)	F2	B(CHECK)	B(ACTUAL)	NL/(B*N+)
1	1	0	0		9.4362731E+19	0.0000000E+00	0.0000000E+00	0.0000000E+00	1.0737047E+15	1.0737047E+15	1.0597404E-20
2	2	0	0		0.0000000E+00	1.1597567E+20	0.0000000E+00	0.0000000E+00	1.0950908E+12	1.0950908E+12	8.6224984E-21
3	2	1	1		1.2865979E+07	3.7700009E+09	5.5303704E+06	1.2068034E+02	3.1994921E+02	3.1994921E+02	2.5712114E-20
4	3	0	0		1.0193884E+08	1.6740420E+10	3.6584276E+07	2.1798098E+03	3.6120702E+03	3.6120702E+03	8.4259830E-21
5	3	1	1		9.5648714E+06	4.2821961E+08	4.8132494E+05	1.0442881E+02	2.1880951E+02	2.1880951E+02	2.5235828E-20
.
.
.
30	100	0	0		9.2732992E+03	1.2002970E+05	4.5014386E-05	4.4865574E+00	4.5932069E+00	4.5932069E+00	8.2867359E-17
LEVELS OF MULTIPLICITY 3											
0	IR	N	L	LT	F1(I)	F1(II)	F1(III)	F2	B(CHECK)	B(ACTUAL)	NL/(B*N+)
31	2	0	0		0.0000000E+00	0.0000000E+00	3.8351874E+19	0.0000000E+00	1.1980260E+14	1.1980260E+14	2.6074345E-20
32	2	1	1		3.6114582E+07	2.1225959E+09	1.3754551E+11	5.2880585E+04	4.8297269E+05	4.8297269E+05	7.7332539E-20
.
.
.
57	80	0	0		3.5531061E-05	6.1125850E-04	2.0290738E+05	1.9135280E+01	1.9769117E+01	1.9769117E+01	1.5910655E-16
58	90	0	0		1.1637887E-05	2.1689818E-04	8.9550399E+04	8.9357444E+00	9.2154797E+00	9.2154797E+00	2.0136833E-16
59	100	0	0		3.2309871E-06	7.0890962E-05	3.9861521E+04	4.4877036E+00	4.6122220E+00	4.6122220E+00	2.4860208E-16
B = F1(I)*(N1/N+) F1(II)*(N2/N+) +F1(III)*(N3/N+) +F2 N1 = POPULATION OF THE 1s2 1S METASTABLE N2 = POPULATION OF THE 2s 1S METASTABLE N3 = POPULATION OF THE 2s 3S METASTABLE N+ = POPULATION OF GROUND STATE OF NEXT IONISATION STAGE NL = POPULATION OF RESOLVED NL QUANTUM SHELL OF ION B = SAHA-BOLTZMANN FACTOR FOR RESOLVED NL QUANTUM SHELL EH = NEUTRAL HELIUM BEAM ENERGY W = RADIATION DILUTION FACTOR Z0 = NUCLEAR CHARGE Z1 = ION CHARGE+1											
NIP = 2 INTD = 3 IPRS = 1 ILOW = 1 IONIP = 1 NIONIP = 2 ILPRS = 1 IVDISP = 1 ZEFF = 4.0 TS = 1.00D+08 W = 0.00D+00 CION = 0.0 CPY = 0.0 W1 = 0.00D+00 ZIMP = 4.0 (2.50D+04)											

Table 3.3 Typical output from the Bundled-nISL model. The first half concerns the singlet spin system while the remainder deals with the triplet spin system. At the bottom of the tabulated data a summary of the input parameters is given.

In a similar manner as with ADAS310, we evaluate the effective cross coupling and emission coefficients over a wide range of plasma parameters. The typical output for a single plasma impurity is around 7.0 Mb. To assist in archiving and extracting the

effective coefficients from the adf26 type files, we have also developed an interactive program specifically for this task. The program is called ADAS313 and we show in figure 3.7 the main processing screen.

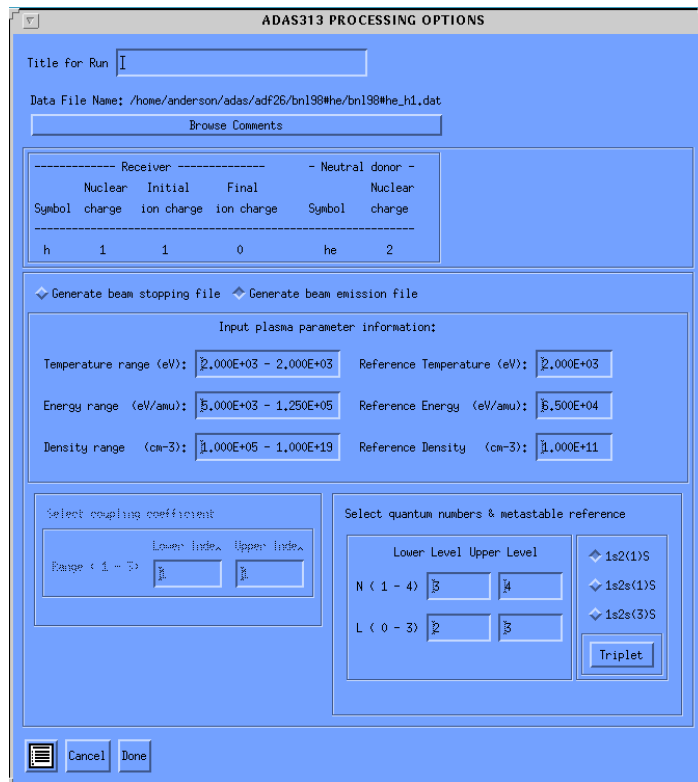


Figure 3.7 Snapshot of the main processing screen of ADAS313.

A series of panels allows the user to interactively select and enter their choices. The panel in the middle displays the parameter range over which the contents of the adf26 type file has been evaluated. This panel also houses two toggle buttons which allows the user to select between extracting effective cross coupling or emission coefficients from the adf26 type file. If the user activates the cross coupling button, the bottom left hand panel is sensitised which allows the user to specify what cross coupling coefficient is required. The coupling coefficients are specified according to the index notation of equation 3.53. If the user activates the beam emission button, the panel on the bottom right hand side is now sensitised. This panel allows the user to specify the quantum numbers according to the transition of interest. Also since the equilibrium populations are calculated relative to the ground state and the two metastables. The user also has to enter the non-equilibrium reference. Once the user

has completed their selection and activated the ‘Done’ button, a similar output screen as in ADAS312 appears. The user is then presented with the choice of either writing the effective coefficients to a file or to view the data via a surface plot or in fact both. The surface plot is generated using the same graphical window as shown for ADAS312. The effective coupling coefficients are archived as adf21 type files, while the effective emission coefficients are stored as adf22 type files.

3.4.2 Validation of ADAS310, the bundled-nS model

As discussed earlier the collisional-radiative ionisation coefficients, which are calculated by ADAS310, represents the rate at which the beam neutrals are ionised as the beam penetrates into the plasma. This rate of ionisation is determined by the outcome of the competing collisional and radiative processes which in turn are governed by the plasma density. In the case of a low density plasma where collisional excitation is balanced by spontaneous emission. The only processes which contribute to the ionisation of the beam neutrals are direct process from the ground state via charge exchange and impact ionisation. Therefore the low density ionisation rate is simply the sum of these direct rate coefficients. This low density ionisation rate was compared with the ionisation coefficient calculated by ADAS310 in the low density regime. A similar approach was applied to a high density plasma. In a high density plasma the rate at which the beam neutrals are ionised is simply the sum of the collisional excitation and ionisation coefficients from the ground state of the neutrals. A variety of composite target plasmas were considered. As an example we show in figure 3.8 the results for both a pure D^+ and C^{6+} plasma.

If we confine ourselves with the asymptotic limits of the stopping coefficient for a pure D^+ plasma. It can be observed that in the low density regime the results from ADAS310 and the theoretically predicted values agree exactly. In the high density limit a maximum difference of 1.92 % can be seen. If we now consider the plot on the right in figure 3.8 which illustrates the asymptotic limits for a pure C^{6+} plasma. In the low density limit the results between ADAS310 and theory agree exactly and in the high density regime a maximum difference of 4.13 % can be observed. This difference arise due to the fact that the theoretical values have been evaluated using the rate coefficients for the atomic processes only up to the $n=4$ shell.

If we were to include more atomic processes while evaluating the theoretical limits the difference would tend to zero.

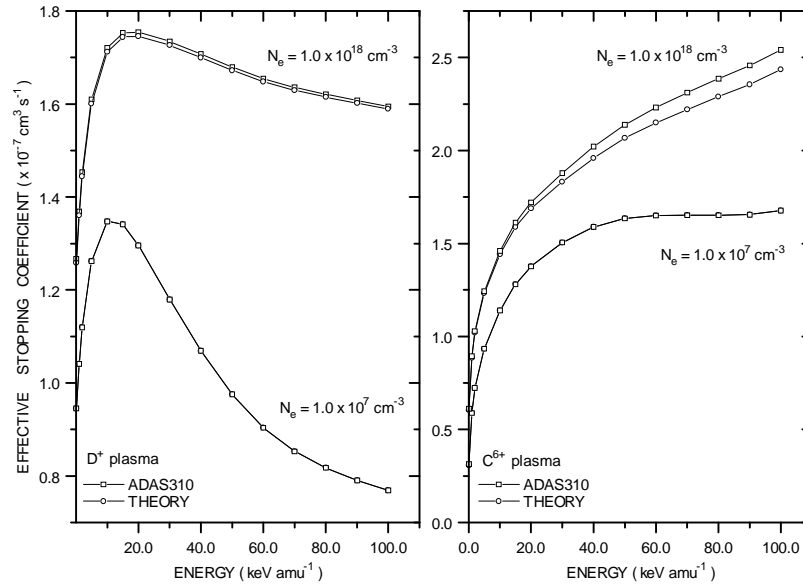


Figure 3.8 Comparison between the results of ADAS310 and the theoretical predictions of the asymptotic limits of the stopping coefficient. The plot on the left shows the results in the low and high density limit for a pure D^+ plasma. Similar results are shown for a pure C^{6+} plasma in the plot on the right. The low and high density limit respectively correspond to an electron density of 1.0×10^7 and $1.0 \times 10^{18} \text{ cm}^{-3}$. At $1.0 \times 10^7 \text{ cm}^{-3}$ the low density limit and ADAS310 for a D^+ plasma are superimposed. The plasma temperature was $1.0 \times 10^3 \text{ eV}$

We then went on to ensure that the excited state population were being evaluated correctly. To achieve this we compared the excited state population structure of ADAS310 with an independent low level population code ADAS205[26]. ADAS205 calculates the excited population structure of neutral deuterium, ignoring higher levels, in a thermal plasma. It was necessary to define a set of low levels in ADAS310 to simulate the same conditions as in ADAS205. It should also be noted that ADAS205 only includes electron collisions, therefore it was necessary to suppress any ion collisions in ADAS310. We found that the excited state populations were in agreement.

3.4.3 Validation of ADAS311, the bundled-nlSL model

To validate ADAS311 a similar approach was adopted. However while investigating the asymptotic limits of the effective coupling coefficient we ran the program with only the ground state specified as the non-equilibrium level. This enable us to be able to focus on one effective coefficient. We found that it agreed with the value predicted by summing the appropriate rate coefficients. We then compared the populations obtained from ADAS208[26] to that of ADAS311. ADAS208 calculates the excited population structure of an arbitrary ion in an nl-resolved picture and is a more advance version of ADAS205. To ensure the comparison was equivalent a similar set of representative levels were selected. For a wide range of plasma parameters we found that there was excellent agreement. As an example we show the equilibrium populations for the first few levels calculated by ADAS311 and ADAS208 for a pure D^+ plasma.

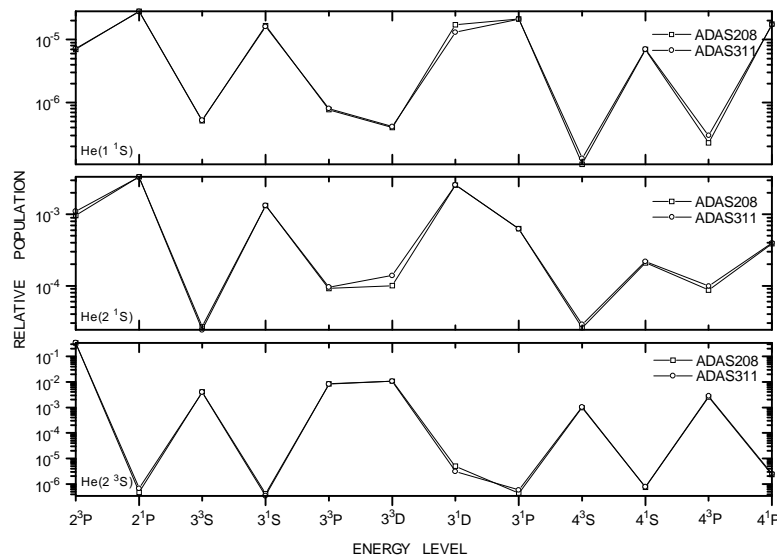


Figure 3.9 Comparison between the excited population structure calculated using ADAS208 and ADAS311. Working downwards, the population of each levels are calculated relative to the He(1 1S) ground state and the two metastables, He(2 1S) and He(2 3S). The electron density and the plasma temperature was respectively $1.0 \times 10^{13} \text{ cm}^{-3}$ and $2.0 \times 10^3 \text{ eV}$.

3.5 Summary

We have described the formulation and implementation of the bundled-nS and bundled-nlSL model. The bundled-nS model is employed to calculate the attenuation and excited population structure of neutral deuterium beam atoms, while the bundled-nlSL model is employed to calculate the attenuation and excited population structure of neutral helium beam atoms.

The bundled-nS model in the context of ADAS is known as ADAS310. During the course of this work we have developed an interactive program which interrogates the output from ADAS310. This program is called ADAS312 and its role is to extract and archive effective beam stopping and emission coefficients in their respective formats of adf21 and adf22.

The Bundled-nlSL model, which has also been developed during the course of this work, is intended to be placed into the ADAS packaged as ADAS311. At the moment it is an off line program which is driven by an ASCII file containing the appropriate input parameters. The output of ADAS311 is also interrogated by a new post processing program which is called ADAS313. ADAS313 extracts cross coupling and effective emission coefficients which are respectively stored in their ADAS data formats of adf21 and adf22.

4.0 Parameter dependencies and application of the derived atomic data relevant to neutral deuterium beam attenuation and emission

4.1 Introduction

There are two methods which can be employed to determine the neutral deuterium beam density as a function of penetration depth into a tokamak plasmas, see chapter 1.0. The first is a numerical attenuation calculation, which requires theoretical effective stopping coefficients. The second and more accurate method, involves the use of Balmer-alpha beam emission spectroscopy and requires theoretical effective emission coefficients. In this chapter we explore the parameter dependencies of the effective stopping and Balmer-alpha emission coefficients. Particular emphasis is placed on identifying the underlying atomic processes which contribute to both of these coefficients. We then consider the practical method of archiving such data and assembling effective coefficients for a composite plasma. The effective coefficients presented in this chapter have been calculated in a bundled-nS picture up to $n=110$ using ADAS310.

4.2 Effective collisional-radiative ionisation coefficients

In the following sub-sections we show the primary parameter dependencies of the collisional-radiative ionisation coefficients. The collisional-radiative ionisation coefficient is usually referred to as the effective beam stopping coefficient in fusion beam studies, where it describes the rate at which the beam neutrals are ionised as the beam traverses the plasma. Figure 4.1 shows the general behaviour of the effective stopping coefficient as a function of electron density and neutral beam energy for a deuterium beam penetrating into a pure D^+ plasma. The parameters to which the effective beam stopping coefficient is most sensitive include the electron density, the neutral beam energy, plasma temperature and the nuclear charge of fully stripped plasma impurity ions. It should be noted that the collisional-radiative ionisation coefficient is also strongly dependent on the ion density, in the present work however the coefficients are calculated in terms of the electron density with charge neutrality imposed.

We also wish to achieve two further objectives. Firstly we want to show the importance of including the influence of all the impurities contained in a composite plasma while evaluating effective stopping coefficients. To achieve this we evaluate the effective coefficients using ADAS310 for a range of composite plasmas and identify the individual contributions due to each impurity ion. We emphasise however that it is common practise to assemble composite coefficients using the rapid look up tables as discussed in section 4.4. Secondly we want to illustrate the sensitivity of the effective beam stopping coefficient following small changes in the fundamental atomic data which enters into the modelling as input.

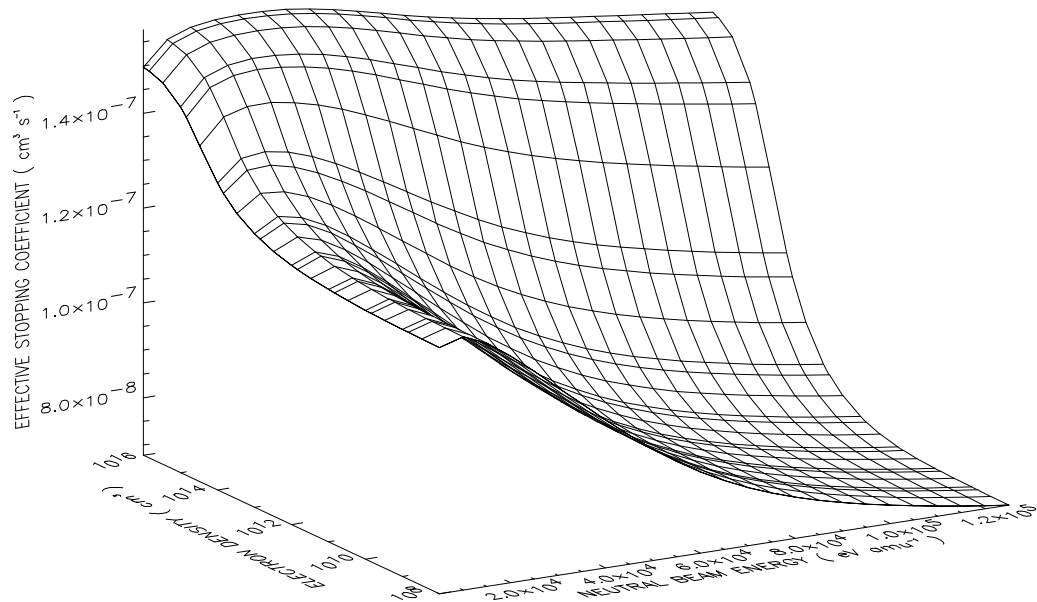


Figure 4.1 A surface plot of the effective stopping coefficient for a pure deuterium plasma with a temperature of 2×10^3 eV. Near the coronal limit at 1×10^8 cm^{-3} , the behaviour of the stopping coefficient reflects the rate coefficients for direct ionisation from the ground state of the beam neutrals via charge exchange and ion impact ionisation. As the density is increased the collisional losses from the excited states increases until a high density limit is reached.

4.2.1 Density dependence

The electron and ion density both control the effectiveness at which the atomic processes contribute to the beam stopping coefficient. Due to the efficiency of ion collisions the ion density is more influential. In figure 4.2 the influence of the

electron density on the effective stopping coefficient can be observed as a function of beam energy.

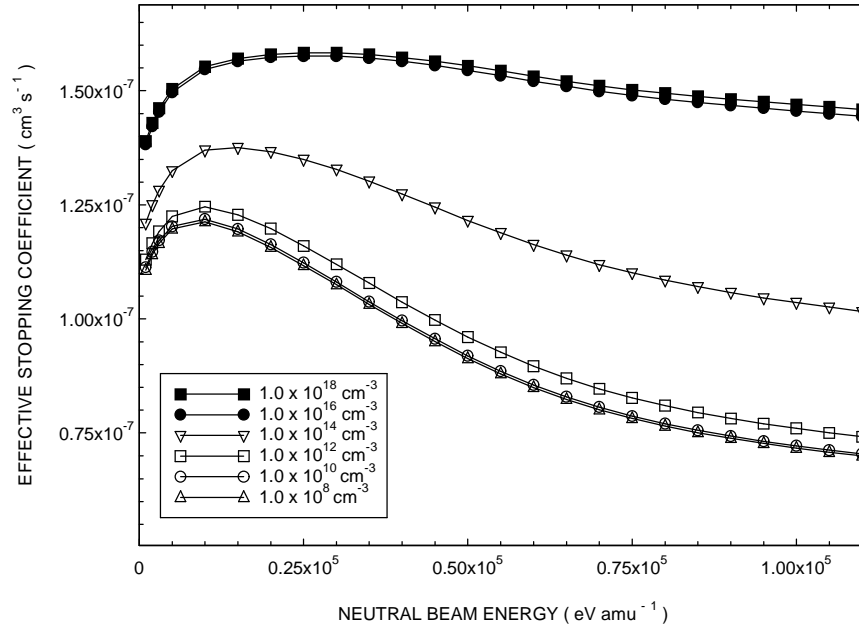


Figure 4.2 Effective beam stopping coefficient Vs neutral beam energy for a pure D^+ plasma. The ion temperature is 2×10^3 eV. The density dependence of the effective coefficient is clearly illustrated with the assistance of the low and high density limit.

As can be seen in figure 4.2, the departure from the low density coronal limit appears around $\sim 10^{10} \text{ cm}^{-3}$, while the formation of the high density limit is approached at $\sim 1 \times 10^{18} \text{ cm}^{-3}$. The characteristic density dependence of the stopping coefficient is not only confined to a pure D^+ plasma. We have undertaken similar behavioural studies for a wide range of plasmas with a different impurity content. As an extreme example we show in figure 4.3 the density dependence of the effective stopping coefficient for a deuterium beam penetrating into a hypothetical plasma of pure C^{6+} . We should emphasise that it is the ion density which governs the behaviour of the effective stopping coefficient even though we show the behaviour of the effective coefficient in terms of the electron density.

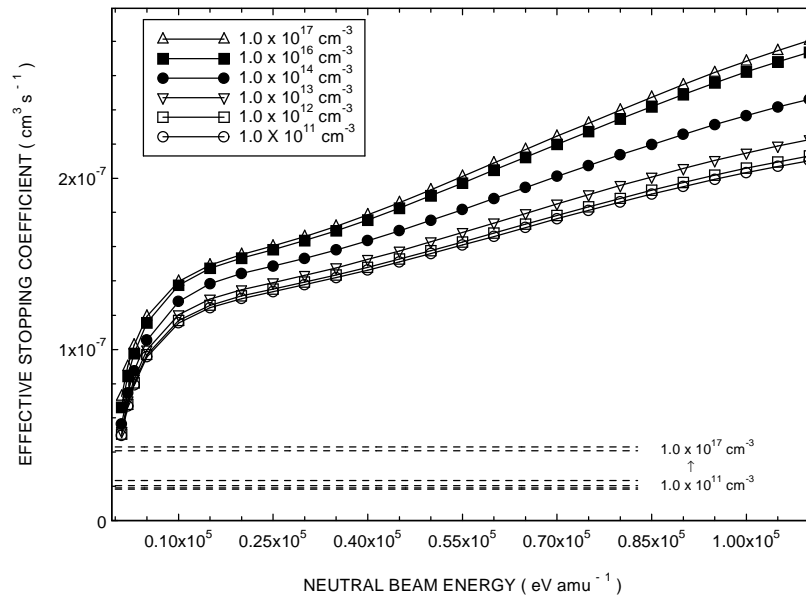


Figure 4.3 Beam stopping coefficient Vs the neutral beam energy for a hypothetical plasma of pure C^{6+} . The ion temperature is 2×10^3 eV. Also shown in the figure, with the dashed lines, is the contribution to the effective coefficient due to electron collision for a range of electron densities.

The low density coronal limit can be observed to form around $\sim 1.0 \times 10^{11} \text{ cm}^{-3}$, which corresponds to an ion density of $\sim 1.6 \times 10^{10} \text{ cm}^{-3}$, while the high density picture occurs at an electron density of $\sim 1.0 \times 10^{17} \text{ cm}^{-3}$. Also shown in the figure, with the dashed lines, is the contribution to the effective stopping coefficient due to electrons collisions. The electrons are moving at such great speeds that their small contribution is independent of the beam energy. It is of interest to point out the difference in the magnitude of the stopping coefficient for a pure D^+ and C^{6+} plasma. The latter is substantial larger and is due to the greater efficiency of the C^{6+} plasma ions at stripping the electrons from the beam atoms. The influence of the nuclear charge of the plasma impurity ions is discussed in 4.2.4.

4.2.2 Neutral beam energy dependence

The neutral beam energy governs the relative efficiency of electrons and ions causing the attenuation and population redistribution of the neutral beam atoms. However the extent of the energy dependence of the effective stopping coefficient is also

coupled to the ion density. In figure 4.4 we illustrate the influence of the neutral beam energy on the stopping coefficient as a function of electron density for a pure D^+ plasma.

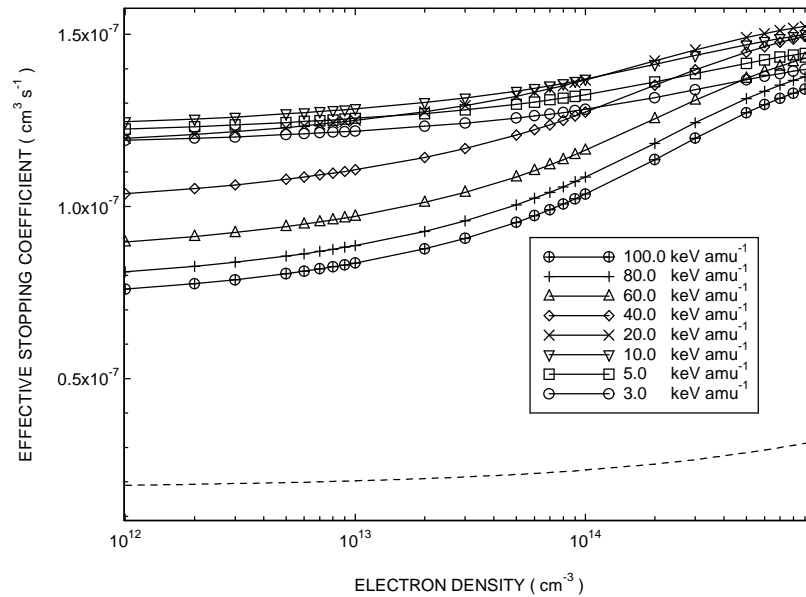


Figure 4.4 A plot of the effective stopping coefficient Vs electron density for a pure D^+ plasma. The influence of the neutral beam energy on the effective stopping coefficient for a fixed ion temperature of 2×10^3 eV is shown. Also shown, with the dashed line, is the small contribution to the effective stopping coefficient due to electron collisions.

It can be seen that for a fixed beam energy the effective stopping coefficient increases as the electron density is increased. This is due to the role of stepwise atomic processes which become important as the electron and hence the ion density is increased. Also shown, with the dashed line, is the small contribution to the effective stopping coefficient due to electron collisions. The contribution due to electrons also increases as the electron density is increased. However the rate of increase is substantially smaller since collisional redistribution due to electron collision is less efficient. It can also be observed in figure 4.4, that for a fixed electron density the effective stopping coefficient increases and then decreases as the beam energy is increased from 3.0 to 100 keV amu^{-1} . This simply reflects the energy dependence of the underlying atomic processes, see chapter 2.0. The net effect of all the competing processes is that the effective stopping coefficient can be observed to increase and then slowly decrease as a function of beam energy.

4.2.3 Temperature dependence

The plasma temperature dependence of the stopping coefficient arises from the relative collision velocities between the beam atoms and the fully stripped thermal plasma ions. The relative collision velocities govern the behaviour of the collision cross sections which in turn influence the rate coefficients which enter into the statistical balance equations. In the simplest form, the expression for the rate coefficient for an arbitrary process is given as,

$$\langle \sigma v \rangle = \int_{v_{\min}}^{\infty} |v_r| f(v_t) \sigma(|v_r|) dv_t \quad 4.1$$

where $f(v_t)$ is the velocity distribution of the thermal plasma ions, $\sigma(|v_r|)$ is the collision cross section and v_r is the relative collision velocity between the beam atoms and the thermal ions, i.e. $|v_r| = |v_b - v_t|$.

In the case where the beam velocity, v_b , is substantially greater than the thermal velocity of the plasma ions, it can be shown that the rate coefficients and hence the effective beam stopping coefficients are independent of the plasma temperature. The temperature dependence of the stopping coefficients can only be observed when the beam velocity is not vastly different from the thermal velocity of the plasma ions. In such circumstances, an increase or decrease in the plasma temperature alters the relative collision velocity as well as the shape and position of the velocity distribution. Depending on the behaviour of the underlying collision cross sections this may result in either increasing or decreasing the effective stopping coefficient. When the beam velocity is slightly greater than the thermal velocity of the plasma ions, an increase in the plasma temperature contributes to decreasing the relative collision velocity. In figure 4.5 we show the temperature dependence of the stopping coefficient as a function of beam energy for such a scenario.

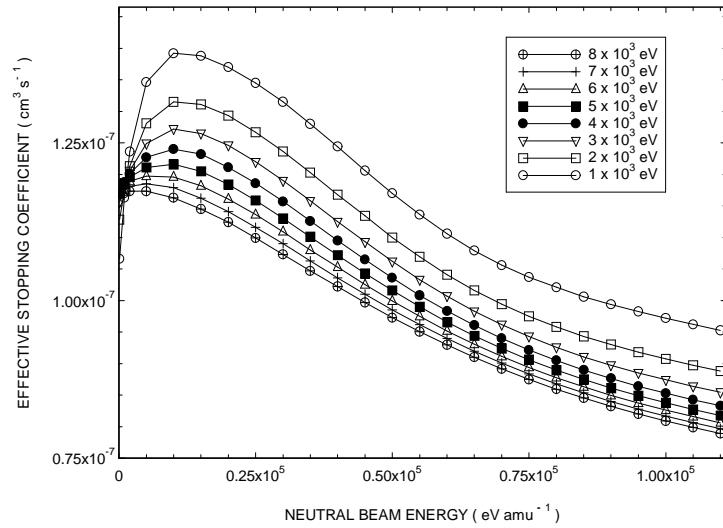


Figure 4.5 A plot of the effective stopping coefficient Vs neutral beam energy for a pure D^+ plasma with a density of $3.0 \times 10^{13} \text{ cm}^{-3}$.

As the plasma temperature increases, it can be observed from figure 4.5 that the effective stopping coefficient decreases. This is attributed to the fact that as the relative collision velocity decreases the collision cross sections also decrease. It is of interest to point out that when the thermal velocity of the plasma ions is slightly greater than the beam velocity the opposite occurs. As the plasma temperature increases the relative collision velocity and the collision cross sections also increase, see figure 4.6.

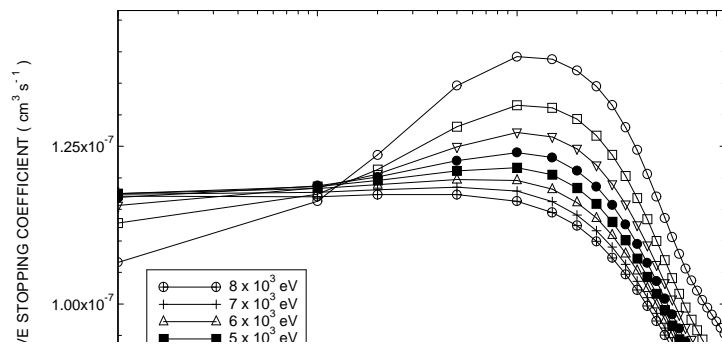


Figure 4.6 Beam stopping coefficient Vs neutral beam energy for D^+ plasma with a density of $3.0 \times 10^{13} \text{ cm}^{-3}$. In the low energy regime an increase in the plasma temperature results in an increase in the effective stopping coefficient.

In the low energy regime of figure 4.6, as the plasma temperature increases the effective stopping coefficients also increase. It should be noted that an increase or decrease in the relative collision velocity does not necessary result in a similar increase or decrease in the effective stopping coefficient. The influence of the relative collision velocity depends on the behaviour of the collision cross sections. Nevertheless the temperature dependence of the stopping coefficient is weak and is almost independent of the beam energy and the electron density. As illustrated in figure 4.5 and 4.6, increasing the temperature by a factor of 5 only results in an average change of 12 % in the effective stopping coefficient.

4.2.4 Nuclear charge dependence

The nuclear charge of a fully stripped plasma ion characterises how effective the ion will be at ionising the neutral beam atoms. As the nuclear charge increases, the associated cross sections which describe the behaviour of charge exchange and ion impact ionisation also increase, see chapter 2.0. In this section we briefly illustrate the influence of fully stripped plasma ions on the effective stopping coefficient. We show in figure 4.7, the effective stopping coefficient as a function of beam energy for a variety of pure impurity plasmas.

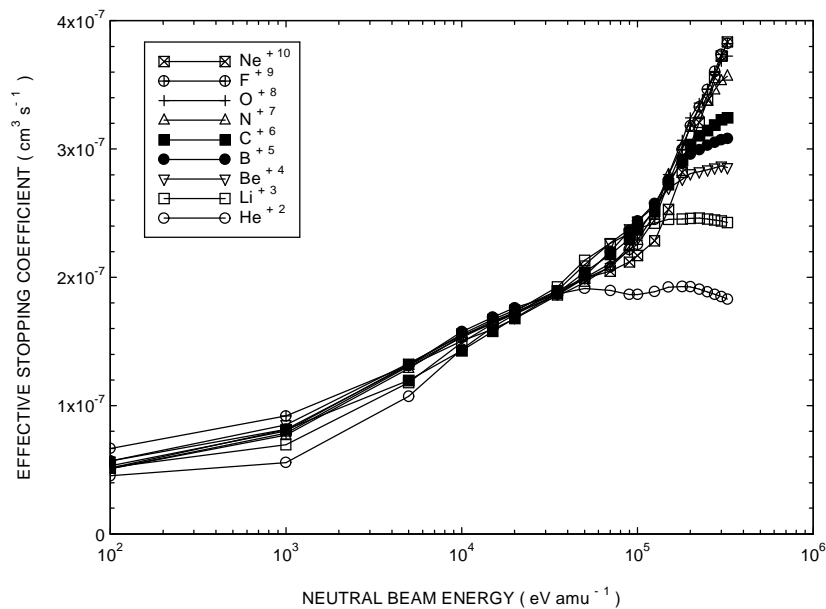


Figure 4.7 Beam stopping coefficient Vs neutral beam energy for a pure impurity plasma. Note the asymptotic behaviour of the beam stopping coefficient for each impurity. The electron density was $3.0 \times 10^{13} \text{ cm}^{-3}$ and the plasma temperature was $2.0 \times 10^3 \text{ eV}$.

In the low energy regime we can observe a charge dependence of the effective stopping coefficient. This is simply due to the behaviour of the underlying charge exchange cross sections. The charge exchange cross sections scale approximately with the nuclear charge of the receiver ion. As the beam energy is increased a near coincidence of curves in the relevant beam range of current tokamaks can be observed. Finally in the high energy regime, the charge dependence of the effective stopping coefficient can again be observed. On this occasion however it is due to the charge dependence of the ion impact ionisation cross sections. The ion impact ionisation cross sections also scale approximately with the nuclear charge of the impurity ion. From the results shown in figure 4.7, it would appear that the effective stopping coefficient also scales approximately with the nuclear charge. However the electron density was fixed at a value of $3.0 \times 10^{13} \text{ cm}^{-3}$ and charge neutrality had been imposed. Therefore as the nuclear charge of the plasma ion increased, the corresponding number density decreased. Therefore the behaviour of the effective stopping coefficient in fact scales with a value which is slightly larger than the nuclear charge .

4.2.5 The importance of impurities

So far we have presented data showing the primary parameter dependencies of the effective stopping coefficients for pure plasmas. Working fusion plasmas consist of electrons and deuterons together with unavoidable small concentrations of various fully stripped impurity species. The different components which make up the composition of the plasma all contribute to exciting and ionising a penetrating beam. In this sub-section we attempt to illustrate the influence of such mixed impurities while evaluating effective stopping coefficients. This allows one to quantitatively assess the importance of considering the mixed impurity content of the plasma. The approach taken was to evaluate effective stopping coefficients for a range of composite plasma and in each case highlight the individual contribution from each impurity contained in the plasma.

We begin by considering a simple plasma which consists of 98 % D^+ and 2 % He^{2+} . In figure 4.8 we show the energy and density dependence of the effective

stopping coefficient, also shown in both figures are the individual contributions due to each ion.

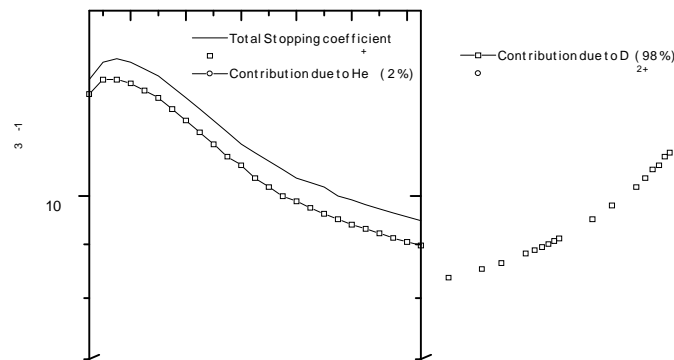


Figure 4.8 A plot of the effective beam stopping coefficient for a composite plasma consisting of 98% D^+ and 2% He^{2+} . The plot on the left exhibits the energy dependence of the effective stopping coefficient while the plot on the right illustrates the density dependence. The ion temperature was 2.0×10^3 eV and the electron density for the plot on the left was 3.0×10^{13} cm^{-3} . The beam energy corresponding to the plot on the right was 5.0 keV amu^{-1} .

If we first consider the energy dependence of the composite stopping coefficient which is shown in the plot on the left of figure 4.8. It can be observed that the contribution to the total stopping coefficient due to the 2% concentration of He^{2+} , increases from 2.5% at 5.0 keV amu^{-1} to 5.3% at 120.0 keV amu^{-1} . The contribution due to the He^{2+} ions is in fact greater than their total concentration in the plasma. This simply reflects the larger cross sections associated with He^{2+} ions and hence their greater efficiency at stripping electrons from the beam atoms in comparison with the D^+ ions. This effect can also be observed in the plot on the right in figure 4.8, which illustrates the electron density dependence of the composite stopping coefficient. At a density of 1.0×10^{12} cm^{-3} the contribution due to He^{2+} is 5.69%, which decreases to a value of 4.81% as the electron density is increased.

We now consider a slightly different plasma which consists of 96 % D^+ , 2% He^{2+} and 2% Be^{4+} . The energy and density dependence of the composite stopping coefficient can be seen in figure 4.9.

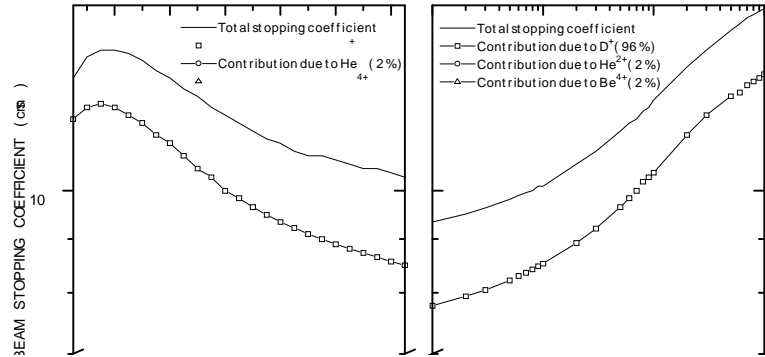


Figure 4.9 A plot of the effective beam stopping coefficient for a composite plasma consisting of 96% D^+ , 2% He^{2+} and 2% Be^{4+} . The plot on the left shows the energy dependence of the composite coefficient while the plot on the right exhibits the density dependence. The ion temperature was 2.0×10^3 eV and the electron density for the plot on the left was $3.0 \times 10^{13} \text{ cm}^{-3}$. The beam energy for the plot on the right was 5.0 keV amu^{-1} .

As shown in the plot on the left of figure 4.9, the contribution to the total stopping coefficient due to the He^{2+} ions increases from 2.41 to 4.66 % at the respective beam energies of 5.0 and 120.0 keV amu^{-1} . The corresponding contributions due to the Be^{4+} ions is 6.31 and 12.78 %. The larger contribution due to the Be^{4+} ions is due to the increase in the associated charge exchange and ion impact ionisation cross sections. The increase in the cross sections is so great that the decrease in the number density of Be^{4+} ions in comparison to the He^{2+} ions, since charge neutrality is imposed, has little effect. If we now consider the electron density dependence of the composite stopping coefficient which is shown in the plot on the right in figure 4.9. It can be seen that at a density of $1.0 \times 10^{12} \text{ cm}^{-3}$, the contributions to the total stopping coefficient due to the He^{2+} and Be^{4+} ions are respectively 5.1 and 11.67 %. The

contribution due to each ion decreases as the electron density is increased. This reflects the increased contribution due to the D^+ ions as a result of stepwise atomic processes. At a density of $1.0 \times 10^{15} \text{ cm}^{-3}$, the contribution due to He^{2+} and Be^{4+} ions are now respectively 4.45 and 9.32%.

The final plasma which is under scrutiny consists of 93 % D^+ , 2% He^{2+} , 2% Be^{4+} and 3% C^{6+} . The energy and density dependence of the composite stopping coefficient and the associated contributions from each ion is shown in figure 4.10.

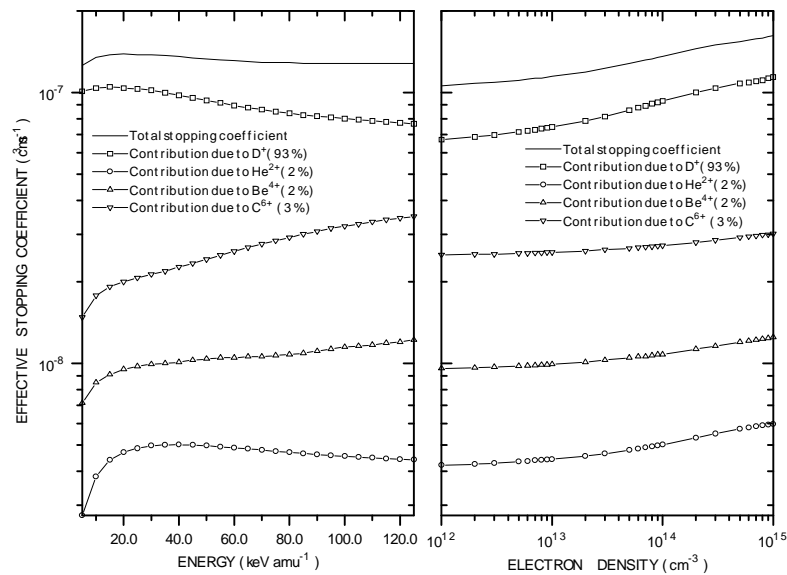


Figure 4.10 A plot of the effective beam stopping coefficient for a composite plasma consisting of 93 % D^+ , 2% He^{2+} , 2% Be^{4+} and 3% C^{6+} . The plot on the left shows the energy dependence while the plot on the right exhibits the electron density dependence. The plasma temperature was 2.0×10^3 eV and the electron density for the plot on the left was $3.0 \times 10^{13} \text{ cm}^{-3}$. The neutral beam energy for the plot on the right was 5.0 keV amu^{-1} .

The energy dependence of the composite stopping coefficient and the contributions from each ion are shown in the plot on the left of figure 4.10. It can be seen that at 5.0 keV amu^{-1} , the contributions to the total stopping coefficients due to the He^{2+} , Be^{4+} and C^{6+} ions are respectively 2.18, 5.67 and 11.74 %. These contributions can be observed to increase and reach a maximum of 3.44 %, 9.53 % and 27.26 % at 125 keV amu^{-1} . It is somewhat surprising that a mere 3 % concentration of C^{6+} can contribute as much as 27.26 % to the total stopping coefficient. This is due to the

large cross sections associated with the C^{6+} ions. Similar results can be seen in the plot on the right in figure 4.10, which illustrates the electron density dependence of the composite stopping coefficient.

4.2.6 Influence of fundamental low level data

In this sub-section we probe the influence of the fundamental atomic data on the effective stopping coefficients. The approach taken here was to modify the cross sections for each of the atomic processes individually, and then investigate what effect it had on the stopping coefficient. Since ion-atom collisions dominate the population redistribution and attenuation, we have restricted ourselves to modifying only the ion-atom collision database. For convenience we only consider a pure D^+ plasma.

We begin by first assessing the implications of increasing the cross sections which describe the behaviour of direct charge exchange and ion impact ionisation by 10 %. The results can be seen in figure 4.11, where we show the effective stopping coefficient as a function of beam energy for three different electron densities. The electron densities were selected to correspond to the coronal, collisional-radiative and high density picture. Also shown in the figure are the results obtained from the unmodified ion-atom collision database.

In the low density coronal picture, it can be observed from figure 4.11 that a 10 % change in the cross sections results in an increase in the stopping coefficient by 8.54 % at 3.0 keV amu^{-1} , which then increases slightly and then decreases to 7.29 % at 120.0 keV amu^{-1} . Due to processes which counter direct charge exchange and ion impact ionisation a change of 10 % in the fundamental data does not give rise to a 10 % change in the effective stopping coefficient. An example of such a process would be collisional excitation, which contributes to depopulating the ground state without ionising the beam atoms and hence reducing the influence of such direct processes. The evidence to suggest this can be seen when the electron density is increased. At an electron density of $3.0 \times 10^{13} \text{ cm}^{-3}$, the influence of the modified data results in a change of 8.06 % at 3.0 keV amu^{-1} , which then decreases to 5.85 % at 120.0 keV amu^{-1} . The increase in the density has enhanced the influence of collisional excitation

and stepwise atomic processes, which in turn reduces the influence of the fundamental data for direct charge exchange and impact ionisation. At an electron density of $1.0 \times 10^{15} \text{ cm}^{-3}$ the result of modifying the cross sections is now only 7.14 % at 3.0 keV amu^{-1} and 3.78 % at $120.0 \text{ keV amu}^{-1}$.

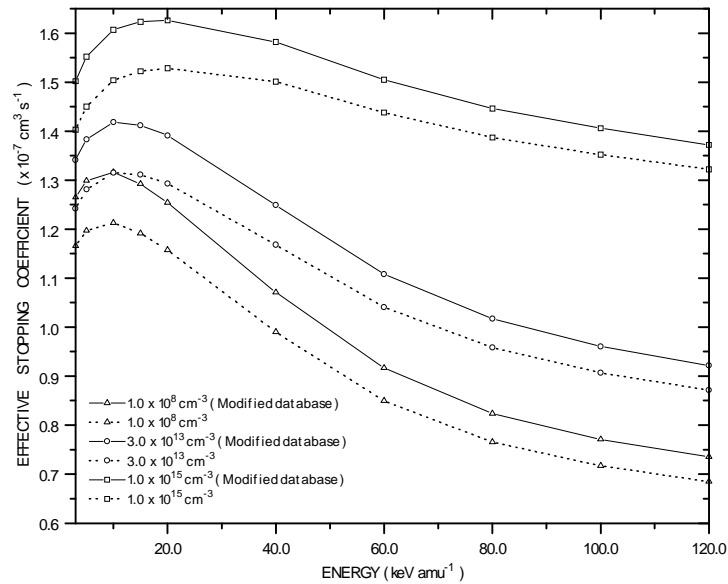


Figure 4.11 Effective stopping coefficient Vs the neutral beam energy for a range of electron densities. The electron densities were selected to correspond to the coronal, collisional-radiative and high density picture. The dashed lines represent the results obtained from the unmodified database. The solid lines represent the results obtained by increasing the direct charge exchange and ion impact ionisation cross-sections by 10 %. The ion temperature was $2.0 \times 10^3 \text{ eV}$.

It is of interest to identify which of the atomic processes associated with the ground state has the most significant effect on the stopping coefficient. In figure 4.12 we show the results of individually modifying the direct charge exchange and ion impact ionisation cross sections by 10 %.

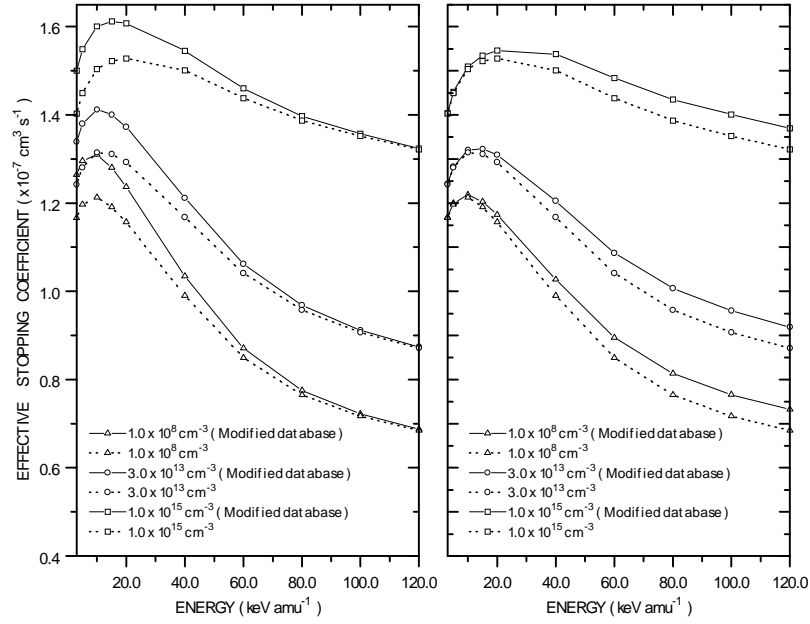


Figure 4.12 Effective stopping coefficient Vs the neutral beam energy for a pure D^+ plasma. The dashed lines are the results from the unmodified database. The solid lines are the results obtained from the modified database. The plot on the left shows the results of increasing the direct charge exchange cross section by 10%. The plot to the right shows the effect of increasing the direct ion impact ionisation cross section by 10 %.

If we first consider the plot on the left in figure 4.12. In this plot the results of changing the direct charge exchange cross section can be observed as a function of beam energy for three different electron densities. At an electron density of $1.0 \times 10^8 \text{ cm}^{-3}$, it can be observed that the modified data has resulted in the effective stopping coefficient differing substantially in the low energy regime. However as the beam energy is increased the difference becomes less significant and eventually the results from the modified and unmodified data agree. An increase in the effective stopping coefficient by 7.69 % can be seen at 3.0 keV amu^{-1} , however at $60.0 \text{ keV amu}^{-1}$ it is only 2.47 % and at 120 keV amu^{-1} it is now just 0.43 %. If we increase the electron density the difference between the modified and unmodified data decrease in the same manner as show in figure 4.11. The influence of the charge exchange data is as expected. It is interesting to point out that in figure 4.11 a difference of 8.54 % was observed at a density of $1.0 \times 10^8 \text{ cm}^{-3}$, therefore we can infer that the contribution

due to altering the ion impact ionisation cross section by 10 % is only 0.85 % at 3.0 keV amu^{-1} . If we now focus on the plot on the right in figure 4.12. This plot contains the results of modifying the direct ion impact ionisation cross section by 10%. As can be observed for an electron density of $1.0 \times 10^8 \text{ cm}^{-3}$, as the beam energy increases the influence of the modified data also increases. At an energy of 3.0 keV amu^{-1} the influence is negligible, however at an energy of 60.0 keV amu^{-1} an increase in the effective coefficient by 5.41 % can be seen, which increases further to reach a value of 7.0 % at 120.0 keV amu^{-1} . As before, an increase in the electron density enhances stepwise atomic processes, which reduces the influence of modifying the direct cross sections.

We now consider the implications of modifying the ion impact excitation cross sections. The ion-atom collision database contain ion impact excitation cross sections from the ground state to the $n=2,3,4$ and $n=5$ shell. In figure 4.13 we show the results of modifying all of the ion impact excitation cross sections by 20%.

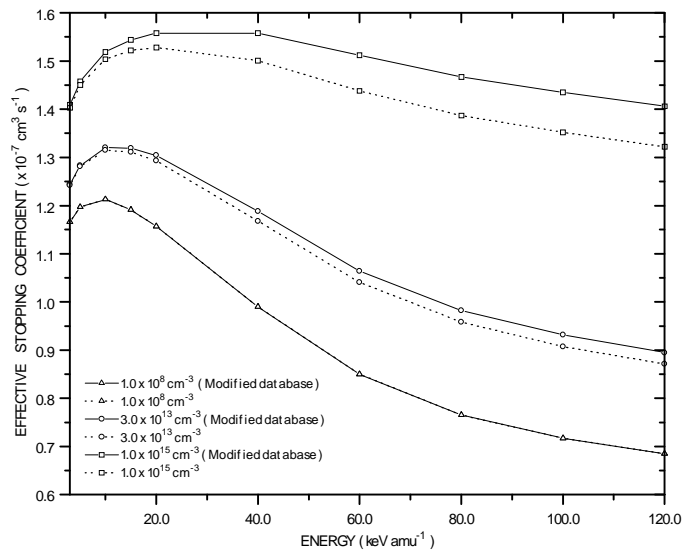


Figure 4.13 Effective stopping coefficient Vs the neutral beam energy for a range of electron densities. The ion temperature was $2.0 \times 10^3 \text{ eV}$. The dashed lines represent the results from the unmodified database. The solid lines are the results obtained by modifying the ion impact excitation cross sections by 20 %.

In the low density regime, the influence of modifying the fundamental data is negligible. As the electron density is increased the influence of the modified data becomes more significant, even though it is still small. At an electron density of $3.0 \times 10^{13} \text{ cm}^{-3}$, the difference between the effective stopping coefficient calculated with and without the modified data, increases as the beam energy also increases. At a beam energy of $20.0 \text{ keV amu}^{-1}$, the difference is only 0.77 % which increases to 2.75 % at $120.0 \text{ keV amu}^{-1}$. Even at $1.0 \times 10^{15} \text{ cm}^{-3}$, the largest difference which can be observed is 6.81 % at $120.0 \text{ keV amu}^{-1}$. In figure 4.14 we show the results of individually changing the ion impact excitation cross sections, we have refrained from showing the results for the excitation cross section from the ground state to the $n=5$ shell, since the effect was insignificant.

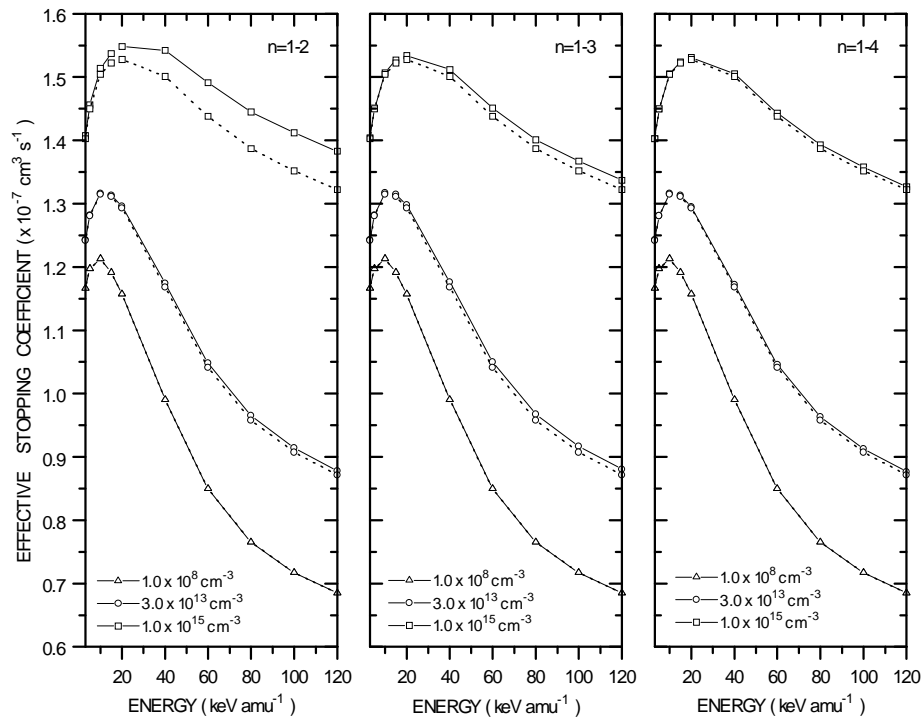


Figure 4.14 Effective stopping coefficient Vs the neutral beam energy for a pure D^+ plasma. Working from left to right the plots illustrate the results of changing the ion impact excitation cross sections from the ground state to the $n=2$, 3 and $n=4$ shell. The dashed lines represents the results from the unmodified database. The ion temperature was $2.0 \times 10^3 \text{ eV}$ and the excitation cross sections were increased by 20%.

Working from left to right, the results of modifying the ion impact excitation cross sections from the ground state to the $n=2,3$ and $n=4$ shell can be seen in figure 4.14. The influence of the modified data only becomes important when the electron density is increased. Modifying the excitation cross section for the $n=1 \rightarrow 2$ transition has the most significant effect. A maximum increase in the effective stopping coefficient by 0.96 % at $3.0 \times 10^{13} \text{ cm}^{-3}$ can be observed, which then increases to 4.54 % at $1.0 \times 10^{15} \text{ cm}^{-3}$. This is due to the large ion impact ionisation cross section associated with the $n=2$ shell, as the $n=2$ population is enhanced by increasing the $n=1 \rightarrow 2$ excitation cross section, the rate at which electrons are stripped from the beam atoms increases.

The influence of changing the cross sections for charge exchange and ion impact ionisation associated with excited states is now of interest. The ion-atom database contains such data for the $n=2,3,4$ and $n=5$ shell. In figure 4.15 the results of increasing all of the cross sections by 30 % can be seen as a function of beam energy for three different electron densities.

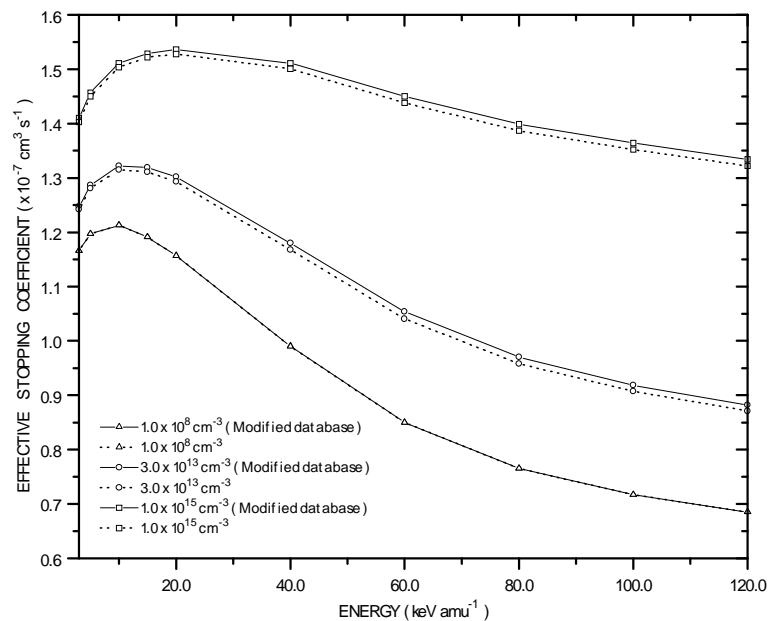


Figure 4.15 Effective stopping coefficient Vs the neutral beam energy for a pure D^+ plasma. The electron densities were selected to correspond to the coronal, collisional-radiative and the high density picture. The ion temperature was $2.0 \times 10^3 \text{ eV}$. The charge exchange and ion impact ionisation cross sections associated with the $n=2,3,4$ and 5 shell were increased by 30 %.

As can be observed, a change in the cross section by 30 % at an electron density of $1.0 \times 10^8 \text{ cm}^{-3}$ has no effect. Even as the density is increased the effect is minimum. This is due to the fact that the excited state populations are very small. A maximum difference of 1.26 % at $1.0 \times 10^{15} \text{ cm}^{-3}$ can be observed. In figure 4.16 we show the results of separately modifying the charge exchange and ion impact ionisation cross section by 30%.

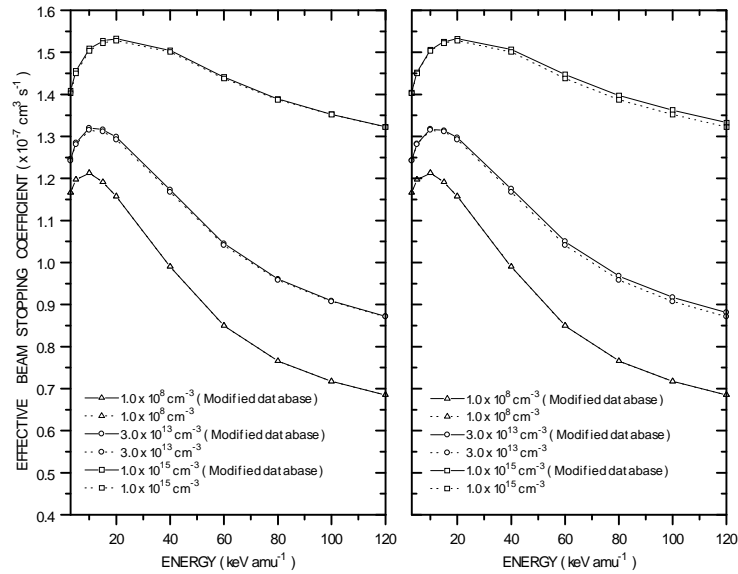


Figure 4.16 Effective stopping coefficient Vs the neutral beam energy for a pure D^+ plasma. The figure on the left illustrates the results of increasing the charge exchange cross sections associated with the excited states ($n=2,3,4$ and 5 shell) by 30%. The plot on the right shows the behaviour of altering the ion impact ionisation cross sections also associated with the excited states ($n=2,3,4$ and 5 shell) by 30%.

4.2.7 Conclusion

A collisional-radiative treatment is necessary to evaluate the effective stopping coefficients. The coronal picture leads to errors at the operating densities of current tokamaks ($\sim 3.0 \times 10^{13} \text{ cm}^{-3}$), see figure 4.2.

The neutral beam energy governs which atomic process are primarily responsible for the attenuation of the neutral beam atoms, see chapter 2.0.

The plasma temperature influences the relative collision velocity between the beam atoms and the thermal plasma ions. This contributes to either increasing or

decreasing the effective stopping coefficient. The influence of the temperature on the effective stopping coefficient is considerably weaker than the electron density and the neutral beam energy, see figure 4.5. A difference of approximately 12% can be observed when the temperature is changed by a factor of 5.

The nuclear charge of fully stripped plasma ion characterises how effective the ion will be at stripping the electrons from the beam atoms. We have shown that as the nuclear charge of a plasma impurity ion increases, the more effective the ion becomes at ionising the beam atoms.

The role of impurities contained in the plasma has also been shown to be of great importance while evaluating effective stopping coefficients. From the examples that we considered, the contribution to the total stopping coefficients due to each of the impurity ions can be substantial. For a basic plasma consisting of 98% D^+ and 2% He^{2+} , the contribution to the total stopping coefficient due to the He^{2+} ions ranged from 2.5 to 5.69 %. In the case of a more detailed plasma consisting of 93% D^+ , 2% He^{2+} , 2% Be^{4+} and 3% C^{6+} , the C^{6+} ions alone contributed up to 27.73 % to the total stopping coefficient.

The influence of the fundamental atomic data on the effective stopping coefficients was investigated. A 10 % increase in the cross sections for direct charge exchange and ion impact ionisation resulted in an increase of approximately 8 % in the stopping coefficient. Stepwise atomic processes counter the influence of direct charge exchange and ion impact ionisation. Increasing the electron density, which enhances stepwise atomic processes, results in reducing the influence of modifying the fundamental data for the direct processes.

Individually increasing the cross sections for each of the direct processes illustrated the energy dependence of their contribution to the stopping coefficient. The contribution due to charge exchange was dominant at the lower energies whilst ion impact ionisation was more significant at the higher energies.

Modifying the ion impact excitation cross sections by 20% had little effect at densities around $1.0 \times 10^8 \text{ cm}^{-3}$. This is due to the fact that at this density the excited states are barely populated. As the density was increased the influence of modifying the excitation cross section was evident. At a density of $3.0 \times 10^{13} \text{ cm}^{-3}$ a change in

the excitation cross sections by 20 % resulted in a change in the stopping coefficient by 2.75 %. Even at $1.0 \times 10^{15} \text{ cm}^{-3}$ a maximum change of 6.81 % could only be observed. Modifying the excitation cross section for the $n=1 \rightarrow 2$ transition had the most significant effect.

The influence of modifying the charge exchange and ion impact ionisation cross sections associated with excited states was negligible. Altering the cross sections by 30 % only resulted in a maximum change of 1.26 % in the stopping coefficient. This again is attributed to the fact that the excited states populations are very small.

4.3 Effective Balmer-alpha emission coefficients

In a similar manner as in section 4.2, we illustrate the main parameter dependencies of the Balmer-alpha effective emission coefficient. The Balmer-alpha effective emission coefficient directly reflects the population of the $n=3$ shell of the excited beam neutrals. Figure 4.17 illustrates the global behaviour of the emission coefficient for a neutral deuterium beam penetrating into a pure D^+ plasma.

The main parameter dependencies of the Balmer-alpha effective emission coefficient which are considered include the electron density, the neutral beam energy, plasma temperature and the nuclear charge of the impurity ions contained in the plasma. The ion density is also an important parameter but in the present work the effective emission coefficients are also calculated in terms of the electron density with the condition of charge neutrality imposed.

We also concern ourselves here with two additional physics issues. Firstly, we illustrate the influence of the fundamental atomic data, following small changes, on the behaviour of the Balmer-alpha effective emission coefficient. Secondly we show the importance of taking into account the impurity content of the plasma while evaluating effective emission coefficients.

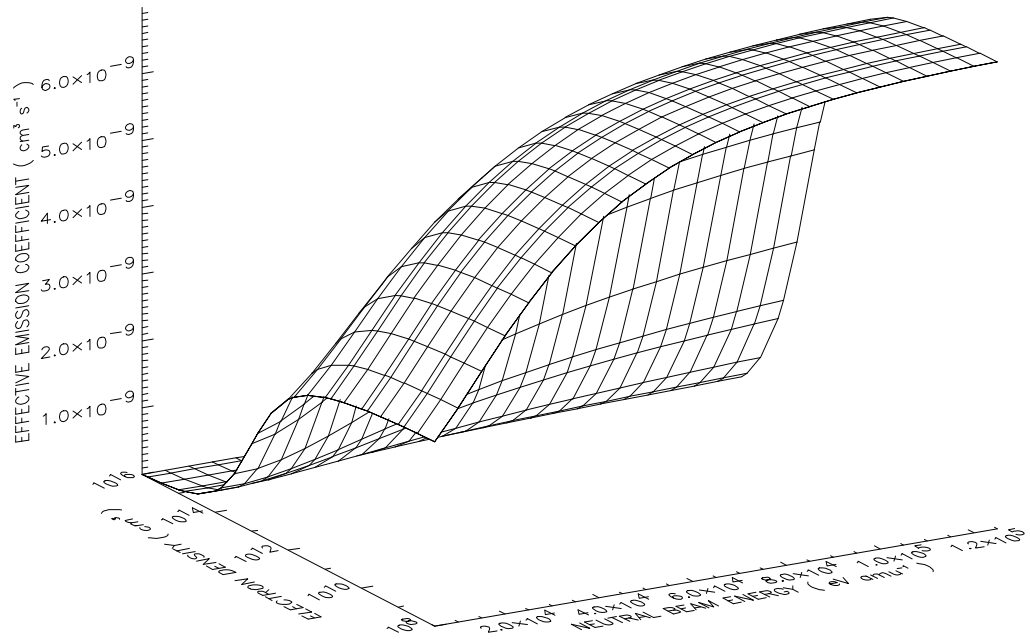


Figure 4.17 A surface plot of the Balmer-alpha emission coefficient for a pure deuterium plasma with a temperature of 2×10^3 eV. The behaviour of the emission coefficient in the coronal limit directly reflects the rate coefficients contributing to populating and depopulating the $n = 3$ shell. As the density is increased the $n = 3$ shell becomes considerably depopulated which results in a decrease in the emission coefficient.

4.3.1 Density dependence

The electron and ion density are both responsible for promoting collisional redistribution amongst the excited states of the neutral beam atoms. The latter being of greater influence. We show in figure 4.18 the behaviour of the Balmer-alpha emission coefficient as a function of energy for a range of electron densities.

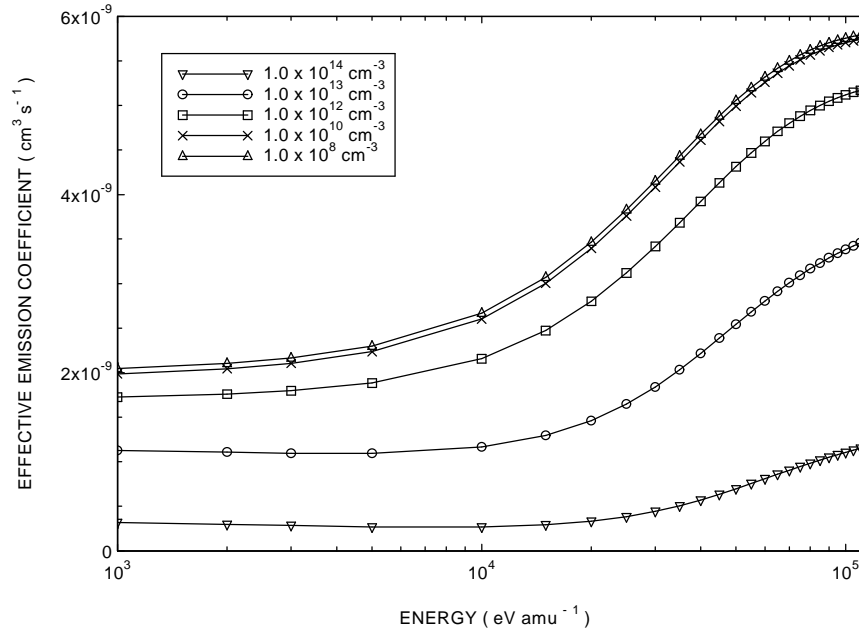


Figure 4.18 Balmer-alpha effective emission coefficient Vs the neutral beam energy for a pure D^+ plasma. The electron density dependence of the effective emission coefficient is clearly illustrated. The plasma temperature was 2.0×10^3 eV

The departure from the low density coronal limit can be observed to occur around $\sim 10^{10} \text{ cm}^{-3}$ (c.f. figure 4.2). As the electron density is increased, the collisional processes begin to compete with the radiative processes. This results in the $n=3$ shell also being collisionally depopulated and a decrease in the effective emission coefficient can be observed.

A similar behaviour can be observed when considering plasmas with a different impurity composition. As an example we show in figure 4.19 the density dependence of the effective emission coefficient for a deuterium beam penetrating into a hypothetical C^{6+} plasma. We emphasise, once again, that it is the ion density which is primarily responsible for the collisional redistribution. As mentioned before, the effective emission coefficients in this work are calculated in terms of the electron density.

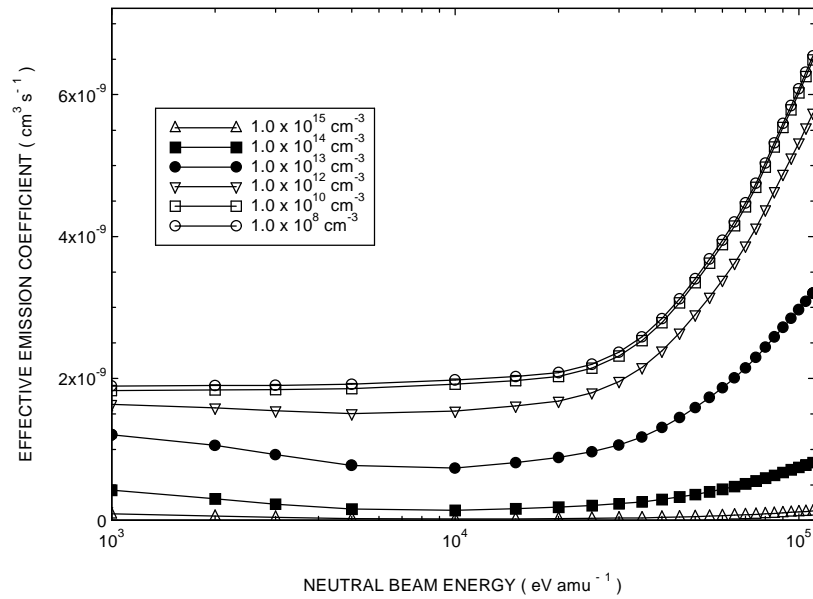


Figure 4.19 Effective emission coefficients Vs the neutral beam energy for a pure C^{6+} plasma. The plasma temperature was 2.0×10^3 eV. The coefficient has been calculated in terms of the electron density with the condition of charge neutrality imposed.

It is of interest to point out that in the low energy regime of figures 4.18 and 4.19, the magnitude of the effective emission coefficients are comparable. This is due to the fact that in this regime, electron collisions are primarily responsible for populating the $n=3$ shell. However as the beam energy increases, the role of the ion collisions become important and the results in each figure begin to differ due to the influence of the nuclear charge associated with each ion. The nuclear charge of the plasma impurity ion determines how effective the ion will be at depopulating the $n=3$ shell and is discussed in section 4.3.4.

4.3.2 Neutral beam energy dependence

The neutral beam energy controls the efficiency of the fundamental atomic processes which contribute to populating and depopulating the $n=3$ shell. We show in figure 4.20 the behaviour of the Balmer-alpha effective emission coefficient as a function of electron density for a range of beam energies.

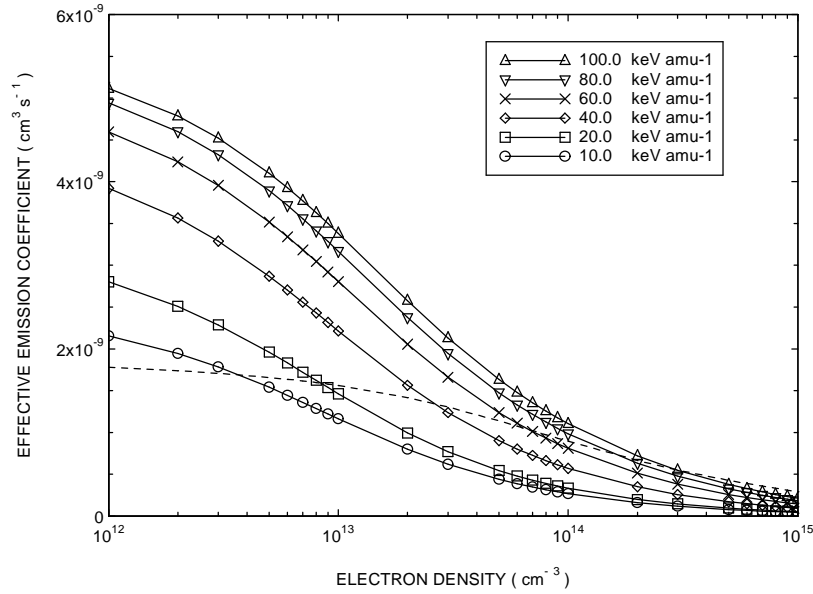


Figure 4.20 The Balmer-alpha effective emission coefficients Vs the electron density for a pure D^+ plasma with a temperature of 2.0×10^3 eV. The energy dependence of the Balmer-alpha emission coefficient is clearly illustrated. Also shown, with the dashed lines, is the contribution to the effective stopping coefficient due to electron collisions.

At a density of $1.0 \times 10^{12} \text{ cm}^{-3}$, an increase in the beam energy results in an increase in the effective emission coefficient. This simply reflects the energy dependence of the underlying atomic processes which contribute to populating the $n=3$ shell. In the low energy regime, collisional excitation by electrons is the dominant process. As the neutral beam energy is increased, ion impact excitation, which is more efficient, becomes substantial, see chapter 2.0. It can also be observed that as the electron density is increased the effective emission coefficient decreases. This can be attributed to the influence of stepwise atomic processes, particularly charge exchange and ion impact ionisation from the $n=3$ shell. Also shown in the figure, with the dashed line, is the contribution to the Balmer-alpha emission coefficient due to electron collisions. This also exhibits a decrease as the electron density is increased.

4.3.3 Temperature dependence

The plasma temperature dependence of the effective emission coefficient also exhibits the same behaviour as shown for the effective stopping coefficients, see

section 4.2.3. In summary, when the beam velocity is slightly greater than the thermal velocity of the plasma ions, an increase in the plasma temperature results in a decrease the relative collision velocity. This in turn may lead to either an increase or decrease in the collision cross sections for the processes which populate the $n=3$ shell. Where as when the thermal velocity of the ions is slightly greater than the beam velocity, an increase in the temperature results in an increase in the relative collision velocity. In figure 4.21 we show the temperature dependence of the Balmer-alpha emission coefficient as a function of beam energy.

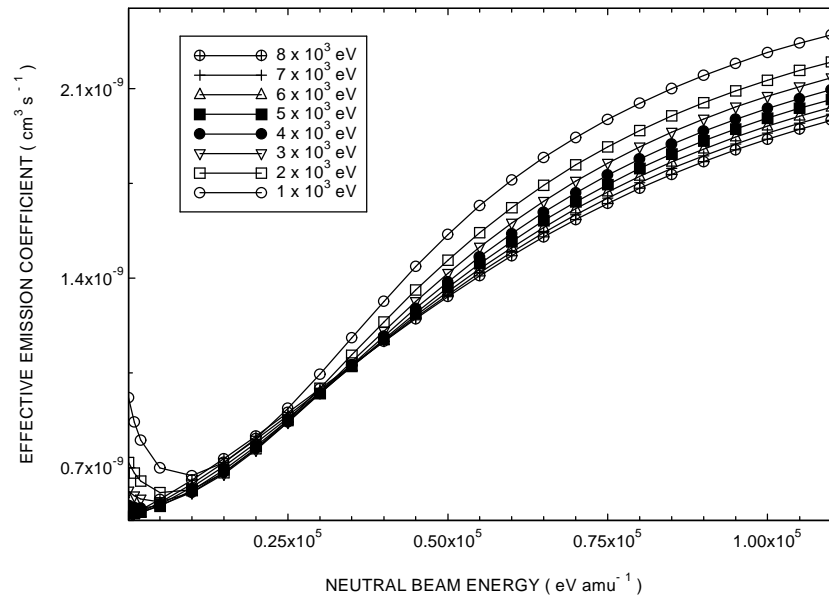


Figure 4.21 Effective Balmer-alpha emission coefficient Vs neutral beam energy for a D^+ plasma . The electron density and plasma temperature was $3.0 \times 10^{13} \text{ cm}^{-3}$ and $2.0 \times 10^3 \text{ eV}$ respectively. A change in the effective coefficient by 6.8 % at a beam energy of 30 keV amu^{-1} can be achieved by modifying the temperature by a factor of 5, this increases to 12.7 % at 70 keV amu^{-1} .

As shown in figure 4.21, in the low energy regime an increase in the plasma temperature gives rise to an increase in the effective emission coefficient. This is simply due to an increase in the collision cross sections as a result of increasing the relative collision velocity between the beam atoms and the thermal plasma ions. In the high energy regime the opposite can be observed. It can also be seen that at an energy of 30 keV amu^{-1} , a change in the emission coefficient of 6.8 % can be

achieved by modifying the temperature by a factor of 5. This increases to 12.7 % at 70 keV amu⁻¹. A point to note however is that below 10 keV amu⁻¹ a change of up to 40 % can be observed. The temperature dependence of the emission coefficient is larger than that for the effective stopping coefficient. This is due to the increased role of electron collisions which contribute to populating the n=3 shell, see figure 4.20, where as for the effective stopping coefficients, the contribution due to the electrons is very small, see figure 4.4

4.3.4 Nuclear charge dependence

As discussed in 4.2.4, the nuclear charge of a fully stripped plasma ion governs how effective the ion will be at stripping the electrons from the beam atoms. The nuclear charge also determines the extent to which the ion will contribute to the collisional redistribution of the excited states of the beam atoms. In general, the efficiency of the ion increases with nuclear charge. If we consider the population of the n=3 shell, as the nuclear charge of the plasma ion increases, the cross sections for the collisional processes which populate the n=3 shell, such as excitation, also increase. We would then expect the n=3 shell population and hence the Balmer-alpha coefficient to increase. However the cross sections for ion impact ionisation and charge exchange from the n=3 shell also become larger. The net effect is that the population of the n=3 shell becomes smaller as the nuclear charge of the plasma ion increases. We show in figure 4.22, the behaviour of the Balmer-alpha effective emission coefficient as a function of beam energy for a range of pure impurity plasmas.

In the low energy regime the n=3 shell is populated primarily by electron collisions and the Balmer-alpha emission coefficient is almost independent of the beam energy, see figure 4.22. There is a small thermal contribution from each ion, which gives rise to the nuclear charge dependence of the effective emission coefficient. As the beam energy is increased the ion collisions become important and as can be observed the larger the nuclear charge the smaller the effective emission coefficient. We highlight here that the electron density was fixed at $3.0 \times 10^{13} \text{ cm}^{-3}$ and charge neutrality was imposed. Therefore as the nuclear charge of the impurity ion increases the corresponding number density decreases.

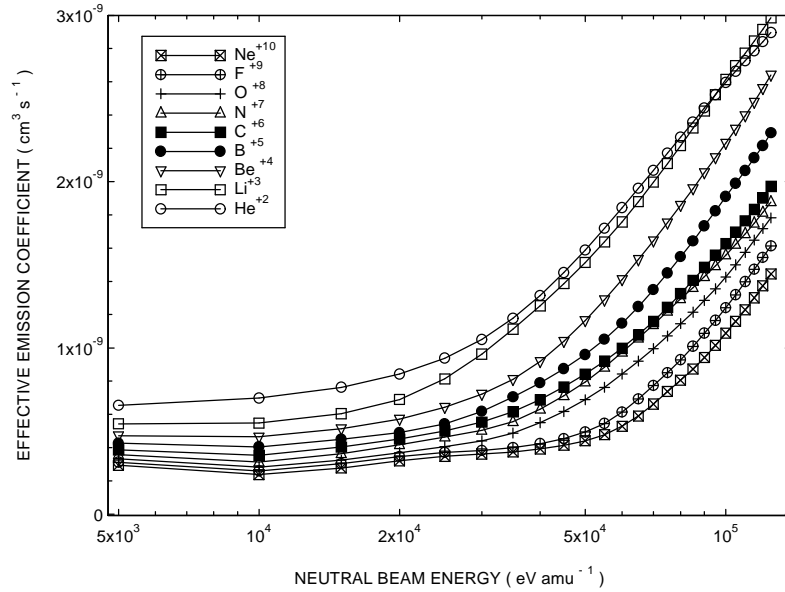


Figure 4.22 Effective emission coefficient Vs neutral beam energy for a range of pure impurity plasmas. The electron density and the plasma temperature was respectively $3.0 \times 10^{13} \text{ cm}^{-3}$ and $2.0 \times 10^3 \text{ eV}$. A point to note is that charge neutrality has been imposed, therefore the number density of impurity ions decreases as the nuclear charge of the impurity species increases.

4.3.5 The importance of impurities

In fusion plasmas, the typical concentration of each impurity ion rarely exceeds 5 %. To simplify the evaluation of the effective emission coefficient, it may then appear to be valid to neglect the impurity content of the plasma. However this is not the case. In this section we illustrate the importance of taking the impurity content of the plasma into account while evaluating effective emission coefficients. The approach adopted here is similar to that of section 4.2.5, here we calculate the effective Balmer-alpha emission coefficient for a range of composite plasmas and in each case illustrate the contribution due to each impurity ion. This will allow us to quantitatively assess the implications of neglecting the impurity content of the plasma while evaluating effective emission coefficients.

We first begin with a composite plasma which consists of 98 % D^+ and 2 % He^{2+} . The energy and density dependence of the composite emission coefficient is shown in figure 4.23. Also shown are the individual contributions due to the D^+ and He^{2+} ions.

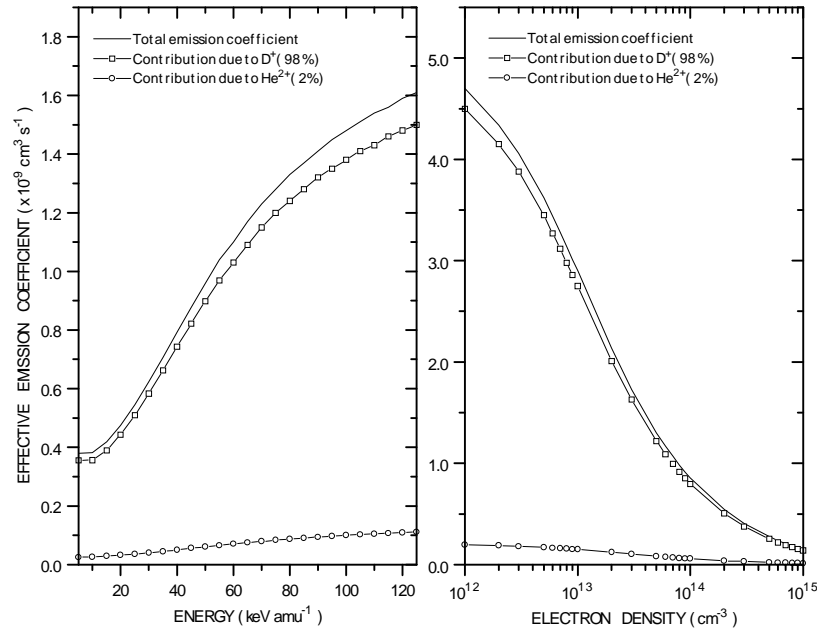


Figure 4.23 A plot of the Balmer-alpha effective emission coefficient for a composite plasma consisting of 98% D^+ and 2% He^{2+} . The plot on the left illustrates the energy dependence of the composite stopping coefficient, while the plot on the right shows the corresponding density dependence.

The energy dependence of the effective emission coefficient is shown in the plot on the left in figure 4.23. It can be observed that the contribution to the total emission coefficient due to the 2% concentration of He^{2+} ions, increases from 6.6 % at 5.0 keV amu^{-1} to 6.95 % at 125 keV amu^{-1} . A similar result can be observed in the plot on the right in figure 4.23, which illustrates the electron density dependence of the emission coefficient. As the electron density is increased the contribution to the composite emission coefficient slowly increases. At a density of $1.0 \times 10^{12} \text{ cm}^{-3}$, the contribution due to the He^{2+} ions is 4.14 %, which then increases to a maximum value of 8.70 % at a density of $1.0 \times 10^{15} \text{ cm}^{-3}$.

We now consider a slightly different plasma which consists of 96 % D^+ , 2% He^{2+} and 2% Be^{4+} . The energy and density dependence of the composite coefficient can be seen in figure 4.24.

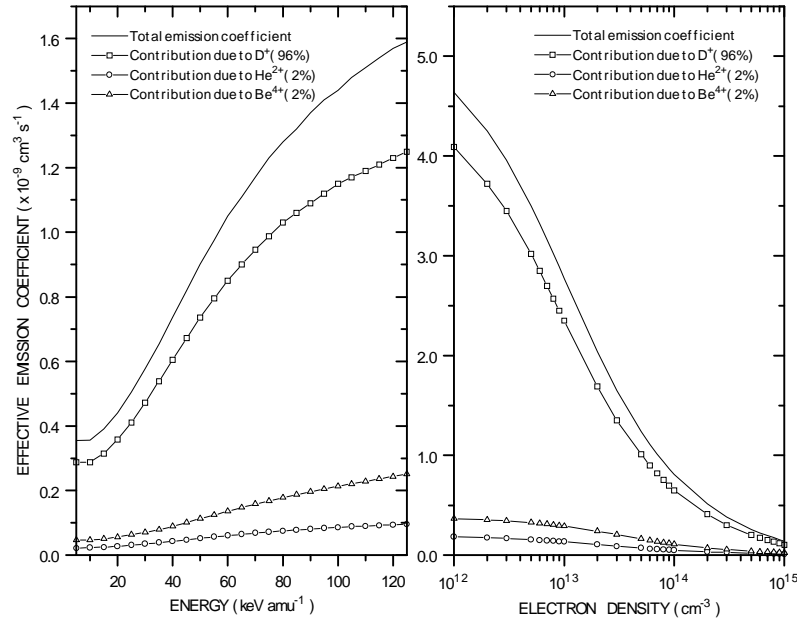


Figure 4.24 A plot of the Balmer-alpha effective emission coefficient for a composite plasma consisting of 96 % D^+ , 2 % He^{2+} and 2% Be^{4+} . The plot on the left exhibits the energy dependence of the composite emission coefficient, while the plot on the right illustrates the density dependence. Also shown are the individual contributions due to each ion.

The plot on the left illustrates the energy dependence of the emission coefficient. The individual contributions due to the He^{2+} and Be^{4+} ions respectively increase from 5.97 and 13.12 % at 5.0 keV amu^{-1} to 6.03 and 15.78 % at 125 keV amu^{-1} . The contribution from the Be^{4+} ions is greater since the associated cross sections are larger. In figure 4.24 we also show the electron density dependence of the composite emission coefficient. At a density of $1.0 \times 10^{12} \text{ cm}^{-3}$, the contribution due to He^{2+} and Be^{4+} ions are respectively 3.94 and 7.82%. These increase to a maximum value of 8.02 and 16.78 % at a density of $1.0 \times 10^{15} \text{ cm}^{-3}$.

The last plasma which we consider consists of 93% D^+ , 2 % He^{2+} , 2% Be^{4+} and 3% C^{6+} , see figure 4.25.

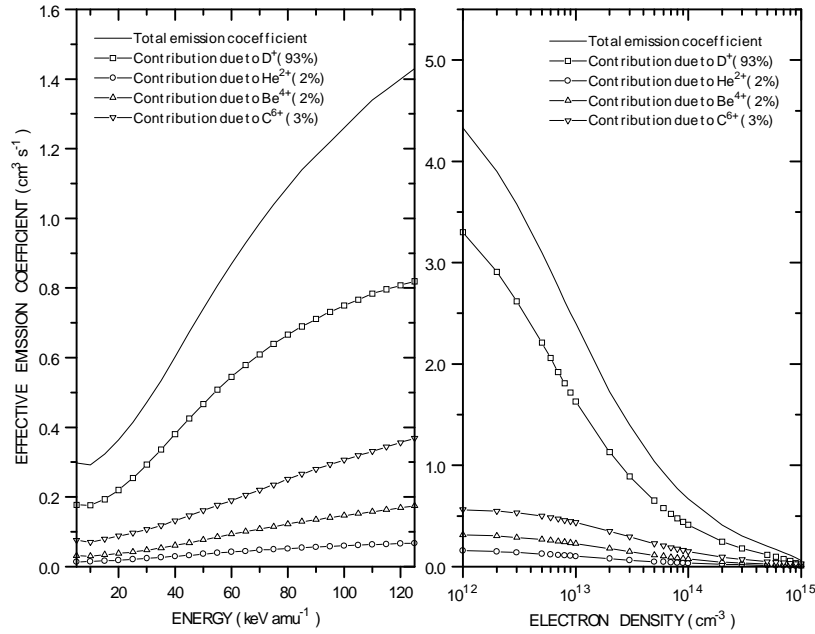


Figure 4.25 A plot of the Balmer-alpha effective emission coefficient for a composite plasma consisting of 93 % D⁺, 2% He²⁺, 2% Be⁴⁺ and 3% C⁶⁺. The plot on the left shows the energy dependence of the emission coefficient. The plot on the right illustrates the density dependence. The ion temperature was 2.0×10^3 eV.

The plot on the left exhibits the energy dependence of the coefficient while the plot on the right illustrate the corresponding density dependence. If we confine ourselves with the energy dependence of the effective emission coefficient. It can be observed that the contribution to the total emission coefficient due to the impurity ions increases as a function of energy. At 5.0 keV amu^{-1} the contribution due to He²⁺, Be⁴⁺ and the C⁶⁺ ions are respectively 4.73, 10.43 and 25.26 %. We now consider the electron density dependence of the composite emission coefficient. It can be observed that at a density of $3.0 \times 10^{13} \text{ cm}^{-3}$, which is typical the operating density of present day tokamak devices, the contribution due to the He²⁺, Be⁴⁺ and the C⁶⁺ ions are respectively 4.6, 10.5 and 21.07 %. A total combined contribution to the effective emission coefficient due to the impurity ions is $\sim 36\%$.

4.3.6 Influence of fundamental low level data

In this sub-section we investigate the influence of the fundamental atomic data on the effective Balmer-alpha emission coefficient. The approach adopted is similar to that of section 4.2.6, where we individually modify the cross sections associated with each atomic process for a pure D^+ plasma.

We begin by considering the implications of increasing the cross sections for direct charge exchange and ion impact ionisation by 10 %. The results are shown in figure 4.26 as a function of beam energy for three different electron densities.

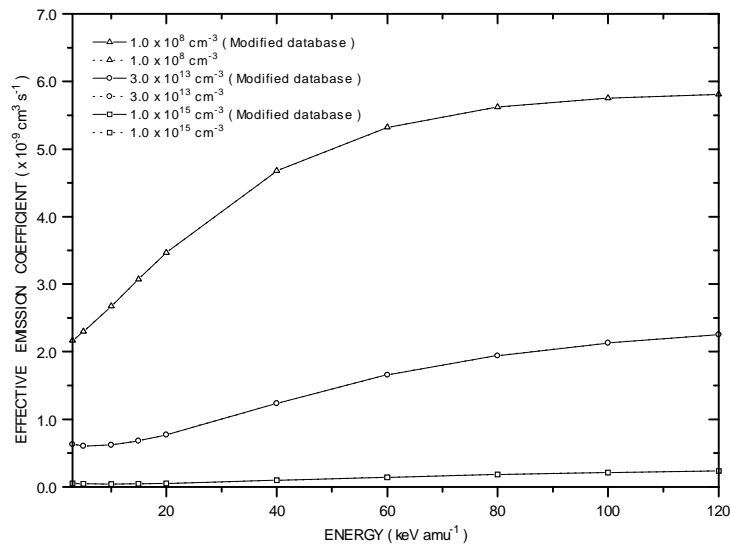


Figure 4.26 A plot of the effective emission coefficient for a pure D^+ plasma. The three densities have been selected to correspond to the coronal, collisional-radiative and the high density picture. The solid lines show the results obtained by increasing the direct charge exchange and ion impact ionisation cross sections by 10 %. The ion temperature was 2×10^3 eV.

As can be observed, increasing the direct charge exchange and ion impact ionisation cross sections has a negligible effect. This is such a contrast to the behaviour of the effective stopping coefficients. Earlier we saw that such a change in the fundamental data gave rise to an increase of approximately 8 % in the effective stopping coefficient.

The influence of the ion impact excitation cross sections is now of interest. The ion-atom collision database contains excitation cross sections from the ground

state to the $n=2,3,4$ and $n=5$ shell. In figure 4.27 we show the results of increasing all of the excitation cross sections by 20 %, the dashed lines are the results obtained from the unmodified database.

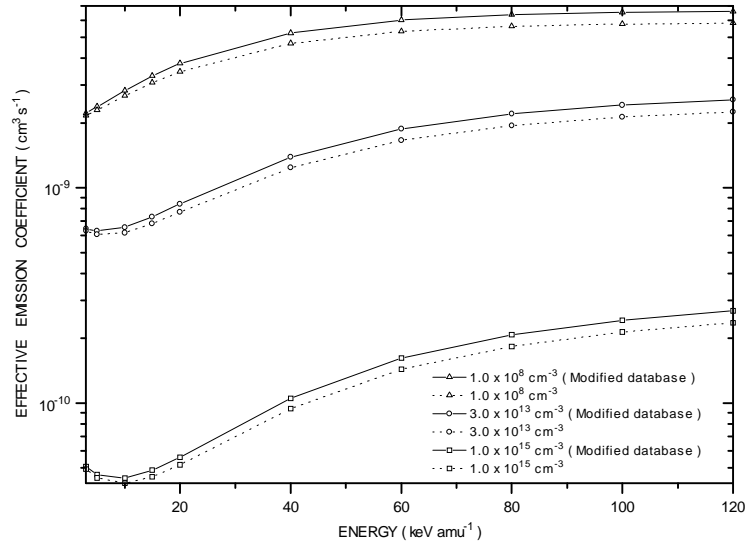


Figure 4.27 A plot of the effective emission coefficient for a pure D^+ plasma. The solid lines illustrate the results obtained by increasing all of the ion impact excitation cross sections by 20%. The dashed lines correspond to the results obtained from the unmodified database. The plasma temperature was 2.0×10^3 eV.

It can be observed that the influence of the modified data increases as a function of beam energy and electron density. At $1.0 \times 10^8 \text{ cm}^{-3}$, the 20 % increase in the excitation cross sections has given rise to an increase in the emission coefficient by 2.30 % at 3.0 keV amu^{-1} , which then increases to a maximum value of 13.42 % at 120 keV amu^{-1} . As the electron density is increased, the influence of the modified data is slightly enhanced. At $1.0 \times 10^{15} \text{ cm}^{-3}$ the effective emission coefficient increases from 2.83 % at 3.0 keV amu^{-1} to 13.55 % at 120 keV amu^{-1} .

It is of interest to identify which excitation rate is primarily responsible for influencing the effective emission coefficient. In figure 4.28 we show the results of individually increasing each of the ion impact excitation cross sections by 20 %.

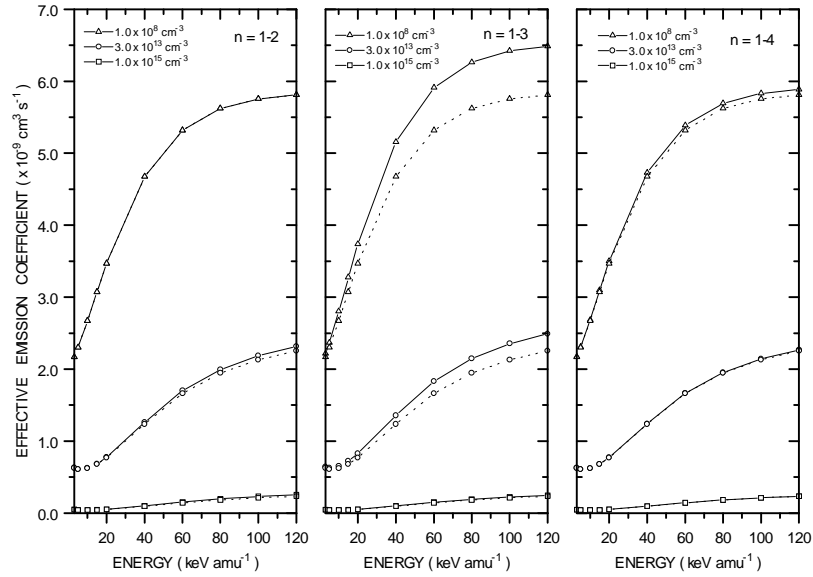


Figure 4.28 A plot of the effective emission coefficient for a pure D^+ plasma. The solid lines indicate the results obtained from modifying the fundamental data, while the dashed lines show the results from the unmodified database. Working from left to right are the results obtained by increasing the excitation cross sections from the ground state to the $n=2,3$ and $n=4$ shell by 20%. The plasma temperature was 2.0×10^3 eV.

The results of increasing the excitation cross sections associated with the ground state to the $n=2,3$ and $n=4$ shell can be observed. The dashed lines represent the results obtained from the unmodified database. Modifying the collisional excitation cross section for the $n=1 \rightarrow 3$ transition has the greatest influence on the effective emission coefficient. At a density of $3.0 \times 10^{13} \text{ cm}^{-3}$, an increase of 20 % in this cross section results in the emission coefficient increasing from 2.38 % at 3.0 keV amu^{-1} to 10.66 % at $120.0 \text{ keV amu}^{-1}$. It is worth noting that the influence of the cross section for the $n=1 \rightarrow 3$ transition was very small on the behaviour of the stopping coefficient, the most influential data was that associated with the $n=1 \rightarrow 2$ transition.

We now investigate the influence of the fundamental data which describes charge exchange and ion impact ionisation associated with the excited states. The ion-atom collision database contains such data for the $n=2,3,4$ and $n=5$ shell. In figure 4.29, we show the results of increasing all of the charge exchange and ion impact ionisation cross sections by 30%.

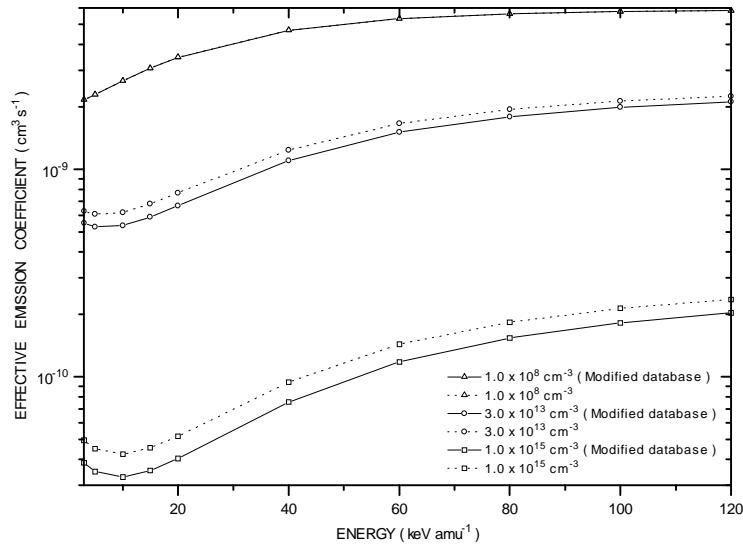


Figure 4.29 A plot of the effective emission coefficient for a pure D^+ plasma. The solid lines show the results obtained by increasing the cross sections for charge exchange and ion impact ionisation associated with the excited states by 30 %. The dashed lines are the results from the unmodified database.

At $1.0 \times 10^8 \text{ cm}^{-3}$, increasing the excited state cross sections has little effect. This is due to the fact that at such low densities the excited states are scarcely populated. As the electron density is increased, the excited state populations begin to increase and the influence of the excited state cross sections becomes important. Generally speaking, an increase in the charge exchange and ion impact ionisation cross sections associated with the excited states gives rise to a decrease in the emission coefficient. From figure 4.29, it can be observed that at an electron density of $1.0 \times 10^{15} \text{ cm}^{-3}$, the effective emission coefficient decreases by 21.8 % at 3.0 keV amu^{-1} . The influence of the modified data becomes less as the beam energy increases, at 120 keV amu^{-1} a difference of 13.98 % can be observed. Interestingly though, the influence of such data on the effective stopping coefficients was negligible.

In figure 4.30 we show the results of individually increasing the charge exchange and ion impact ionisation cross sections associated with the excited states by 30 %.

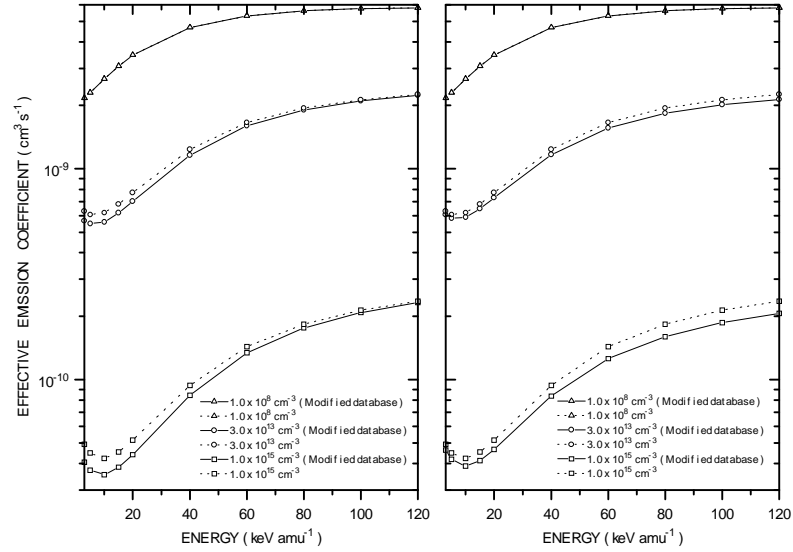


Figure 4.30 A plot of the effective emission coefficient for a pure D^+ plasma. The plot on the left illustrates the results of increasing all of the charge exchange cross sections associated with the excited states by 30 %. The plot on the right shows the influence of increasing the ion impact ionisation cross sections associated with the excited states by 30 %. The solid lines are the results from the modified database. The dashed lines are the results from the unmodified database.

If we consider the plot on the left, which shows the results of increasing the charge exchange cross sections associated with the excited states. It can be observed that as the beam energy increases, the reduction in the effective emission coefficient decreases. This simply reflects the energy dependence of the charge exchange cross sections. A similar type of behaviour can be observed on the plot on the right, which illustrates the results of changing the ion impact ionisation cross sections. However in this case, the decrease in the effective emission coefficient increases as function of beam energy.

4.3.7 Conclusion

At the operating densities of current tokamaks, a collisional-radiative treatment is also required to evaluate the effective emission coefficients, see figure 4.18.

The neutral beam energy determines the efficiency of the atomic processes which contribute to populating the $n=3$ shell. Electron impact excitation is the

dominant process in the low energy regime, as the energy is increased ion collision become important, see chapter 2.0.

A change in the plasma temperature alters the relative collision velocity between the beam atoms and the plasma ions. This gives rise to either an increase or decrease in the effective emission coefficient.

The temperature dependence of the effective emission coefficient is greater than that for the effective stopping coefficients. This is due to the increased role of electron collisions which contribute to populating the $n=3$ shell, see figure 4.20.

The nuclear charge of a fully stripped plasma impurity ion governs the effectiveness at which the ion contributes to depopulating the $n=3$ shell. For a fixed electron density, as the nuclear charge of the impurity ion increases, the Balmer-alpha effective emission coefficient decreases.

We explored the implications of neglecting the impurity content of a plasma while evaluating effective emission coefficients. From the composite plasmas that we considered, we found that each plasma impurity ion contributes substantially to the effective emission coefficient. For a composite plasma consisting of 96% D^+ , 2% He^{2+} and 2% Be^{4+} , the minimum contribution to the emission coefficient from each impurity ion was respectively 3.94 and 7.82 %. Even for a plasma consisting of 93 % D^+ , 2% He^{2+} , 2% Be^{4+} and 3% C^{6+} , the combined contribution to the emission coefficient due to all of the impurity ions was as much as ~ 36 %.

The influence of the fundamental data on the behaviour of the emission coefficient was investigated. Increasing the cross sections for direct charge exchange and ion impact ionisation by 10 % had a negligible effect. This is such a contrast to the behaviour of the effective stopping coefficients, see section 4.2.6.

Modifying the ion impact excitation cross sections gave rise to a maximum increase in the effective emission coefficient of 13.55 % . The cross section for the $n=1 \rightarrow 3$ transition had the greatest influence on the Balmer-alpha emission coefficient. Increasing this cross section by 20% gave rise to an increase in the effective emission which ranged from 2.28 % at 3.0 keV amu^{-1} to 10.66 % at 120 keV amu^{-1} . It is of interest to point out here that the excitation cross section for the $n=1 \rightarrow 3$ transition had little effect on the stopping coefficient.

The influence of charge exchange and ion impact ionisation associated with the excited states was studied. Increasing the cross sections for these processes resulted in decreasing the effective emission coefficient. This was simply due to the fact that charge exchange and ion impact ionisation associated with the excited states contributes to depopulating the $n=3$ shell.

4.4 Application to experimental programs

4.4.1 Introduction

As discussed earlier, there are two methods which may be employed to determine the neutral beam density at points along the beam line. A numerical attenuation calculation and an experimental spectroscopic method. The latter involves measuring the intensity of the D- α light emitted from the excited beam neutrals and is formally known as beam emission spectroscopy, see chapter 5.0. The effective beam stopping coefficients are employed in the attenuation calculation, whilst the effective Balmer-alpha emission coefficients are used to recover the neutral beam density via beam emission spectroscopy. To satisfy the demands of experimental analysis for inter pulse reduction of data and physical parameters, for example at JET, there is a requirement to compute the neutral beam density on a rapid and automatic basis. Therefore ab initio calculations of the effective stopping or emission coefficients for each changed set of plasma conditions in real time are impractical and a method of constructing and storing fast look up tables of the effective coefficients is sought.

In the following sections we discuss the practical production, archiving and application of such fast look up tables. A linear combination and interpolation method for multiple impurity plasmas has been suggested and used by Summers[26]. The effective coefficients for a plasma containing a variety of impurities are assembled from a collection of look up tables. Each separate look up table contains coefficients calculated for a single impurity species. We examine the accuracy of this linear combination and interpolation method.

4.4.2 Production and archiving the derived data

As discussed in detail in chapter 3.0, the calculation of the effective beam stopping and emission coefficients is done using a bundled-nS collisional-radiative model called ADAS310. Using ADAS310, very complete calculations of the excited population structure are in fact performed. The tabulated population structure and the effective stopping coefficients are stored as a function of plasma parameters in the ADAS data format of adf26. The plasma parameters include the neutral beam energy, electron density, the plasma temperature and impurity species mix (multiple or single). To assemble fast look up tables an interactive program, ADAS312, is employed to extract the effective stopping and emission coefficients, this is discussed in chapter 3.0. An overview of the production and storage of the derived data is shown in figure 4.31.

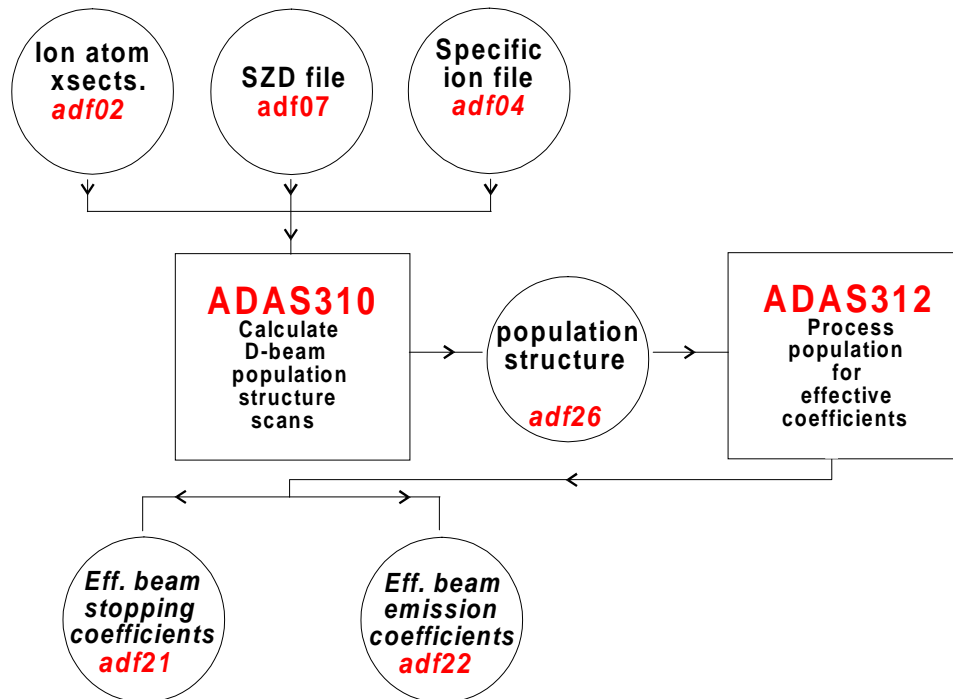


Figure 4.31 Schematic overview of the production of the derived coefficients. Starting with the fundamental data which is used as input for ADAS310. A detailed calculation of the excited population structure and effective stopping coefficients are performed. The output is tabulated in the format of ADAS data type adf26. An interrogation code ADAS312 is then employed to extract the effective stopping and emission coefficients from the adf26 type file.

4.4.3 Linear interpolation scheme

The storage of the derived data in both the adf21 and adf22 type files is designed to economise on the access time of retrieving the stored coefficients. To achieve this the coefficients are stored in a format consisting of a two dimensional scan in energy and density and a one dimensional scan in temperature. Since the temperature dependence of the coefficients is almost independent of the beam energy and density, the one and two dimensional grid can be used to compute the coefficient for any parameter value contained within the tabulated range. The two dimensional scan is achieved by tabulating the coefficients as a function of neutral beam energy and electron density at a fixed reference temperature, while the one dimensional scan is assembled as a function of temperature at fixed reference values for the beam energy and electron density. The schematic in figure 4.32 shows the relationship between the one and two dimensional scan.

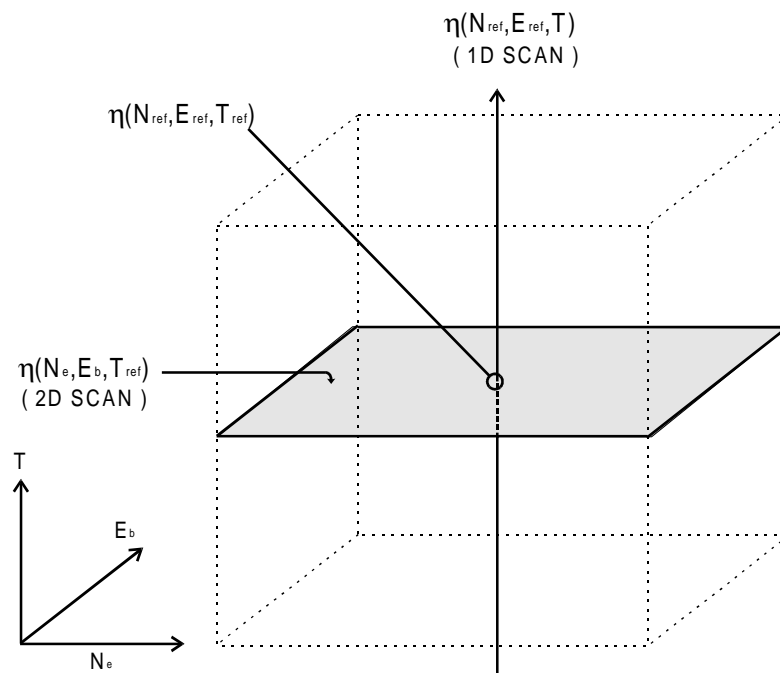


Figure 4.32 Illustration of the one and two dimensional scan employed to create compact data sets. The plasma temperature, neutral beam energy and the electron density are respectively represented using T , E_b and n_e . The subscript 'ref' indicates that the parameter is being treated as a reference value and is held as a constant.

To evaluate the effective coefficient using the one and two dimensional scan the following relation is then employed,

$$\eta(E_b, n_e, T) \approx \left[\frac{\eta(E_b^{REF}, n_e^{REF}, T)}{\eta(E_b^{REF}, n_e^{REF}, T^{REF})} \right] \eta(E_b, n_e, T^{REF}) \quad 4.2$$

where η represents either effective beam stopping or emission coefficients. The quantities E_b , n_e and T respectively correspond to the beam energy, electron density and the plasma temperature. The associated superscripts simply indicate the value is employed as a reference.

4.4.4 Linear combination scheme

In designing compact data sets for the storage of the effective coefficients, we now require a method which would allow one to assemble effective coefficients for a plasma contaminated with impurities. The method adopted in this work was first developed by Summers[26] and can be described as a linear combination scheme. The effective coefficient data sets for each fully stripped impurity species up to the first period are calculated as though the species alone is present in the plasma. A linear combination of the individual data sets is then used to synthesis a composite coefficient for a plasma which may contain a variety of impurity species. The combination of the pure impurity data sets is based on the assumption that the contributions from each impurity ion in the plasma are additive. To obtain the total composite coefficient one simply adds the contribution from each impurity species according to there appropriate concentration found in the plasma. In the case of the effective beam stopping coefficients which are calculated in terms of the electron density. The total stopping coefficient for a plasma consisting of n impurities is given as,

$$S_{CR}^{Total}(E_b, n_e, T) = \sum_{n=1} z_0^n f^{Z_0^n} S_{CR}^{Z_0^n}(E_b, n_e^{Z_0^n}, T) \Big/ \sum_{n=1} z_0^n f^{Z_0^n} \quad 4.3$$

The quantity $n_e^{z_0^n}$ is the effective electron density due to the n^{th} impurity and is given by the following expression,

$$n_e^{z_0^n} = \left[\frac{\sum_{n=1} z_0^{n2} f^{z_0^n}}{\sum_{n=1} z_0^n f^{z_0^n}} \right] \frac{n_e}{z_0^n} \quad 4.4$$

The effective stopping coefficient due to the n^{th} impurity species is $S_{\text{CR}}^{(z_0^n)}$ and $f^{z_0^n}$ is the corresponding fraction contained in the plasma, which is specified in terms of the total electron density, n_e . The beam emission coefficients are handled in the same manner.

An interactive program as well as a selection of FORTRAN routines which implement the linear interpolation and combination method can be found in ADAS. The interactive program, ADAS304[26], is designed to allow one to interactively assemble either effective stopping or emission coefficients for a composite plasma using the pure impurity data sets. The selection of FORTRAN routines enable one to directly implement the linear combination method in an experimental analysis program.

4.4.5 Accuracy of the linear combination and interpolation scheme

In this section we investigate the accuracy of the linear interpolation and combination scheme. This is achieved by simply comparing our results obtained from the true calculation of ADAS310 with the linear methods of ADAS304. We first consider effective beam stopping coefficients and then extend our study to include effective beam emission coefficients. In both cases we have considered a wide range of scenarios but only summarise the main features here.

4.4.5.1 Effective beam stopping coefficients

In the following series of examples we show the percentage difference between the results obtained from the true calculation and the linear combination and interpolation method. It is convenient to consider the accuracy of the linear combination and interpolation method separately. This can be achieved by first studying the assembly of the effective coefficients using a temperature which

corresponds to the reference temperature. Therefore the linear interpolation along the one dimensional temperature grid is suppressed. This allows us to investigate the accuracy of the linear combination method. We can then study the assembly of the effective stopping coefficients under conditions which requires the linear interpolation along the one dimensional temperature grid. This enables us to study the combine accuracy of both linear methods.

The first hypothetical plasma that we consider consist of 75 % D^+ and 25 % Be^{4+} . The impurity content of the plasma has been exaggerated to illustrate the accuracy of the linear methods under extreme conditions. We show in figure 4.33, as a function of beam energy the accuracy of the linear combination method for a range of electron densities. The plasma temperature has been selected to correspond to the reference temperature

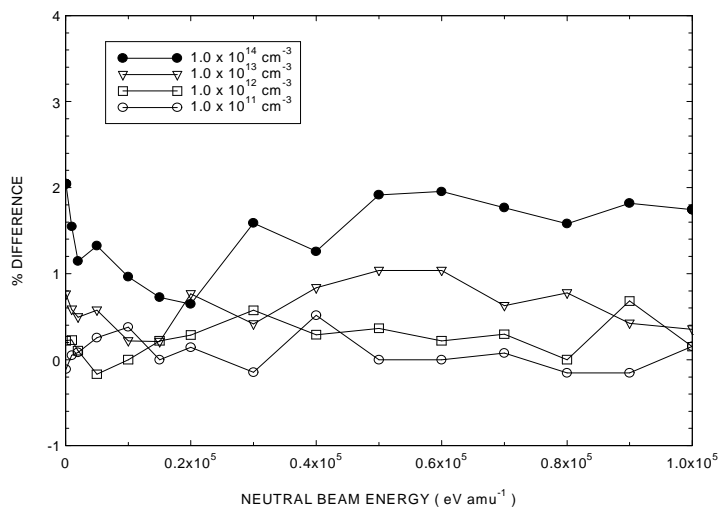


Figure 4.33 A plot of the percentage difference between the output from ADAS304 & ADAS310. The above illustrates that accuracy of the linear assembly performed by ADAS304, a maximum difference of 1.79 % can be observed. The reference density and temperature are respectively $6.78 \times 10^{10} \text{ cm}^{-3}$ and $2.0 \times 10^3 \text{ eV}$.

A maximum difference between the results of ADAS310 and ADAS304 of 1.79 % can be observed. We now consider the evaluation of the effective coefficients using both the linear interpolation and combination method. In figure 4.34 we show the

results as a function of energy for a range of temperatures. Therefore interpolation along the temperature grid is required.

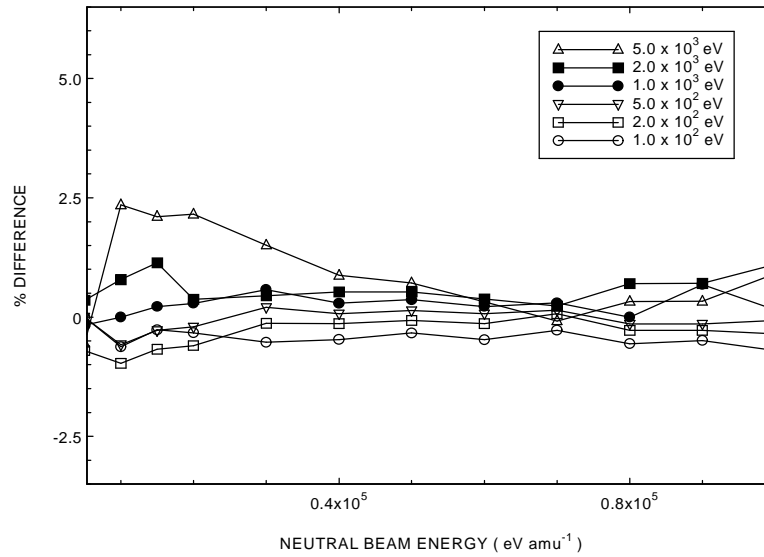


Figure 4.34 A plot of the percentage difference between the output of ADAS304 & ADAS310. Using a reference temperature of 2×10^3 eV , the maximum difference can be observed to be 1.96 %. However below 2×10^3 eV amu^{-1} the difference rises to 2.64 % and continues to reach a peak of 20.70 % at 100 eV amu^{-1} . The electron density was set to a value of 1×10^{12} cm^{-3} and the reference density was 6.78×10^{10} cm^{-3} .

Above 2.0 keV amu^{-1} a maximum difference of 1.96 % can be observed, however below this energy value the difference rises to a peak of 20.70 % at 100 eV amu^{-1} . We now extend our investigation by considering a more complicated plasma. The plasma which is under scrutiny consists of 70% D^+ , 20% C^{6+} and 10% Be^{4+} . The accuracy of the linear combination method is first considered, see figure 4.35. A maximum difference of 1.86 % can be observed between the results obtained from ADAS310 and ADAS304. In figure 4.36 we show the accuracy of both the linear interpolation and combination method. Above 2.0 keV amu^{-1} a difference of 2.33 % can be seen. This difference decreases as the beam energy increases. As mentioned earlier, we have undertaken a wide study and a similar accuracy obtained by the linear methods was observed.

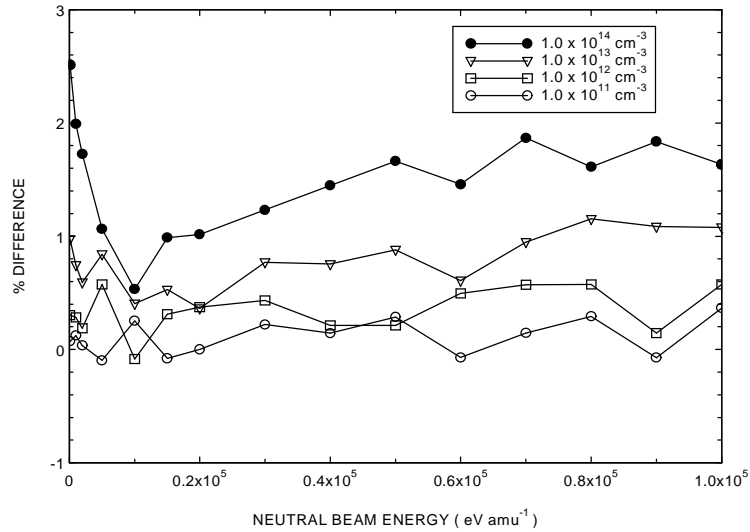


Figure 4.35 A plot of the percentage difference between the output of ADAS304 & ADAS310. The maximum difference seen above is 1.86 %, below 2×10^3 eV amu⁻¹ this difference rises to 2.514 %. The electron density was set to a value of 1×10^{12} cm⁻³ and the reference density was 6.78×10^{10} cm⁻³.

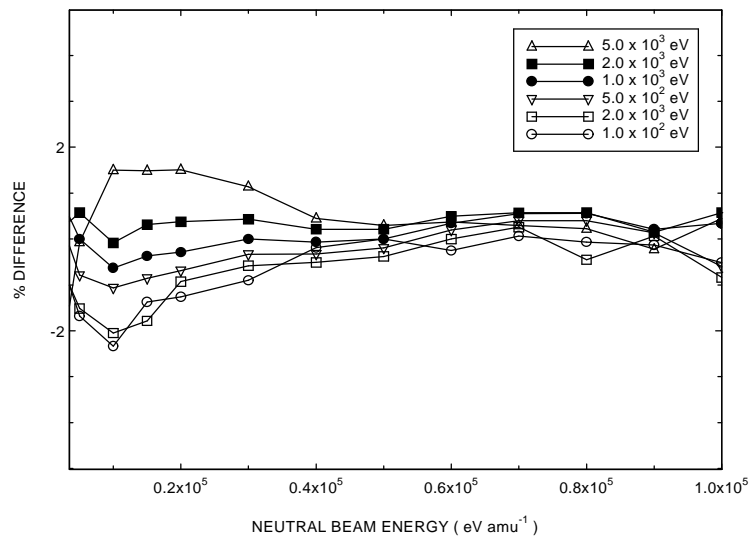


Figure 4.36 A plot of the percentage difference between ADAS304 & ADAS310. Using a reference temperature of 2×10^3 eV, the maximum difference that can be observed is 2.33 %, however below 2×10^3 eV amu⁻¹ the difference rises to 5.86 % and continues to reach a value of 23 % at 100 eV amu⁻¹. The electron density was set to a value of 1×10^{12} cm⁻³ and the reference density was 6.78×10^{10} cm⁻³.

4.4.5.2 Effective beam emission coefficients

We now turn our attention to the accuracy of the linear combination and interpolation method when used to assemble effective emission coefficients for a composite plasma. The approach adopted here is much the same as with the effective stopping coefficients. We first consider the accuracy of the linear combination method and then we study the combined accuracy of both linear methods. It is expected here that the accuracy of the linear methods will be less due to the increased temperature dependence associated with the effective emission coefficient.

We first consider a plasma consisting of 75% D^+ and 25% Be^{4+} . The results can be seen in figure 4.37 as a function of beam energy for a range of densities. The temperature has been selected to correspond to the reference temperature, therefore no interpolation along the temperature grid is required and the results in figure 4.37 simply reflect the accuracy of the linear combination method.

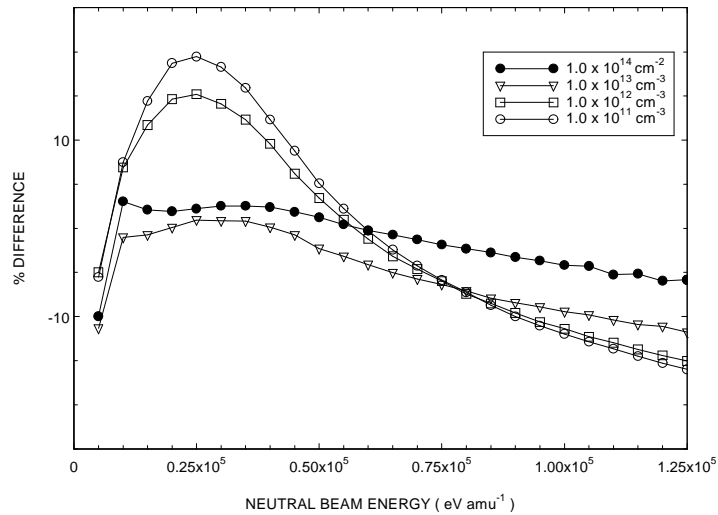


Figure 4.37 Percentage difference between the results from ADAS310 and ADAS304. The temperature was 2.0×10^3 eV and the reference values for the beam energy and electron density were respectively 4.0×10^4 eV amu⁻¹ and 6.78×10^{11} cm⁻³.

At a density and beam energy of 1.0×10^{12} cm⁻³ and 25 keV amu⁻¹ respectively, a maximum difference of 19.46 % can be observed. We now investigate the combine accuracy of the linear interpolation and combination. In figure 4.38 we show the difference between the results obtained from ADAS310 and ADAS304 as a function

of beam energy for a range of temperatures. In this case, interpolation using the one dimensional temperature grid is required.

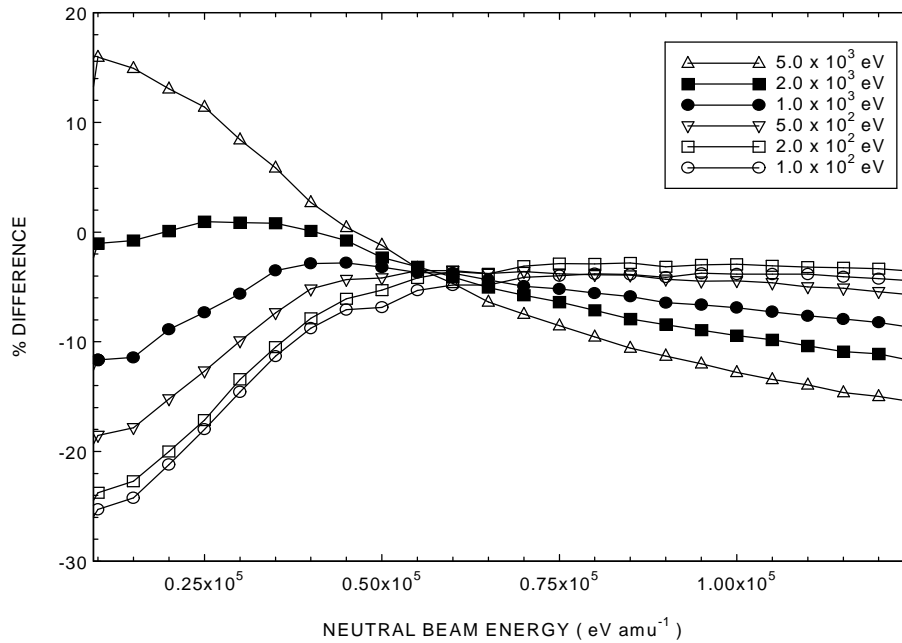


Figure 4.38 Percentage difference between the results obtained by ADAS310 and ADAS304. The reference values for the temperature, beam energy and density were respectively 2.0×10^3 eV, 40 keV amu^{-1} and $6.78 \times 10^{11} \text{ cm}^{-3}$.

As can be observed, a maximum difference of 25 % occurs at a temperature of 100 eV and a beam energy of 15 keV amu^{-1} . However, this difference decreases as the neutral beam energy increases.

We now extend our study by considering a slightly different plasma. The plasma which is of interest now consists of 70% D^+ , 20% C^{6+} and 10% Be^{4+} . In figure 4.39 we show the accuracy of the linear combination method where the temperature has been selected to avoid any interpolation along the temperature grid.

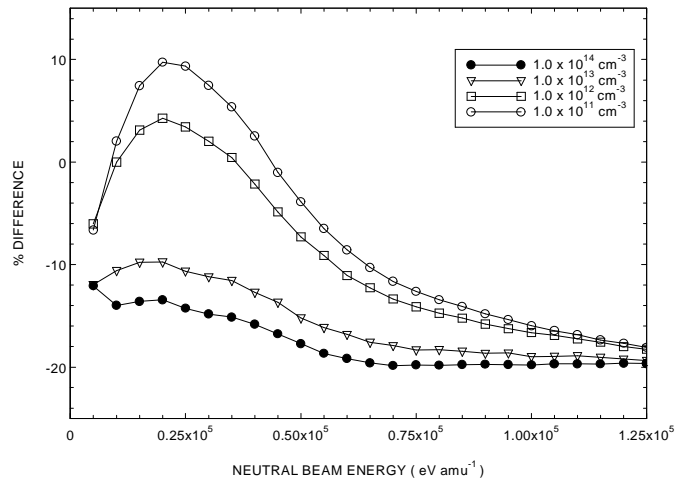


Figure 4.39 Percentage difference between the results obtained from ADAS310 and ADAS304. The composite plasma consist of 70% D^+ , 20% C^{6+} and 10% Be^{4+} . The reference values for the temperature, beam energy and density were respectively 2.0×10^3 eV, 40 keV amu^{-1} and $6.78 \times 10^{11} \text{ cm}^{-3}$.

A maximum difference of 19.86 % at $1.0 \times 10^{15} \text{ cm}^{-3}$ can be seen. We now show in figure 4.40 the results where the linear interpolation along the one dimensional temperature grid is required.

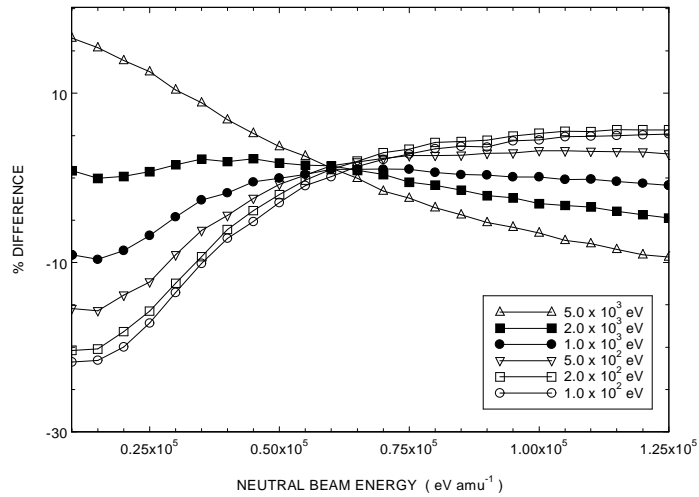


Figure 4.40 Percentage difference between the results obtained by ADAS310 and ADAS304. The reference values for the temperature, beam energy and density were respectively 2.0×10^3 eV, $6.67 \times 10^{11} \text{ cm}^{-3}$ and 40 keV amu^{-1} .

A difference of 21.75 % can be observed at a temperature of 100 eV and similar results can be observed for different composite plasmas.

4.4.6 Conclusion

The creation of compact look up tables enables effective stopping and emission data to be available for routine experimental analysis. The linear combination and interpolation method is successful at assembling effective stopping or emission coefficients for typical composite plasma with speed and reasonable accuracy.

In the case of the effective beam stopping coefficients, the linear combination and interpolation scheme proved to be capable of rapidly assembling composite coefficients which were within 5 % of the values obtained from ADAS310. This level of accuracy however was not retained when we considered the effective emission coefficients. On average, the linear combination and interpolation method could only assemble a composite emission coefficient which was within 20% of the value obtained from the calculation of ADAS310. However this level of accuracy is sufficient for the present application.

5.0 Beam emission spectroscopy at JET

5.1 Historical overview

Observations of the D- α emission feature emitted by excited beam neutrals was first recorded at JET Joint Undertaking[59] and then subsequently studied on other fusion devices[60,61]. Due to the unique nature of the Stark resolved spectrum, the diagnostic application of the D- α beam emission feature provided a means of measuring a novel set of important plasma parameters[62]. Information regarding the internal magnetic field structure [61,63,64,65,66] and ion density fluctuations of the plasma [67,68] were the first quantities studied using beam emission spectroscopy .

However progress in exploiting the beam emission signal to obtain information on the neutral beam density was slow. The neutral beam density is an important plasma parameter which beam emission spectroscopy was envisaged to yield. It is a key piece of information required to validate the impurity content of the plasma deduced via charge exchange spectroscopy[69] and modelled beam stopping.

Prior to the discovery of the diagnostic implications of the beam emission signal, the neutral beam density could only be obtained from an attenuation calculation for the rate at which the neutral beam atoms were being ionised as the beam traversed the plasma. As discussed by von Hellermann[70] the accuracy of this method is limited by error amplification, particularly in high density plasma scenarios such as the anticipated operating regime of ITER[71]. Therefore the possibility of utilising the beam emission signal to provide a local accurate measurement of the neutral beam density was encouraging.

The first detailed attempt to exploit the beam emission signal following the initial work of Boileau[62] at JET was by Mandl[20,72]. Mandl explored the feasibility of utilising the beam emission spectrum to deduce the neutral beam density as well as other parameters such as the magnetic field strength, the divergence and energy composition of the beam as well as the location of the observation volume. His work focused on the beam emission signal originating from single beam bank pulses where the observed spectra, even though complicated, were in their simplest form. He suggested that it was possible to deduce the neutral beam density reliably for single bank pulses and that beam emission spectroscopy certainly had the potential to replace the numerical attenuation calculation. However single bank pulses only

constitute a minority of pulses at JET, high power double beam bank pulses are more common. Also Mandl's analysis, though fruitful, was in fact limited to just one pulse. The aim of the present work was to extend the analysis to include double beam bank scenarios.

Since the work of Mandl in 1991, the beam emission diagnostic had been relocated to a different observation port. The status of the diagnostic after the appropriate modifications were implemented was such that the neutral beam density inferred from the beam emission spectra differed from the values obtained from the numerical attenuation calculation, in many cases by up to a factor of two. This was such a contrast to the original results reported by Mandl that there was an obvious need to revisit each stage of the analysis to investigate the nature of the discrepancy.

In this work we address this issue while focusing our attention on the analysis of the beam emission spectra originating from single and double beam bank pulses.

5.2 The JET beam emission spectroscopy diagnostic

5.2.1 Diagnostic apparatus

The beam emission spectrum at JET is recorded using a back illuminated CCD camera. A fan of twelve fibre optics are focused along the trajectory associated with injectors 6 and 7 of octant eight from the diagnostic port illustrated in figure 5.1. Injectors 6 and 7 are members of the normal and tangential bank respectively and conveniently share a similar trajectory as can also be seen in figure 5.1. Each of the twelve fibre optics are employed to relay the D- α emission feature back to a Czerny-Turner type spectrometer (KS5b). On leaving the exit slit of the spectrometer the emission feature is then focused onto the CCD camera. The signals recorded by the camera are then collected and stored awaiting analysis. A schematic overview of the diagnostic system is shown in figure 5.2 and a detailed description can be found in [66] and references therein.

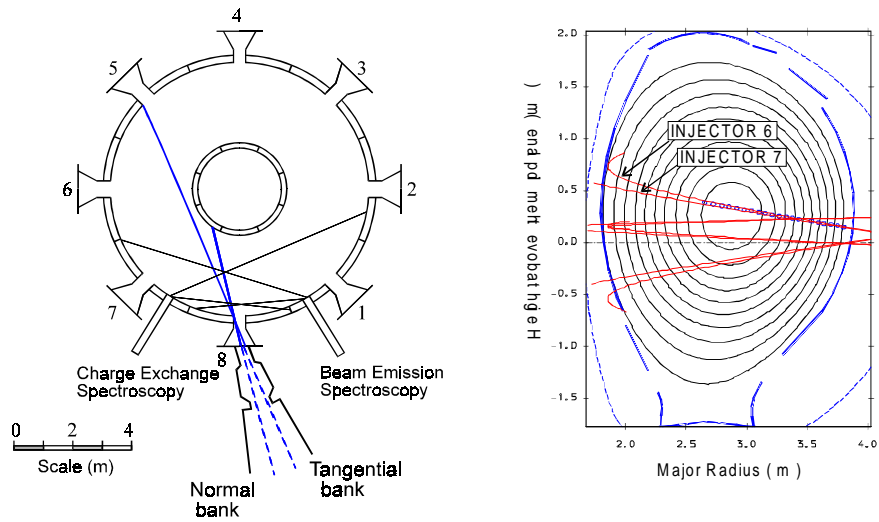


Figure 5.1 Plan view and side elevation of the tokamak. The figure on the left illustrates the location of the observation ports for charge exchange and beam emission spectroscopy. The figure on the right shows the typical trajectories of each neutral injector, particular attention should be drawn to the diagnostic injectors 6 and 7 which are annotated.

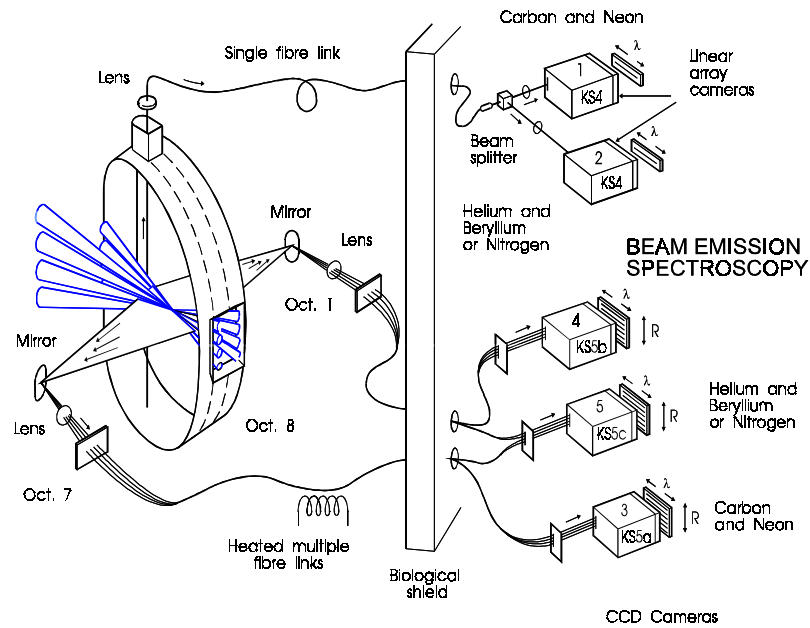


Figure 5.2 Schematic overview of the diagnostic system employed to measure both the neutral beam density and the impurity content of the plasma. Situated on octant one, a fan of twelve fibre optics focused along the trajectory of the neutral beams are used to relay the D- α emission feature back to a Czerny-Turner type spectrometer (KS5b). On leaving the exit slit of the spectrometer the emission feature is recorded via a back illuminated CCD camera.

5.2.2 Observed beam emission spectrum

The primary beam emission observation is of a series of overlapped Doppler shifted Stark multiplet features. The appearance of the 6560 - 6620 Å spectral interval for a single bank pulse is shown in figure 5.3,

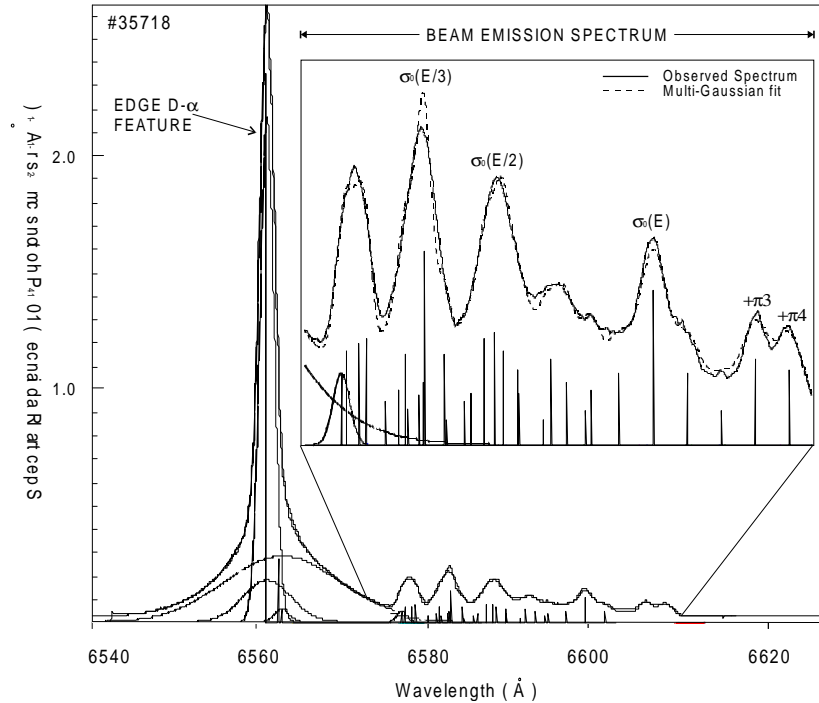


Figure 5.3 Observed motional Stark D- α feature. The emission feature was recorded during the JET pulse 35718 using track 4 of the multichord system. The tangential bank was active with a primary energy of 140 KeV/amu. The constrained multi-gaussian fit is also shown. Particular attention should be brought to the annotation of the full, half and third σ_0 Stark components. Due to the existence of the three fractional energy components in the beam this gives rise to three Stark multiplets. Each Stark multiplet is Doppler shifted according to the velocity of the relevant beam neutrals and as a result the overall picture is an overlap of each Stark feature.

where only one diagnostic neutral injector ('pini') is active. The existence of three fractional energy components in each diagnostic injector gives rise to three Stark multiplet features. Each Stark multiplet is Doppler shifted according to the velocity of the relevant energy component and the viewing angle between the neutral injector and the line of sight. The fractional energy components in each injector are due to the production of D^+ , D^+_2 and D^+_3 during ion generation[73]. As the ions are neutralised their different atomic masses contribute to producing three energy components, i.e. a full energy E_0 , half energy $E_{0/2}$ and a third energy $E_{0/3}$ component.

The salient features of the spectrum as we move in the direction of increasing wavelength commences with the large D- α edge emission line situated at 6560 Å. The origin of this is the presence of partially ionised species between the last closed magnetic flux surface and the vessel wall. Next we encounter a cluster of Stark multiplet features which are collectively known as the beam emission spectrum. Each Stark multiplet feature consists of nine observable Stark components (up to $\pm\pi 4$). The higher order components of the Stark resolved spectrum are too weak in intensity to observe reliably.

The beam emission spectrum is highly determined. The local magnetic field orthogonal to the neutral beam particle path together with precisely known velocities of the energy fractions determines the wavelength separation of the Stark components. The relative intensities of the σ and π polarisation components are also determined since Stark fine structure populations are fully mixed at the JET core plasma densities ($> 2 \times 10^{13} \text{ cm}^{-3}$) and the geometry is specified.

In the case of double beam bank pulses, which are more common, the recorded beam emission spectrum originates from the excited beam neutrals of two diagnostic injectors so that the spectrum comprises of six overlapping Stark multiplet features. In figure 5.4, the beam emission spectrum during the single bank period of the pulse 32969 showing the three Stark multiplets increases in complexity suddenly during the double beam bank period of the pulse.

In both the single and double bank spectra, additional spectral lines in the vicinity of the beam emission spectrum can also be observed, particularly near the base of the D- α edge emission line, see figure 5.3. Our concern here however is with the Stark multiplet features of the beam emission spectrum (see [20] for a detailed description of the full spectrum) .

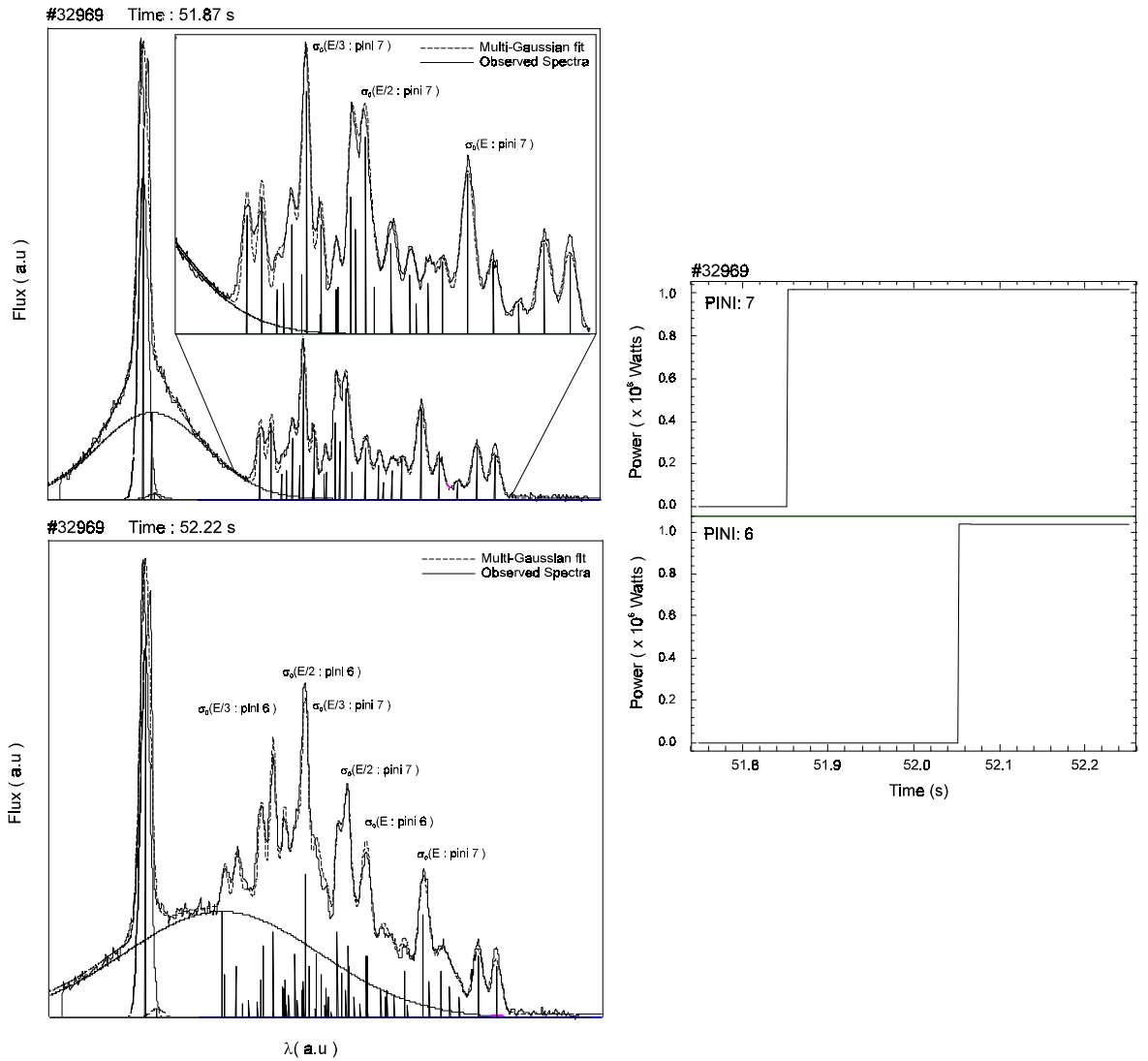


Figure 5.4 Complexity of the beam emission signature. Top left hand figure shows the beam emission feature during a single bank period of the pulse 32969. The figure at the bottom left illustrates the increasing complexity of the observed spectrum during the double beam bank period. The single figure to the right shows the power associated with each diagnostic injector and the time interval when the single or double bank scenario is in operation.

5.2.3 Experimental analysis

5.2.3.1 Method and objectives

The analysis of the beam emission feature involves generating a synthetic model spectrum based on measured and calculated parameters. The synthetic spectrum is then employed to extract the total flux associated with each Stark multiplet contained within the spectrum. The total flux together with knowledge of the electron density

and the effective beam emission coefficient enables the neutral beam density to be recovered from the beam emission spectrum. At JET a computer program written in FORTRAN 77 is employed to automate the spectral analysis. The program was originally written by Mandl[20] and extended by English[74] and Howman[75] to include the analysis of the spectral originating from the excited neutrals of two active injectors. The procedure consists of two stages as illustrated in figure 5.5.

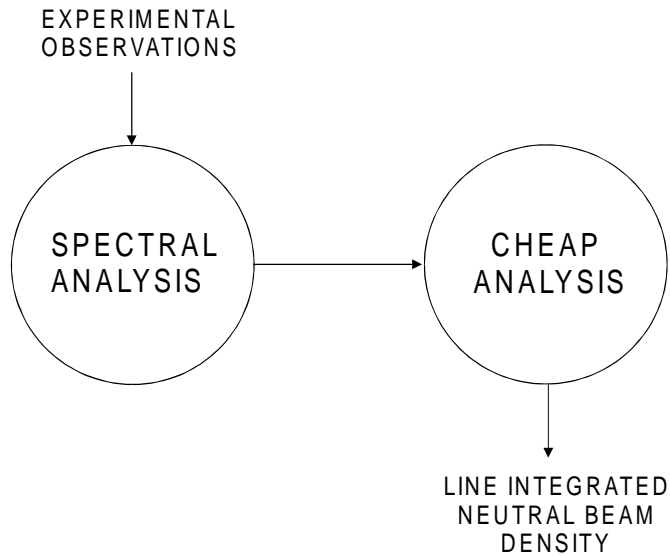


Figure 5.5 Overview of the two stage procedure involved in obtaining the line integrated neutral beam density. The first stage involves running the spectral analysis code to obtain the total flux from each Stark multiplet. The second stage of the analysis involves evaluating the neutral beam density using the flux measurements together with derived atomic data.

The first stage uses the spectral analysis program to extract the total flux associated with each Stark multiplet. The second stage is a post processing step. The post processing code, which is known as the Charge Exchange Analysis Package (CHEAP), evaluates the neutral beam density using the flux measurements. The CHEAP code was written in FORTRAN 77 by von Hellermann[59] and serves as the main analysis tool for the core spectroscopy group at JET (see section 5.3).

5.2.3.2 Motional Stark Effect

The motional Stark effect is the descriptive name for the Stark effect when atoms move through a magnetic field and experience a Lorentz electric field within their own frame of reference. The Lorentz electric field acts as a perturbation on the atom's

Hamiltonian and influences the wavelength and intensities of the emission. Neutral deuterium beam atoms, which cross the confining magnetic field of the JET tokamak with a typical velocity of around 10^6 m s^{-1} , experience an electric field of up to 10^6 Vm^{-1} . In this regime the linear Stark effect is dominant and the influence of the electric field removes the degeneracy associated with each hydrogenic energy level. This gives rise to a Stark resolved energy level structure where the splitting of the energy levels is directly proportional to the electric field. As discussed by Sobelman[76] the splitting of the energy levels are given by,

$$\Delta E = \frac{3}{2}n(n_1 - n_2)eE_L a_0 \quad 5.1$$

where n_1 and n_2 are the so-called parabolic quantum numbers and E_L is magnitude of the Lorentz electric field. In figure 5.6 we show a schematic for the transition from a degenerate energy level structure to a Stark resolved picture for neutral hydrogen. Also shown are the expected emission patterns.

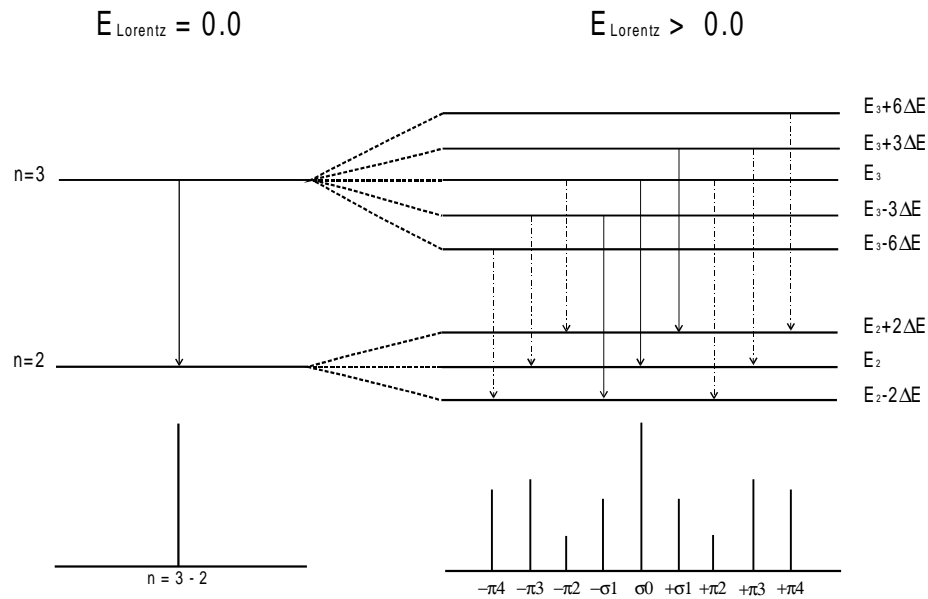


Figure 5.6 Influence of an external electric field on the degenerate energy levels of hydrogen. The electric field acts as a perturbation and removes the degeneracy associated with each energy level and gives rise to a Stark resolved energy level structure. The schematic illustrates the transition from a degenerate energy level structure to a Stark resolved picture showing the subsequent emission patterns.

5.2.3.3 Spectral analysis

The analysis of the beam emission spectrum involves identifying the position and amplitude of every feature contained within the spectrum region. Each feature is then represented by a Gaussian specified by width and amplitude. The array of Gaussians which collectively represent all of the individual spectral features is then used to construct a synthetic spectrum which is adjusted to extract the flux associated with each Stark multiplet.

The analysis program first accesses the JET pulse process file database system[77] to ascertain the atomic mass and velocity of the beam species. The program then searches the spectrum for the D- α edge emission line. Since this emission originates from the edge of the vessel it is free of any Doppler shift from the bulk motion of the plasma. It is utilised as a wavelength reference.

The spectral analysis code then attempts to locate the position of the Doppler shifted primary σ_0 Stark components associated with each Stark multiplet. The position of each primary Stark component is determined by the velocity, v_b , of the relevant energy fraction and the viewing angle, α , between the neutral injectors and the line of sight. Mandl[20] expresses the Doppler shifted wavelength as,

$$\Delta\lambda_{DOPPLER} = \lambda_0 \frac{v_b}{c} \cos(\alpha) \quad 5.2$$

where λ_0 is the natural wavelength.

The location of the remaining Stark components for each multiplet are identified by assuming the Stark splitting is constant over the spectral region. The Stark splitting is then evaluated using the following expression,

$$\Delta\lambda_{STARK} = \frac{3}{2} \frac{ea_0}{hc} \lambda^2 E_L \quad 5.3$$

where λ is the unperturbed wavelength. The analysis program obtains estimates for the electric field using the results from magnetic equilibrium calculations[78] together with knowledge of the beam velocity and experimental geometry. The position of the components are then specified relative to the appropriate Doppler shifted primary Stark feature, as illustrated in figure 5.7 for a single multiplet.

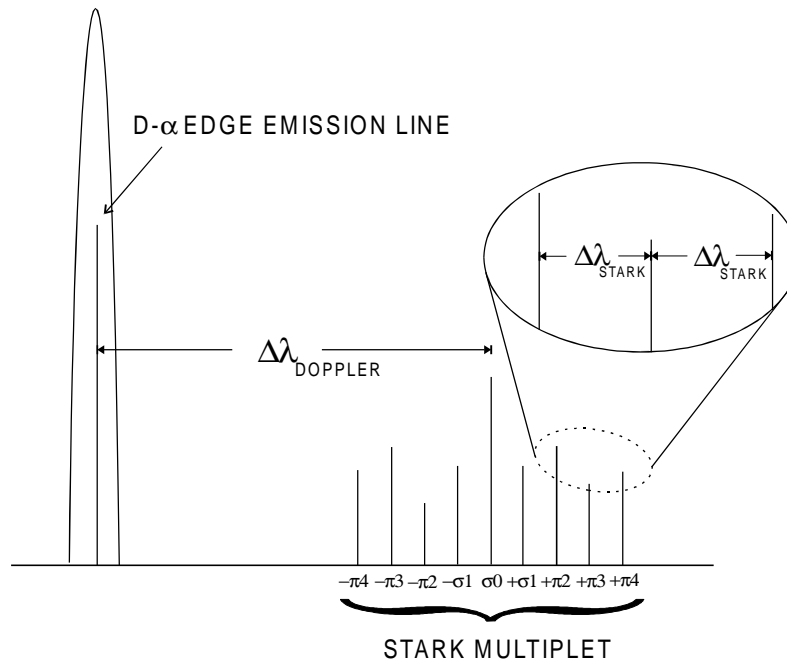


Figure 5.7 Schematic illustration of how the primary Stark component for a single multiplet feature is fixed relative to the D- α edge emission line and the remaining Stark components are then specified relative to the primary Stark component by the wavelength separation due to the linear Stark effect.

The next step for the analysis program is to obtain amplitudes for the Gaussians used to represent each spectral feature. The amplitudes of the Gaussians for the primary σ_0 Stark components in both single and double bank spectra are treated as the search parameters of the fit, whilst the amplitudes of the Gaussians for the remaining Stark features are specified by a parametric relationship to the σ_0 components. This relationship is based on intensity ratios of individual Stark components which are entered by the user as input[74].

The resulting parameterised array of Gaussians is optimised by the NAG routine E04UPF to obtain a best fit synthetic spectrum to the experimentally observed spectrum. The degree of accuracy of the fit is monitored and after each spectrum is analysed a diagnostic report is automatically written to a file which includes the NAG error flag for the success of the fitting procedure[79]. It should be noted that the analysis program also addresses the spectral lines which can be observed near the base of the D- α edge emission feature.

5.3 The Charge Exchange Analysis Package

5.3.1 The role of the charge exchange analysis package

The charge exchange analysis package (CHEAP) is a computational tool employed at JET to automate the process of combining spectroscopic observations, derived atomic data and experimental conditions to infer self consistently various plasma parameters. The main application of CHEAP is the deduction of absolute impurity concentrations via charge exchange emission measurements, which are recorded using the apparatus shown in figure 5.2. A schematic overview of CHEAP illustrating the flow of derived atomic data and experimental observations is shown in figure 5.8

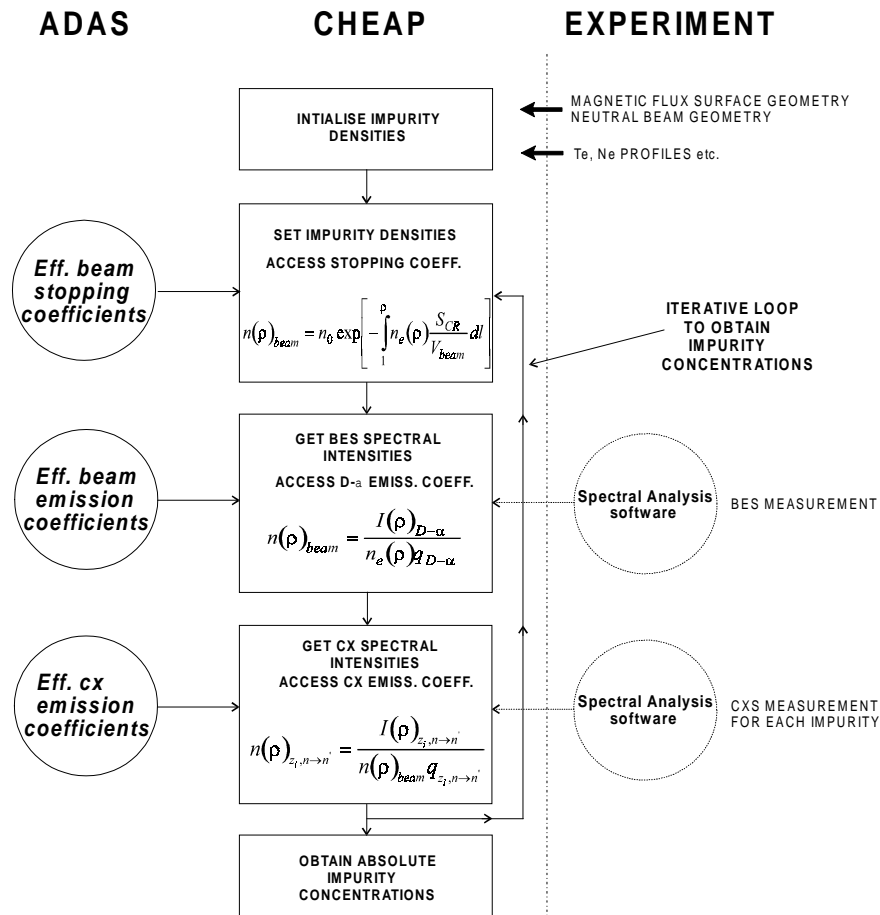


Figure 5.8 Schematic overview of the Charge Exchange Analysis Package, CHEAP. The deduction of the impurity content of the plasma within CHEAP involves utilising charge exchange emission flux measurements together with derived atomic data. The assembly of the neutral beam density using the

flux measurements from the beam emission signal as well as the attenuation calculation is carried out within CHEAP.

5.3.2 Iterative path to absolute impurity concentrations

The charge exchange spectroscopy diagnostic at JET utilises the subsequent emission by impurity ions following the capture of an electron to obtain information on the impurity content of the plasma. The impurity concentration of a species of nuclear charge z_0 , as discussed in chapter 1.0, is given as

$$n_{z_0} = \frac{4\pi \int \Phi_{CX}(\lambda) d\lambda}{q_{CX} \int n_b ds} \quad 5.4$$

where Φ_{CX} is the recorded charge exchange flux, q_{CX} is the effective charge exchange emission coefficient[19] and $\int n_b ds$ is the line integrated neutral beam density.

Evaluation of the line integrated neutral beam density from either the attenuation calculation or the beam emission spectrum requires prior knowledge of the impurity densities in the plasma to enable the relevant effective coefficients to be evaluated. This requires an iterative approach for the concentration of the different impurities in the plasma to be inferred via charge exchange spectroscopy. The CHEAP package implements such an iterative calculation making use of bremsstrahlung and charge exchange flux measurements together with derived atomic data, see figure 5.8. To reconstruct the radial density profiles for each impurity CHEAP begins by estimating the impurity content of the plasma. This estimate is obtained from the bremsstrahlung observations along the vertical line of sight shown in figure 5.2. The measurement enables the line integrated effective ion charge of the plasma to be inferred using the following equation[80],

$$\langle Z_{eff} \rangle = \frac{1}{B} \left[\frac{\pi k}{2m} \right]^{\frac{1}{2}} \phi_{brems} / \int \frac{n_e^2}{\sqrt{T}} \frac{g^{III}}{\lambda} \exp\left[\frac{E_v}{kT}\right] dl \quad 5.5$$

where g^{III} is the free-free Gaunt factor and ϕ_{brems} is the intensity of the emission. It is then assumed that the contribution to the bremsstrahlung emission is due to the

presence of only one impurity in the plasma. This is the dominant impurity (normally known) such as carbon. The value obtained for $\langle Z_{\text{eff}} \rangle$, is then used as a first approximation in the following expression for the local ion charge, Z_{eff} .

$$Z_{\text{eff}} = 1 + \sum_i Z_i(Z_i - 1) \frac{n_i}{n_e} \quad 5.6$$

This enables the carbon concentration to be estimated. Measurements of the bremsstrahlung emission are repeated. This time the contribution to the emission is assumed to be due to the presence of carbon and an additional impurity. The impurity density for each species is thus calculated using the first estimate for the carbon concentration as a starting point. This procedure is continued until all the main impurities have been included and a stable solution for the vertical line of sight has been obtained.

The reconstruction of the radial density profiles can now be considered. The present implementation of CHEAP employs the theoretical attenuation calculation to evaluate the neutral beam density during the analysis. Using the values for the impurity content of the plasma obtained from the vertical line of sight as an initial guess, the effective stopping coefficients are evaluated to obtain the neutral beam density. Together with knowledge of the neutral beam density and the charge exchange flux measurements a new set of values for the impurity content of the plasma can be calculated. These are then used to evaluate new stopping coefficients and the process continues until a converged solution for the impurity concentrations has been achieved.

5.3.3 Evaluation of the neutral beam density

An efficient method to calculate the neutral beam density is required for the impurity concentrations to be deduced within a reasonable time scale. This is done by acquiring the theoretical data through the linear interpolation and combination method with look up tables as discussed in chapter 4.0.

5.3.3.1 Numerical attenuation calculation

Utilising the rapid look up tables of type adf21, the CHEAP code assembles effective stopping coefficients for a composite plasma as a function of temperature, density and neutral beam energy (T_e , n_e and E_b). In the case of a single injector the neutral beam density as a function of radial position, ρ , can then be obtained using the following relation,

$$n(\rho)_b = n_0 \exp\left(-\int_1^{\rho} n_e \frac{S_{CR}(n_i, E_b, T_e)}{v_b} dl\right) \quad 5.7$$

where dl is along the path taken by the neutral beam, S_{CR} is the effective stopping coefficient in terms of the ion density, and n_0 is the initial beam density on entry to the plasma.

For charge exchange spectroscopy, we require the line integrated neutral beam density i.e. $\int n_b ds$, where ds is along the line of sight across the neutral beam profile. Test bed measurements[81] show that the neutral beam density distribution at JET can be described by a Gaussian which has a full width half maxima (FWHM) in the x and y plane of w_x and w_y respectively, see figure 5.9.

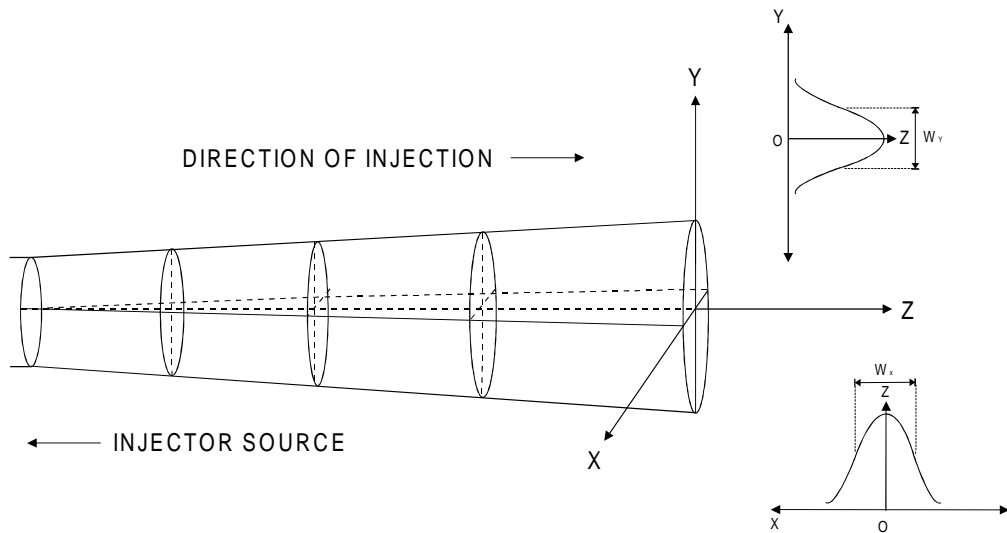


Figure 5.9 An illustration of a single beam showing the natural beam divergence . Also shown is the Gaussian distribution in both the x and y plane which is used to describe the neutral beam density distribution of the beam.

Therefore the line integrated neutral beam density evaluated by CHEAP is,

$$\langle n(\rho)_b \rangle = \int n(\rho)_b ds = n_0 \int_{-\infty}^{+\infty} \exp\left(-\frac{x^2}{w_x^2} - \frac{y^2}{w_y^2}\right) \exp\left(-\int_1^{\rho} n_e \frac{S_{CR}(n_i, E_b, T_e)}{v_b} dl\right) ds \quad 5.8$$

The FWHM of the Gaussian in the x and y plane at any radial position is obtained by assuming that the beam source is a point[81]. The values for the beam divergence can then be used to obtain the widths, w_x and w_y . The electron density is obtained from Thomson scattering measurements from the LIDAR diagnostic[82]. The initial beam density, n_0 , is obtained from calorimetry measurements of the beam current in the neutral injector[83].

5.3.3.2 Spectroscopic measurement

The CHEAP code employs the look up tables of type adf22 to assemble effective beam emission coefficients for a composite plasma. The relationship between the beam emission flux and the line integrated neutral beam density as evaluated by CHEAP for a single injector is,

$$\langle n(\rho)_b \rangle = \frac{\chi}{n_e(\rho)} \sum_{k=1}^{k=3} \frac{I(E_{0k})}{q(n_e, T_e, E_{0k})_{D-\alpha}} \quad 5.9$$

where $I(E_{0k})$ is the flux associated with the Stark multiplet corresponding to the fractional energy component k , $q(n_e, T_e, E_{0k})$ is the effective D- α beam emission coefficient and χ is the window transmission factor. The latter is used to compensate for the observation window being optically degraded by the deposition of impurities. It is evaluated by comparing the $\langle Z_{\text{eff}} \rangle$ inferred from the bremsstrahlung measurements recorded from the charge exchange diagnostic port and the vertical line of sight as shown in figure 5.2. The observation port for the vertical line of sight is a considerable distance away from the plasma and the window is assumed to be free of any optical degradation. A detail discussion of the cross calibration technique is given by Morsi et. al.[9].

5.4 Examination of the analysis procedure

5.4.1 Overview

To address the nature of the discrepancy between the neutral beam density inferred from the numerical attenuation calculation and the beam emission signature, a systematic approach was adopted which involved investigating each stage of the analysis. There were three areas of uncertainty, namely the spectral analysis, the CHEAP analysis and the derived atomic data. Our strategy involved investigating each area in turn in an attempt to identify the source of the discrepancy.

5.4.2 The spectral analysis

Due to the large quantity of spectral data to be analysed on a daily basis at JET, the spectral analysis program operates in a batch mode. In this mode the program automatically analyses every spectrum recorded over the duration of a particular pulse selected by the user.

To operate the analysis code in this manner involved configuring the input parameters to ensure that the synthetic spectra generated by the code would give an accurate fit to all of the recorded spectra. In practise this was achieved by considering a few spectra from different time frames and lines of sight. It was then assumed that the optimum input parameters obtained would then be valid for the analysis of all the other spectra.

We found that some of the spectra were not being fitted to the required accuracy. The acceptance criteria of the goodness of fit from the NAG algorithm was too loose. The failure rate was sensitive to poor input parameter choice such as ignoring the variability between different lines of sight. Also the temporal variation of the CII passive emission lines which pollute the beam emission signal, see figure 1.5, were not taken into account. During observations the intensity of these lines would unpredictably become stronger or weaker and directly influence the success of the fitting procedure. The obvious solution would be to check each spectrum individually but this would be impractical due to the large volume of data. An alternative approach was sought.

In all of the spectra associated with single bank pulses, it was observed that the $+\pi/3$ and $+\pi/4$ Stark components of the full energy fraction were separated from the

dense cluster of Stark lines, see figure 5.3 . As suggested by Howman[75], the fit could be biased in favour of these two components (while neglecting the remaining features) and together with knowledge of the intensity ratios of the remaining Stark components, the total flux associated with the full energy fraction could be reconstructed. The total flux for the Stark multiplet feature due to the full energy fraction of a single injector, assuming that the feature is symmetrical around the primary σ_0 component, is given as,

$$\Phi_{Total} = 2[\phi_{\pi 3} + \phi_{\pi 4}] + 2[\phi_{\pi 2} + \phi_{\sigma 1}] + \phi_{\sigma_0} \quad 5.10$$

This expression can be reduced to a simple relation involving the measurement of the flux associated with only the $+\pi 3$ and $+\pi 4$ Stark components,

$$\Phi_{Total} = \kappa[\phi_{\pi 3} + \phi_{\pi 4}] \quad 5.11$$

where κ is a constant obtained from the intensity ratios of the remaining Stark lines.

The contribution to the neutral beam density due to the full energy fraction could be recovered from the spectrum while reducing the number of spectral features which are taken into account. To obtain the contribution to the neutral beam density from the remaining fractional energy components, Howman[75] suggested that one could use the following relation.

$$N_{E_0/k}^{Measured}(\rho) = \frac{N_{E_0/k}^{Theory}(\rho)}{N_{E_0}^{Theory}(\rho)} N_{E_0}^{Measured}(\rho) \quad 5.12$$

where $N_{E_0/k}^{Theory}$ is the contribution to the total beam density due to the fractional energy component k , which is obtained from the attenuation calculation. $N_{E_0}^{Measured}$ is the contribution to the total neutral beam density due to the full energy fraction which is obtained from the $+\pi 3$ and $+\pi 4$ Stark components.

This method could also be extended to include the analysis spectra associated with double beam bank pulses. In which case the line ratios of the Stark components are assumed to be identical for each bank and the reconstruction of the flux associated with each full energy component is carried out in the same manner.

As part of a feasibility study we implemented this method in an attempt to improve the reliability of the spectral fitting . To obtain a value for κ we conducted a

statistical survey of the experimental data from which we obtained the line ratios shown in table 5.1, also shown in the table are the theoretical values predicted by Mandl[20].

<i>Ratio</i>	<i>Experimental</i>	<i>Theoretical</i>
σ_1/σ_0	0.430	0.353
π_3/σ_0	0.550	0.421
π_2/σ_0	0.195	0.133
π_4/σ_0	0.450	0.307

Table 5.1 Experimental and theoretical line intensity ratios of the Stark components. The experimental values were obtained from a statistical analysis of the observed spectra. The theoretical values were obtained from the work of Mandl[20].

Using the values contained in table 5.1, this gave κ a value of 3.625. We conducted a detailed study of the analysis using the $+\pi_3$ and $+\pi_4$ components to conclude that it was more reliable than the existing method. The existing method which involved extracting the flux associated with each individual Stark component is more applicable when the analysis of the spectra is done on an interactive basis rather than in a batch mode. We decided to continue the $+\pi_3$ and $+\pi_4$ method on a permanent basis. Nonetheless by adopting this new approach we have lost important diagnostic information concerning the half and third energy components. We had originally planned to use the fractional Stark components to verify the energy dependence of the effective emission coefficients and hence the fundamental cross section data. This opportunity is no longer available.

5.4.3 The CHEAP analysis

The CHEAP package utilises a vast amount of derived atomic data and anxieties regarding the correct use of the atomic data was of immediate concern. A careful study of CHEAP revealed an error in the implementation of the linear combination

method. This was corrected. This error did not have any significant impact on the discrepancy between the measured and calculated beam density.

5.4.4 Review of the fundamental and derived atomic data.

In this section we summarise the results obtained by reviewing the fundamental atomic data which is used as input to calculate the effective stopping and emission coefficients. Due to the energy regime of the JET heating beams, the ion-atom collisions govern the population structure and hence the attenuation. Therefore we restricted ourselves to the fundamental atomic data concerning ion-atom collisions.

The atomic database containing ion-atom collision cross sections, which is of the ADAS data format of adf02, was constructed in 1989 and periodically updated until 1993. Using the best available data we updated this data base, a detailed account can be found in appendix A. As an example we contrast the new 1997 cross-section data for ion impact ionisation from the $n=3$ shell of the beam neutrals with the 1989 data, see figure 5.10. At the operating densities of the JET tokamak, the role of ionisation from the excited states of the beam atoms is significant. A point to note is that the new 1997 database contains more accurate cross-sections for atomic processes associated with excited states which were not available when the 1989 database was compiled.

Using the new ion-atom collision database we then calculated new effective stopping and emission data for all of the fully stripped impurities up to the first period. In Figure 5.11 and 5.12 we illustrate the influence of the revised ion-atom collision data on both the effective Balmer-alpha emission coefficient and the line integrated neutral beam density deduced from the beam emission spectrum.

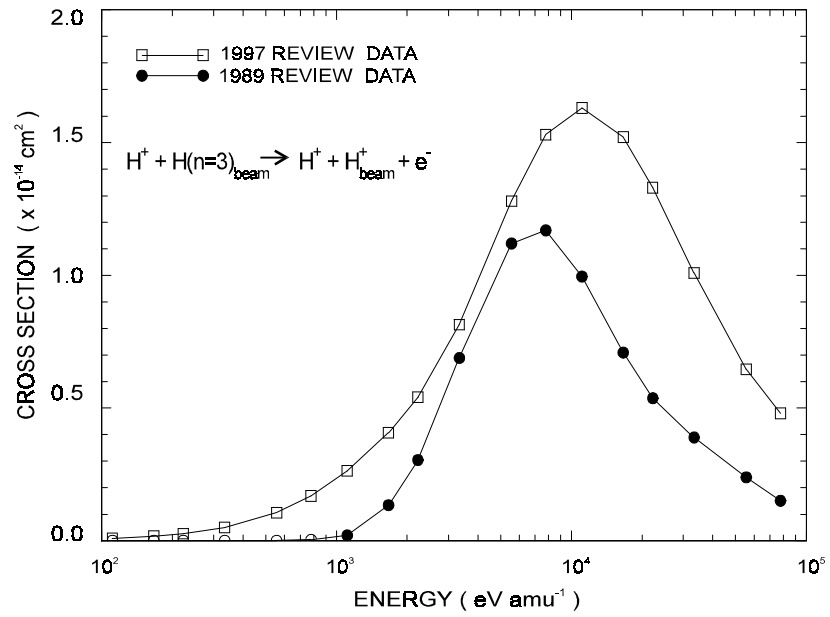


Figure 5.10 Ion impact ionisation cross section Vs energy. The 1997 data is based on the data compiled by Janev & Smith [Janev R K, Smith J J, J. Nucl. Fusion (Supplement), Vol.4,1993].

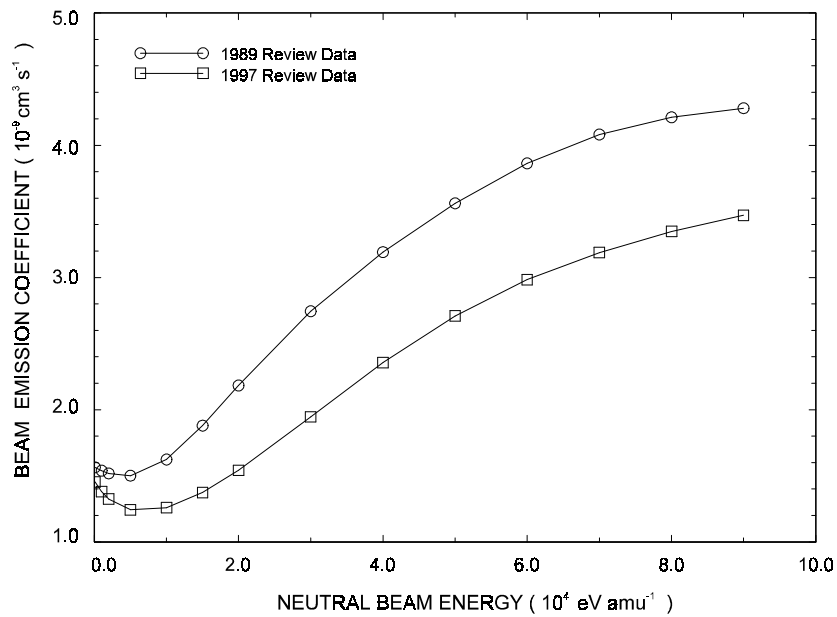


Figure 5.11 The Balmer-alpha effective emission coefficient for a pure D^+ plasma calculated using the 1989 and 1997 ion-atom collision database. The electron temperature is 1×10^3 eV and the electron density is $1 \times 10^{13} \text{ cm}^{-3}$.

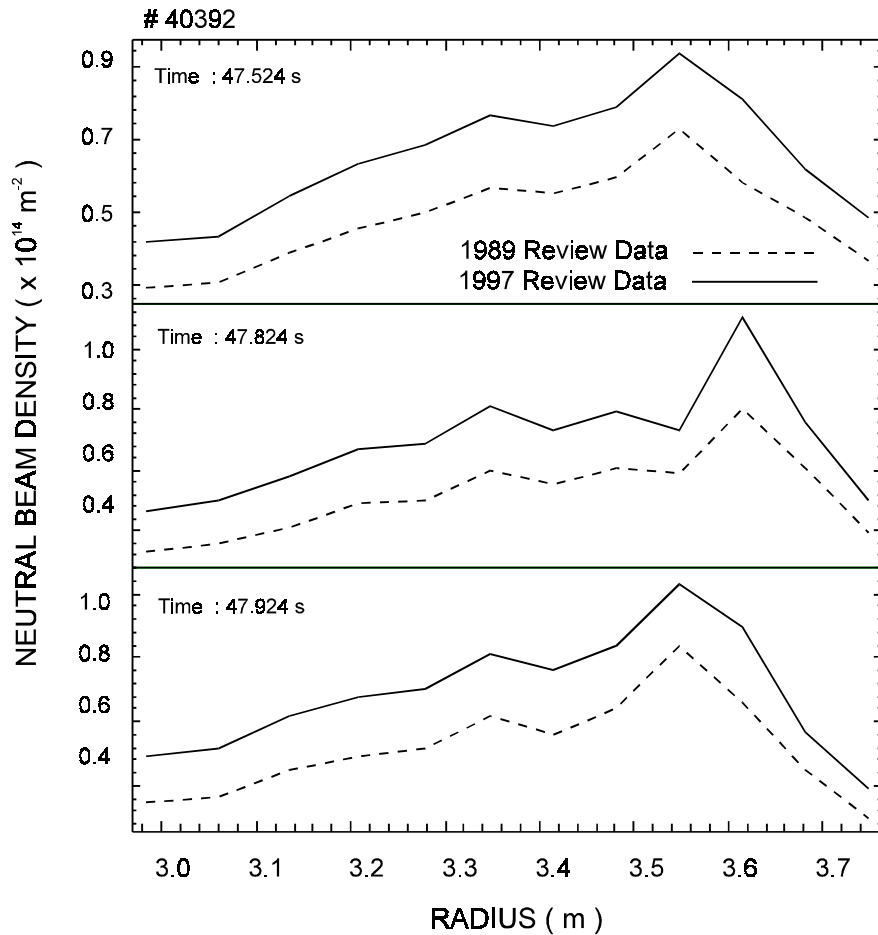


Figure 5.12 Line integrated neutral beam density for three different time periods obtained from the beam emission signal. The plot shows the direct influence of the fundamental data on the effective emission coefficient and hence the line integrated neutral beam density.

As can be observed from figure 5.11, the influence of the fundamental data on the effective Balmer-alpha coefficient is substantial. Using the new effective emission coefficients an average change of approximately 30 % in the neutral beam density inferred from the beam emission spectrum can be seen in figure 5.12.

We now illustrate the influence of the revised ion-atom collision data on the effective stopping coefficient and the line integrated neutral beam density obtained from the attenuation calculation, see figures 5.13 and 5.14 respectively.

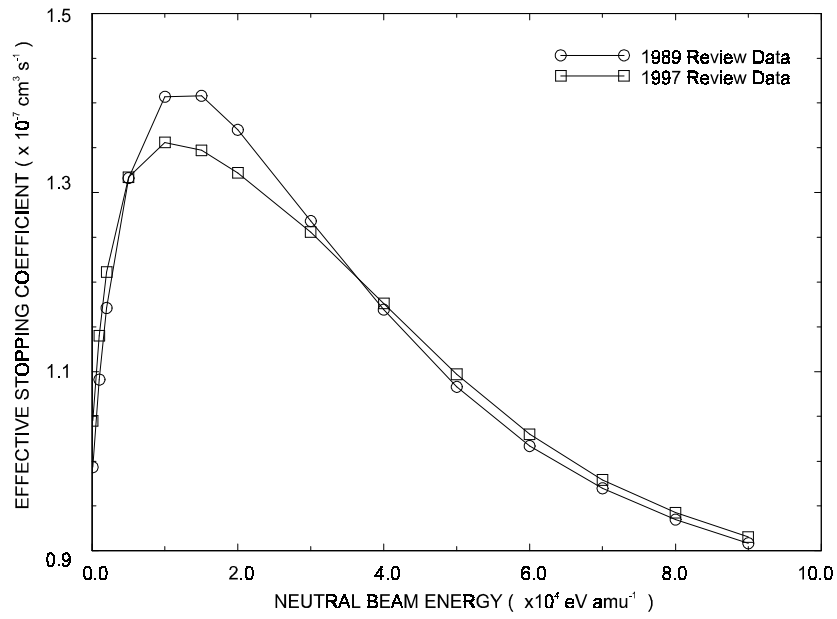


Figure 5.13 Comparison between the effective stopping coefficients calculated using the 1989 and 1997 ion-atom collision database. The plasma density was $1.0 \times 10^{13} \text{ cm}^{-3}$ and the temperature was $1.0 \times 10^3 \text{ eV}$. As can be observed the change with the revised 1997 data is small.

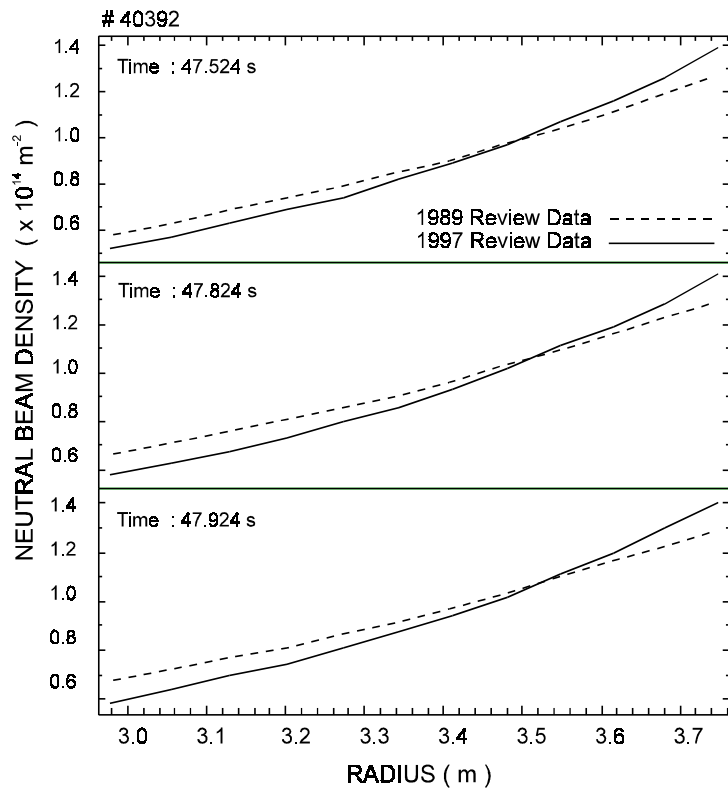


Figure 5.14 The line integrated neutral beam density for three different time periods evaluated using the attenuation calculation with the 1989 and 1997 data.

As can be seen in figure 5.13, the influence of the revised atomic data on the effective stopping coefficient and hence the line integrated neutral beam density obtained from the attenuation calculation is small, see figure 5.14. The new 1997 ion-atom collision database includes more accurate cross sections describing the atomic processes associated with the excited states. The changes in such cross sections contributes very little to the effective stopping coefficients since less than 1% of the beam neutrals are in their excited state, see figure 5.15.

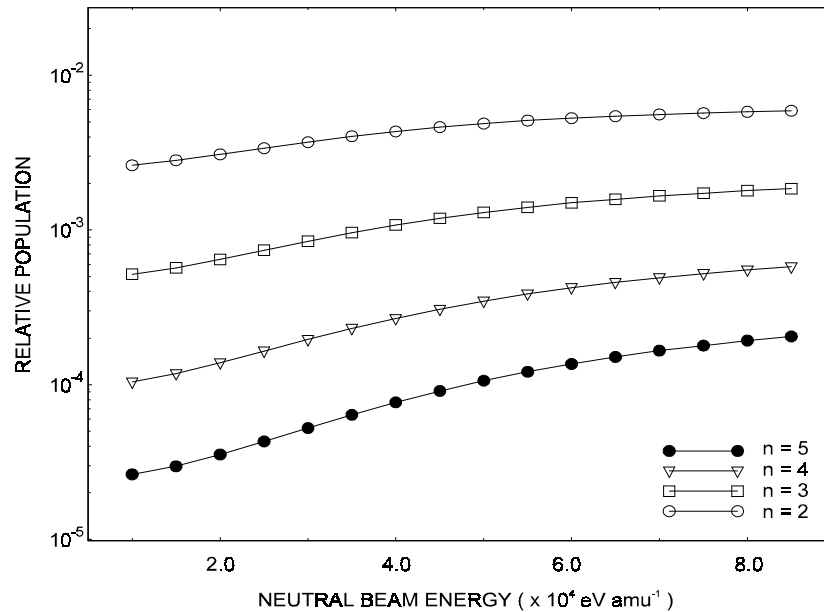


Figure 5.15 Population of the excited states relative to the ground state of the beam neutrals for a pure D^+ plasma. The plasma density and temperature are respectively $6 \times 10^{13} \text{ cm}^{-3}$ and 2 keV. As can be observed the population of the excited states is less than 1% of the ground population.

5.4.5 Conclusion

The original approach of analysing the beam emission spectrum by fitting all the Stark components proved to be unreliable when done in an unsupervised batch mode. A more reliable method was implemented which relies on reconstructing the flux from a fit of only the $+\pi 3$ and $+\pi 4$ components.

The review of the fundamental atomic data has led to a more accurate description of the behaviour of the atomic processes associated with the excited states. The revised atomic data has a substantial influence on the effective emission coefficients and hence the neutral beam density obtained from the beam emission

spectrum. The revised data had a much smaller effect on the effective stopping coefficients and hence the attenuation calculation.

5.5 Results

In this section we show separately the results obtained from the analysis of spectra recorded during single and double beam bank pulses. In both cases we compare the measured beam density with the values obtained from the numerical attenuation calculation. In each case we first illustrate the typical radial and time dependence of the measured and calculated neutral beam density. We then show the pulse to pulse variation between the results obtained from both methods.

5.5.1 Single beam bank pulses

In figure 5.16 we illustrate at three different time periods the behaviour of the radial dependence of the measured and calculated neutral beam density for a typical pulse.

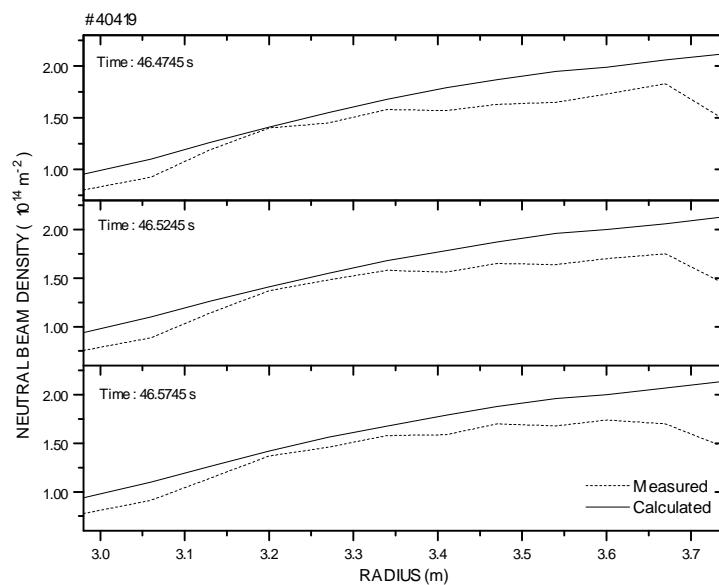


Figure 5.16 Radial dependence of the measured and calculated neutral beam density for the single beam bank pulse 40419. Three time slices have been selected to illustrate the results. A characteristic feature which can be observed in the majority of pulses is the fall off of the measured beam density as we move towards the edge (~ 3.7 m).

There is generally good agreement between the measured and calculated values although the figure shows a sudden decrease of the measured beam density near the edge of the plasma (~ 3.7 m). This unexplained fall off was first observed by Mandl[20] and appears in the radial dependency of the measured beam density for all single beam bank pulses.

The time dependency of the measured and calculated neutral beam density for a typical pulse is shown in figure 5.17.

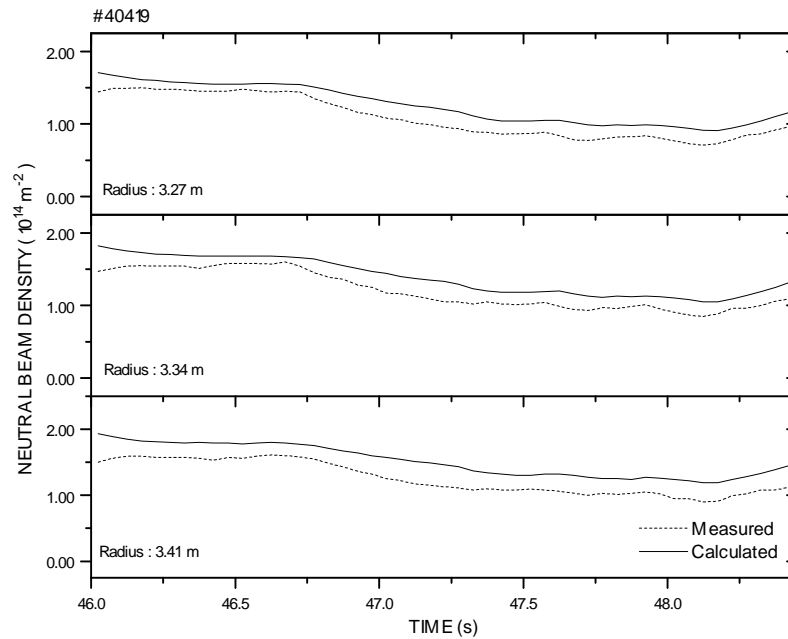


Figure 5.17 Time dependency of the measured and calculated neutral beam density for the single beam bank pulse 40419. Three radial positions have been selected to illustrate the results.

There is remarkably good agreement between the measured and calculated values at all times for the three different radial positions.

We also illustrate the pulse to pulse variation of the results. The criteria for the selection of pulses was simply that the pulses must have continuous neutral beam injection, see figure 5.18.

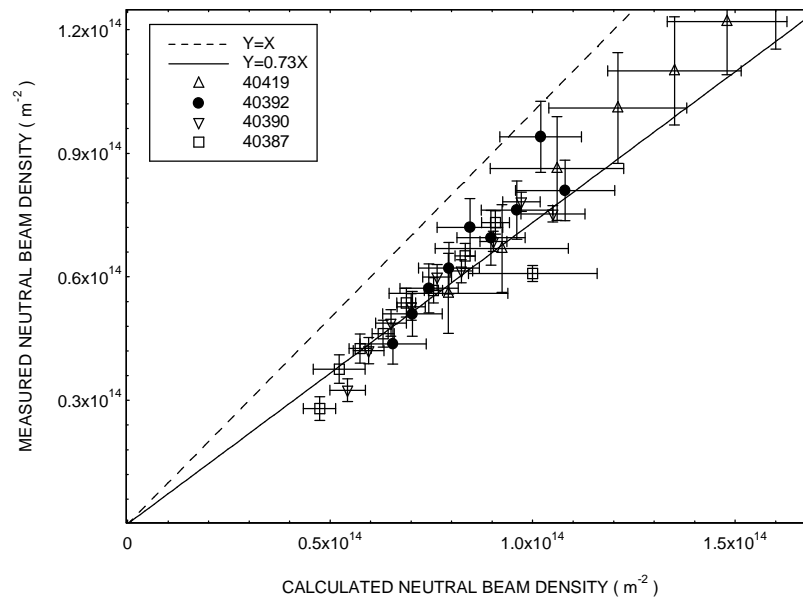


Figure 5.18 Variation of the measured and calculated beam density for a range of single beam bank pulses. Each data point represents a time averaged value for a fixed radial position. A measure of the deviation between the measured and calculated beam density is obtained by comparing the solid straight line with that of the dashed line which represents perfect agreement.

Each data point represents a time averaged value for a fixed radial position. The assigned error bar is simply the standard deviation associated with the time averaged value. A measure of the deviation between the measured and calculated beam density is obtained by comparing the solid straight line with that of the dashed line which represents perfect agreement. As shown in figure 5.18, an average difference of $\sim 27\%$ can be observed between the measured and the calculated neutral beam density.

5.5.2 Double beam bank pulses

The radial dependence of the measure and calculated neutral beam density for a typical double beam bank pulse is shown in figure 5.19. Three time periods of the pulse have been selected to illustrate the results.

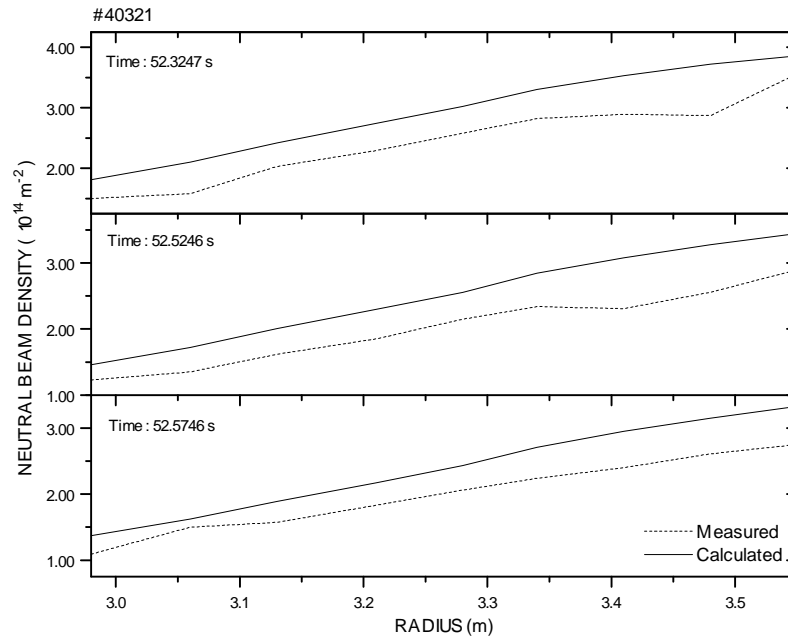


Figure 5.19 Radial dependence of the measured and calculated neutral beam density for three different time periods of the double beam bank pulse 40321.

The measured and calculated values show good agreement. However due to experimental difficulties we have no data near the edge of the plasma (~ 3.7 m), therefore we cannot confirm the fall off of the measured beam density as observed from the analysis of single beam bank spectra.

In figure 5.20 we show the time dependence of the measured and calculated values for three radial positions. We now consider the pulse to pulse variation between the measured and calculated neutral beam density. The selection criteria were the same as for single beam bank pulses. The results can be seen in figure 5.21, where an average difference of $\sim 20\%$ can be observed between the measured and the calculated neutral beam density. It should be noted that each point represents a time averaged value for a fixed radial position.

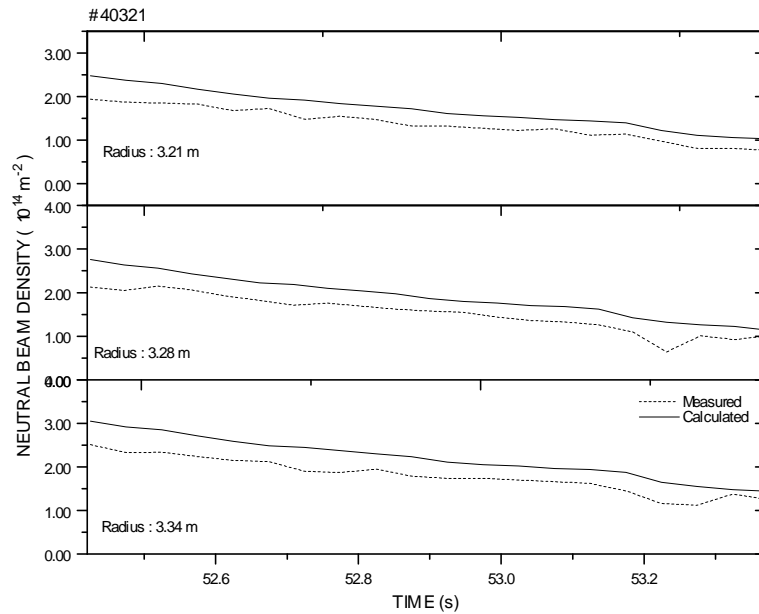


Figure 5.20 Time dependence of the measured and calculated neutral beam density at three radial positions for the double beam bank pulse 40321. Good agreement between the measured and calculated values as a function of time can clearly be observed.

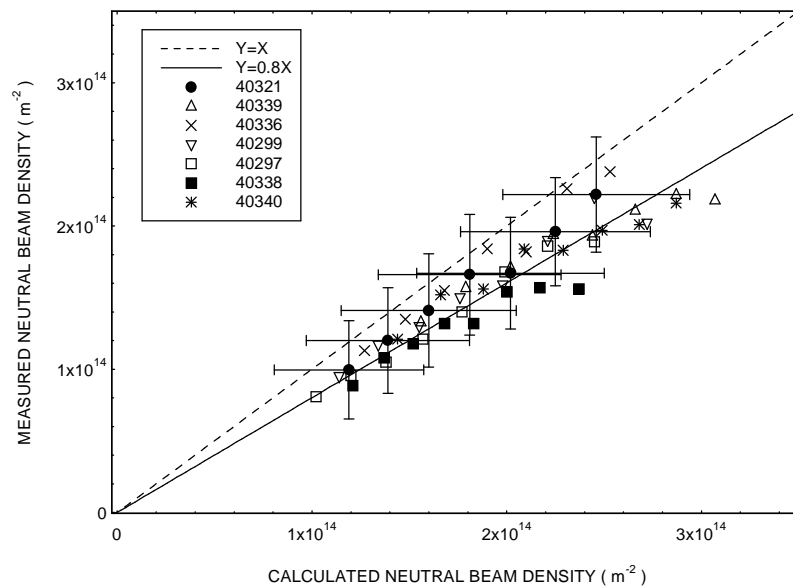


Figure 5.21 The variation between the measured and calculated neutral beam density for a range of double beam bank pulses. The solid straight line represents a line of best fit through the data points. A measure of the deviation between the measured and calculated beam density is obtained by comparing the solid straight line with that of the dashed line representing perfect agreement.

5.6 Conclusion

Refinements in the spectral fitting, consistency in the charge exchange analysis and the use of improved data which enters into the modelling to evaluate the effective coefficients, have led to the reliable deduction of the neutral beam density from the single and double beam bank spectra.

For single beam bank spectra we are able to recover a neutral beam density to within 27 % of the values obtained from the attenuation calculation. In the case of double beam bank pulses, we can recover the neutral beam density to within 20% of the numerical attenuation calculation.

In both single and double beam bank scenarios the time dependence between the measure and calculated beam density is remarkably good and this adds some credence to the atomic modelling. It should be noted however that from the results it appears that we can measure the beam density from double beam bank pulses with a greater accuracy than that for single beam bank pulses. This is somewhat surprising since the beam emission spectrum from a single beam bank pulse is much easier to analyse.

6.0 Predictive studies of helium beam attenuation and emission

6.1 Introduction

During tokamak experiments it is convenient to keep the neutron flux from the plasma to a minimum so that access to the vessel may be unrestricted. To minimise the beam driven neutron production rate, fast helium beam atoms can be injected into the plasma instead of neutral deuterium atoms. The neutral helium beams still heat the fusion plasma but without the production of unwanted neutrons[84]. There are also potential diagnostic benefits of injecting neutral helium beam atoms into the plasma rather than deuterium atoms. Due to the efficiency of the resonant process of double charge exchange, helium beam atoms in their ground state can act as donors to the fully stripped alpha particles contained in the plasma. The neutralised alpha particles can be measured and the associated slowing down time can be obtained[22]. Also due to the presence of metastable levels in the beam, preferential charge exchange between the ground state and the He(2 ³S) metastable may be possible. As suggested by Hoekstra[85], in circumstances where the He(2 ³S) metastable population is significant it may be the case that it will be primary donor for the C VI(n=8 -7) charge exchange line, with a small contribution from the He(1 ¹S) ground state. Where as the He(1 ¹S) ground state would be the primary donor for the HeII(n=4-3) charge exchange line, with a small contribution from the He(2 ³S) metastable. Another important diagnostic benefit is with the application of beam emission spectroscopy. Due to the degenerate nature of deuterium atoms, the motional Stark effect resulted in a complicated array of Stark components which was difficult to analyse (see chapter 5.0). In the case of neutral helium, the influence of the motional Stark effect on the observed emission lines is not as significant and so the spectrum is simpler to analyse.

In this chapter we show the behaviour and parameter dependencies of the helium beam collisional-radiative ionisation and cross coupling coefficients required to model the beam attenuation and the non-equilibrium metastable populations. In particular, we highlight the difference in the rate at which electrons are ionised from the ground state and the two metastables. We also explore the parameter dependencies of the quasi-static excited population structure required to predict the

emission from the beam atoms themselves and hence extract the local plasma conditions from measurements. We examine in detail the influence of the non-equilibrium metastables on the quasi-static excited populations of the levels contained in the $n=4$ shell. The motivation for this is that if we can identify which metastable is most effective at populating each of the levels in the $n=4$ shell, we can utilise the spectral emission originating from the $n=4$ shell of the beam atoms to gauge the metastable content of the beam.

Focusing our attention on the metastability associated with the $\text{He}(2\ ^1\text{S})$ and $\text{He}(2\ ^3\text{S})$ levels, we investigate the implications of assuming that the metastables have relaxed and reached equilibrium relative to the ground state. To achieve this we calculate the metastable populations, for JET plasma conditions, using a spatial dependent treatment and we compare the results with that obtained from the quasi-static approximation.

Finally, we consider the attenuation of the neutral helium beam. We investigate the attenuation of ground state and metastable populations and study the influence of changing the initial metastable fractions of the beam. We also briefly consider the influence of sudden changes in the electron temperature and density. Our main motivation here is to describe quantitatively what happens to the metastable populations as the beam progresses through the plasma.

6.2 Review of the collisional-radiative coupling coefficients

It was discussed at length in chapter 2.0 the origin and application of the collisional-radiative cross coupling coefficients. It is worth briefly reviewing the main features at this point. To calculate the beam attenuation and the non-equilibrium level populations we construct a set of coupled equations using the collisional-radiative cross coupling coefficients. As mentioned earlier the coupling coefficients take into consideration the influence of stepwise atomic processes. For example the cross coupling coefficient which describes the rate at which the $\text{He}(2\ ^3\text{S})$ metastable is populated by the $\text{He}(1\ ^1\text{S})$ ground state will include the influence of all possible reaction pathways rather than just the rate for direct excitation. The coupled equations are of the form,

$$\begin{aligned}
v_b \frac{dN_{1^1S}}{dx} &= n_e S_{1^1S} N_{1^1S} - n_e S_{2^1S \rightarrow 1^1S} N_{2^1S} - n_e S_{2^3S \rightarrow 1^1S} N_{2^3S} \\
v_b \frac{dN_{2^1S}}{dx} &= -n_e S_{1^1S \rightarrow 2^1S} N_{1^1S} + n_e S_{2^1S} N_{2^1S} - n_e S_{2^3S \rightarrow 2^1S} N_{2^3S} \\
v_b \frac{dN_{2^3S}}{dx} &= -n_e S_{1^1S \rightarrow 2^3S} N_{1^1S} - n_e S_{2^1S \rightarrow 2^3S} N_{2^1S} + n_e S_{2^3S} N_{2^3S}
\end{aligned} \tag{6.1}$$

where v_b and n_e are respectively the beam velocity and the electron density. The quantity dx is along the beam path and $N_{n^{2S+1}L}$ represents the population of the non-equilibrium level specified by the quantum numbers n , L and S . The collisional-radiative cross coupling coefficients are represented by the symbol $S_{n^{2S+1}L \rightarrow n^{2S+1}L}$, where the subscripts specify the initial and final non-equilibrium level. The cross coupling coefficients for which the subscript only specifies the initial state e.g. $S_{n^{2S+1}L}$, refer to what can be described as the total loss coefficient from the level $n^{2S+1}L$. The total loss coefficient includes the collisional-radiative ionisation rate from the level $n^{2S+1}L$ as well as the contribution to populating the remaining levels. As discussed in chapter 2.0, the collisional-radiative ionisation coefficients represent the rate at which the non-equilibrium levels of the beam atoms are ionised and are obtained from the cross coupling coefficients using the following expression,

$$S_\rho = S_{\rho\rho} - \sum_{\sigma=1}^{\rho-1} S_{\rho\sigma} - \sum_{\sigma=\rho+1}^m S_{\rho\sigma} \tag{6.2}$$

where S_ρ and $S_{\rho\sigma}$ are respectively the effective ionisation and cross coupling coefficients, and the subscripts ρ and σ represent the initial and final states. In figure 6.1 we schematically show the physical significance of the collisional-radiative ionisation and cross coupling coefficients.

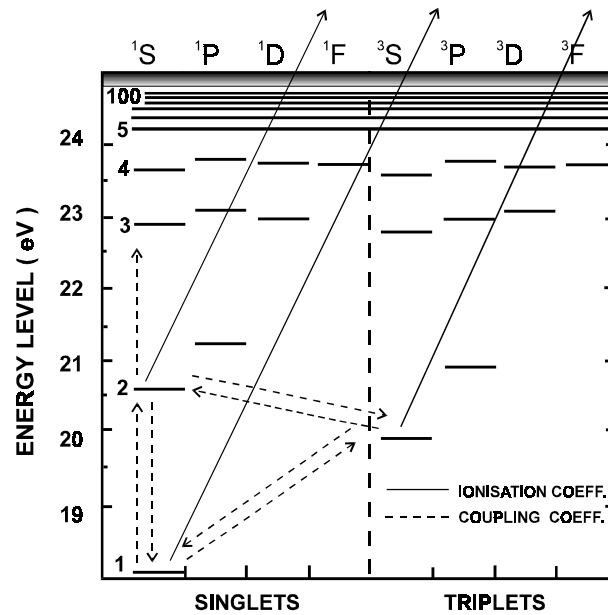


Figure 6.1 Schematic illustration of the energy levels structure of neutral helium. Highlighted with the dashed lines are the collisional-radiative cross coupling coefficients. Also shown in the figure with the solid lines are the effective ionisation coefficients associated with each metastable level. Note that the coefficients which connect two metastables include the influence of all indirect paths.

6.3 Collisional-radiative cross coupling coefficients

The cross coupling coefficients describe the rate at which the metastable levels, including the ground state, are populated and depopulated within a collisional-radiative frame work. They include the influence of stepwise atomic processes and can be used to define an effective ionisation coefficient associated with the ground state and each metastable. In figure 6.2 we show the behaviour of the cross coupling and effective ionisation coefficients as a function of beam energy for a pure D^+ plasma.

The parameter dependencies which are of interest are the electron density, neutral beam energy and the electron temperature. We also wish to separate the contributions to the coupling coefficients due to electron and ion collisions and finally, explore the dependence on the nuclear charge of the impurity ions contained in the plasma. We have categorised the coupling coefficients into two groups of similar parameter dependency. The first group are associated with spin changing transitions, while the second group contains the remaining coefficients and is referred

to as the non-spin changing group. It should be noted that in the present work all of the coefficients are calculated in terms of the electron density with the condition of charge neutrality imposed.

Figure 6.2 Collisional-radiative cross coupling and effective ionisation coefficients for a pure D^+ plasma. Working down from the top we first consider the coefficients associated with the $He(1^1S)$ ground state and then the $He(2^1S)$ and $He(2^3S)$ metastables. Also shown are the effective ionisation coefficients. The electron density was $1.0 \times 10^{13} \text{ cm}^{-3}$ and the electron temperature was 100 eV.

6.3.1 Non spin changing transitions

The cross coupling coefficients which have been categorised into the non-spin changing group are schematically shown in figure 6.3.

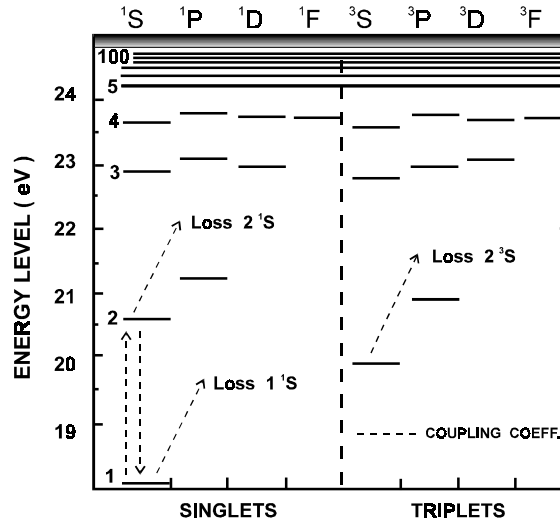


Figure 6.3 Schematic illustration of the five effective coupling coefficients which have been placed in the non-spin changing category.

There are five coupling coefficients in the non-spin changing group. The coefficients which connect the He($1\ ^1S$) and the He($2\ ^1S$) levels are the true cross coupling coefficients while the remaining three coefficients describe the total rate at which electrons are lost from each level. The latter contain the effective ionisation coefficient, as well as the coupling coefficients which connect to the other two remaining levels. We use the name ‘cross coupling’ coefficient to refer to all these types of effective coefficients

We shall first consider the density dependence of a non spin changing coupling coefficient for a pure D^+ plasma. In figure 6.4 we illustrate the behaviour of the coupling coefficient, which describes the total loss rate associated with the He($1\ ^1S$) ground state, as a function of beam energy for three different densities. The electron densities which have been selected to represent the coronal, collisional-radiative and high density regimes are 10^6 , 10^{13} and 10^{15} cm^{-3} respectively.

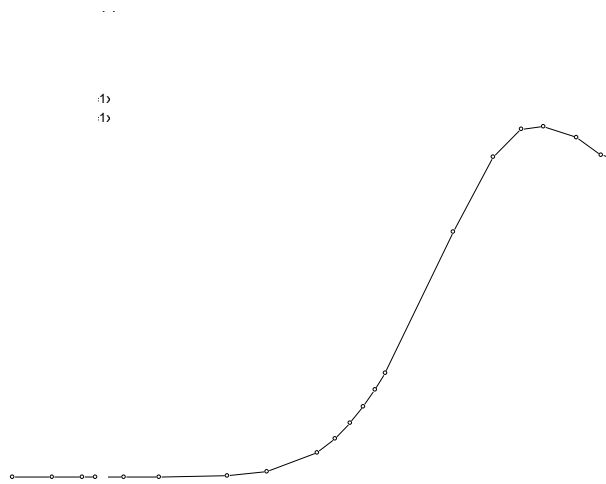


Figure 6.4 Cross coupling coefficient describing the total loss rate from the He(1^1S) ground state for a pure D^+ plasma . The coefficient has been plotted for three different densities as a function of neutral beam energy. Also shown in the figure is the contribution to the coefficient due to electrons collisions only. The electron temperature was 100 eV.

In the coronal regime only the direct processes contribute to the coefficient. The component of the cross coupling coefficient which represents the effective ionisation coefficient is just the rate for direct ionisation due to electrons and ions, while the remaining component of the cross coupling coefficient, which connects the He(1^1S) ground state to the other two metastables levels, is simply the sum of the corresponding direct excitation rates. When the electron density is increased to around $1 \times 10^{13} \text{ cm}^{-3}$, we are in the collisional-radiative regime where the role of stepwise atomic processes is important. This results in an overall increase in the effective cross coupling coefficient. The effective ionisation component of the coupling coefficient now includes a contribution due to ion and electron impact ionisation from excited levels and the remaining component of the coupling coefficient includes the influence of stepwise atomic processes. At an electron density of $1.0 \times 10^{15} \text{ cm}^{-3}$, we are in the high density regime, see figure 6.4. The coupling coefficient has reached a maximum value. The component of the coupling coefficient which represents the effective ionisation rate includes the influence of ion

and electron impact ionisation from the ground and the excited states. Even excitation contributes to ionisation. The contribution of the cross coupling coefficient which connects the ground state with the two metastable levels now includes the full influence of stepwise processes as well as direct excitation.

It is of interest to contrast the behaviour of the cross coupling coefficient calculated with and without the inclusion of ions. As can be observed in figure 6.4, the contribution to the effective coefficient due to electrons, regardless of the electron density, is independent of the beam energy. This is due to the fact that the electrons are moving in the plasma with such a large velocity that the speed of the beam is insignificant. If however we introduce ions into the plasma the effective coefficient changes. In the low energy regime the contribution to the cross coupling coefficient is primarily due to electrons. The ions collisions are only driven by their thermal ion temperature and the net contribution is small. As the neutral beam energy is increased the influence of the ion collision becomes significant and results in an increase in the effective coupling coefficient, see figure 6.4. The increase in the coupling coefficient directly reflects the energy dependence of the cross sections which describe the behaviour of ion impact excitation and ionisation. The latter being of greater importance above 10 keV amu^{-1} .

The temperature dependence of the coupling coefficient is the next issue we want to address. In figure 6.5 we show for a low density D^+ plasma ($\sim 1.0 \times 10^6 \text{ cm}^{-3}$), the coupling coefficient which described the total loss rate associated with the $\text{He}(1^1\text{S})$ ground state as a function of the beam energy for a selected range of temperatures.

It can be observed that an increase in the electron temperature results in an increase in the coupling coefficient. This is due to the temperature dependence of the electron collisions which contribute to the cross coupling coefficient. At a temperature of 10 eV the component of the coupling coefficient which represents the effective ionisation coefficient is simply the corresponding electron impact ionisation rate. As we increase the temperature, the behaviour of the effective ionisation component reflects the behaviour of electron impact ionisation rate. It is of interest to note that as we increase the temperature from 10 to 100 eV there is a substantial

increase in the coupling coefficient. However as we increase the temperature from 100 to 1 keV the change in the coupling coefficient is less. This is a clear illustration of the temperature dependence of the electron collisions, particularly the electron impact ionisation rate which is also shown in figure 6.5. We also show in figure 6.5 the contribution to the coupling coefficient due to electron collisions alone. As before we can observe that the electron contribution is independent of the beam energy and is governed by the electron temperature.

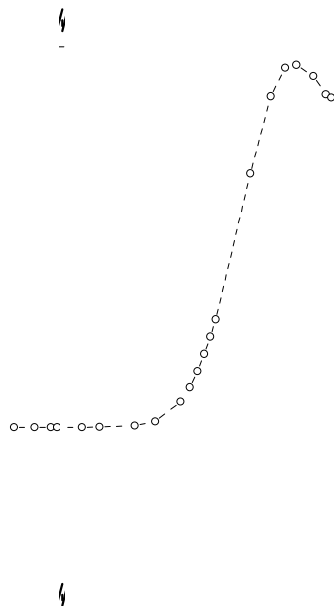


Figure 6.5 Temperature dependence of the coupling coefficient describing the total loss rate associated with the He(1^1S) ground state for a pure D^+ plasma. The plot on the left illustrate the coupling coefficient as a function of neutral beam energy for a selected range of electron temperatures. Also shown is the contribution to the coupling coefficient due to electron collisions. The electron density was $1.0 \times 10^6 \text{ cm}^{-3}$. The plot on the right illustrates the temperature dependence of the electron impact ionisation rate coefficient associated with the He(1^1S) ground state.

Due to the unavoidable presence of impurities in tokamak plasmas we must also take into consideration their influence on the cross coupling coefficients. In figure 6.6 we show the behaviour of the coupling coefficient which describes the total loss rate associated with He(1^1S) ground state for pure impurity plasmas. The electron density is fixed and the number density for each impurity species is such that charge

neutrality is maintained. Therefore as the nuclear charge of the impurity species increases the corresponding impurity number density decreases.

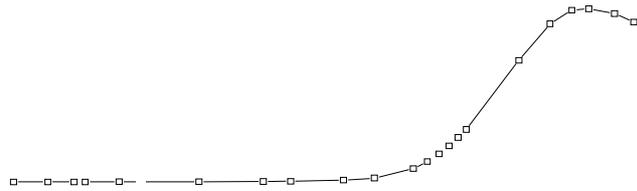


Figure 6.6 Cross coupling coefficient associated with the He(1^1S) ground state as a function of neutral beam energy for a range of pure impurity plasmas. The electron density is fixed at $1.0 \times 10^{13} \text{ cm}^{-3}$ and the number density of impurity species is such that charge neutrality is maintained. The electron temperature was 100 eV.

In the low energy regime the contribution to the coupling coefficient is primarily dominated by electron collisions. It can be observed however that some of the impurity ions are capable of effectively contributing to the coupling coefficient at such a low energy. Their influence in this case is due to their thermal ion temperature. As the beam energy is increased, the influence of ion impact excitation becomes important at around 10^4 eV/amu and as the beam energy is increased further ion impact ionisation dominates. The influence of the impurity ions as shown in figure 6.6, increases with nuclear charge, even though the number density of the impurity species decreases.

As mentioned before, all of the coefficients grouped into the non-spin changing category exhibit a similar type of parameter dependency and we have focused on the coupling coefficient associated with the He(1^1S) ground state merely

as an example. In figure 6.7 we show the behaviour of the coupling coefficient which describes the total loss rate associated with the $\text{He}(2^3\text{S})$ metastable for a pure D^+ plasma.

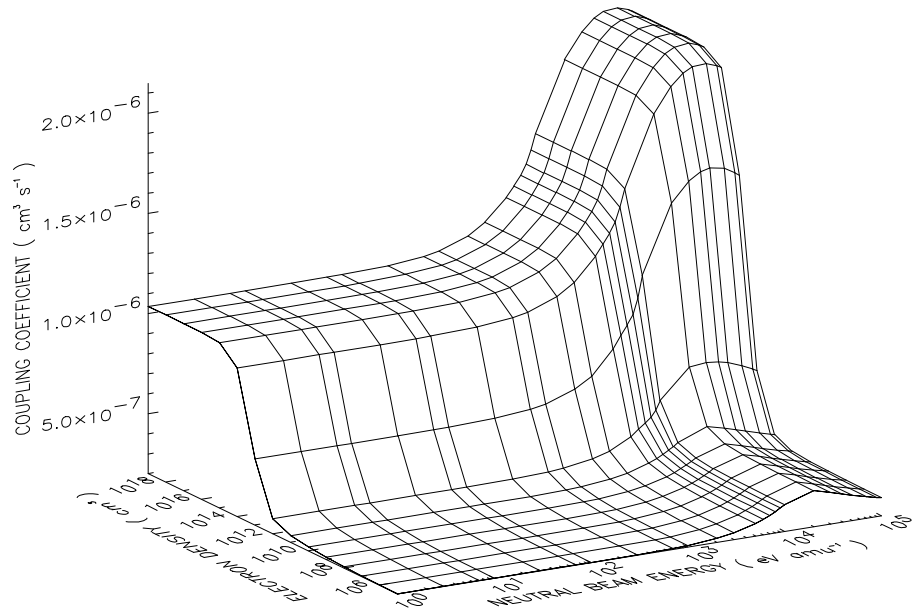


Figure 6.7 Behaviour of the cross coupling coefficient describing the total loss rate associated with the $\text{He}(2^3\text{S})$ metastable for a pure D^+ plasma. In the low energy regime the contribution to the coefficient is primarily driven by electron collisions. As the beam energy is increased the role of ion collisions becomes significant and an increase in the coupling coefficient can be observed. If we increase the electron density the role of step wise atomic processes becomes important and results in the coupling coefficient increasing to a maximum value which corresponds to the high density limit.

As can be observed, in the low energy region the contribution to the coupling coefficient is small, it is driven purely by electrons. As we increase the beam energy the influence of the ion collisions becomes significant and results in an increase in the coupling coefficient. An increase in the electron density encourages the atomic processes associated with the excited states to contribute to the coupling coefficient. If we continue to increase the density the high density limit is reached and the coupling coefficient tends to a constant value.

6.2.2 Spin changing transitions

We schematically show in figure 6.8 the cross coupling coefficients which are contained in the spin changing group.

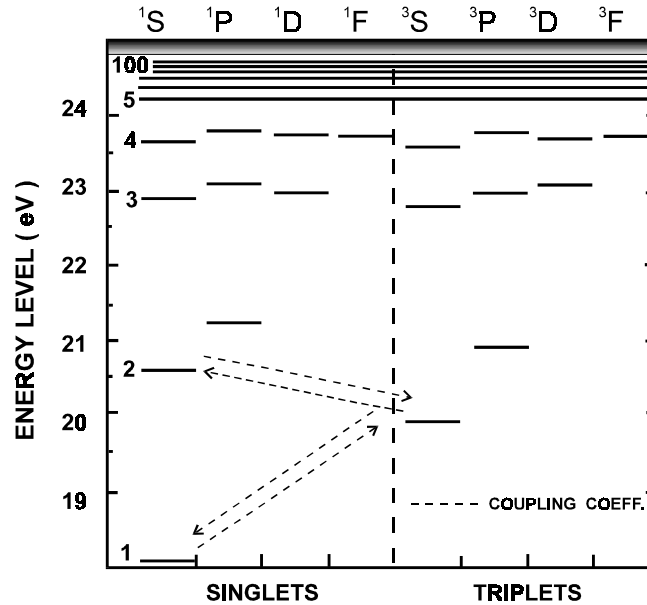


Figure 6.8 Schematic illustration of the four collisional-radiative cross coupling coefficients which are contained in the spin changing group.

There are four cross coupling coefficients in total. Each of the coefficients represent the rate at which the metastable levels, including the ground state, are populated and depopulated through spin changing processes. It is important to mention that ion collisions are strictly spin conserving. Only electron collisions are involved in spin changing transitions. Therefore in the present context the ions collisions can only populate the singlet spin systems of the beam atoms by promoting electrons from the ground state. Electron collisions however can contribute to populating both the singlet and triplet spin systems through a variety of spin and non-spin changing transitions.

We shall first consider the density dependence of the spin changing cross coupling coefficients for a pure D^+ plasma. In figure 6.9 we show the behaviour of the coupling coefficient for the transition $He(2\ ^1S) \rightarrow He(2\ ^3S)$ as a function of beam

energy for three different densities. Also shown are the cross coupling coefficients for a pure electron plasma.

Figure 6.9 Collisional-radiative cross coupling coefficient for the $\text{He}(2^1\text{S}) \rightarrow \text{He}(2^3\text{S})$ spin changing transition for a pure D^+ plasma. The coupling coefficient has been plotted as a function of neutral beam energy for three different electron densities. The electron temperature was 100 eV.

As can be observed, in the above figure we are presented with some interesting results. Since electron collisions drive the spin changing transitions it would have been expected that the cross coupling coefficient would have been independent of the neutral beam energy. This is in fact the case when we look at the cross coupling coefficient as a function of beam energy in the low density regime at $1 \times 10^6 \text{ cm}^{-3}$. However as we increase the electron density the role of atomic processes associated with excited states comes into to play. At a density of around $1 \times 10^{13} \text{ cm}^{-3}$, as shown in figure 6.9, in the low energy regime the cross coupling coefficient is driven purely by electron collisions and is therefore independent of the beam energy. As we increase the beam energy the influence of the ion collisions becomes important. In the above figure it can be seen that the ion collisions contribute to reducing the cross coupling coefficient. This phenomena can be attributed to the fact that in the low density regime the reaction path ways from the $\text{He}(2^1\text{S})$ metastable is dominated by

spin changing electron collisions, even at high beam energies. As we increase the density the influence of the ion collisions contribute to increasing the reaction path ways associated with the He(2 ¹S) metastable level. As the beam energy increases it becomes more favourable to excite or ionise the contents of the He(2 ¹S) level rather than contributing to populating the He(2 ³S) metastable via a spin changing transitions, see figure 6.10. The energy dependence of the spin changing cross coupling coefficients should be consider as a secondary effect .

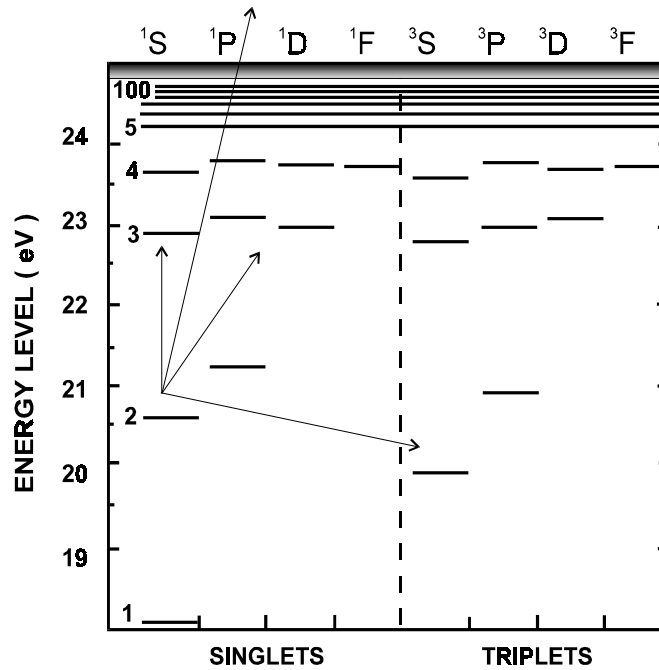


Figure 6.10 Schematic illustration of the increasing reaction pathways associated with the He(2 ¹S) metastable level. In the low density region the contents of the He(2 ¹S) metastable acts as a source to populate the He(2 ³S) metastable. As the electron density is increased the role of ion collisions result in the content of the He(2 ¹S) metastable being preferentially excited or ionised rather than contributing to populating the He(2 ³S) metastable, particularly as high energies.

We now consider the temperature dependence of the spin changing cross coupling coefficient. In figure 6.11 we show the behaviour of the cross coupling coefficient for the transition He(2 ³S)→ He(2 ¹S).

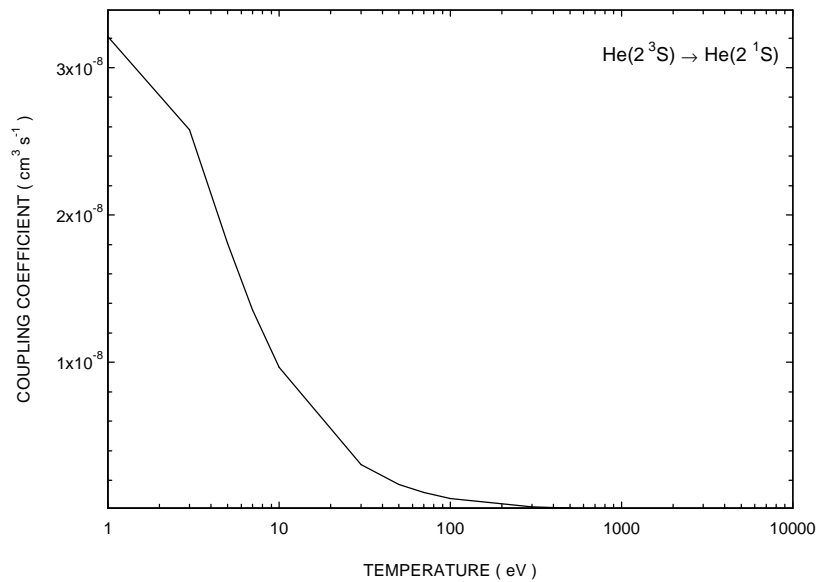


Figure 6.11 Temperature dependence of the cross coupling coefficient for the transition $\text{He}(2^3\text{S}) \rightarrow \text{He}(2^1\text{S})$. The behaviour of the cross coupling coefficient directly reflects the temperature dependence of the fundamental data.

Spin changing transitions are driven purely by the electron collisions and since the influence of the electron collision is governed by the temperature we would expect a strong temperature dependence of the coupling coefficient. This indeed can be observed in the above figure. The behaviour of the coupling coefficient directly reflects the temperature dependence of the electron collisions which are involved in the spin changing transition. It is of interest to note how the coupling coefficient decreases as the temperature increases.

We now consider the dependency of the cross coupling coefficient on the nuclear charge of typical impurity species. Once again we emphasise that the electron density is fixed and the number density of impurity ions is such that charge neutrality is maintained. In figure 6.12 we show the behaviour of the coupling coefficient corresponding to the transition $\text{He}(2^1\text{S}) \rightarrow \text{He}(2^3\text{S})$ for a selected range of pure impurity plasmas.

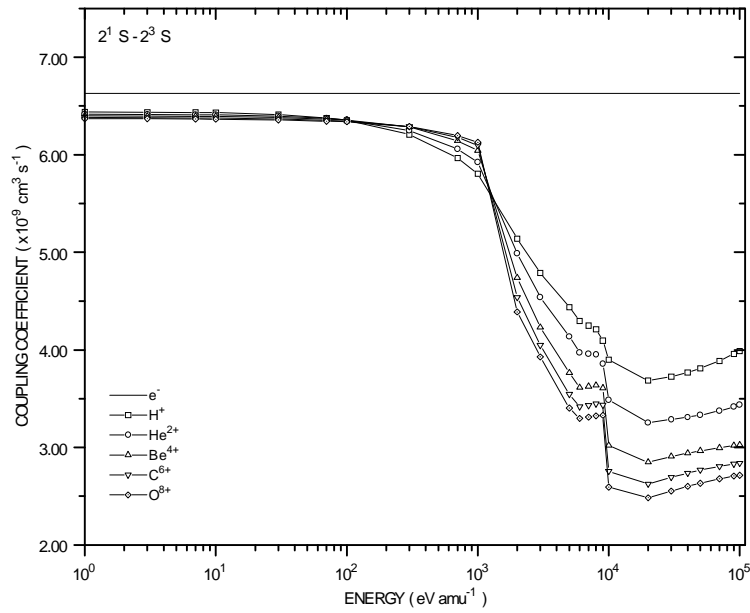


Figure 6.12 Cross coupling coefficient for the transition $\text{He}(2^1\text{S}) \rightarrow \text{He}(2^3\text{S})$ for a selected range of pure impurity plasmas. Also shown is the contribution to the coefficient due to electrons only. The electron density and temperature were respectively $1.0 \times 10^{13} \text{ cm}^{-3}$ and 100 eV. The number density of impurity ions is such that charge neutrality is maintained.

The greater the nuclear charge of the impurity species the more effective it is at encouraging collisional redistribution amongst the excited states and opening up additional reaction pathways associated with the $\text{He}(2^1\text{S})$ metastable. Also shown in the figure is the coupling coefficient due to electrons only. It is of interest to note that even at very low beam energies, the contribution to the coupling coefficient due to the some of the impurity ions is of significance. The driving mechanism for the impurity ions in this regime is their thermal ion temperatures.

The parameter dependencies of the remaining cross coupling coefficients contained in the spin changing group show a similar parameter dependency. As an example we show in figure 6.13 the behaviour of the coupling coefficient for the transition $\text{He}(2^3\text{S}) \rightarrow \text{He}(2^1\text{S})$ for a pure D^+ plasma.

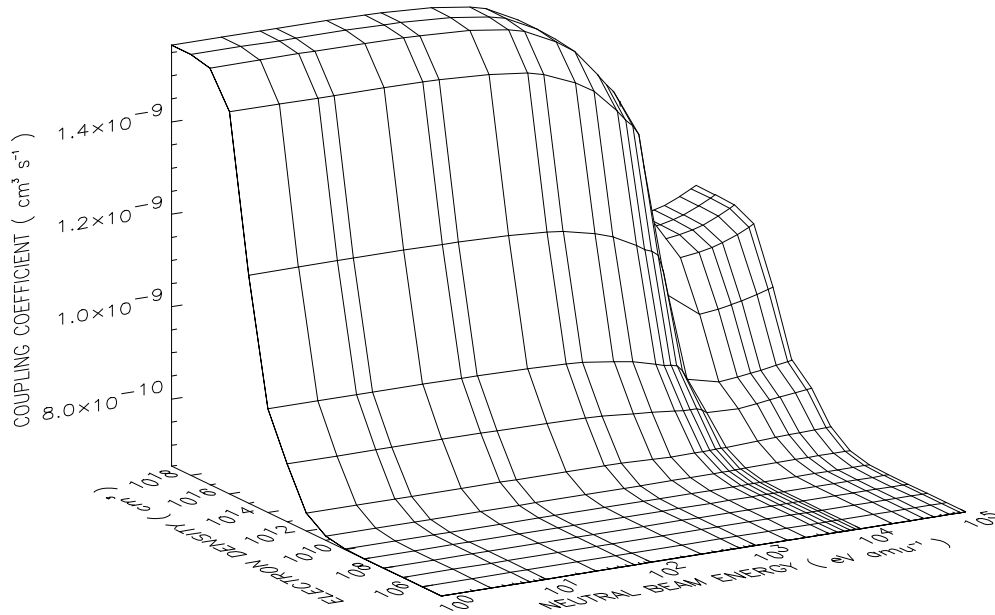


Figure 6.13 Behaviour of the $\text{He}(2^3\text{S}) \rightarrow \text{He}(2^1\text{S})$ cross coupling coefficient for a pure D^+ plasma. In the low density regime the coefficient is independent of the neutral beam energy since it is driven purely by electron collisions. As we increase the density the influence of the ion collisions opens up additional reaction pathways associated with the $\text{He}(2^3\text{S})$ and a decrease in the coefficient can be observed.

As can be observed, in the low density regime the cross coupling coefficient is independent of the neutral beam energy. As the electron density is increased the role of the ion collisions opens up additional reaction pathways associated with the $\text{He}(2^3\text{S})$ metastable. It is instructive to compare the above figure with the surface plot shown in figure 6.7. In the latter figure, which shows the behaviour of the coupling coefficient describing the loss rate from the $\text{He}(2^3\text{S})$ metastable, we can see that as the electron density and neutral beam energy is increased the influence of the ion collisions result in the electrons being preferentially ionised. This is consistent with the above figure, which shows that as the electron density and beam energy is increased the reaction rate for the transition $\text{He}(2^3\text{S}) \rightarrow \text{He}(2^1\text{S})$ substantially decreases.

6.3.3 Collisional-radiative ionisation coefficients

It of interest to show the behaviour of the effective ionisation coefficients associated with the ground state and each metastable. However it is important to note that even though we can assign an effective ionisation coefficient to each non-equilibrium level and hence an effective stopping coefficient in principle, to implement a numerical attenuation calculation involves solving a set of coupled equations which describe how the metastable and ground state populations evolve as the beam traverses the plasma. Due to the presence of metastable levels we can not describe the attenuation of the beam with a single coefficient. The helium beam attenuation calculation, which is the subject of section 6.5, is analogous to modelling the attenuation of three beams which are not independent of each other. In figure 6.14 we show the general behaviour of the effective ionisation coefficients associated with each level for a pure D^+ plasma. The effective ionisation rates associated with the $He(2^1S)$ and $He(2^3S)$ metastable levels are order of magnitudes greater than the ionisation coefficient associated with the ground state. A similar behaviour is shown by both ionisation coefficients. In the low density and energy regime each of the coefficients are purely driven by electron collisions. As the neutral beam energy is increased the contribution due to ion collisions results in a sudden increase in the effective coefficients. As we increase the electron density the contribution due to stepwise processes results in a further increase until the high density limit is reached.

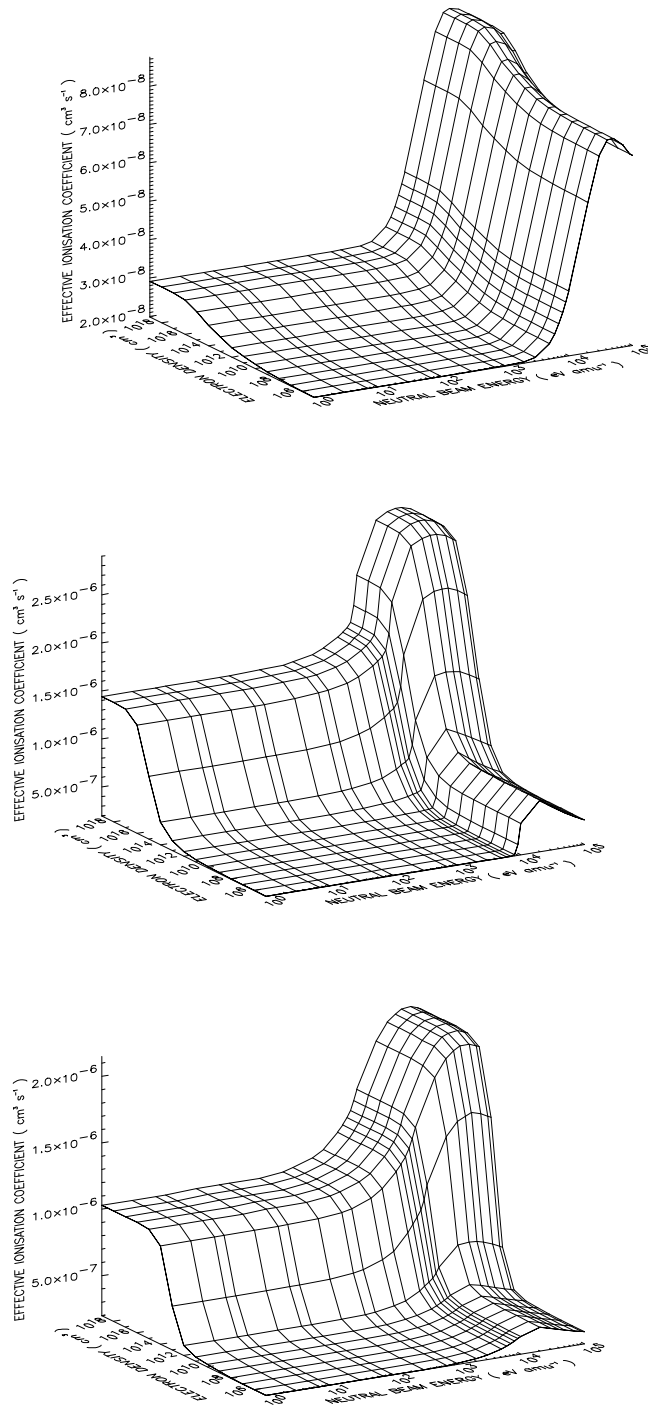


Figure 6.14 Collisional-radiative effective ionisation coefficients for a pure D^+ plasma. Starting from the top we show the effective coefficients associated with the ground state and then the $\text{He}(2^1\text{S})$ and $\text{He}(2^3\text{S})$ metastables. As can be observed the magnitude of the coefficients associated with the two metastable levels are substantially greater than the ionisation coefficient associated with the ground state. The electron temperature was fixed at 100 eV.

6.4 Quasi-static excited state population structure

In this section we illustrate the dependence of the excited population structure on the neutral beam energy, electron density and the electron temperature. We also show the influence of the metastable levels on the excited population structure, particularly the $n=4$ shell. Since the excited states have reached equilibrium relative to the ground state and the two metastables, it is of interest to be able to identify the extent to which each metastable is responsible for driving the population of each of the excited levels. For the higher levels above the $\text{He}(3\ ^3\text{D})$ this certainly is not obvious. Finally, we illustrate the dependency of the excited population structure on the nuclear charge of the impurity ions. We have restricted our study of the excited levels up to the $n=4$ shell, since this encompasses the important levels for visible spectroscopy. The quasi-static population of these levels have been calculated in a resolved $n\text{l}^{2S+1}\text{L}$ picture up to the $n=5$ shell which then continues into a bundled- $n\text{S}$ picture and terminates at $n = 110$.

6.4.1 Neutral beam energy dependence

The efficiency of the ion collisions in collisional redistribution and ionisation of the excited population structure is beam energy dependent. Also since ion collisions are spin conserving we would expect their influence to be confined within a spin system. In figure 6.15 we show the excited population structure of the singlet and triplet spin systems relative to the $\text{He}(1\ ^1\text{S})$ ground state as a function of neutral beam energy for a D^+ plasma.

Considering the singlet spin system, in the low energy regime the excited states are predominantly populated by electron collisions and are independent of the neutral beam energy. There is an insignificant contribution by ion collisions, due to their thermal temperature. As the beam energy is increased the influence of the ion collisions becomes significant. This results in a decrease in the excited state populations which can be attributed to ion impact ionisation depopulating each of the levels. If we continue to increase the beam energy the depleted populations begin to recover and increase as a function of beam energy. This is due to the fact that it becomes more energetically favourable to populate most of the levels by ion impact

excitation than to depopulate each of them by ion impact ionisation. The extent to which each level is populated depends on their associated ionisation energy and the excitation energy required to populate the level from the nearest neighbour. For example, if we consider the He(3 ¹P) level, the ionisation energy is ~1.499 eV while the excitation energy to populate this level from the He(3 ¹S) is only ~0.166 eV. We would therefore expect the population of He(3 ¹P) level to increase as ion impact excitation strongly competes with ion impact ionisation. However if we consider a higher lying level, for example He(4 ¹S), in this case ion impact ionisation will have a larger influence than the contribution due ion impact excitation from neighbouring levels and we would expect the increase in the He(4 ¹S) population to be of less significance as shown in figure 6.15.

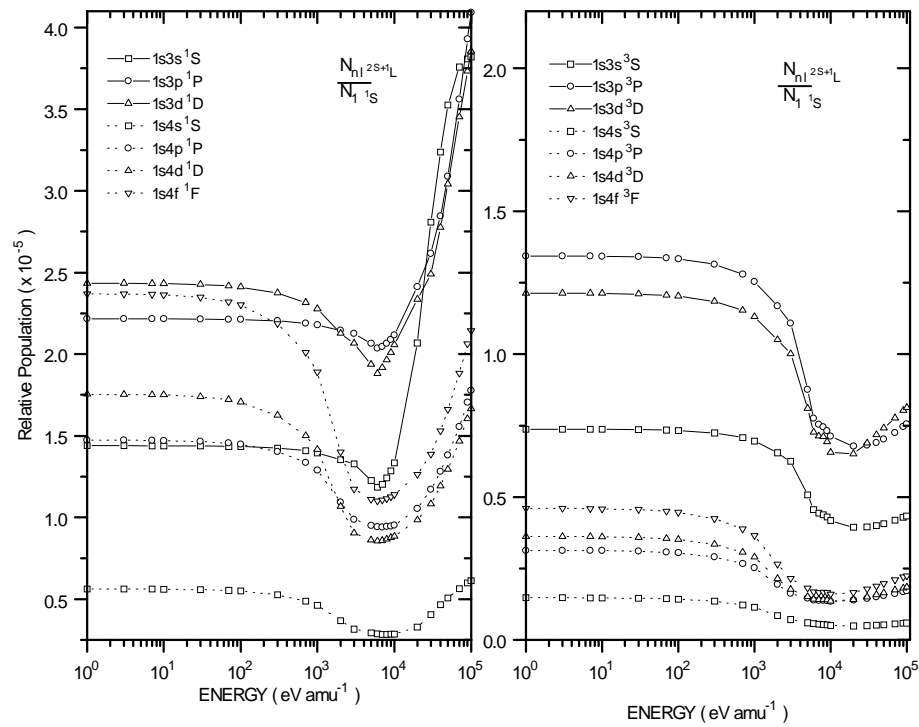


Figure 6.15 Quasi-static excited state populations of the singlet and triplet spin system relative to the He(1 ¹S) ground state for a D⁺ plasma. The plot to the left shows the population structure of the singlet spin system while the figure to the right illustrate population structure of the triplet spin system. The electron density was $1.0 \times 10^{13} \text{ cm}^{-3}$ and the temperature was 100 eV.

If we now consider the population structure of the triplet spin system driven by the He(1^1S) ground state, as mentioned before, only electron collisions are responsible for populating the triplet spin system. This can occur through direct excitation from the ground state or via spin changing transitions from the excited states of the singlet to the triplet spin system. As shown in figure 6.15, in the low energy regime the population structure is independent of the neutral beam energy. However as we increase the beam energy the excited triplet populations can be observed to decrease. This is due to the fact that as we increase the beam energy, ion impact ionisation which promotes the singlet populations to the continuum becomes important. The singlet populations decrease and the contribution from the excited state spin changing collisions to the triplet spin system is reduced. If we continue to increase the beam energy the population of the triplet levels can be observed to slightly recover. This is due to the rise in the populations of the singlet spin system and hence an increase in the contribution to the population of the triplets due to excited state spin changing transitions.

A similar type of behaviour can be observed for the singlet and triplet populations relative to the He(2^1S) and He(2^3S) metastable levels, see figure 6.16. It should be noted though, that in both these cases it is more energetically favourable to populate the excited levels of the singlet spin system via ion impact excitation, than to depopulate them by ion impact ionisation. Therefore the extent to which the excited states of the singlet spin system are depopulated is minimal.

The singlet populations relative to the He(2^1S) and He(2^3S) metastables can be observed to decrease slightly as we increase the beam energy. The populations however soon rapidly recover due to the contribution from ion impact excitation, see figure 6.16.

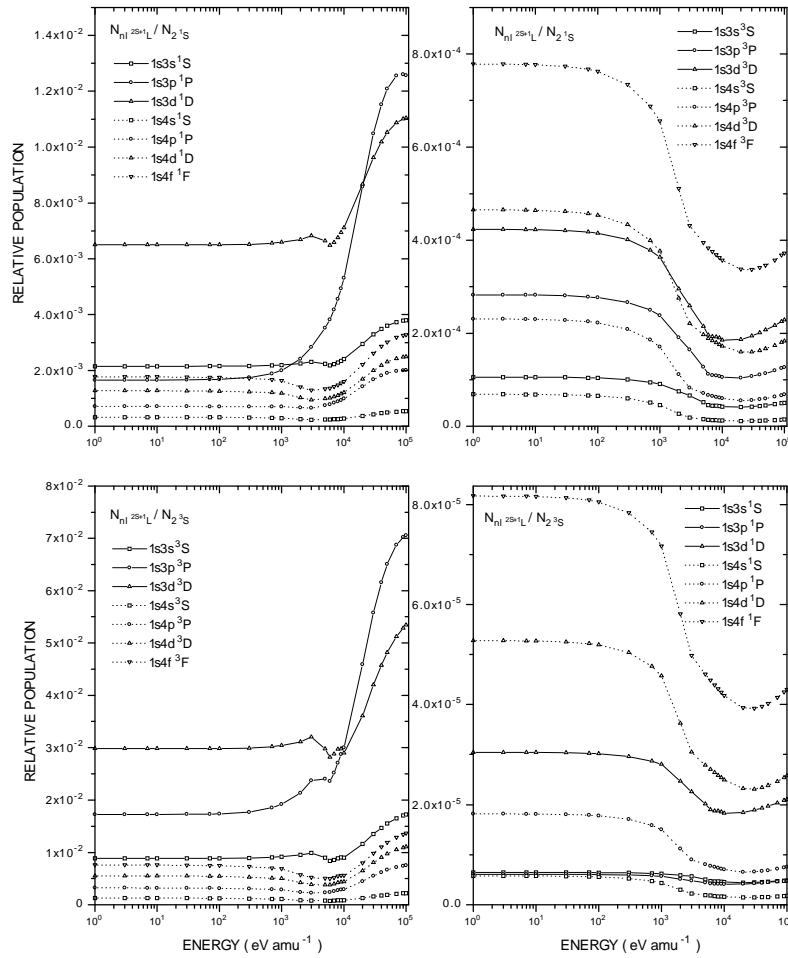


Figure 6.16 Quasi-static excited population structure of the singlet and triplet spin systems relative to the He(2 ¹S) and He(2 ³S) metastable levels for a D⁺ plasma. The two plots at the top show the behaviour of the singlet and triplet excited population structure relative to the He(2 ¹S) metastable. The two plots at the bottom show the behaviour of the excited population structure relative to the He(2 ³S) metastable. The electron density was $1.0 \times 10^{13} \text{ cm}^{-3}$ and the temperature was 100 eV.

6.4.2 Density dependence

In figure 6.17 we show the behaviour of the singlet and triplet population structure relative to the He(1 ¹S) ground state as a function of electron density for a D⁺ plasma.

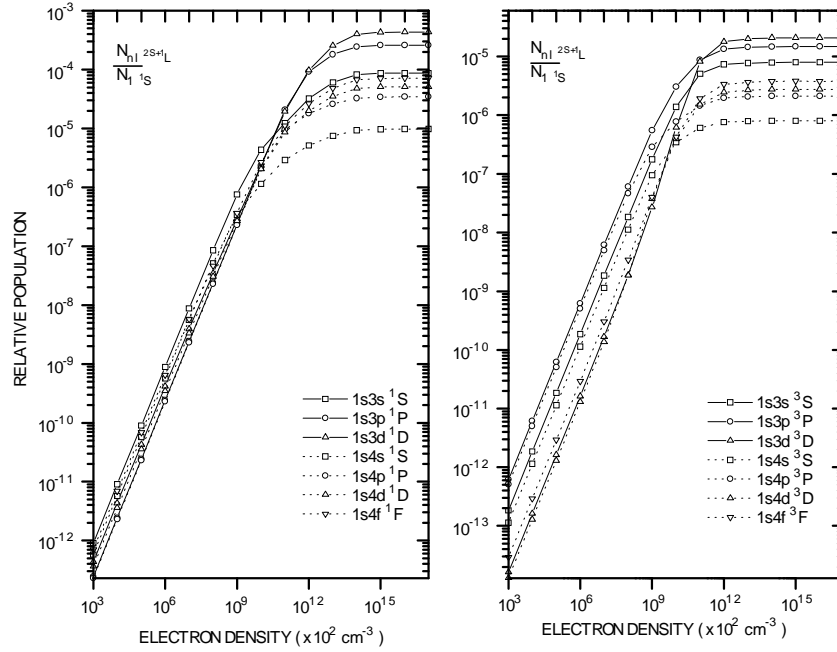


Figure 6.17 Quasi static excited population structure of the singlet and triplet spin system relative to the He(1^1S) ground state for a D^+ plasma. The beam energy and temperature are respectively 5.0 keV amu^{-1} and 100 eV . The populations are calculated in terms of the electron density but it is in fact the ion collisions which dominate the collisional redistribution. The number density of the ions is such that charge neutrality is maintained.

In the low density regime the excited levels of the singlet spin system associated with the beam atoms are populated by electron and ion collisions. The triplet spin system is populated by electron collisions. Regardless of the spin system the excited levels are depopulated by radiative decay. The excited populations relative to the He(1^1S) ground state are directly proportional to the electron density. At $1.0 \times 10^{13} \text{ cm}^{-3}$ in figure 6.17 we are in the collisional-radiative regime. As we continue to increase the electron density the excited populations reach the high density limit. A similar parameter dependency of the singlet and triplet population structure, relative to the He(2^1S) and He(2^3S) metastable levels, is shown in figure 6.18.

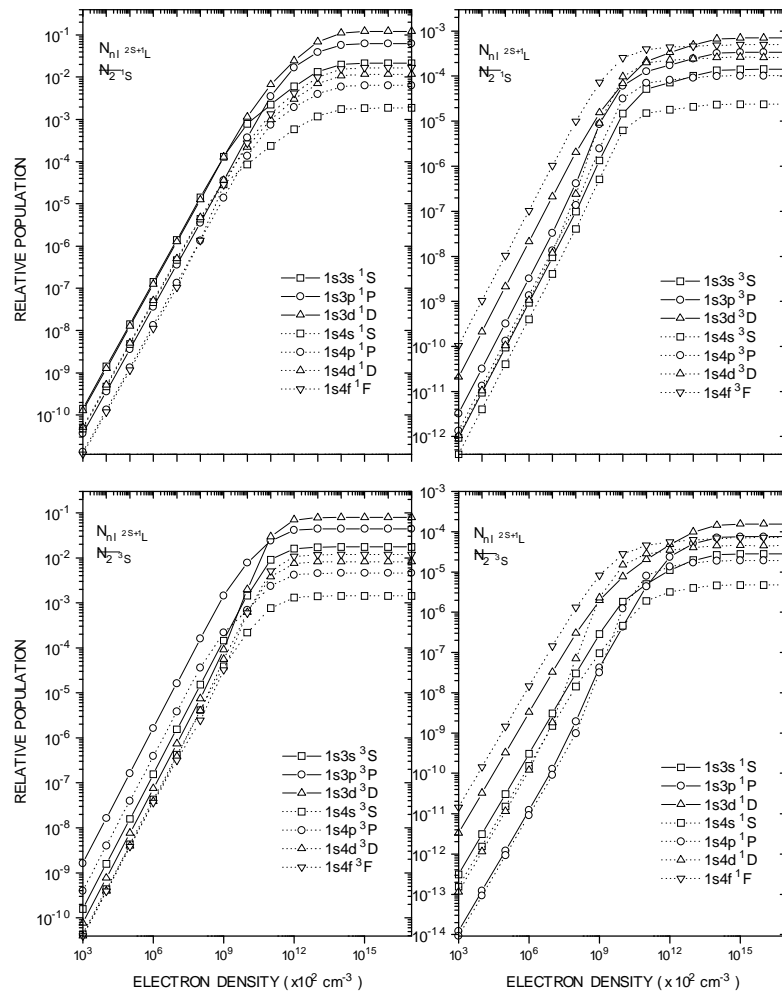


Figure 6.18 Quasi-static equilibrium populations of the singlet and triplet spin systems relative to the He(2^1S) and He(2^3S) metastables for a D^+ plasma. The beam energy and temperature are respectively 5.0 keV amu^{-1} and 100 eV .

6.4.3 Temperature dependence

In figure 6.19 we illustrate the temperature dependence of the population structure of the singlet and triplet spin system relative to the He(1^1S) ground state for a D^+ plasma.

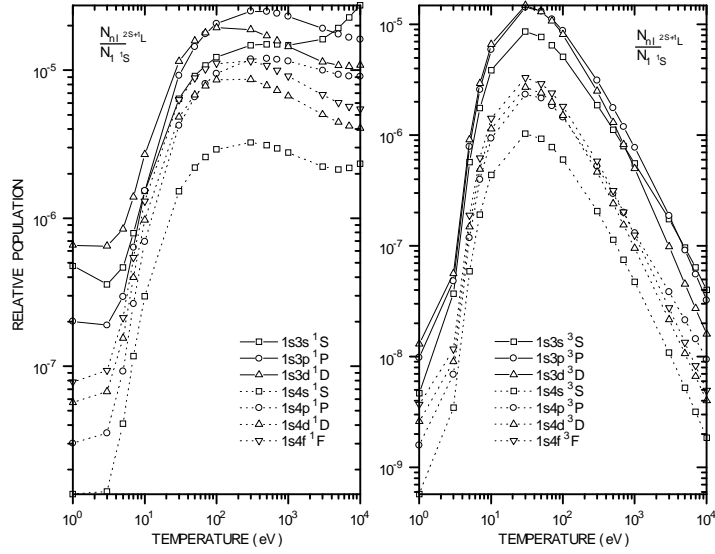


Figure 6.19 Temperature dependence of the quasi-static excited population of the singlet and triplet spin system relative to the He(1^1S) ground state for a D^+ plasma. The electron density was $1.0 \times 10^{13} \text{ cm}^{-3}$ and the neutral beam energy was 5.0 keV amu^{-1} .

As can be observed, the population structure of the triplet spin system is strongly dependent on the electron temperature. This is because the excited states of the triplet spin system can only be populated by electrons collisions via direct spin changing excitation from the ground or via spin changing transitions from the excited states of the singlet spin system. The singlet excited states can be populated by both electrons and ion collisions and the dependency of the electron temperature is somewhat less. These observations reflect the character of the electron impact excitation rates involved[86]. In terms of the upsilon parameters, these (asymptotic) behaviours are,

$$\text{Dipole allowed} \quad : \quad \gamma_{ij} \sim \text{constant} \cdot \ln(T_e) \quad 6.10$$

$$\text{Non Dipole} \quad : \quad \gamma_{ij} \sim \text{constant} \quad 6.11$$

$$\text{Spin changing} \quad : \quad \gamma_{ij} \sim \text{constant} / T_e^2 \quad 6.12$$

For example in the case of the triplet spin system, see figure 6.19, as we increase the electron temperature the rise and decay of the excited state populations directly

reflect the behaviour of the underlying spin changing electron excitation rates. In figure 6.20 we now show the temperature dependence of the singlet and triplet excited population structure relative to the He(2^1S) and He(2^3S) metastables, where a similar parameter dependence can be observed.

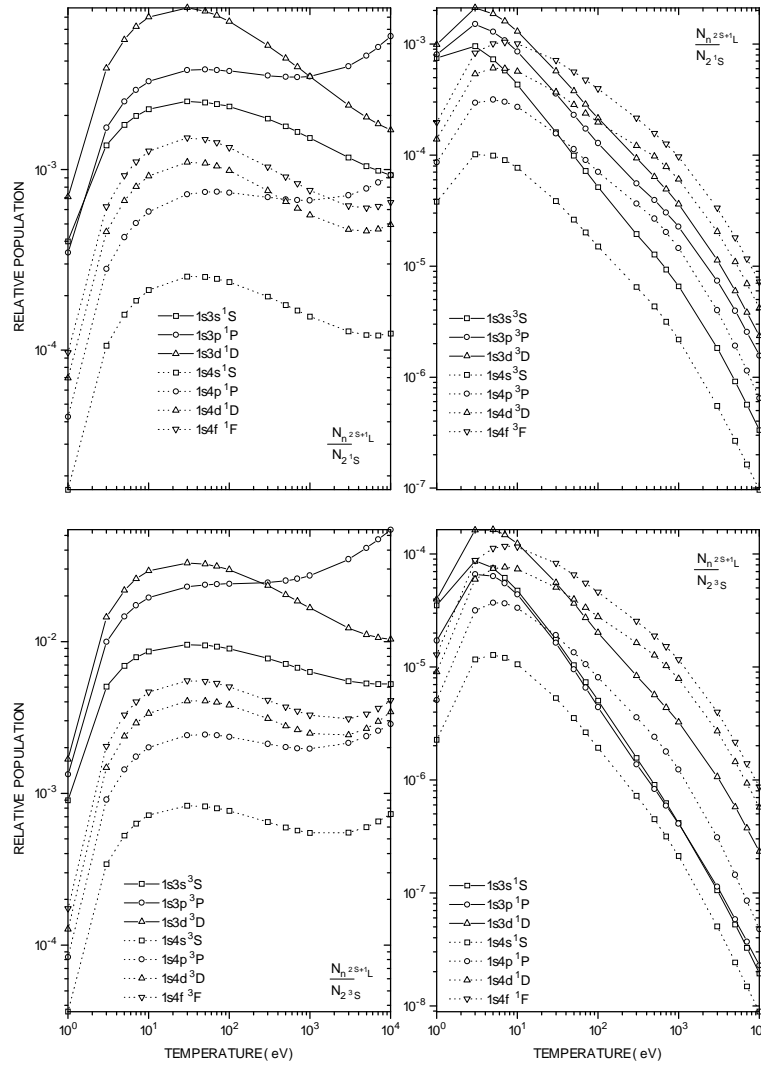


Figure 6.20 Temperature dependence of the quasi-static equilibrium populations of the singlet and triplet spin systems relative to the He(2^1S) and He(2^3S) metastable levels for a D^+ plasma. The electron density was $1.0 \times 10^{13} \text{ cm}^{-3}$ and the neutral beam energy was 5.0 keV amu^{-1} .

6.4.4 Comparison of the role of the metastable levels

In this sub-section, we summarise the relative importance of the metastables in driving the population structure. We confine our study to the levels contained within the $n=4$ shell. In figure 6.21 we show the energy dependence of the quasi-static populations of each level contained within the $n=4$ shell, relative to the ground state and the two metastable levels for a D^+ plasma. By this we mean the contribution functions (FI, FII and FIII) given by equation 3.52. For the singlet spin system it can be seen that the $He(2^1S)$ metastable is as expected most effective in populating the excited levels within the $n=4$ shell. It can also be observed that there is a competition between the relative effectiveness of the $He(2^3S)$ metastable and the $He(1^1S)$ ground state. If we consider the population of the $He(4^1S)$ level, we observed that in the low energy regime the contributions from the ground state and the $He(2^3S)$ metastable are comparable. However as the beam energy increases the contribution from the $He(1^1S)$ exceeds that from the $He(2^3S)$ metastable. This is simply due to the fact that the influence of the ion collisions on the singlet spin system is to reduce the $He(2^3S)$ population's relative importance. If we now study the $He(4^1P)$ level, in the low energy regime the contribution from the $He(2^3S)$ metastable is now greater than that from the $He(1^1S)$ ground state, but as the beam energy increases the effectiveness of the $He(2^3S)$ metastable decreases and the contribution from the $He(1^1S)$ dominates. The difference though between the ground state and the triplet metastable, in the high energy regime, is considerably less than that for the $He(4^1S)$ level. In the case of the $He(4^1D)$ and $He(4^1F)$ levels, a similar behaviour in the low energy regime can be observed where the contribution from the $He(2^3S)$ metastable exceeds that from the $He(1^1S)$ ground state. However in the high energy regime the contribution from the $He(2^3S)$ metastable is now greater than that from the ground state. This is quite different from what was observed for the $He(4^1S)$ and $He(4^1P)$ levels.

Focusing now on the population structure of the triplet spin system we see that the $He(2^3S)$ metastable is the dominant non-equilibrium level for populating the excited states contained within the $n=4$ shell. The contribution from the $He(2^1S)$

metastable is considerably less but greater than the contribution from the He(1^1S) ground state.

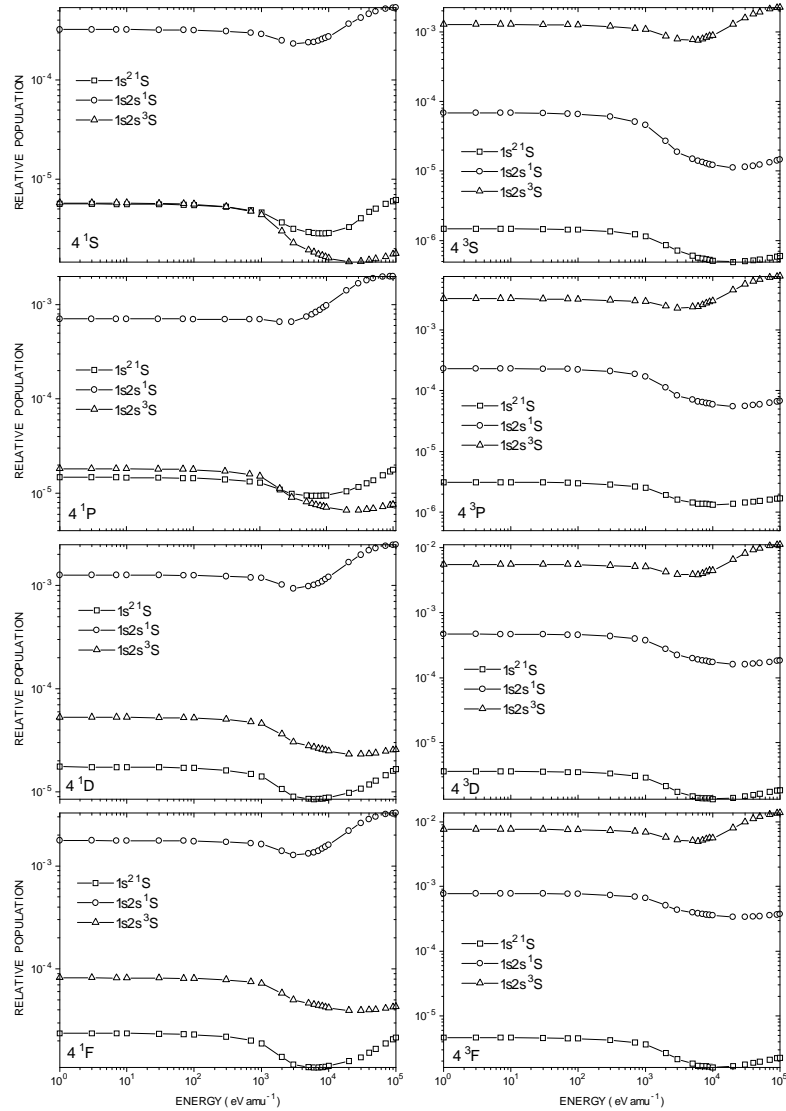


Figure 6.21 Quasi static equilibrium populations of each of the levels contained within the $n=4$ shell, relative to the ground state and each metastable level for a D^+ plasma. The plots contained in the column to the left concerns the singlet spin system while column to the right involves the triplet spin system. The electron density was $1.0 \times 10^{13} \text{ cm}^{-3}$ and the electron temperature was 100 eV.

In figure 6.22 we now show the density dependence of the quasi-static populations of the levels contained within the $n=4$ shell, relative to the ground state and the two metastable levels for a pure D^+ plasma.

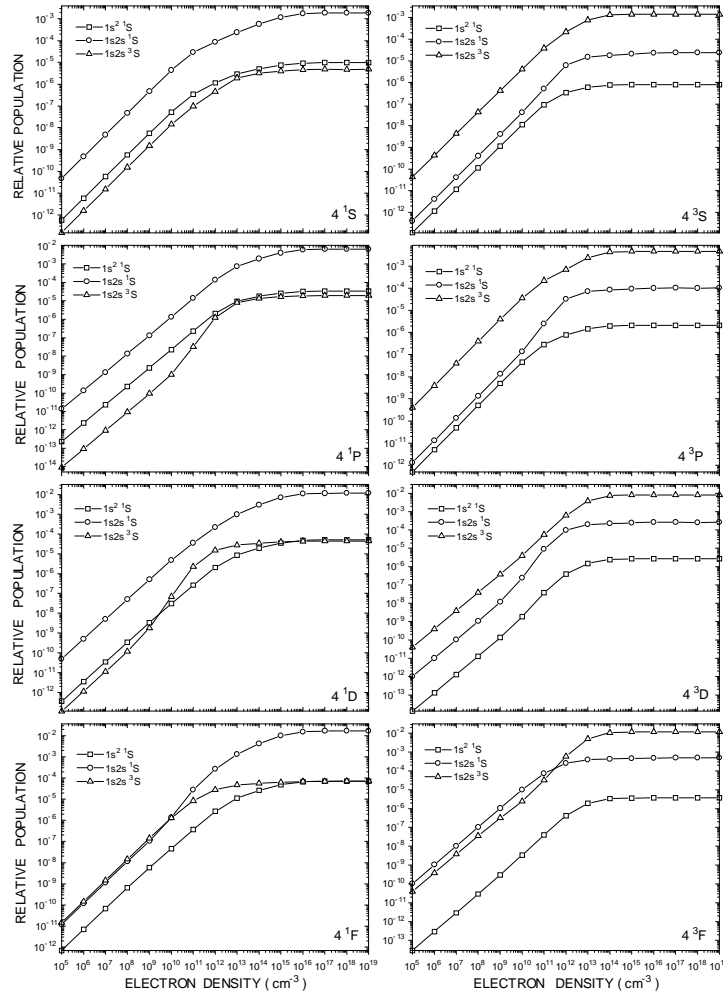


Figure 6.22 Density dependence of the equilibrium populations of the levels contained within the $n=4$ shell, relative to the ground state and each metastable for a pure D^+ plasma. The electron density was $1.0 \times 10^{13} \text{ cm}^{-3}$ and the beam energy was 5.0 keV amu^{-1} .

Starting first with the excited populations of the singlet spin system. If we consider the $\text{He}(4^1S)$ level, it can be seen that the contribution from the $\text{He}(2^1S)$ metastable

dominates that from the ground state, which is considerably greater than the contribution from the He(2 ³S) metastable. The He(4 ¹P) level exhibits a similar behaviour but we can see the onset of a competition between the contribution from the ground state and the triplet metastable, particular at high densities. This competition is more evident in the case of the He(4 ¹D) level where the contribution due to the He(2 ³S) metastable temporarily exceeds that from the ground state. In the case of the He(4 ¹F) level we can observe that in the low density region the contribution due to the He(2 ³S) level is even greater than the contribution from the He(2 ¹S) metastable. However as the electron density is increased the situation changes.

Similar observation can be made with the populations of the n=4 shell of the triplet spin system. For the He(4 ³S) level the dominant contribution is due to He(2 ³S) metastable and the contribution from the He(2 ¹S) level is considerably less but not as small as that from the He(1 ¹S) ground state. However as we study the He(4 ¹P) level the onset of the competition between the He(1 ¹S) and the He(2 ¹S) can be observed. This competition continues and for the He(4 ¹F), in the low density regime, the contribution from the He(2 ¹S) metastable even exceeds that from the He(2 ³S) metastable. As the electron density is increased the He(2 ³S) metastable begins to dominate once again.

We now consider the temperature dependence of the quasi-static population of the levels contained within the n=4 shell, relative to the ground and the two metastable levels for a pure D⁺ plasma, see figure 6.23. It can be seen that for the singlet spin system, the dominant non-equilibrium level which is most effective at populating the excited levels is the He(2 ¹S) metastable. It can also be observed that there is a competition between the contributions from the He(1 ¹S) ground state and the He(2 ³S) metastable level. In the case of all of the excited levels, at relatively low temperatures the contribution due to the He(2 ³S) metastable exceeds that from the He(1 ¹S) ground state. However as the temperature increases the opposite occurs and the contribution from the He(1 ¹S) ground state is now greater than that from the He(2 ³S) metastable. This type of behaviour is simply due to the temperature dependence of the electron collisions as mentioned earlier.

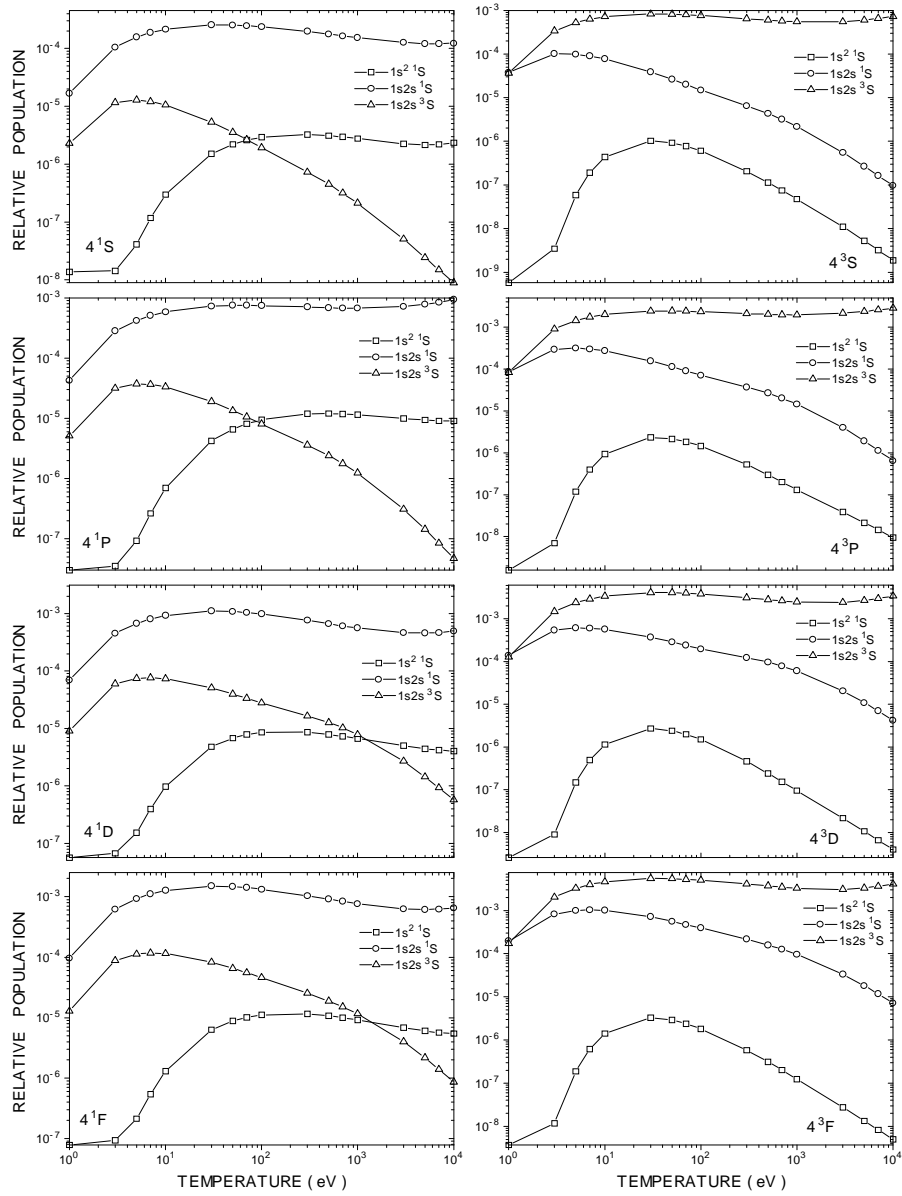


Figure 6.23 Temperature dependence of the quasi static population of the levels contained within the $n=4$ shell, relative to the ground state and each metastable level for a pure D^+ plasma. The plots contained in the column on the left concern the singlet spin system while the column on the right pertains to the triplet spin system. The electron density was $1.0 \times 10^{13} \text{ cm}^{-3}$ and the neutral beam energy was 5.0 keV amu^{-1} .

6.4.5 The influence of impurities

Due to the presence of impurities in tokamak plasmas we examine their differential influence on the excited population structure of the beam atoms. We show in figure 6.24 the excited population structure of the singlet spin system relative to the He(1^1S) ground state for a pure D^+ , He^{2+} and C^{6+} plasma.

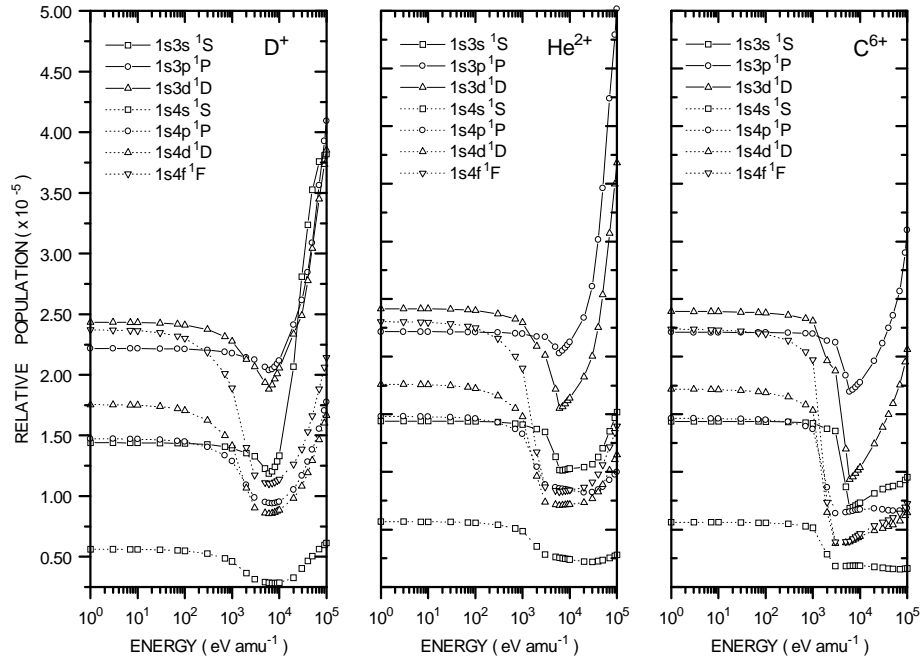


Figure 6.24 Quasi static equilibrium population structure for the singlet spin system relative to the He(1^1S) ground state. Working from left to right we show the population structure for a pure D^+ , He^{2+} and then C^{6+} plasma. The beam energy was 5.0 keV amu^{-1} and the electron density was fixed at $1.0 \times 10^{13} \text{ cm}^{-3}$. The number density of impurity ions is such that charge neutrality is maintained.

If we first confine ourselves to the population structure associated with the beam atoms for a pure D^+ plasma. As mentioned before, we can observe that in low energy regime the population of each level is independent of the beam energy and the contribution due to thermal ion collisions is insignificant. If we now consider the population structure of the beam atoms for a pure He^{2+} plasma. In the low energy regime the small contribution from the ion collisions, due to their thermal velocity, is now larger. As the beam energy is increased the efficiency of the He^{2+} ions at depopulating the excited levels can clearly be observed. We emphasise at this point

that the excited populations are calculated in terms of the electron density, even though it is in fact the ions which are primarily responsible for the collisional redistribution and ionisation of the excited levels. For a fixed electron density the number density of impurity ions is such that charge neutrality is achieved. Therefore with reference to the results shown in figure 6.24, there are twice as many D^+ ions which contribute to modifying the excited population structure than He^{2+} ions. Finally, we consider the population structure of the beam atoms for a pure C^{6+} plasma. The most salient feature which can be seen is the extent to which the excited levels are depopulated due to the influence of ion impact ionisation.

We now consider the excited population structure of the triplet spin system for a pure D^+ , He^{2+} and C^{6+} plasma, see figure 6.25.

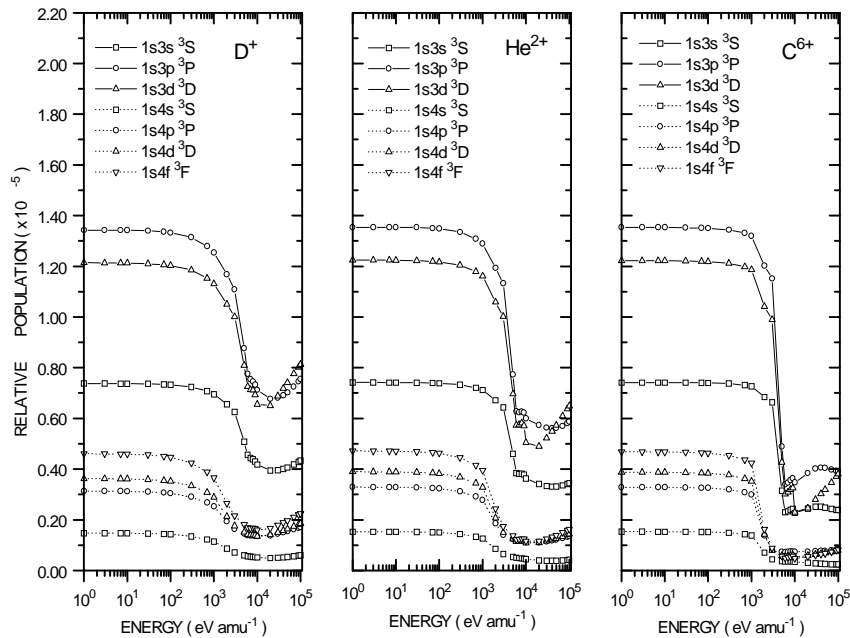


Figure 6.25 Quasi static equilibrium population structure for the triplet spin system relative to the $He(1^1S)$ ground state. Working from left to right we show the population structure for a pure D^+ , He^{2+} and then C^{6+} plasma. The beam energy was 5.0 keV amu^{-1} and the electron density was fixed at $1.0 \times 10^{13} \text{ cm}^{-3}$. The number density of impurity ions is such that charge neutrality is maintained.

In the low energy regime electrons are responsible for populating the excited levels, therefore the excited populations are independent of the neutral beam energy and there is no contribution due to thermal ion collisions. The secondary influence of the

beam energy on the population structure of the triplet spin system can clearly be observed. As the nuclear charge of the plasma impurity ion increases their influence on the triplet spin system is enhanced. In the present work we only considered pure D^+ , He^{2+} and C^{6+} plasmas but similar observations can be seen when considering other pure or mixed impurity plasmas.

6.5 Evolution of the metastable populations under JET conditions

If we neglect the metastable nature of the $He(2^1S)$ and $He(2^3S)$ levels, then the quasi-equilibrium model would provide the whole population structure including the metastable populations, relative to the ground state. There would be no need to consider the spatial history of each metastable and the attenuation of the beam as a whole would be characterised by only one collisional-radiative coefficient. However in working plasmas the metastables do not reach equilibrium. In this section we calculate the $He(2^1S)$ and $He(2^3S)$ metastable populations and contrast with the non-equilibrium metastable populations in an actual beam model. We explore the attenuation of the neutral helium beam and the influence of altering the initial metastable content on entry to the plasma. Finally, we investigate the influence of the electron density and temperature profiles on the beam attenuation.

6.5.1 Method of calculation

We seek the solution of the coupled equations for the metastable and ground state population evolution as the beam traverses the plasma. As discussed earlier we construct the set of such equations using collisional-radiative cross coupling coefficients,

$$\begin{aligned}
v_b \frac{dN_{1^1S}}{dx} &= n_e S_{1^1S} N_{1^1S} - n_e S_{2^1S \rightarrow 1^1S} N_{2^1S} - n_e S_{2^3S \rightarrow 1^1S} N_{2^3S} \\
v_b \frac{dN_{2^1S}}{dx} &= -n_e S_{1^1S \rightarrow 2^1S} N_{1^1S} + n_e S_{2^1S} N_{2^1S} - n_e S_{2^3S \rightarrow 2^1S} N_{2^3S} \\
v_b \frac{dN_{2^3S}}{dx} &= -n_e S_{1^1S \rightarrow 2^3S} N_{1^1S} - n_e S_{2^1S \rightarrow 2^3S} N_{2^1S} + n_e S_{2^3S} N_{2^3S}
\end{aligned} \tag{6.13}$$

We solve for both the metastable and ground state populations relative to the neutral beam density on entry to the plasma. The initial neutral beam density is given by the sum of the ground state and metastable populations. For the quasi-static equilibrium metastable populations the equations reduce to the form,

$$\begin{aligned}
v_b \frac{dN_{1^1S}}{dx} &= n_e S_{1^1S} N_{1^1S} - n_e S_{2^1S \rightarrow 1^1S} N_{2^1S} - n_e S_{2^3S \rightarrow 1^1S} N_{2^3S} \\
0 &= -n_e S_{1^1S \rightarrow 2^1S} N_{1^1S} + n_e S_{2^1S} N_{2^1S} - n_e S_{2^3S \rightarrow 2^1S} N_{2^3S} \\
0 &= -n_e S_{1^1S \rightarrow 2^3S} N_{1^1S} - n_e S_{2^1S \rightarrow 2^3S} N_{2^1S} + n_e S_{2^3S} N_{2^3S}
\end{aligned} \tag{6.14}$$

The quasi-static equilibrium population of the He(2 ¹S) and He(2 ³S) metastable levels are calculated relative to the He(1 ¹S) ground state.

For this work we have written a FORTRAN program which implements the fourth-order Runge-Kutta method to integrate the coupled equations. In addition to solving the equations for the local metastable populations, the program also calculates the corresponding quasi-static equilibrium populations. This enables us to compare the quasi-static populations with the results obtained from our spatially dependent treatment. The program also calculates the attenuation of each metastable including the ground state as a function of radial position. This is useful since it allows one to make an assessment on whether the population of the metastables are significant as the beam continues into the plasma. The main parameters which the program requires as input include the beam energy, the fractional metastable and ground state content of the beam on entry to the plasma, as well as suitable electron density and temperature profiles. A schematic illustration of the program is shown in figure 6.26. The program solves the coupled equations while moving in small increments along a spatial grid, the beginning and end of the grid is defined by the electron density profile. The size of the increments, dx , was selected after running the program several times to obtain a step size which was small enough to ensure numerical convergence but without hugely increasing the computational time of the calculation. In addition to evaluating the coupling coefficients at fixed points along

the grid, the fourth order Runge-Kutta method requires coupling coefficients at intermediate points between the fixed step sizes. The program employs several ADAS library routines to implement the linear interpolation method, see chapter 4.0, to assemble the required coefficients at any point along the working grid.

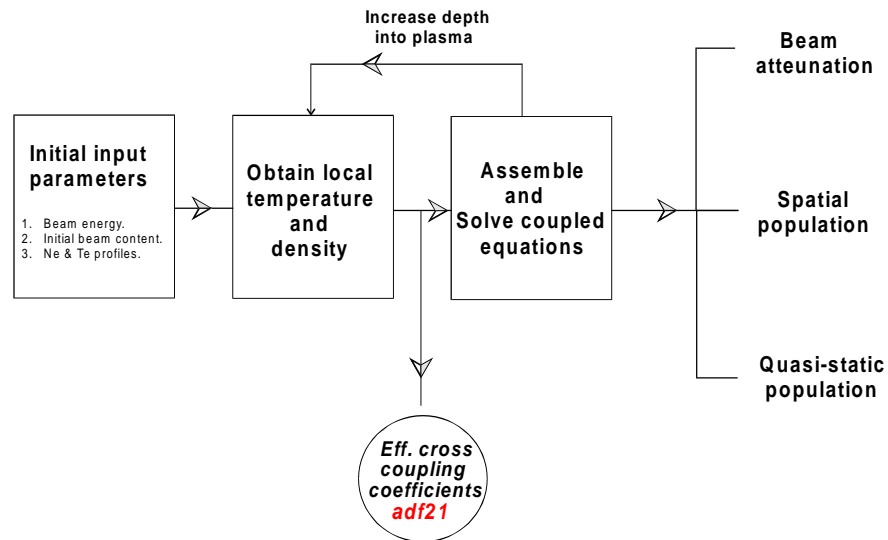


Figure 6.26 Schematic illustration of the FORTRAN program employed to solve the coupled equations which describe the evolution of the ground state and metastable populations. As input the program requires the beam energy, the fractional metastable and ground state content on entry to the plasma, as well as suitable electron density and temperature profiles.

In this study the electron density and temperature profiles, which are used were based on profiles obtained from JET for the pulse number 42676. These can be observed in figure 6.27. Due to the irregular nature of each profile we have fitted 7th order polynomials to each of them using a commercial graph plotting package. This enables us to use the polynomials to look up the electron density and temperature as a function of radial position efficiently. We have also assumed that the plasma for which the model profiles correspond to is of pure deuterium.

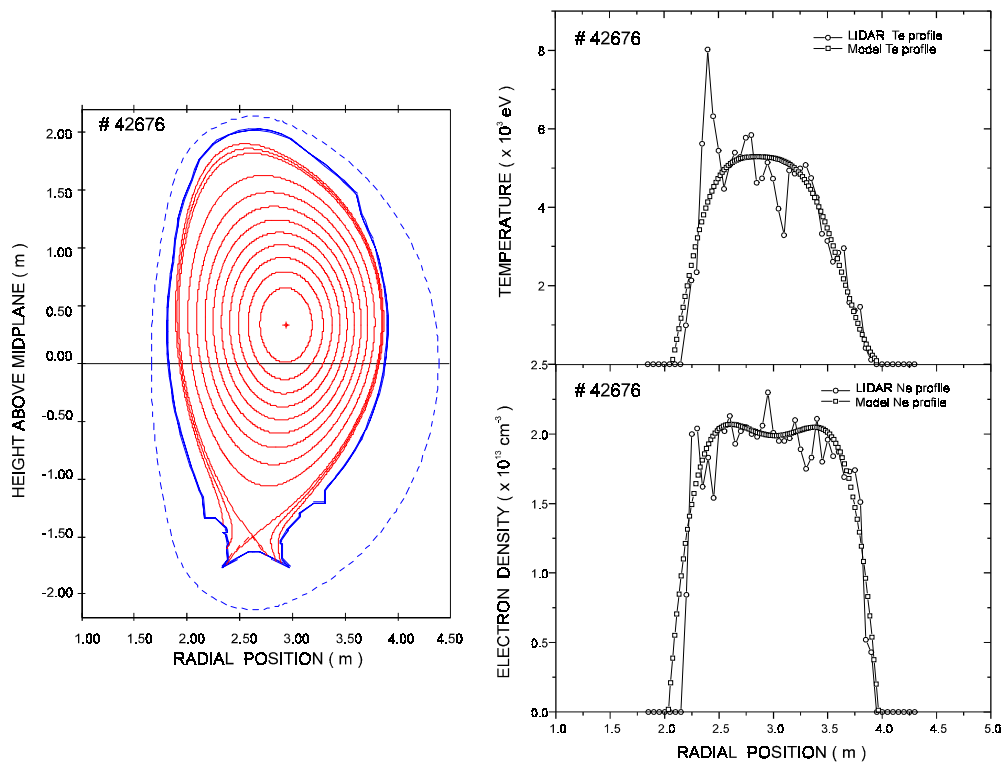


Figure 6.27 Composite figure illustrating the electron density and temperature profiles for the JET pulse 42676. To the left is a schematic of the side elevation of the vessel and should be used as a reference for the radial positions associated with both profiles shown on the right. We have fitted the density and temperature profiles with 7th order polynomials. The motivation for this was to eliminate the irregular structure associated with each profile, also it provided a means of being able to look up the density and temperature as a function of radial position efficiently.

6.5.2 Metastable population : Quasi-static Vs Spatial solution

In working plasmas the scaled lengths (see chapter 2.0) for the electron density and temperature are very short which prevents the metastables reaching equilibrium. In this sub-section we compare the metastable populations from the quasi-static equilibrium model with those of the spatially dependent treatment.

Figure 6.28 shows the population of the He(2 ¹S) level relative to the ground state for the case of no metastable content on entry to the plasma.

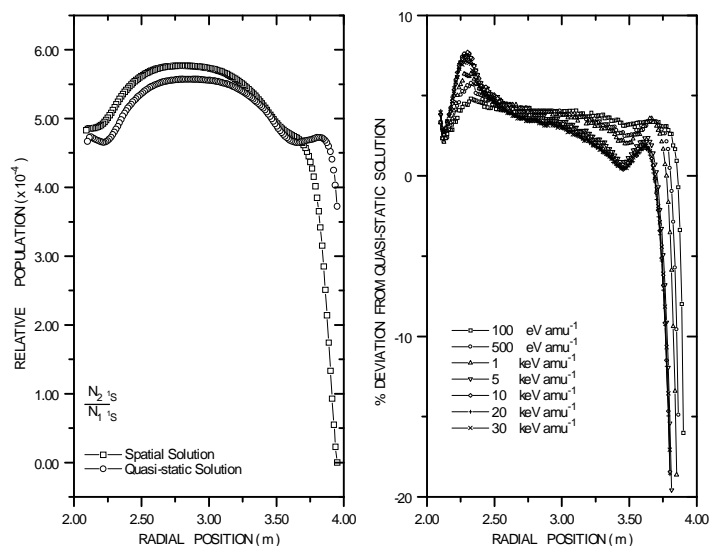


Figure 6.28 Comparison between spatially dependent and quasi-static equilibrium solution for the He(2 ¹S) population relative to the ground state. The plot on the left illustrates the behaviour of the quasi-static and spatially dependent He(2 ¹S) population for a fixed beam energy of 30 keV amu⁻¹. While the plot on the right shows the percentage deviation of the spatial dependent results from that obtained from the quasi-static assumption for a range of beam energies. On entry to the plasma the total metastable content was zero.

As can be observed there is a significant difference between the results obtained from quasi-static and spatially dependent treatment. This difference is greatest near the edge of the plasma where the scaled lengths for the electron density and temperature are very small, see plot on the left in figure 6.28. If we now consider the results from the core of the plasma around ~ 2.75 m, the difference between the quasi-static picture and the spatial dependent treatment is considerably less. Similar observations can be made from the plot on the right in figure 6.28, where we show the percentage deviation of the spatial dependent results from that obtained from the quasi-static solution for a range of beam energies. Regardless of the beam energy the maximum difference between the quasi-static results and the spatial treatment occurs at the edge of the plasma. In the core of the plasma the He(2 ¹S) population does appear to be approaching equilibrium, but does not quite make it within the time scale on which the electron density and temperature change. We can also see from the plot on the left in figure 6.28 the increase in the He(2 ¹S) metastable population. Initially the He(2

$^1S)$ is zero, however as the beam enters into the plasma, electron and ion impact excitation contributes to populating the $He(2^1S)$ level.

We show the $He(2^3S)$ population relative to the ground state. In figure 6.29 the plot to the left shows a comparison between the results obtained from the quasi-static and spatially dependent solution, while the plot on the right shows the percentage deviation of the spatially dependent treatment from that of the quasi-static solution for a range of beam energies.

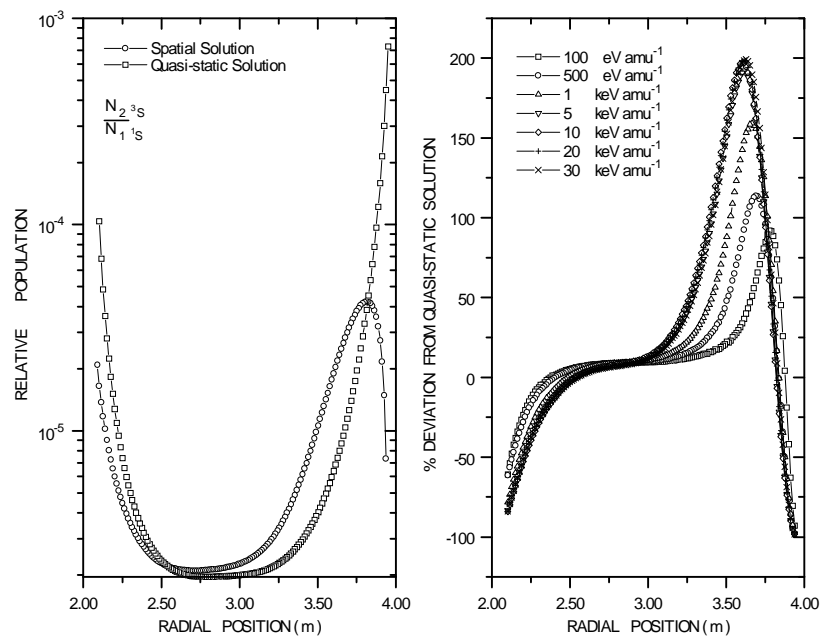


Figure 6.29 Comparison between the quasi-static equilibrium and spatially dependent treatment for the $He(2^3S)$ population relative to the ground state. The plot to the left illustrates the behaviour of quasi-static and spatial dependent $He(2^3S)$ population for a fixed beam energy of $30 \text{ keV } amu^{-1}$. The plot to the right shows the percentage deviation of the spatially dependent results from that obtained from the quasi-static assumption. The total metastable content of the beam on entry to the plasma was set to zero.

It can be observed from the spatially dependent solution, shown in the plot on the left in figure 6.29, that as the beam enters the plasma the $He(2^3S)$ metastable is rapidly populated. This arises due to the fact that the temperature for the first few centimetres into the plasma is optimum (10~200 eV) to promote the influence of spin changing electron collisions, which are the only processes which can populate

the He(2^3S) metastable level from the ground state. However as the beam continues into the plasma the contribution to the He(2^3S) level decreases as the electron temperature increases. Above electron temperatures of around ~ 2 keV the contribution due to electron collisions is very small. This prevents the He(2^3S) metastable population from continuing to increase. As the beam approaches the inner edge of the plasma the spin changing electron collisions become important once again and the He(2^3S) metastable population increases.

In figure 6.30 we show the quasi-static and spatially dependent populations for the He(2^1S) and He(2^3S) metastables, for a beam which initially contains 90 % He(1^1S) and 10 % He(2^3S) on entry to the plasma. Practical experiments on neutral helium beam generation indicate that different neutralisation strategies can yield metastable populations of this order.

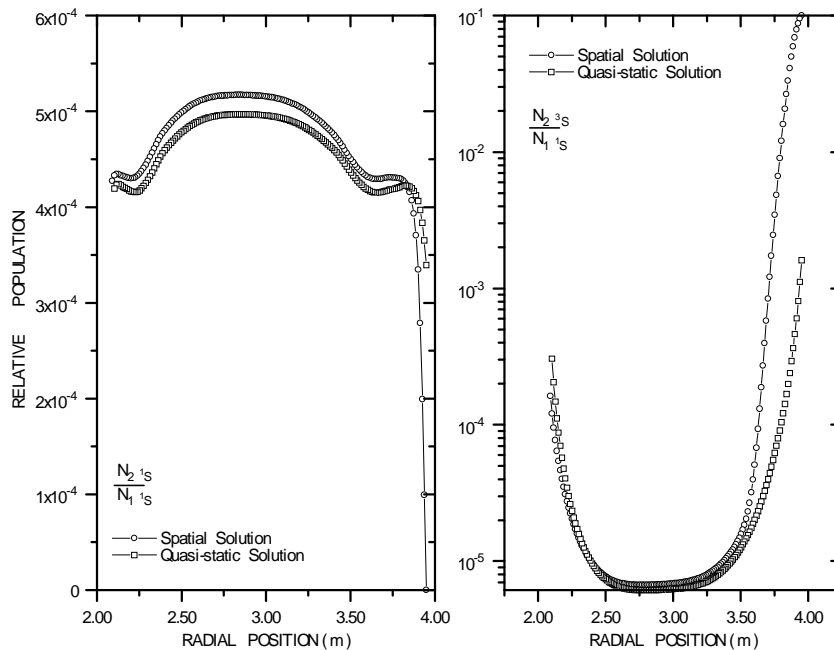


Figure 6.30 Comparison between the quasi-static and spatially dependent populations for the He(2^1S) and He(2^3S) metastables. The plot to the left illustrates the behaviour of the quasi-static and spatially dependent He(2^1S) population. The plot to the right exhibits the behaviour of the quasi-static and spatially dependent population of the He(2^3S) metastable. On entry to the plasma the contents of the beam consisted of 10% He(2^3S) and 90 % He(1^1S).

In the case of the He(2 ¹S) metastable, as the beam penetrates into the plasma the He(2 ¹S) metastable is suddenly populated and follows the same behaviour as the quasi-static population. The He(2 ³S) metastable population on the other hand is strongly attenuated on entry and as the beam approaches the inner edge of the plasma the He(2 ³S) population can be seen to increase. Finally, in figure 6.31 we consider the hypothetical situation where the contents of the beam on entry to the plasma consists of 90 % He(1 ¹S) and 10 % He(2 ¹S), even though it would be difficult to prepare a such beam.

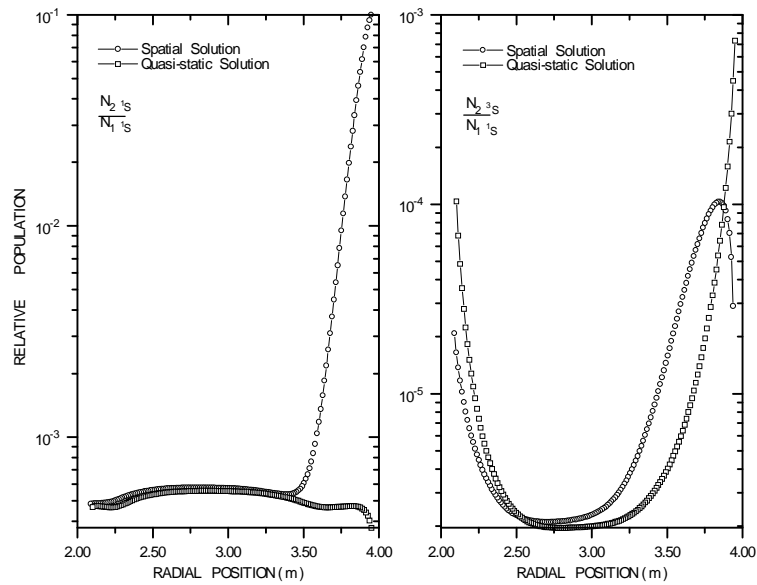


Figure 6.31 Comparison between the quasi-static and spatially dependent populations of the He(2 ¹S) and He(2 ³S) metastables. The plot to the left illustrates the behaviour of quasi-static and spatially dependent He(2 ¹S) population. The plot to the right exhibits the behaviour of the quasi-static and spatially dependent He(2 ³S) population. On entry to the plasma the beam content consists of 10 % He(2 ¹S) and 90 % He(1 ¹S).

As can be observed the He(2 ¹S) is strongly depopulated as the beam penetrates into the plasma. The He(2 ³S) population exhibits the usual temperature dependence where the population rises at the edge, decrease at the core, and then rises again at the inner edge of the plasma. It is clear that regardless of the initial metastable content in the beam the differences between the metastable populations obtained using the quasi-static approximation and the more accurate spatial dependent treatment is substantial.

6.5.3 Attenuation of a neutral helium beam

In this sub-section we investigate the absolute attenuation of the ground state and metastable levels of a neutral helium beam. We wish to assess if the absolute population of the metastables survive or are regenerated sufficiently for them to act as strong charge exchange donors. This would enable the experimental study of preferential charge exchange donation from the ground state and the metastables levels (c.f. C^{6+} and He^{2+} receivers [85])

The results for zero metastable content on entry into the plasma can be seen in figure 6.32 where we show the attenuation of the $He(1^1S)$ ground state for a range of beam energies. In the present work, the attenuation of each metastable, including the ground state, is expressed in terms of the corresponding local value relative to the total beam density on entry to the plasma. The total beam density on entry to the plasma is the sum of the ground state and metastable populations.

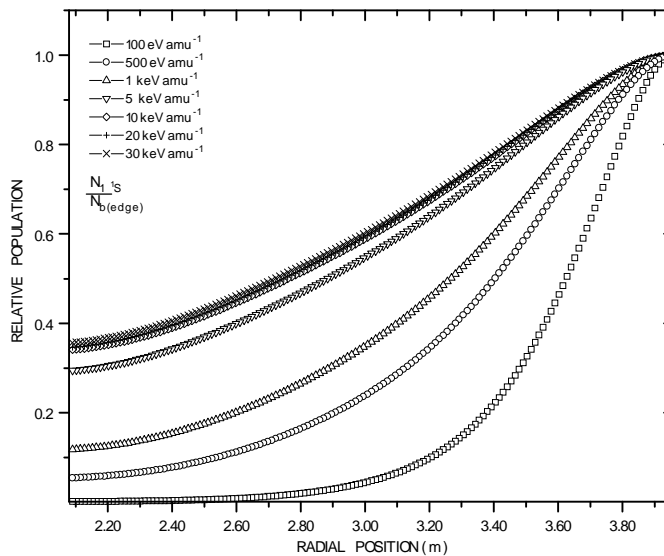


Figure 6.32 Attenuation of the $He(1^1S)$ ground state for a range of beam energies. The initial metastable content of the beam was set to zero. The electron and temperature profiles used are shown in figure 6.27.

As shown in figure 6.32, for a relatively slow beam it is strongly attenuated at the edge of the plasma. As we increase the beam energy the attenuation of the ground

state population becomes less and for a beam of 30 keV amu⁻¹ a total shine through of approximately 36 % is achieved. We show in figure 6.33 the behaviour of the He(2 ¹S) and He(2 ³S) populations as a function of radial position relative to the initial beam density on entry to the plasma.

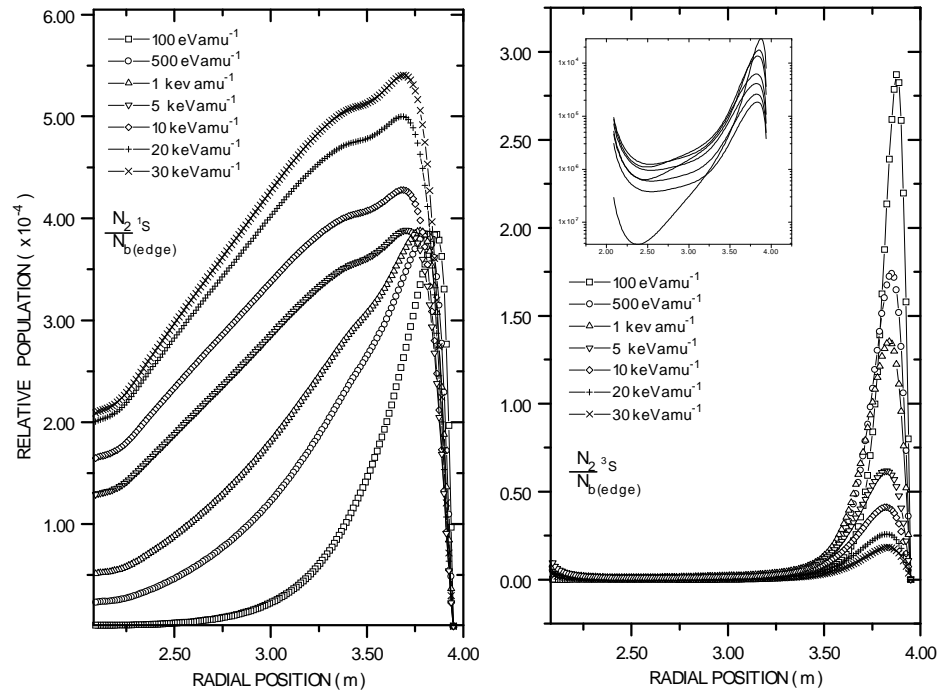


Figure 6.33 Attenuation of the He(2 ¹S) and He(2 ³S) metastable levels. The electron density and temperature profiles used are shown in figure 6.27. It is interesting to note that the initial metastable population was zero on entry to the plasma. Therefore it is clear that there is a sudden rise in the both the He(2 ¹S) and He(2 ³S) populations at the edge of the plasma.

If we confine ourselves with the behaviour of the He(2 ¹S) metastable which can be seen in the plot on the left in figure 6.33, as the beam enters into the plasma the He(2 ¹S) level is suddenly populated and then slowly decays as the beam penetrates through the plasma. For a slow beam the He(2 ¹S) metastable is attenuated relatively quickly. The behaviour of the He(2 ³S) metastable is shown in the plot to the right in figure 6.33. As with the He(2 ¹S) level we can also see a similar increase in the He(2 ³S) level as the beam just enters into the plasma. As the beam continues into the plasma the He(2 ³S) population is attenuated very rapidly. At the inner edge of the

plasma we can observe that the He(2 ³S) population begins to increase again. This is also shown in the insert contained in the plot shown in figure 6.33. The behaviour of the He(2 ³S) metastable directly reflects the strong temperature dependence of the electron collisions, see section 6.4.1.

In figure 6.33 the populations of each metastable are well below 0.1 % of the initial beam density on entry to the plasma. We question whether it is necessary to take into consideration the influence of the metastables while modelling the attenuation of a beam, for which the metastable content on entry to the plasma is zero. We have tabulated in table 6.1, the percentage of the He(1 ¹S) population, which is attenuated as a function of penetration depth for a range of beam energies. Also shown in a separate table, table 6.2, is the percentage of the He(1 ¹S) population which is attenuated when we now neglect the He(2 ¹S) and He(2 ³S) metastables in the attenuation calculation.

Penetration Depth (m)	Neutral beam energy (keV amu ⁻¹)						
	0.1	0.5	1.0	5.0	10.0	20.0	30.0
0.25	36.47	18.88	14.24	8.44	7.46	7.20	7.43
0.50	72.93	45.23	35.72	22.37	19.96	19.24	19.79
0.75	89.90	65.15	53.88	35.81	32.27	31.16	31.94
1.00	96.24	77.93	67.01	47.02	42.78	41.42	42.36
1.25	98.63	86.12	76.53	56.51	51.80	50.28	51.31
1.50	99.52	91.49	83.61	64.51	59.76	58.16	59.24
1.75	99.78	94.08	87.44	69.52	64.81	63.21	64.31

Table 6.1 Helium beam attenuation for which the initial metastable content was set to zero. The tables contain the percentage of the beam which is attenuated as function of penetration depth for a range of beam energies.

Penetration Depth (m)	Neutral beam energy (keV amu ⁻¹)						
	0.1	0.5	1.0	5.0	10.0	20.0	30.0
0.25	36.46	18.86	14.21	8.40	7.43	7.11	7.31
0.50	72.93	45.23	35.71	22.35	19.94	19.19	19.72
0.75	89.90	65.16	53.87	35.79	32.26	31.17	31.97
1.00	96.24	77.94	67.01	47.01	42.78	41.47	42.44
1.25	98.70	86.46	76.94	56.84	52.22	50.77	51.86
1.50	99.52	91.51	83.61	64.51	59.77	58.27	59.40
1.75	99.78	94.09	87.45	69.53	64.82	63.30	64.43

Table 6.2 Helium beam attenuation for which the initial metastable content was set to zero. The tables contain the percentage of the beam which is attenuated as function of penetration depth for a range of beam energies. In this case the metastable nature of He(2 ¹S) and He(2 ³S) has been ignored in the attenuation calculation.

The influence of the metastable levels while modelling the beam attenuation is negligible. Therefore if interest is only in determining the total beam density as a function of penetration depth, for a beam in which the initial metastable content on entry to the plasma is zero, we can neglect the metastable levels. The attenuation of the beam can be characterised using a single collisional-radiative ionisation coefficient which describes the loss rate from the ground state. It should be emphasised though that to exploit the beam fully as a diagnostic probe via charge exchange spectroscopy, the detailed knowledge of the metastable populations is still required as the associated charge exchange cross sections are very large.

We now investigate the implications of modifying the metastable content of the beam on entry to the plasma. Figure 6.34 shows the attenuation of the He(1^1S) population for a beam for which the initial contents consists of 90 % He(1^1S) and 10 % He(2^3S).

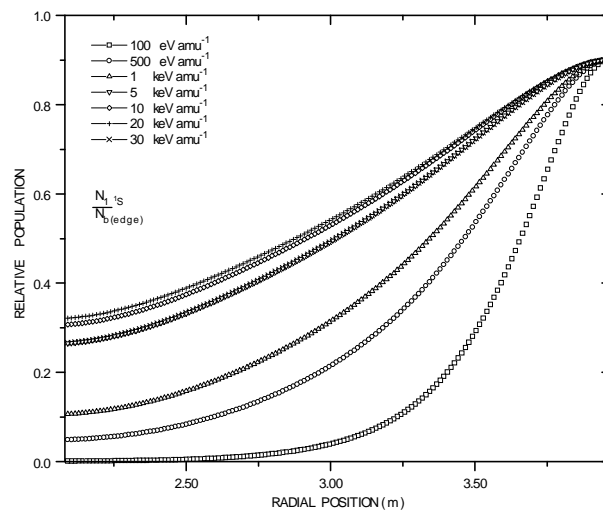


Figure 6.34 Attenuation of the He(1^1S) population. The initial beam content consists of 90 % He(1^1S) and 10% He(2^3S). The electron density and temperature profiles used are shown in figure 6.27.

The attenuation of the He(1^1S) population, as illustrated in figure 6.34, exhibits the same features as shown for the attention of the He(1^1S) ground state for a beam for which the initial metastable content was zero, see figure 6.32. In figure 6.35 we show the attenuation of the He(2^1S) and He(2^3S) metastable levels for the same conditions. The He(2^1S) population exhibits the same features which we highlighted

earlier, namely a sudden increase in the metastable level marking the entry of the beam and then the population decay. The He(2^3S) metastable enters the plasma with a 10 % population, therefore we do not see the sudden rise in the population due to contribution from electron collisions. As the beam penetrates into the plasma we can see the population being strongly attenuated and then near the inner edge of the plasma, the He(2^3S) population begins to rise again, see inset contained in the plot on the right in figure 6.35. Due to the large ionisation coefficient associated with the triplet metastable the attenuation is substantial. For example, the He(2^3S) population for a beam energy of 100 eV amu⁻¹ is attenuated by ~ 55 % within approximately 6 cm of entering the plasma.

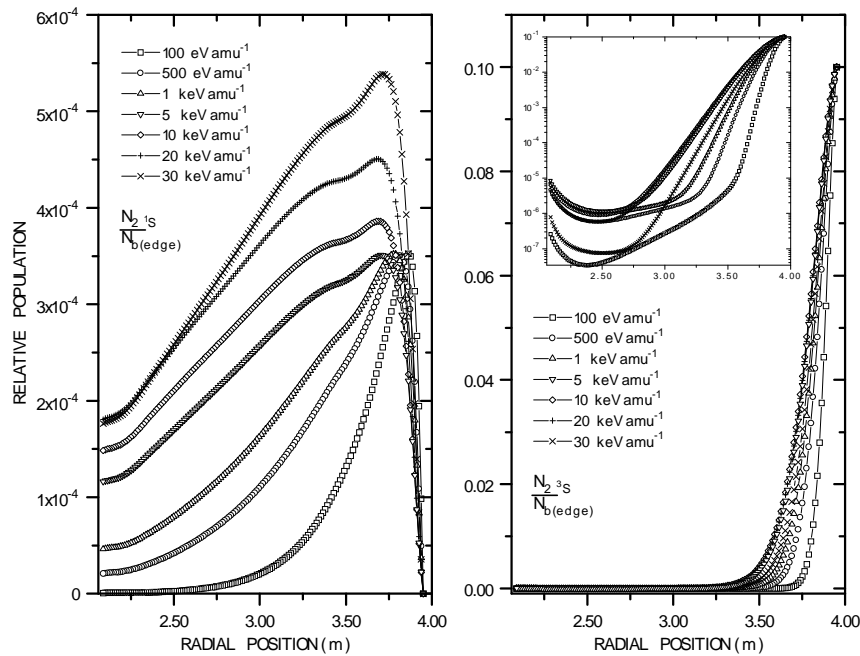


Figure 6.35 Attenuation of the He(2^1S) and He(2^3S) metastable levels. On entry to the plasma the beam content consisted of 10 % He(2^3S) and 90 % He(1^1S). The electron density and temperature profiles used are shown in figure 6.27.

In table 6.3 we have tabulated the percentage of the He(2^3S) metastable population which is attenuated as a function of the penetration depth for a range of beam energies. We have also shown two additional tables (tables 6.4 & 6.5) which illustrate the attenuation of the He(2^3S) metastable as the initial metastable population is increased.

90 % He(1 ¹S) 10 % He(2 ³S)

Penetration Depth (m)	Neutral beam energy (eV amu ⁻¹)						
	100	500	1000	5000	10,000	20,000	30,000
0.0124	6.10	2.90	2.20	1.40	1.30	1.30	1.70
0.0248	14.60	7.20	5.40	3.60	3.40	3.50	4.40
0.0372	24.70	12.50	9.50	6.50	6.20	6.30	8.00
0.0496	35.30	18.60	14.30	9.90	9.50	9.70	12.40
0.0620	45.80	25.20	19.60	13.80	13.20	13.60	17.20

Table 6.3 Attenuation of the He(2 ³S) metastable as a function of penetration depth for a range of beam energies. The tables contain the percentage of the beam which is attenuated as function of penetration depth for a range of beam energies. The initial beam content was 90 % He(1 ¹S) and 10 % He(2 ³S).

80 % He(1 ¹S) 20 % He(2 ³S)

Penetration Depth (m)	Neutral beam energy (eV amu ⁻¹)						
	100	500	1000	5000	10,000	20,000	30,000
0.0124	6.12	2.92	2.18	1.42	1.33	1.33	1.41
0.0248	14.70	7.21	5.45	3.63	3.43	3.47	3.69
0.0372	24.77	12.57	9.58	6.52	6.20	6.31	6.72
0.0496	35.42	18.68	14.38	9.96	9.51	9.72	10.35
0.0620	45.92	25.27	19.66	13.84	13.25	13.56	14.44

Table 6.4 Attenuation of the He(2 ³S) metastable as a function of penetration depth for a range of beam energies. . The tables contain the percentage of the beam which is attenuated as function of penetration depth for a range of beam energies. The initial beam content was of 80 % He(1 ¹S) and 20 % He(2 ³S).

70 % He(1 ¹S) 30 % He(2 ³S)

Penetration Depth (m)	Neutral beam energy (eV amu ⁻¹)						
	100	500	1000	5000	10,000	20,000	30,000
0.0124	6.13	2.92	2.19	1.42	1.33	1.33	1.41
0.0248	14.73	7.22	5.46	3.64	3.43	3.48	3.69
0.0372	24.80	12.59	9.59	6.53	6.20	6.31	6.72
0.0496	35.46	18.70	14.40	9.97	9.51	9.72	10.36
0.0620	45.97	25.29	19.68	13.84	13.26	13.56	14.44

Table 6.5 Attenuation of the He(2 ³S) metastable as a function of penetration depth for a range of beam energies. The tables contain the percentage of the beam which is attenuated as function of penetration depth for a range of beam energies. The initial beam content was 70 % He(1 ¹S) and 30 % He(2 ³S).

In figure 6.36 we show the attenuation of the He(1 ¹S) ground state for a beam with an initial content comprising of 90 % He(1 ¹S) and 10 % He(2 ¹S). It can be seen that the He(1 ¹S) level shows the usual characteristics. However in figure 6.36, we

observe that the He(1^1S) population, within a few centimetres of entering the plasma, exceeds its initial value of 90 % due to the rapid transfer from the He(2^1S) metastable via the He(2^1P). As we increase the beam energy the net contribution from the He(2^1S) metastable to the He(2^1P) level is reduced. This is due to the influence of ion impact ionisation which depopulates the He(2^1S) metastable.

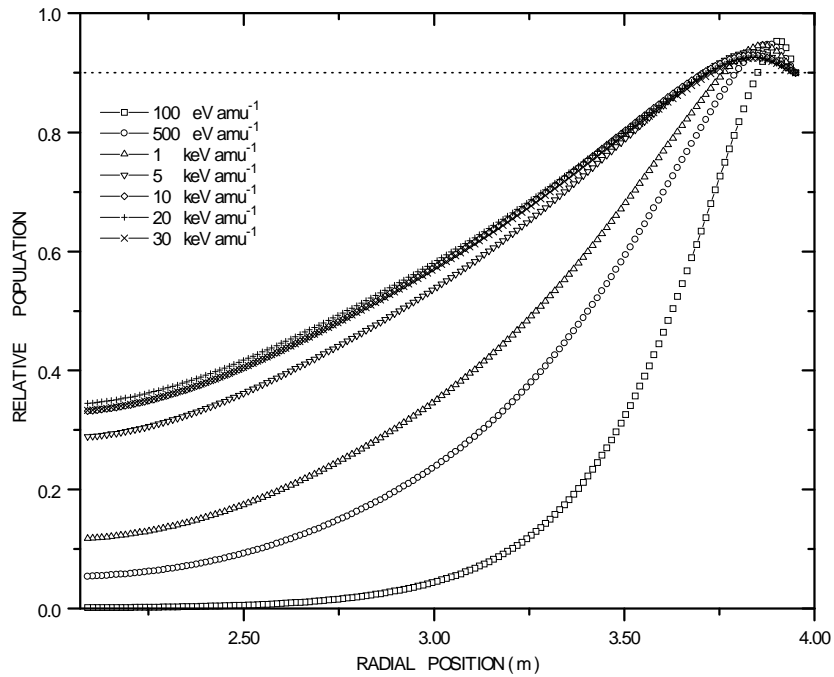


Figure 6.36 Attenuation of the He(1^1S) ground state as a function of radial position for a range of beam energies. The electron and temperature profiles used are that shown in figure 6.27. On entry to the plasma the beam consisted of 10 % He(2^1S) and 90 % He(1^1S).

If we were to increase the initial He(2^1S) metastable population, the contribution to the ground state population would increase. This can be observed in figure 6.37 where we show the behaviour of the He(1^1S) population as a function of radial position for different initial He(2^1S) metastable populations.

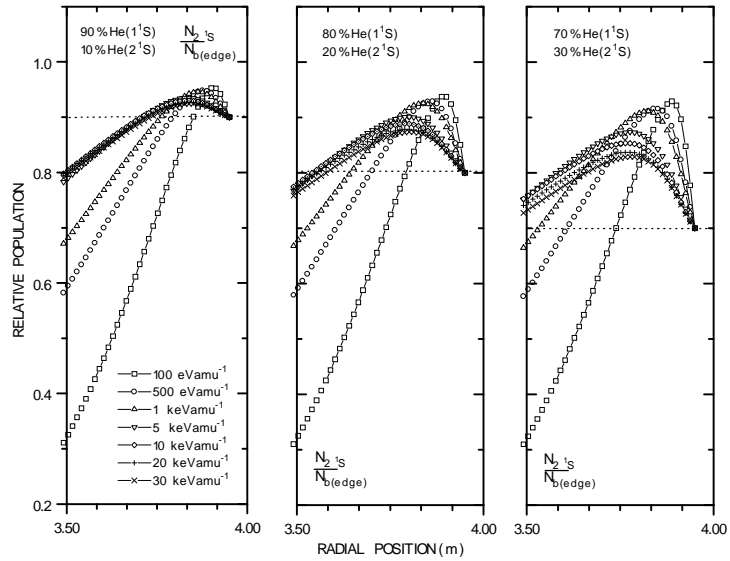


Figure 6.37 Attenuation of the He(1^1S) ground state as a function of radial position for a range of beam energies. From left to right we show the extent of increase the He(2^1S) metastable fraction by 10, 20 and 30 %. The electron and temperature profiles used are that shown in figure 6.27.

In figure 6.38 we now show the attenuation of the He(2^1S) and He(2^3S) metastables

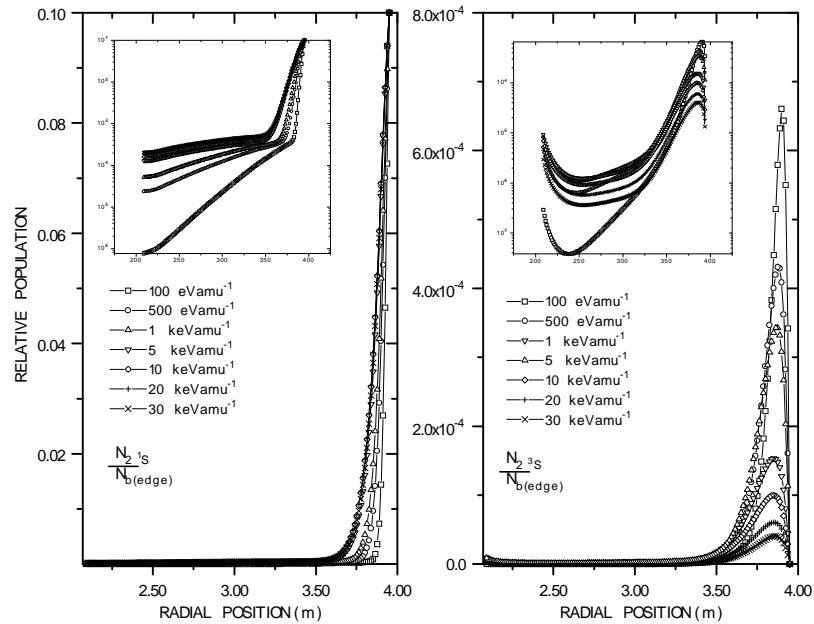


Figure 6.38 Attenuation of the He(2^1S) and He(2^3S) metastable as a function of radial position for a range of beam energies. The initial contents of the beam consisted of 10 % He(2^1S) and 90 % He(1^1S). The electron density and temperature profiles which were used are shown in figure 6.27.

As can be observed, the He(2 ¹S) is also strongly attenuated as the beam enters the plasma. The He(2 ³S) level once again shows the unique rise in population on entry to the plasma and then a decay and then an increase once again. The attenuation of the He(2 ¹S) level is strong and merely reflects the large ionisation coefficient associated with the He(2 ¹S) level. In table 6.6, we have tabulated the percentage of the He(2 ¹S) population which is attenuated as a function of radial position. We have also included two additional tables (tables 6.7 & 6.6) which show similar information but with the initial He(2 ¹S) population increased

90 % He(1 ¹S) 10 % He(2 ¹S)

Penetration Depth (m)	Neutral beam energy (eV amu ⁻¹)						
	100	500	1000	5000	10,000	20,000	30,000
0.0124	27.30	13.80	10.20	6.40	5.90	5.80	6.00
0.0248	53.50	30.00	22.80	14.70	13.60	13.40	14.00
0.0372	73.10	45.70	35.90	23.90	22.10	21.90	22.90
0.0496	85.50	59.60	48.20	33.30	31.00	30.70	32.00
0.0620	92.67	70.80	59.10	42.30	39.60	39.40	40.90

Table 6.6 Attenuation of the He(2 ¹S) metastable level as a function of radial position for a range of beam energies. The tables contain the percentage of the beam which is attenuated as function of penetration depth for a range of beam energies. The initial beam content was 10% He(2 ¹S) and 90% He(1 ¹S).

80 % He(1 ¹S) 20 % He(2 ¹S)

Penetration Depth (m)	Neutral beam energy (eV amu ⁻¹)						
	100	500	1000	5000	10,000	20,000	30,000
0.0124	27.38	13.82	10.24	6.42	5.89	5.79	6.04
0.0248	53.60	30.09	22.84	14.72	13.57	13.41	14.01
0.0372	73.20	45.83	35.94	23.93	22.16	21.96	22.92
0.0496	85.70	59.65	48.50	33.32	31.02	30.81	32.09
0.0620	92.85	70.95	59.25	42.41	39.68	39.46	41.00

Table 6.7 Attenuation of the He(2 ¹S) metastable level as a function of radial position for a range of beam energies. The tables contain the percentage of the beam which is attenuated as function of penetration depth for a range of beam energies. The initial beam content was 20 % He(2 ¹S) and 80 % He(1 ¹S).

70 % He(1 ¹S) 30 % He(2 ¹S)

Penetration Depth (m)	Neutral beam energy (eV amu ⁻¹)						
	100	500	1000	5000	10,000	20,000	30,000
0.0124	27.40	13.83	10.25	6.42	5.90	5.79	6.04
0.0248	53.61	30.04	22.86	14.73	13.58	13.42	14.02
0.0372	73.23	45.85	35.96	23.95	22.18	21.98	22.94
0.0496	85.76	59.70	48.33	33.35	31.04	30.83	32.12
0.0620	92.90	70.96	59.30	42.44	39.71	39.49	41.04

Table 6.8 Attenuation of the He(2 ¹S) metastable level as a function of radial position for a range of beam energies. The tables contain the percentage of the beam which is attenuated as function of penetration depth for a range of beam energies. The initial beam content was 30 % He(2 ¹S) and 70 % He(1 ¹S).

On comparing the results contained in table 6.3 and 6.6, the former of which concerns the attenuation of the He(2 ³S) metastable, we can see that under the present plasma conditions the He(2 ¹S) metastable is attenuated at a greater rate.

Finally, we consider the scenario where both of the metastable levels are populated on entry to the plasma. We show in figure 6.39 the behaviour of both the He(2 ¹S) and He(2 ³S) levels as a function of radial position. The initial content of the beam comprises of 5 % He(2 ¹S), 5 % He(2 ³S) and 90 % He(1 ¹S).

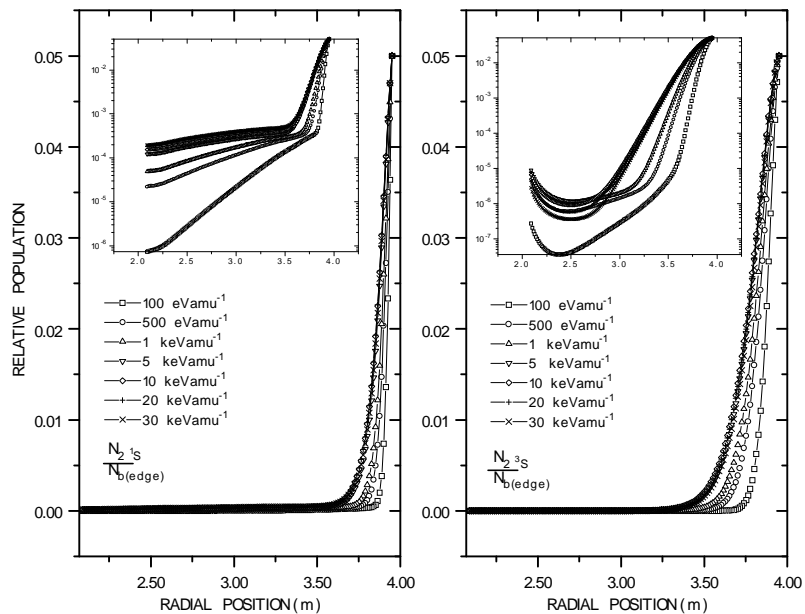


Figure 6.39 Attenuation of the He(2 ¹S) and He(2 ³S) metastable levels . The initial content of the beam consisted of 5 % He(2 ¹S), 5 % He(2 ³S) and 90 % He(1 ¹S). The electron density and temperature profiles can be seen in figure 6.27.

From figure 6.39 we can see that the He(2^1S) metastable is attenuated faster than the He(2^3S) metastable. Both metastables show the typical behaviour as a function of radial position which has been described before.

6.5.4 Additional physics of helium beam attenuation

In tokamak plasma such as JET, fluctuations in the electron temperature and density are common, e.g. see figure 3.27. In this sub-section we explore the influence of such rapid changes on the attenuation of the ground state and the metastable levels. However rather than contrast the beam attenuation using profiles from different types of plasma, we have opted to use theoretical profiles. These profiles have been selected specifically to illustrate the influence due to sudden changes. In our study we only consider the attenuation of a helium beam, for which the initial metastable content on entry to the plasma is zero.

6.5.4.1 Influence of the electron temperature profile

The electron temperature profile which we have selected is sinusoidal in nature and oscillates between a value of 10 eV to 6 keV as a function of radial position. The electron density profile which is employed is as before and can be seen in figure 6.40 together with the hypothetical electron temperature profile.

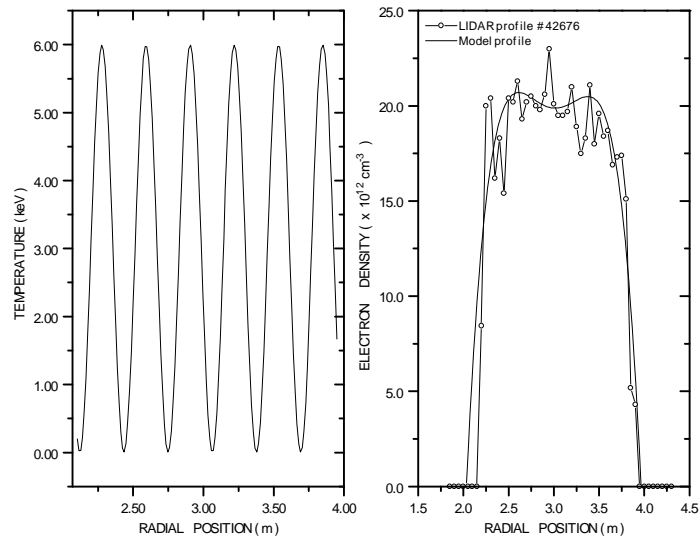


Figure 6.40 Electron temperature and density profile. The temperature profile oscillates between 10 eV and 6 keV. The electron density profile was obtained from the JET pulse 42676, to remove the irregular features we have fitted the profile with a smooth curve.

In figure 3.41 we show the attenuation of $\text{He}(2^1\text{S})$ and $\text{He}(2^3\text{S})$ metastable populations as a function of radial position. The influence of the temperature profile on the $\text{He}(1^1\text{S})$ was negligible.

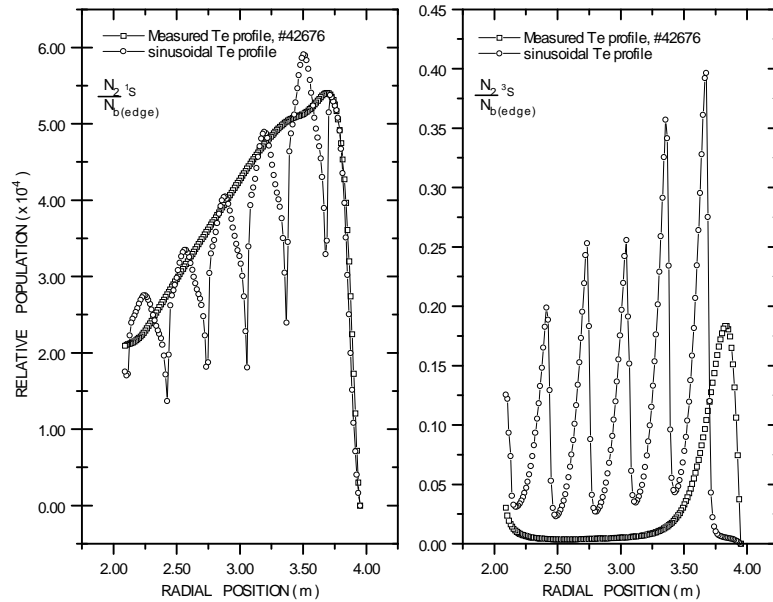


Figure 6.41 Influence of the electron temperature profile on the attenuation of the $\text{He}(2^1\text{S})$ and $\text{He}(2^3\text{S})$ metastable populations. The electron density which was used is that shown in figure 6.40. The initial metastable content of the beam was zero. Also shown is the attenuation of each of the metastable populations using the temperature profile as shown in figure 6.27. The beam energy was 30 keV amu^{-1} .

The attenuation of each metastable has a rather curious temperature dependence. In the case of the $\text{He}(2^1\text{S})$ metastable, as the beam enters the plasma the metastable is rapidly populated. The populating mechanism is primarily due to ion collisions since the edge temperature is greater than 1.5 keV and therefore the contribution due to electron collisions will be small. As the $\text{He}(2^1\text{S})$ population is attenuated it can be observed to show periodic oscillations. The peaks and troughs of these oscillations correspond to when the temperature respectively rises to 6 keV and then falls to 10 eV . When the temperature approaches 10 eV the $\text{He}(2^1\text{S})$ tends to a minimum. The temperature is optimum for spin changing electron collisions which contribute to populating the triplet spin system from the $\text{He}(2^1\text{S})$ metastable. When the

temperature increases the influence of the spin changing electron collisions decreases and the rate at which the He(2¹S) metastable is depopulated is reduced.

If we now consider the behaviour of the He(2³S) population, we can see from figure 6.41 that since the edge temperature is very high, the He(2³S) level is scarcely populated on the immediate entry of the beam into the plasma. As the temperature profile approaches a minimum the spin changing cross sections are active and the He(2³S) population begins to increase. However as the temperature begins to rise the contribution to the He(2³S) metastable is reduced and the population is then strongly attenuated. If we compare the oscillating nature of the He(2¹S) and He(2³S) it can be seen that they are out of phase and when the He(2¹S) population decreases the He(2³S) population suddenly increases as they are both progressively attenuated.

6.5.4.2 Influence of the electron density profile

The electron density profile selected is also sinusoidal in nature and oscillates between 10^{12} to $1.9 \times 10^{13} \text{ cm}^{-3}$ as a function of radial position. We show in figure 6.42 both the electron temperature and density profile which are of concern. The electron density profile which is employed is that as described in figure 6.27.

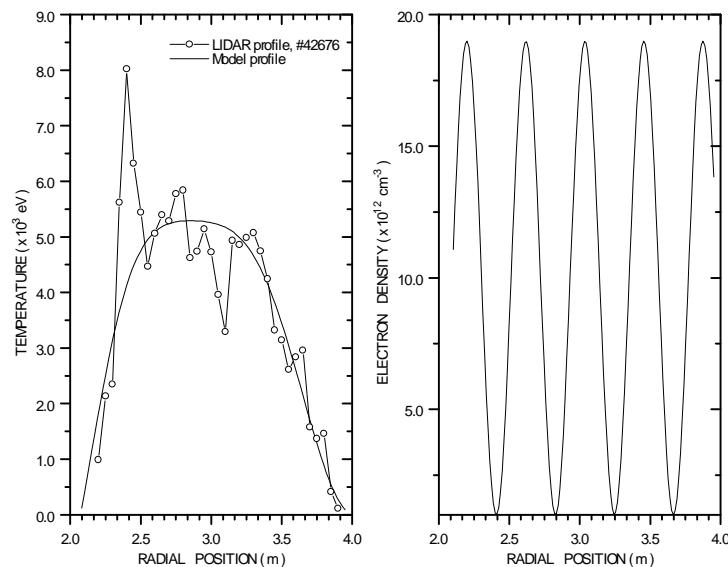


Figure 6.42 Electron density and temperature profiles. The temperature profile was obtained from the JET pulse 42676. The electron density profile oscillates from 10^{12} cm^{-3} to $1.9 \times 10^{13} \text{ cm}^{-3}$.

The behaviour of the He(1^1S) population as it is attenuated as a function of radial position is shown in figure 6.43. We also show the attenuation of the He(1^1S) population using the measured electron density profile obtained from the JET pulse 42676.

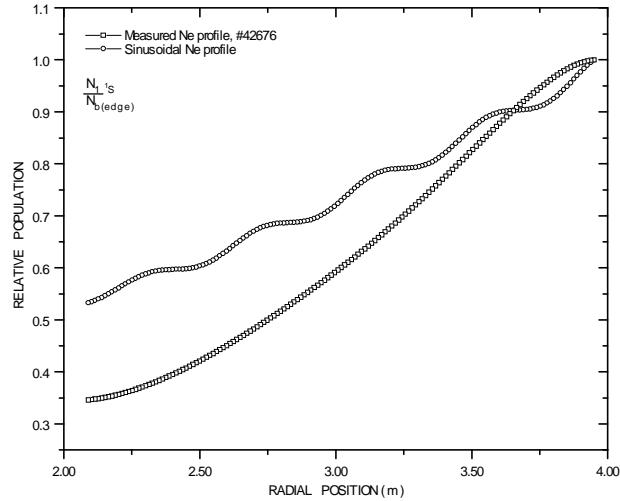


Figure 6.43 Attenuation of the He(1^1S) for a beam energy of 30 keV amu^{-1} , also shown in the figure is the attenuation of the He(1^1S) using the model electron density profile obtained from the JET pulses 42676.

It can be seen that as the beam enters the plasma it is immediately attenuated as a result of the high edge plasma density. As the beam continues into the plasma the behaviour of the He(1^1S) population directly reflects the changes in the electron density profile. When the density profile reaches a minimum the He(1^1S) remains constant as there is little attenuation. However as the density increases the population of the He(1^1S) ground state decreases as a result of enhanced attenuation. A similar behaviour can be observed in figure 6.44 where we show the attenuation of the He(2^1S) and He(2^3S) metastables.

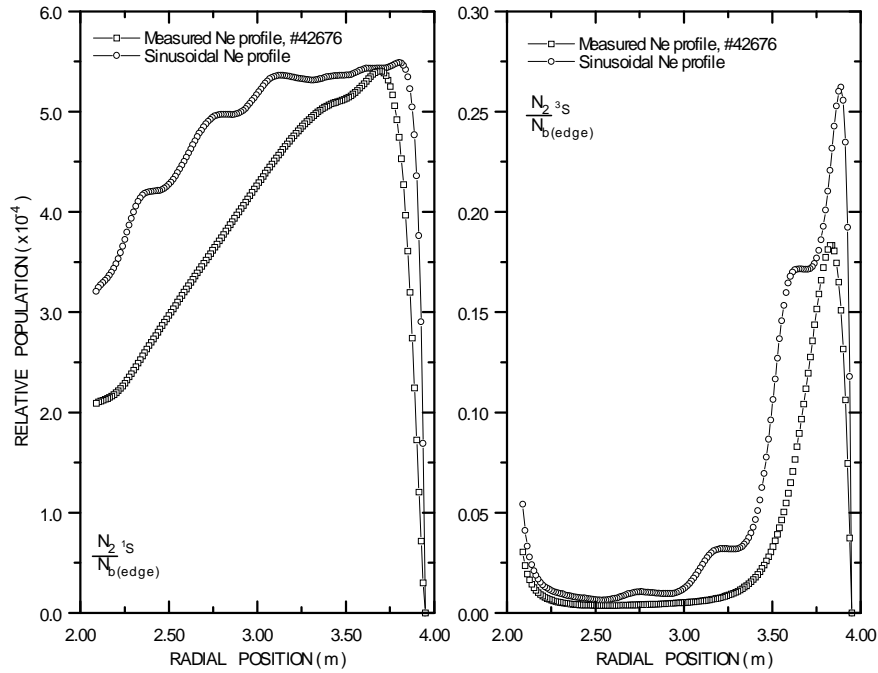


Figure 6.44 Attenuation of the He(2^1S) and He(2^3S) for a beam energy of 30 keV amu^{-1} . The initial metastable content of the beam was zero. Also shown in the figure is the attenuation of each metastable using the measured electron density profile obtained from the JET pulses 42676.

6.6 Conclusion

In summary, we have illustrated the behaviour and parameter dependencies of the collisional-radiative cross coupling coefficients. The neutral beam energy determines the efficiency at which the ion collisions contribute to the coupling coefficients. The electron temperature regulates the effectiveness of the electron collisions. The electron collisions contribute to the spin and non-spin changing coupling coefficients. The spin changing coupling coefficients are dominated by electron collisions and are therefore strongly temperature dependent. Ion collisions can only participate in spin conserving collision. We have however identified a secondary dependence of the spin changing coupling coefficients on the beam energy.

The coupling coefficients can be used to define an effective ionisation coefficient associated with the ground state and the metastable levels. These coefficients represent the rate at which each level is ionised and includes the influence of stepwise atomic processes. We have shown that the effective ionisation

coefficients associated with each metastable is substantially greater than the coefficient associated with the ground state. This indicates that once the metastables are populated they will be ionised very quickly in comparison with the ground state.

The Quasi-static excited population structure has been shown to exhibit a similar parameter dependencies to that of the cross coupling coefficients. Electron and ion collisions contribute to populating the singlet spin system while the triplet spin system is only populated by spin changing electron collisions from the ground state. We also considered the influence of impurities on the excited state population structure and examined the extent to which each metastable contributes to populating each of the excited states contained in the $n=4$ shell.

We have calculated the quasi-static and spatially dependent local metastable population for JET plasma conditions. We have shown that errors can be made by assuming that the metastables have relaxed and reached equilibrium. The extent of which is governed by the beam energy and to a lesser degree the initial metastable content of the beam on entry to the plasma. The beam energy governs the distance the beam atoms can travel within the atomic lifetime of the metastables. If this distance is greater than the scaled lengths associated with the plasma density and temperature, then the metastables will not reach equilibrium. If on the other hand the distance is shorter than the scaled lengths of the plasma dynamics, the metastable levels will relax and reach quasi-static equilibrium.

We have illustrated that the attenuation of a neutral helium beam can be accurately modelled without considering the influence of the metastable populations, provided that the initial metastable population is zero. However consideration of the metastable levels is required if one wants to exploit the possibility of preferential charge exchange from the ground state and the He(2^3S) metastable. Also for use with beam emission spectroscopy a detailed knowledge of the excited state population structure, including the influence of the metastables, is required.

We have shown that the metastable populations are formed at the edge of the plasma and then rapidly decay as the beam continues into the plasma. For the He(2^3S) metastable it was shown that the population increases once again as the beam approaches the inner edge of the plasma. The extent of the attenuation of the

metastables is governed by the rate at which they are ionised. We investigated the influence of modifying the initial metastable population of the beam and also the effects due to rapid changes in the electron density and temperature in the plasma.

The influence of the temperature and density profiles is substantial. The temperature had little effect on the attenuation of the He(1^1S) population while there is an interesting dependency on the He(2^1S) and He(2^3S) metastables. The influence of the electron density was more substantive with the He(1^1S) ground state and the He(2^1S) metastable level. In summary, the metastable populations are difficult to sustain as the beam traverses the plasma. Nevertheless depending on the initial metastable content, the metastable populations may be of significance for charge exchange and of course spectroscopy.

7.0 Thesis summary and discussion

The work in this thesis involved modelling, measuring and predicting the attenuation and emission associated with fast neutral diagnostic beams. There were two main beam species which were of interest. We were first concerned with modelling and measuring the attenuation and emission associated with fast a neutral deuterium beam. Secondly we were involved with developing a collisional-radiative model to predict the attenuation and emission from a fast neutral helium beam.

Focusing on the work regarding a neutral deuterium beam. Using an existing collisional-radiative model from the ADAS system, ADAS310. We calculated and investigated the parameter dependencies of effective beam stopping and Balmer-alpha emission coefficients. We also developed an interactive program to allow one to visually inspect and archive the derived data obtained from ADAS310. This program is now part of the ADAS package and is known as ADAS312. We investigated the accuracy of the linear interpolation and combination method which is employed to archive and facilitate the rapid assembly of composite coefficients.

The effective stopping coefficients were used to model the attenuation of the neutral deuterium beams at JET Joint Undertaking, while the effective emission coefficients were employed to recover the neutral deuterium beam density using Balmer-alpha beam emission spectroscopy. After refinements in the analysis of the beam emission spectrum, consistency in the charge exchange analysis and the use of improved fundamental atomic data which enters as input into ADAS310. We found that that the measured beam densities agree to within 27 % of the values obtained from the numerical attenuation calculation for single beam bank pulses, while for double beam bank pulses the measured neutral beam densities agree to within 20 %.

Nevertheless more work is required to establish beam emission spectroscopy as a truly reliable diagnostic in the sense that it can replace the numerical attenuation calculation. The most immediate difficulty involves analysing vast numbers of spectra accurately and efficiently. Even though we have demonstrated that the spectral fitting of only the $+\pi 3$ and $+\pi 4$ components is sufficient to recover the beam density, it is more accurate to consider the analysis of all of the Stark components. The analysis of the beam emission spectrum should really be done on an interactive

basis where more consideration is given to the residuals obtained from the synthetic and measured spectrum. A possible long term goal would be to build up a database of analysed spectra which could then be used as a training set for a neural network. The neural network could then be used to analyse the bulk of the spectra.

If we now consider the work concerning a fast neutral helium beam. We have developed a collisional-radiative model to predict the attenuation and emission associated with a fast neutral helium beam. This program is an off line FORTRAN code and is intended to be placed into the ADAS package as ADAS311 in the near future. ADAS311 is a spin resolved model which calculates the equilibrium populations of each of the angular sub-states up to an arbitrary principal quantum shell, above which the population of each principal quantum shell is then calculated. The model also calculates collisional-radiative cross coupling and recombination coefficients. We have also developed a computational tool, analogous to ADAS312, which is employed to allow one to inspect and archive the derived atomic data obtained from ADAS311. This program is also intended for use within the ADAS package as ADAS313.

Using ADAS311 and ADAS313 we have studied the quasi-static excited population structure of the beam atoms. We also considered the influence of the non-equilibrium metastables on the population of the levels contained within the $n=4$ shell. The parameter dependencies of the collisional-radiative coupling coefficients were also explored and later used to model the evolution of the metastable populations. For a beam where the initial metastable content is zero, we have shown that the metastable levels are populated on entry to the plasma and are then strongly attenuated as the beam continues. Modifying the initial metastable content of the beam does enhance their survival, however spectroscopic observations are now required to investigate whether the metastable populations are suffice to enable preferential charge exchange from the ground state and the metastable levels to occur.

Spectroscopic observations with a neutral helium beam would also allow us to experimentally validate and improve upon our model. In the case of a fast helium beam ($> 50 \text{ keV amu}^{-1}$), since the fundamental ion-atom collision data is more

accurately known in this region, it is expected that there would be good agreement between theory and experiment. This however is not the case for a low energy beam ($E < 10 \text{ keV amu}^{-1}$), the fundamental data in this region has a greater uncertainty and so discrepancies between theory and experiment are to be expected. Also the influence of the Lorentz electric field has not been taken in account in our model and it is in this region where its influence is most significant.

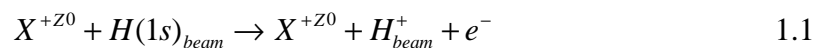
Appendix A.

1.0 Review of the fundamental ion-atom collision database

The ion-atom collision database is utilised by ADAS310 to replace the cross-sections which have been calculated internally using approximate methods. The database, which is of the ADAS ADF02 type format, contains fundamental cross sections for ion impact ionisation and excitation of neutral H with impurity species up to the first period. Charge exchange data from neutral H is also included. The cross sections are tabulated as a function of collision energy per atomic mass unit and can also be used to describe the behaviour of the atomic processes associated with neutral deuterium and tritium. The main species of interest in this work being deuterium. The database was originally constructed in 1989 by Summers[54] and was later reviewed in 1991 and partially updated in 1993. Where possible, theoretical and experimental values were combined to give a composite data set for each individual atomic process. This database is referred to as the JET 1989 data. To update the present database involved reviewing the literature for both theoretical and experimental cross sections. The aim being to either create a new composite data set for each individual process or to simply supplement an existing data set with improved data. The ion-atom data assessment presented here represents the best available data up until March 1997.

1.1 Review of Ion impact ionisation data

The existing database contains fundamental data for ion impact ionisation of neutral $H(1s)_{beam}$ as described in equation 1.1, where Z_0 is the nuclear charge of the impurity and ranges from 1 to 10.



The data used for the case when $Z_0 = 1$, i.e. ion impact ionisation of neutral $H(1s)_{beam}$ with H^+ , was a composite data set compiled from the experimental work of Shah & Gilbody[87], Shah, Elliot & Gilbody[88] and the theoretical calculations of Ryufuku

[89]. This was compared with the data reported by Janev & Smith[90], see figure 1.0. There is excellent agreement. The data reported by Janev & Smith[90] is a composite data set constructed from the experimental and theoretical data reported by eight independent sources. We decided to combine the data reported by Janev & Smith[90] with the existing data to construct a new data set. This was achieved by modifying the peak value of the existing data set to agree with the value reported by Janev & Smith[90]. The new data set is the preferred data for this process and is referred to as the comparative data set.

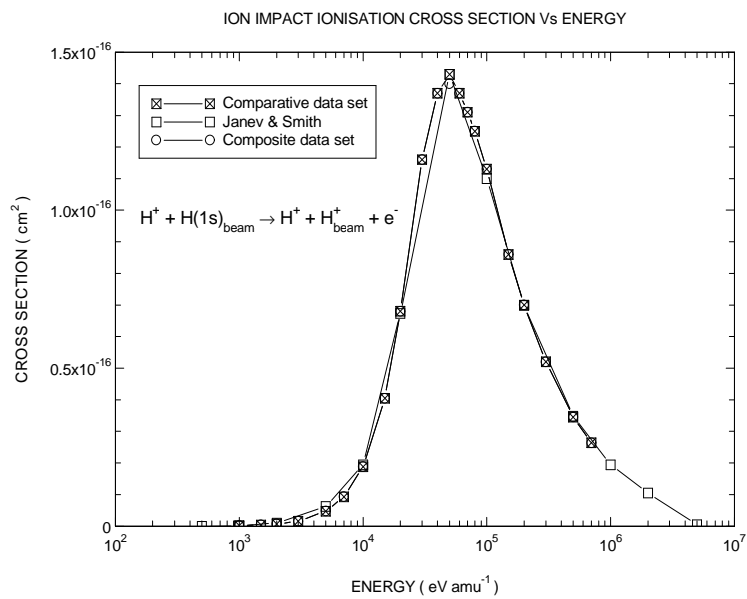


Figure 1.0 A plot of the ion impact ionisation cross section Vs energy. A comparative data set was constructed by modifying the peak value of the existing composite data set to agree with the results reported by Janev & Smith [90]. The comparative data set is taken as the preferred data.

The data employed for $Z_0 = 2$, was a composite data set compiled by Hugh Summers, this data set was based on the experimental work of Shah & Gilbody[87] and Shah, Elliot & Gilbody[88]. A comparison was made between this data set and the theoretical work of Toshima & Tawara[91]. The results can be seen in figure 2.0 . Below 90 keV/amu both data sets agree, however above 90 keV/amu there is a slight difference. Since the composite data set is based on experimental measurements it is taken as the preferred data set for this process. For convenience of reference the new preferred composite data set is called the comparative data set, see figure 2.0

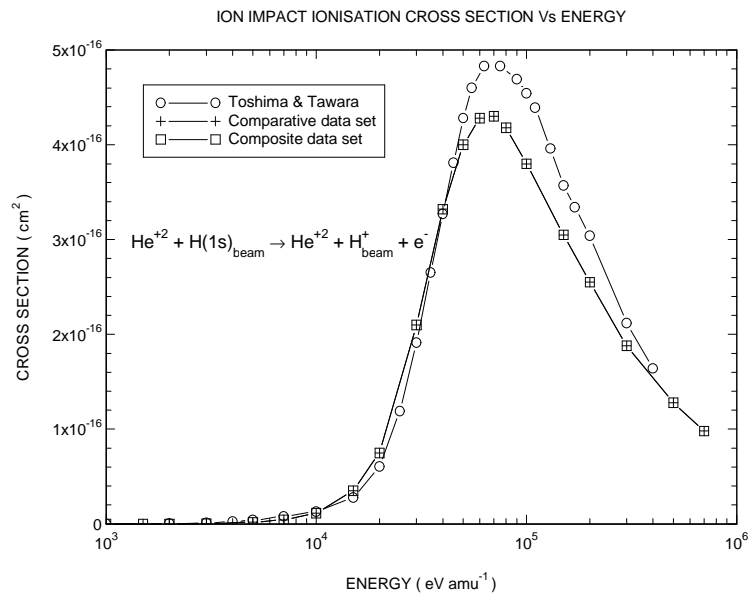


Figure 2.0 A plot of the ion impact ionisation cross section Vs energy. The composite data set is based on experimental measurements and is taken as the preferred data. For convenience the preferred data set is called the comparative data set.

For $Z_0 = 3$, the data used was a composite data set based on the work of Shah & Gilbody[87] . A comparison was made between this data set and the data of Toshima & Tawara[91], see figure 3.0. As before, due to the influence of experimental data, the composite data set it is taken as the preferred data set. The preferred data set is called the comparative data set, see figure 3.0 . The data used for $Z_0 = 4$, was a composite data set which was obtained by interpolating between the data of neighbouring species. This data was compared to the work of Janev & Smith[90] and Toshima & Tawara[91]. The results can be observed in figure 4.0 . The data of Janev & Smith[90], which is based on the work of three independent workers, is taken as the preferred data. When $Z_0 = 5$, a composite data set compiled by Summers[54] was used. This was compared to the new calculations of Toshima & Tawara[91] and the data reported by Janev & Smith[90] , see figure 5.0. The data reported by Janev & Smith[90] is a composite data set based on the work of eight independent sources and is taken as the preferred data.

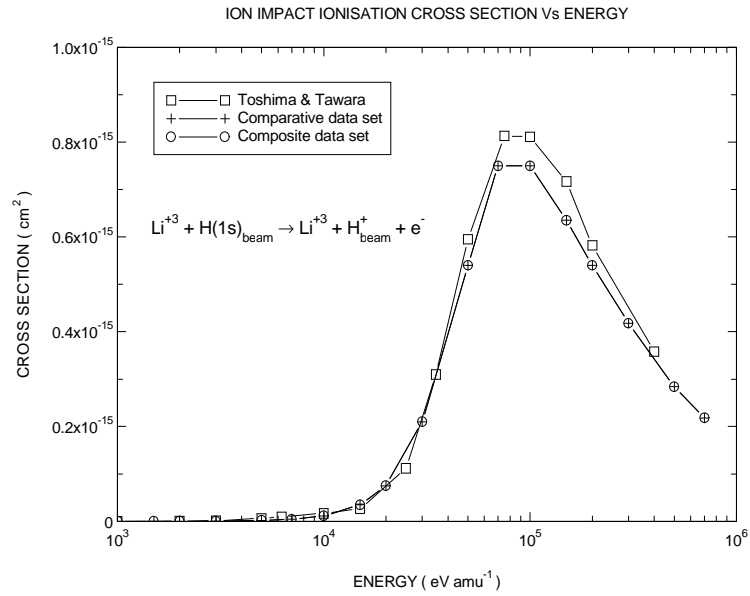


Figure 3.0 A plot of the ion impact ionisation cross section Vs energy. The composite data set is taken as the preferred data set and for convenience it is referred to as the comparative data set.

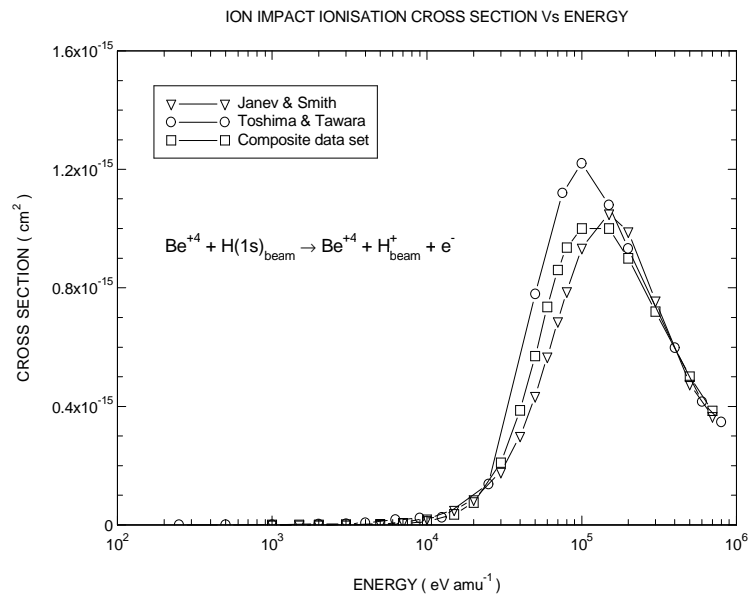


Figure 4.0 A plot of the ion impact ionisation cross section Vs energy. The data of Janev & Smith[90] which is based on the work of three independent sources is taken as the preferred data set.

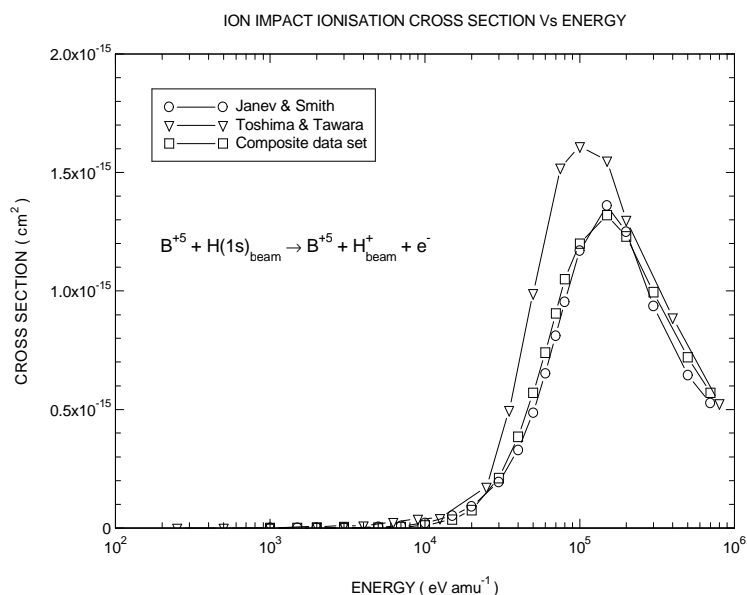


Figure 5.0 A plot of the ion impact ionisation cross section Vs energy. The data of Janev & Smith[90] is based on the work of eight independent sources and is taken as the preferred data set.

A composite data set based on the work reported in the ‘red book’ [92] was used for when $Z0 = 6$. This data set was compared to the work of Janev & Smith[90] and the theoretical calculations of Toshima & Tawara[91]. Figure 6.0 illustrates the results.

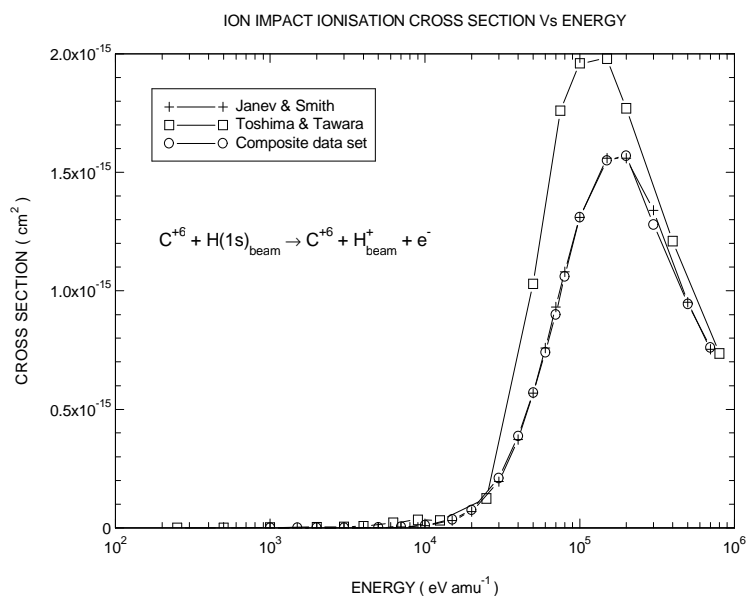


Figure 6.0 A plot of the ion impact ionisation cross section Vs energy. The data of Janev & Smith[90] is taken as the preferred data.

The data of Janev & Smith[90], which is based on the results of many workers, is considered to be the best for this particular process. For $Z_0 = 7$, a data set which has been obtained by interpolating through the data of neighbouring species was used. This data set was compared to the work of Toshima & Tawara[91]. A comparative data set was constructed by interpolating through the data of neighbouring species using the data reported by Janev & Smith[90]. The comparative data set is chosen as the preferred data set for this process, see figure 7.0.

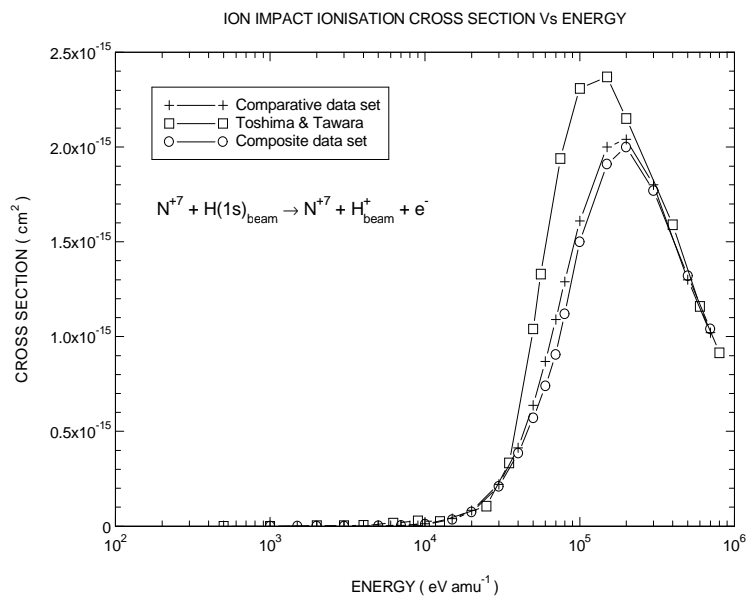


Figure 7.0 A plot of the ion impact ionisation cross section Vs energy. The comparative data set is taken as the preferred data.

When $Z_0 = 8$, data based on the ‘red book’ [92] was used. This data was compared to the calculations of Toshima & Tawara[91] and the composite data reported by Janev & Smith[90]. The results can be seen in figure 8.0. The data of Janev & Smith[90] is based on four independent sources and is taken to be the best. The data used for $Z_0 = 9$ was a composite data set which was obtained by interpolating between neighbouring species, see figure 9.0. For $Z_0 = 10$, a composite data set was used which was obtained by scaling the oxygen data, see figure 9.0. A review of the literature failed to improve the data for these species.

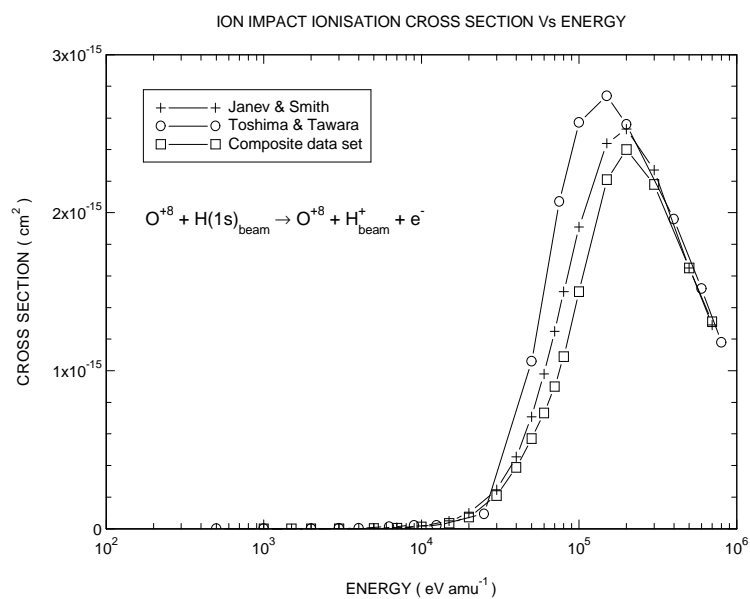


Figure 8.0 A plot of the ion impact ionisation cross section Vs energy. The data reported by Janev & Smith[90] is taken as the preferred data set.

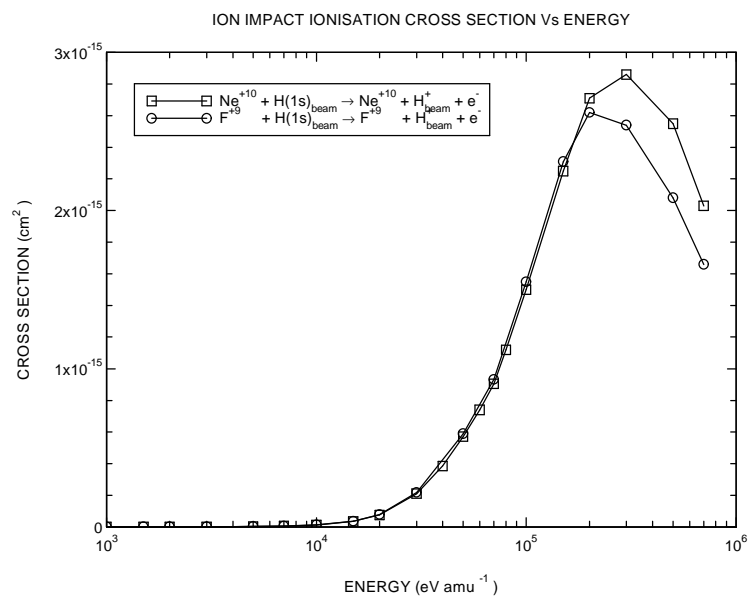
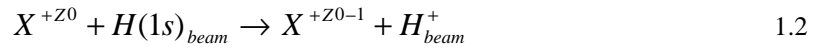


Figure 9.0 A plot of the ion impact ionisation cross section Vs energy. The data for F^{+9} both was obtained by interpolating through the data of neighbouring species. The data for Ne^{+10} was obtained from scaling the data for Oxygen . A review of the literature failed to improve the data for both species.

1.2 Review of charge exchange data

The existing database contains fundamental data for charge exchange from $H(1s)_{beam}$ as described in equation 1.2, where Z_0 is the nuclear charge of the impurity and ranges from 1 to 10.



The data used for $Z_0 = 1$, was a composite data set based on the work of M^c Clure[93] & Greenland[94]. This data was compared to the data reported by Janev & Smith[90], the results can be seen in figure 10.0.

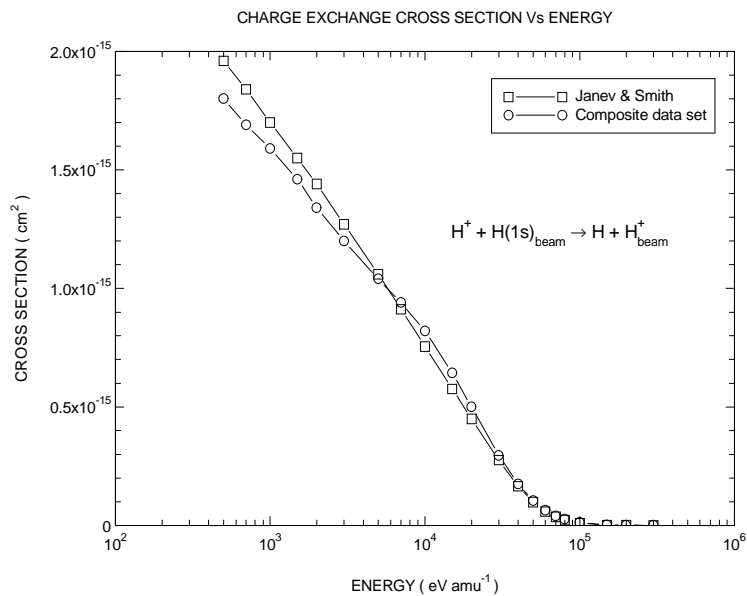


Figure 10.0 A plot of the charge exchange cross section Vs energy. The data of Janev & Smith[90] is taken as the preferred data.

The data of Janev & Smith[90], which is based on the work of twelve independent sources, is the preferred data set. When $Z_0 = 2$, the data which was used is a composite data set based on the work of Frieling[95]. A comparison between this data set and the work of Janev & Smith[90] and Toshima & Tawara[91] can be observed in figure 11.0.

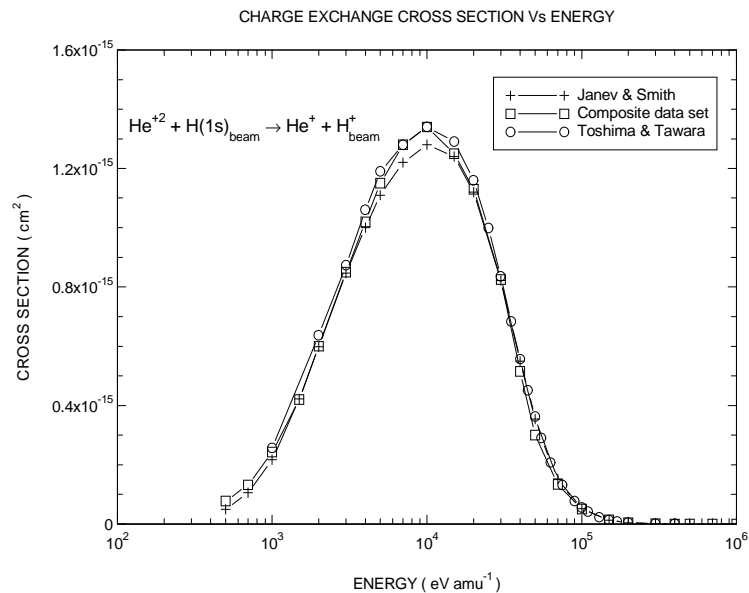


Figure 11.0 A plot of the charge exchange cross section Vs energy. The data of Janev & Smith[90], which is based on the results of many workers, is taken as the preferred data.

The difference between the work of Toshima & Tawara[91] and Frieling[95] is somewhat insignificant. The data reported of Janev & Smith[90], which is based on the results from many workers, is taken as the preferred data set. For $Z0 = 3$, the data which was used is a composite data set constructed from interpolating through the data of neighbouring species. This data set was compared to the theoretical calculations of Toshima & Tawara[91], see figure 12.0. A comparative data set was constructed by interpolating through the data of neighbouring species using the data of Janev & Smith[90]. The new comparative data set is taken as the preferred data set.

The data set used when $Z0 = 4$, was a composite data set based on the work of Greenland[94] and Ryufuku[96]. This data set was compared to the work of Toshima & Tawara[91] and Busnengo et al[97], see figure 13.0. The composite data set is still considered to be the most accurate and is taken as the preferred data set. For $Z0 = 5$, the data which was used is a composite data set based on the work of Ryufuku[96] and influenced by the data of $Z0 = 4$ & 6. A comparison between this data set and the work of Toshima & Tawara[91] and Busnengo et al[97] can be observed in figure 14.0. A comparative data set was constructed from

interpolating through the data of neighbouring species. The new comparative data set is taken as the preferred data set, see figure 14.0.

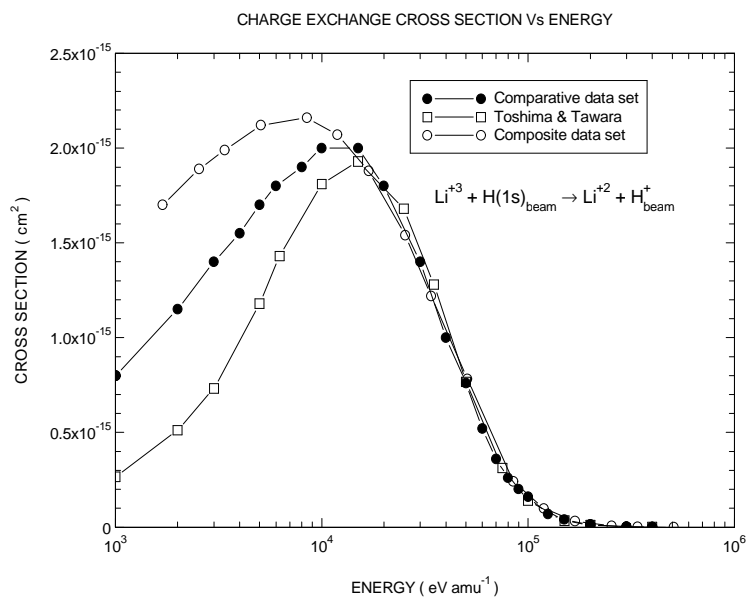


Figure 12.0 A plot of the charge exchange cross section Vs energy. The new comparative data set is the preferred data.

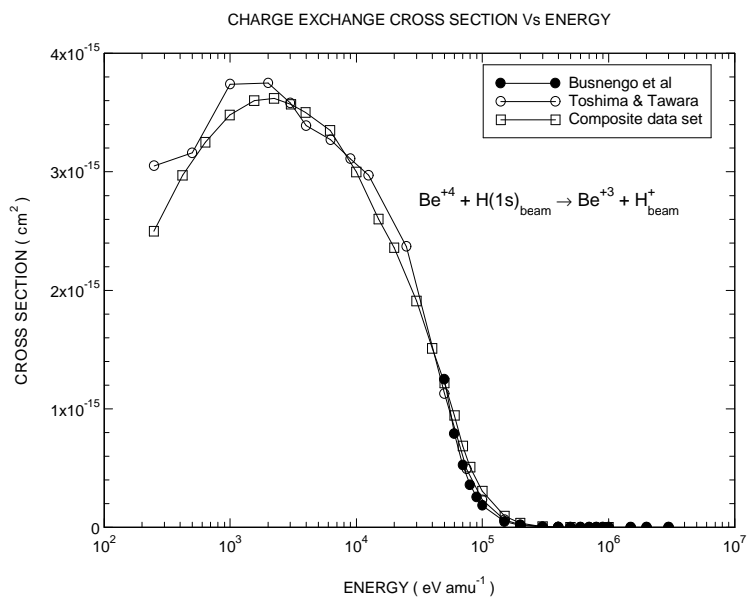


Figure 13.0 A plot of the charge exchange cross section Vs energy. The composite data set is still considered to be the most accurate and is taken as the best data for this particular process.

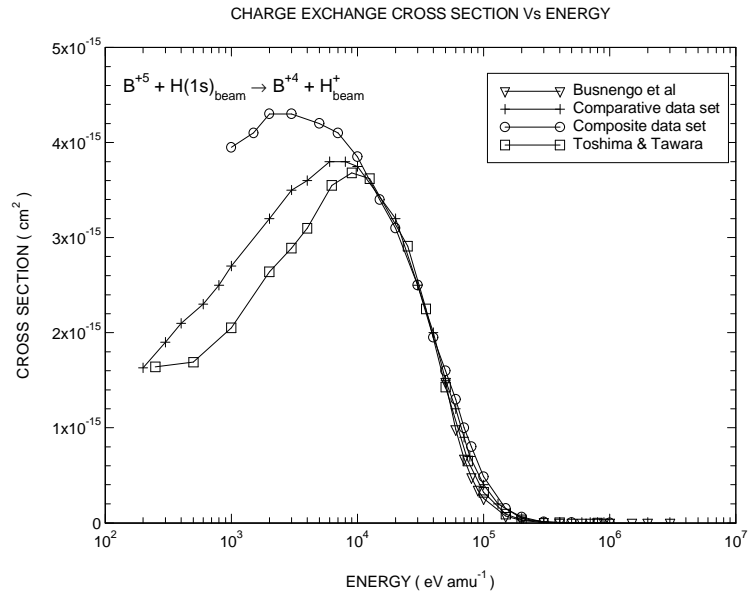


Figure 14.0 A plot of the charge exchange cross section Vs energy. The comparative data set is taken as the preferred data.

When $Z_0 = 6$, a composite data set based on the work of Greenland[94] and Ryufuku [96] was used. A comparison was made between this data set and the work of Janev & Smith[90] and Toshima & Tawara[91]. The results can be seen in figure 15.0 .

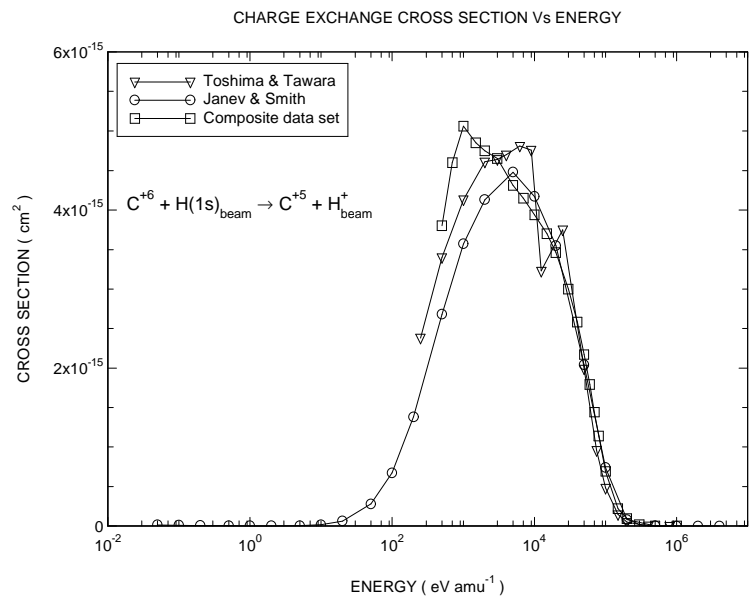


Figure 15.0 A plot of the charge exchange cross section Vs energy. The data reported by Janev & Smith[90] is taken as the preferred data.

The data of Toshima & Tawara[91] and Janev & Smith[90] above ~ 20 keV/amu agree with the existing composite data set. However, there is an anomalous point in the data set of Toshima & Tawara[91] which adds some uncertainty on the reliability of the data. The data of Janev & Smith[90] is therefore taken as the preferred data. For $Z_0 = 7$, a composite data set based on interpolating through the data of neighbouring species was used. This data set was compared to the theoretical calculations of Toshima & Tawara[91], see figure 16.0 . A comparative data set was constructed by interpolating through the data of neighbouring species using the data reported by Janev & Smith[90]. The new comparative data set is taken as the preferred data set.

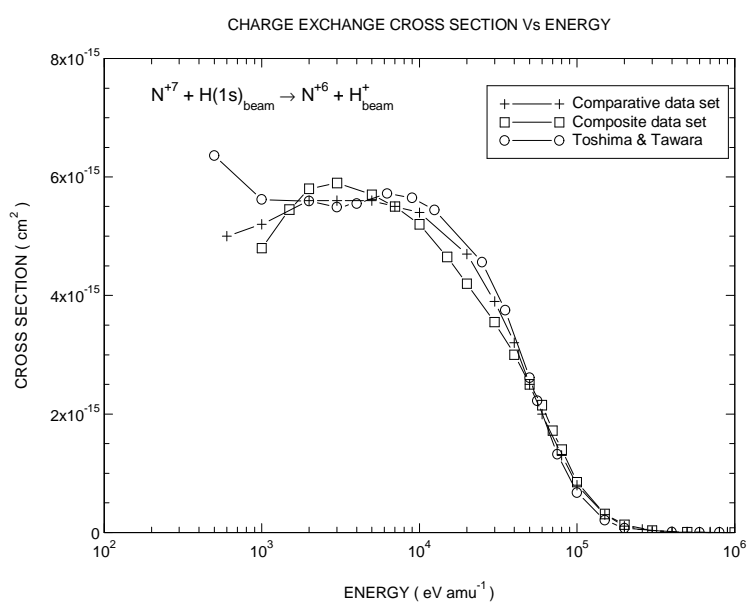


Figure 16.0 A plot of the charge exchange cross section Vs energy. The new comparative data set is taken as the best data for this process.

The data used for $Z_0 = 8$, was a composite data set based on the work of Greenland [94] and Ryufuku[96]. This data set was compared to the data of Janev & Smith[90] and Toshima & Tawara[91]. The results can be seen in figure 17.0 . The data of Janev & Smith[90] is taken as the preferred data. The data used for when $Z_0 = 9$ was a composite data set obtained by interpolating through the data of neighbouring species, see figure 18.0. When $Z_0 = 10$, a data set obtained by extrapolating from the oxygen data, as well as being influence by the work of Ryufuku[96], was used, the

results can be seen in figure 18.0. A review of the literature failed to improve the data for these species.

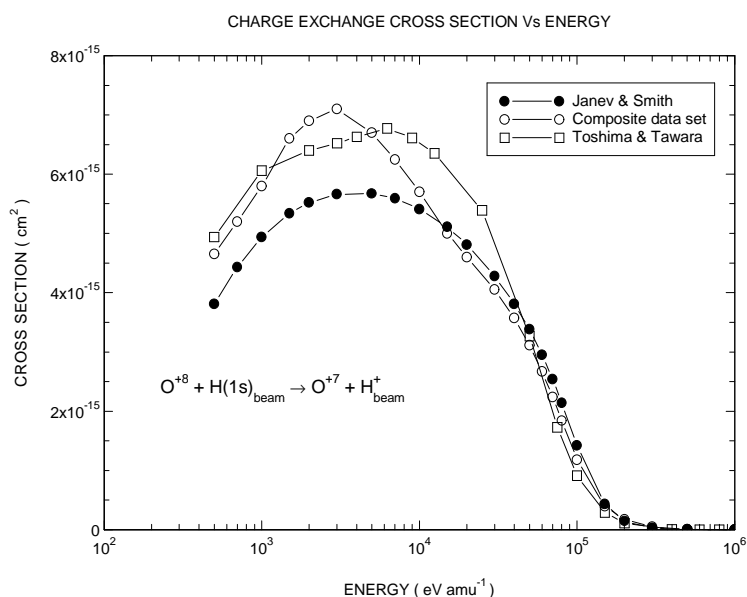


Figure 17.0 A plot of the charge exchange cross section Vs energy. The data reported by Janev & Smith[90] is taken as the preferred data.

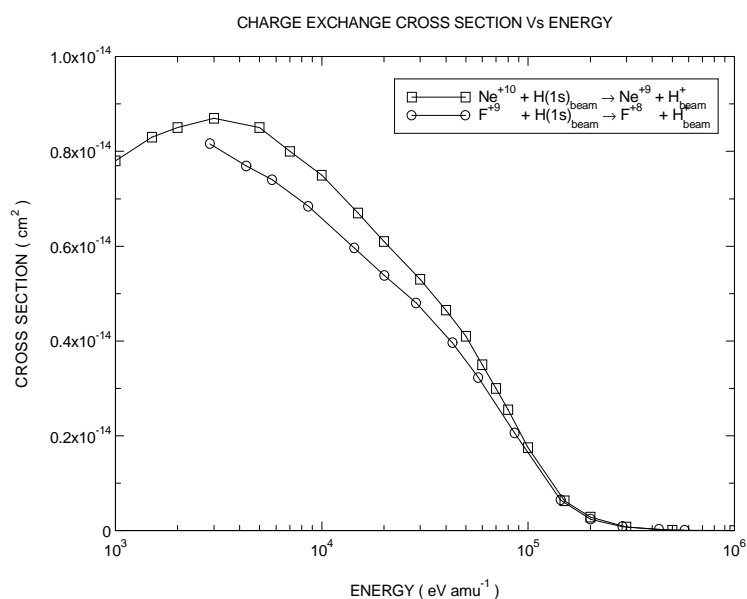
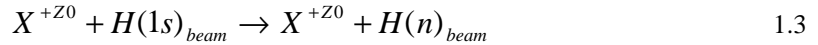


Figure 18.0 A plot of the charge exchange cross section Vs energy. The data for F^{+9} was obtained by interpolating through the data of neighbouring species. The data for Ne^{+10} was obtained from scaling the data for Oxygen . A review of the literature failed to improve the data for both species.

1.3 Review of ion impact excitation data

The existing database contains fundamental data for ion impact excitation of $H(1s)_{beam}$ as described in equation 1.3 , where Z_0 is the nuclear charge of the impurity and n is the principal quantum number with values from 2 to 5 .



In the case were $Z_0 = 1$ and $n = 2$, the data used was a composite data set based on the work of many workers [98], [99], [100], [101] and [102]. This data set was compared to the data reported by Janev & Smith[90], the results can be seen in figure 19.0 .

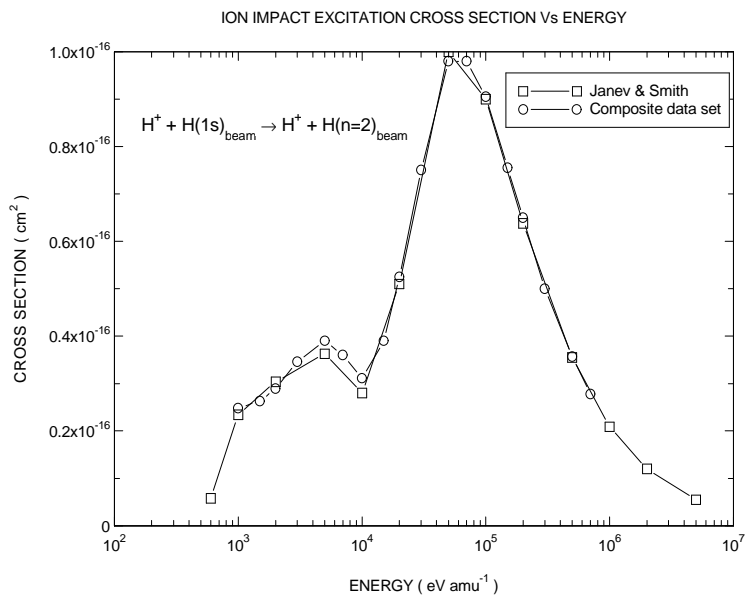


Figure 19.0 A plot of the ion impact excitation cross section Vs energy . The data of Janev & Smith[90], for convenience of reference, is taken as the preferred data for this particular process.

Both data sets agree, however for convenience of reference the data of Janev & Smith[90] is the preferred data set. When $n = 3$ for $Z_0 = 1$, the data which was used is a composite data set based on the 1st Born approximation as well as the work of many others [98], [99], [100], [101], [102] and [103]. This data set was compared to the data reported by Janev & Smith [90], see figure 20.0

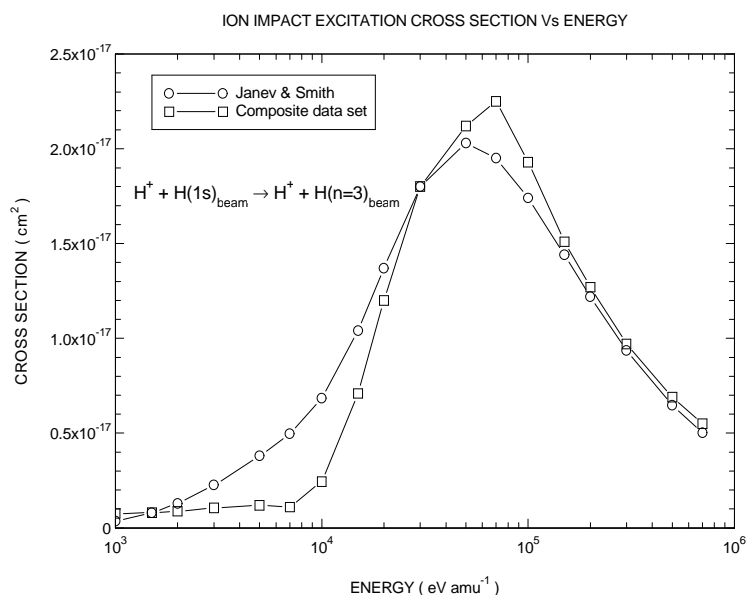


Figure 20.0 A plot of the ion impact excitation cross section Vs energy . The data reported by Janev & Smith[90] is taken as the preferred data set.

The data of Janev & Smith[90] is compiled using various sources such as [98],[99],[100] and [101], however they also include more recent work such as [104] and [105]. Therefore the data of Janev & Smith[90] is the preferred data set. For $n = 4$ and $Z_0 = 1$, the data used is based on the 1st Born approximation and the work of Fritsch [106] and Theodosian[103]. This data set was compared to the data of Janev & Smith[90]. The results can be observed in figure 21.0. The data of Janev & Smith[90], which is based on the work of five independent sources, is taken as the preferred data. A composite data set based on the 1st Born approximation and the work of Theodosian[103] is used when $n = 5$ and $Z_0 = 1$. This data set was compared to the data of Janev & Smith[90], see figure 22.0. The data of Janev & Smith[90] is believed to be more accurate and is taken as the preferred data. When $Z_0 = 2$ and $n = 2$, the data employed was that reported by Fritsch & Lin[107]. This data set was compared to the new theoretical calculations of Toshima & Tawara[91], the results can be observed in figure 23.0 . Due to the uncertainty associated with the anomalous peaks shown in the data of Fritsch & Lin and Toshima & Tawara, a comparative data set was constructed from interpolating between the extremes of the two data sets. The comparative data set is taken as the preferred data for this process.

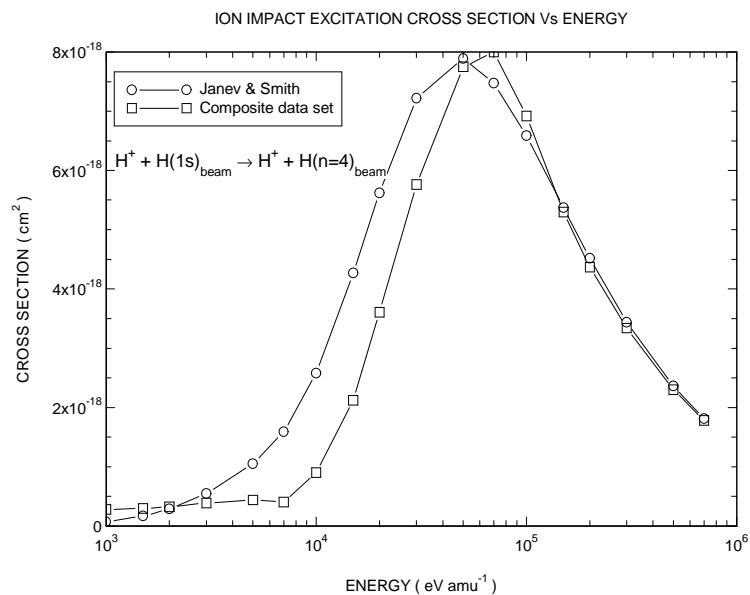


Figure 21.0 A plot of the ion impact excitation cross section Vs energy . The data of Janev & Smith[90] is taken as the preferred data set.

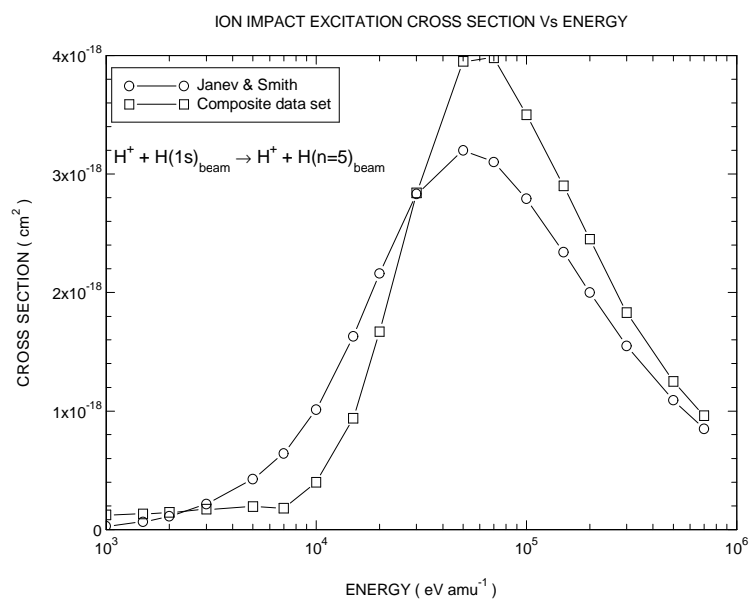


Figure 22.0 A plot of the ion impact excitation cross section Vs energy . The data reported by Janev & Smith[90] is taken as the preferred data for this particular process.

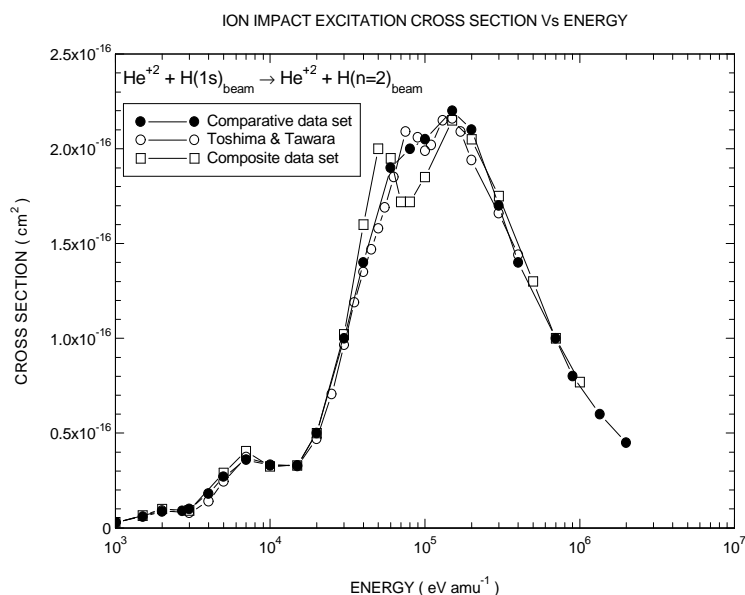


Figure 23.0 A plot of the ion impact excitation cross section Vs energy . Due to the uncertainty associated with the anomalous peaks in the data of Fritsch & Lin and Toshima & Tawara , the comparative data set is taken as the preferred data for this process.

For $n = 3$ and $Z0 = 2$ a composite data set based on the work of Fritsch[107] and Lodge[47] was used. This data set was compared to the data of Toshima & Tawara [91] as well as a comparative data set which has been constructed from interpolating between the extremes of the two data sets, see figure 24.0 . The comparative data set is the preferred data. When $n = 4$ and $Z0 = 2$, the data used is a general data set which is scaled according to the value of n and $Z0$. A comparison between this data set and the data of Toshima & Tawara[91] and Janev & Smith[90] is illustrated in figure 25.0. The data of Janev & Smith is taken as the best data as is referred to as the comparative data set. A general composite data set which is scaled according to the value of n and $Z0$ is used when $Z0 = 3$ and $n = 2, 3$ and 4 . A comparison was made between these data sets and the calculations of Toshima & Tawara[91]. In the case of $n = 2$ and 3 , comparative data sets were constructed by interpolating through the data of neighbouring species, see figures 26.0 and 27.0. In each case the comparative data set is taken as the preferred data. The preferred data for $n=4$ is the general composite data which is scaled according to $Z0$ and n , this is shown in figure 28.0.

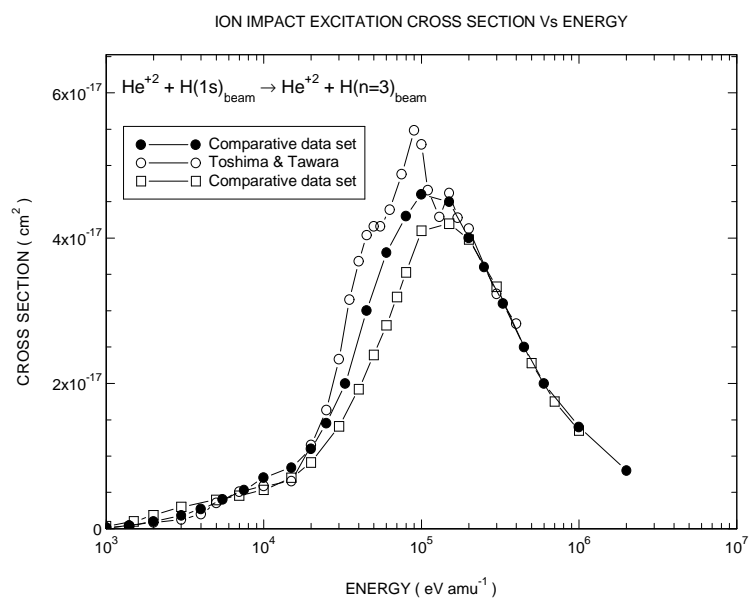


Figure 24.0 A plot of the ion impact excitation cross section Vs energy . The comparative data set is taken as the preferred data.

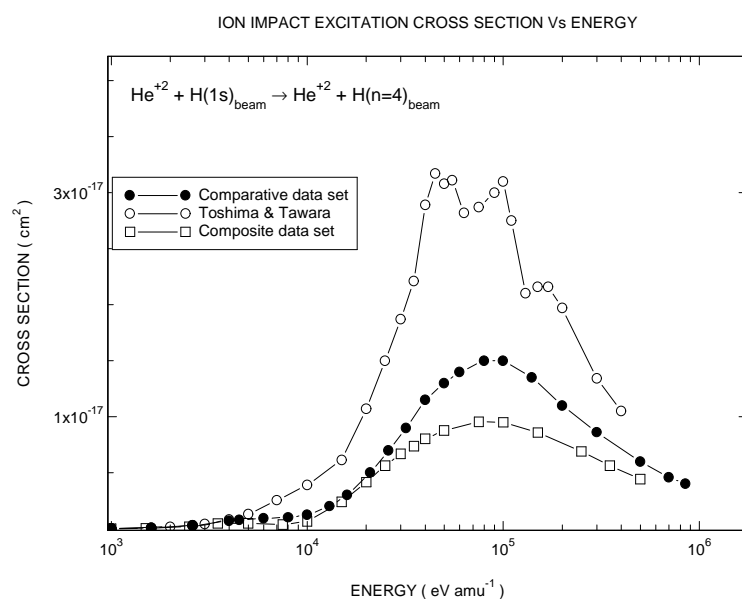


Figure 25.0 A plot of the ion impact excitation cross section Vs energy . The data reported by Janev & Smith[90] is taken as the preferred data. The calculation of Toshima & Tawara[91] only included states up to $n = 4$,therefore some over-estimation is present particular for the $n = 4$ shell.

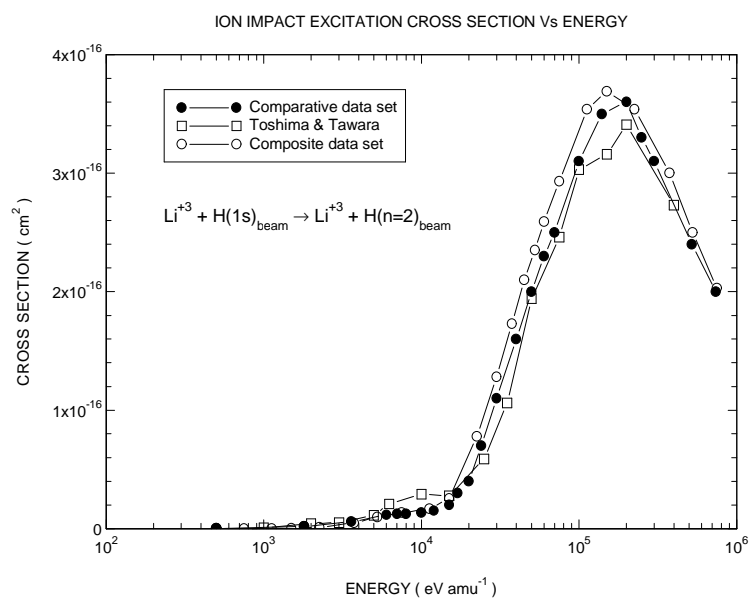


Figure 26.0 A plot of the ion impact excitation cross section Vs energy . The comparative data set is taken as the preferred data set.

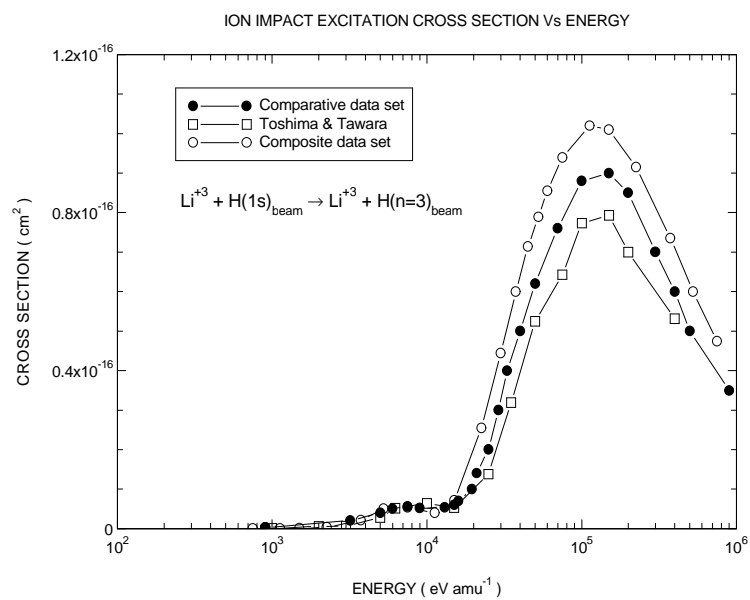


Figure 27.0 A plot of the ion impact excitation cross section Vs energy . The comparative data set is taken as the preferred data set.

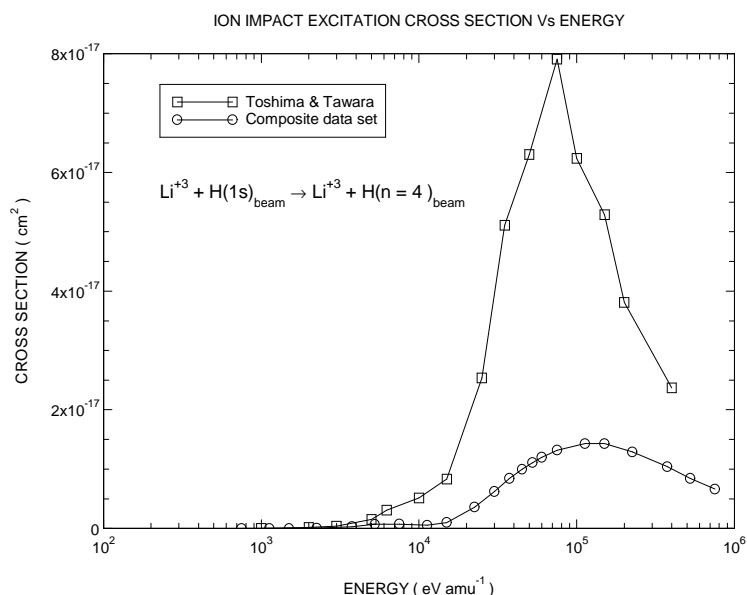


Figure 28.0 A plot of the ion impact excitation cross section Vs energy . The composite data set is taken as the preferred data set. The calculation of Toshima & Tawara only include states up to $n = 4$, therefore some over-estimation is present particular for the $n = 4$ shell .

In the case of $Z_0 = 4$ and $n = 2$, the data which was used is based on the work of Fritsch[107] . A comparison was made between this data set and the work of Toshima & Tawara[91] as well as a comparative data set which was constructed by interpolating through the data of neighbouring species. The results can be observed in figure 29.0 . The comparative data set is taken as the preferred data.

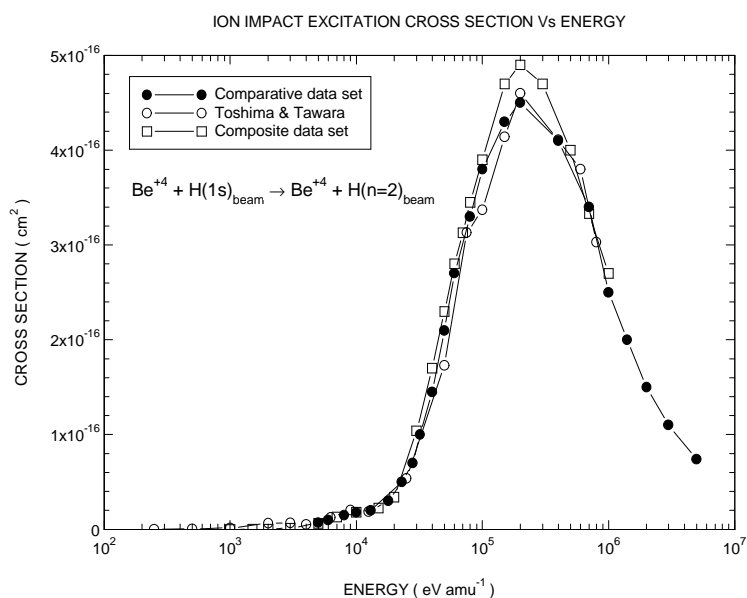


Figure 29.0 A plot of the ion impact excitation cross section Vs energy . The comparative data set is taken as the preferred data.

When $Z_0 = 4$ and $n = 3$ the data which was used is based on the work of Fritsch[107]. This was compared to the data of Toshima & Tawara[91] and a comparative data set which was obtained by interpolating through the data of neighbouring species, see figure 30.0. The comparative data set is considered to be the best data for this process.

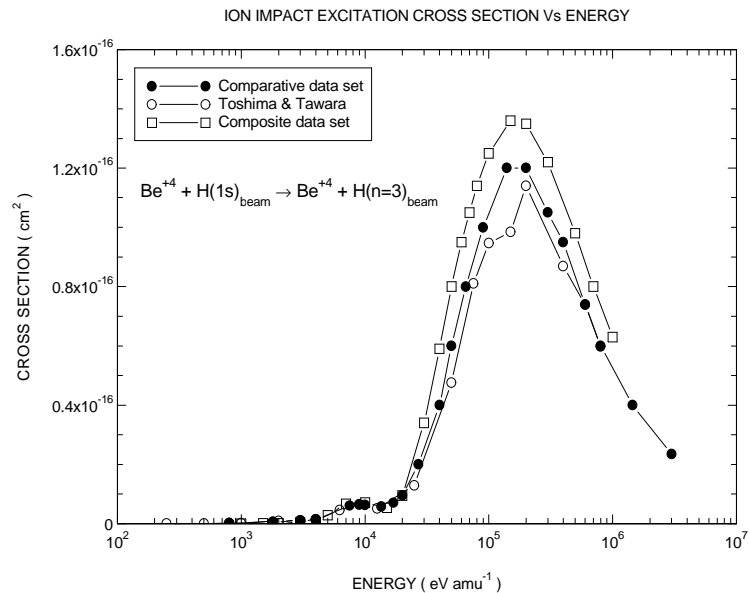


Figure 30.0 A plot of the ion impact excitation cross section Vs energy . The comparative data set is taken as the preferred data for this particular process.

For $Z_0 = 4$ and $n = 4$, a general data set which is scaled according to the value of n and Z_0 is employed. The results of the comparison between this data set and the data of Toshima & Tawara[91] can be observed in figure 31.0 . The general scaled data set, which is referred to as the composite data set, is the preferred data for this process. For all other value of Z_0 , a general data set was used which is scaled according to the value of n and Z_0 . The following figures illustrate the result of comparing the data of Toshima & Tawara[91] with the appropriately scaled data. Where possible a comparative data set, which is taken as the preferred data, was constructed by interpolating through the data of neighbouring species. In cases were it was not possible to construct a comparative data set, the general scaled data set is taken as the preferred data. The general scaled data set is referred to as the composite

data set. Finally, for $Z0 = 9$ and 10 the only data which existed was that of the general scaled data and a review of the literature failed to improve the situation.

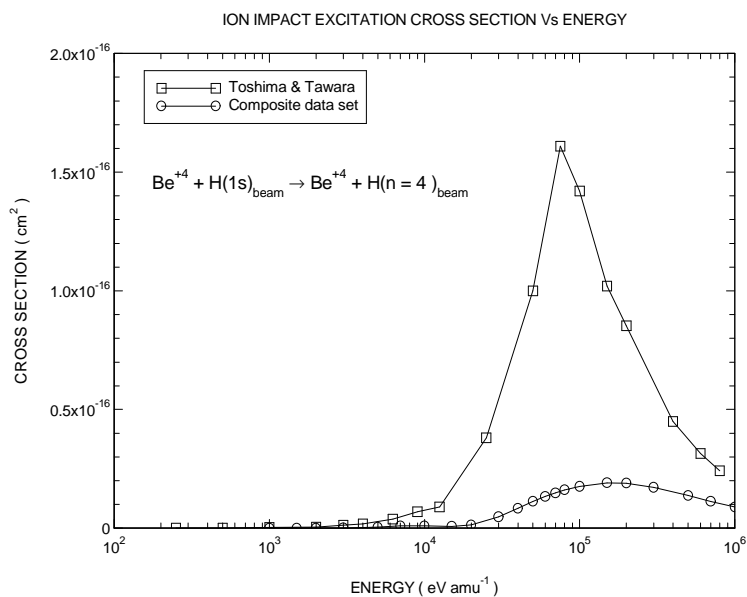


Figure 31.0 A plot of the ion impact excitation cross section Vs energy . The composite data set is taken as the preferred data. The calculation of Toshima & Tawara only include states up to $n = 4$, therefore some over-estimation is present particular for the $n = 4$ shell .

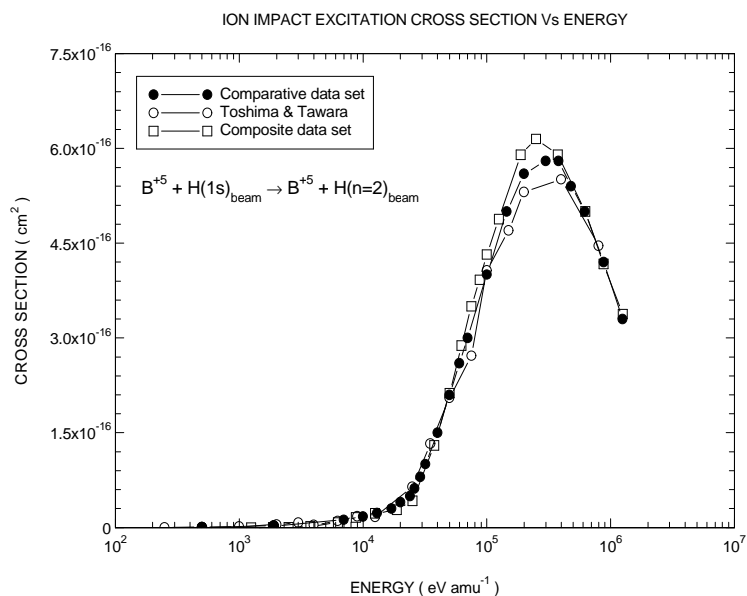


Figure 32.0 A plot of the ion impact excitation cross section Vs energy . The comparative data set is taken as the preferred data set for this process.

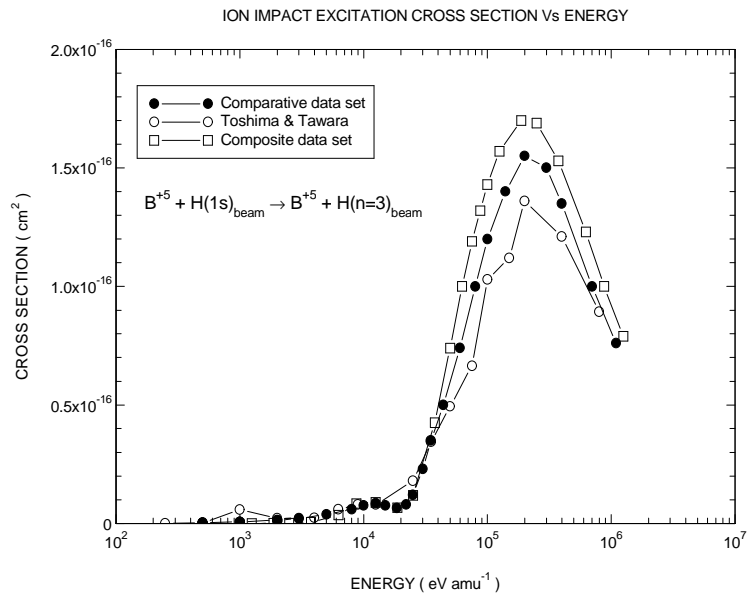


Figure 33.0 A plot of the ion impact excitation cross section Vs energy . The comparative data set is taken as the preferred data.

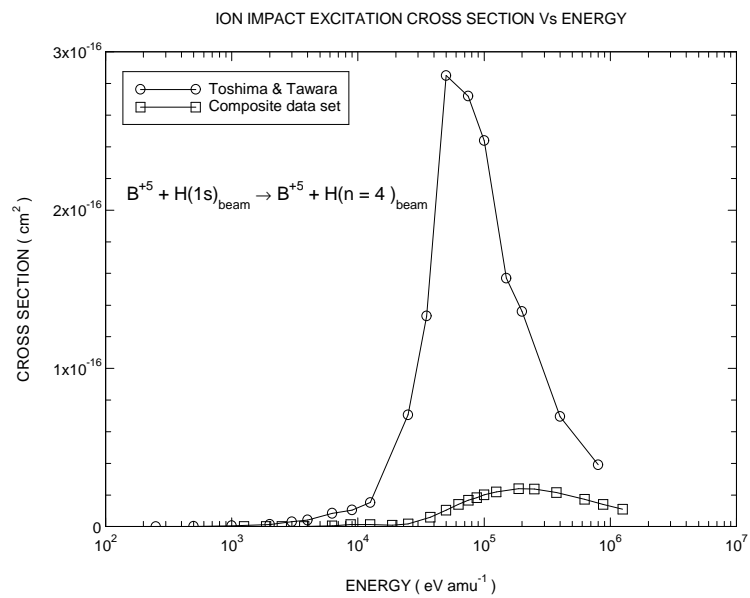


Figure 34.0 A plot of the ion impact excitation cross section Vs energy . The composite data set is taken as the preferred data. The calculation of Toshima & Tawara only include states up to $n = 4$, therefore some over-estimation is present particular for the $n = 4$ shell .

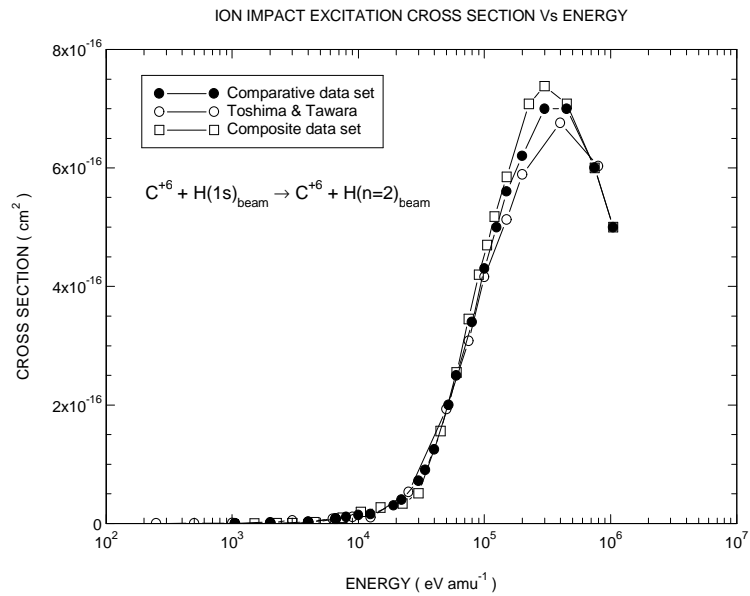


Figure 35.0 A plot of the ion impact excitation cross section Vs energy . The comparative data set is taken as the preferred data.

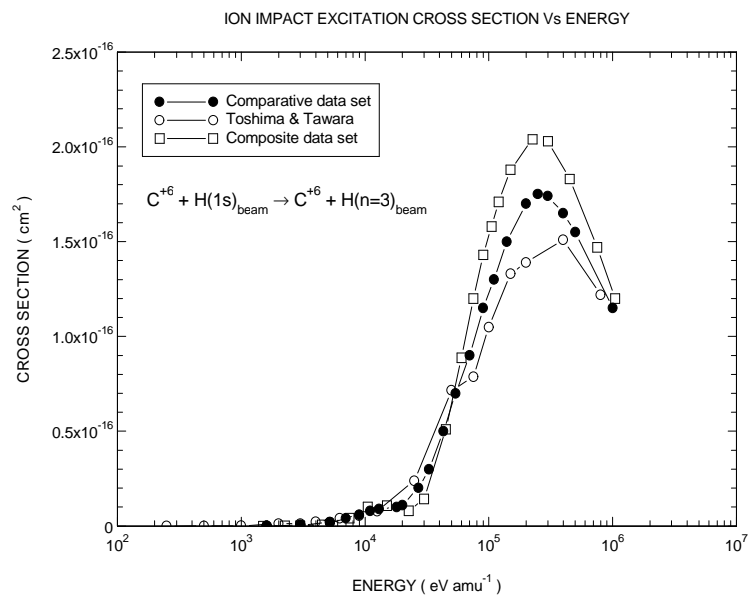


Figure 36.0 A plot of the ion impact excitation cross section Vs energy . The comparative data set is taken as the preferred data.

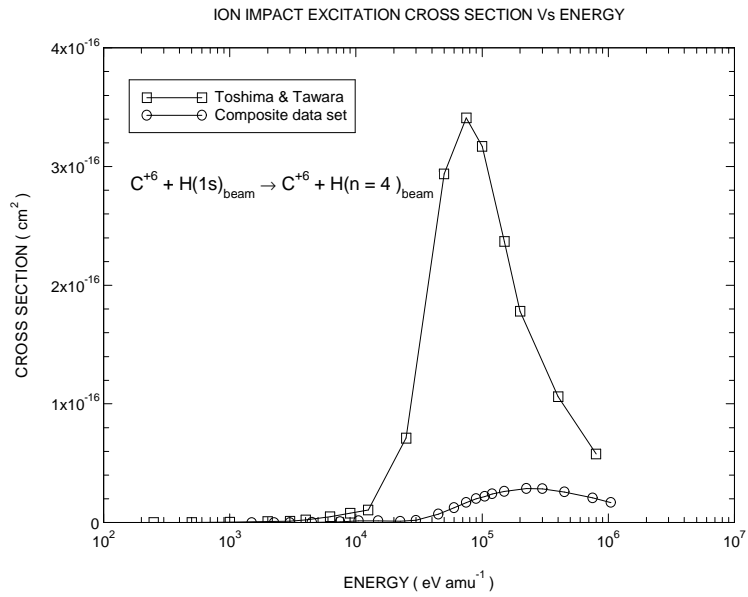


Figure 37.0 A plot of the ion impact excitation cross section Vs energy . The composite data set is taken as the preferred data. The calculation of Toshima & Tawara[91] only include states up to $n = 4$, therefore some over-estimation is present particular for the $n = 4$ shell .

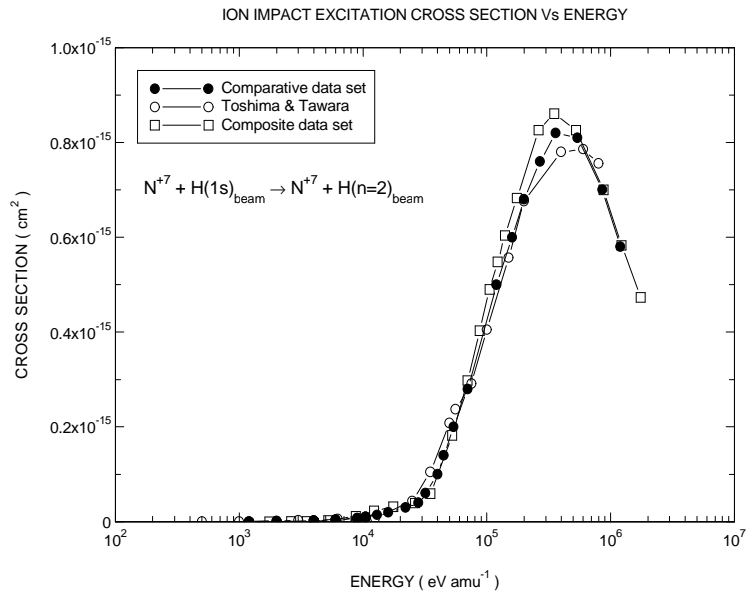


Figure 38.0 A plot of the ion impact excitation cross section Vs energy . The comparative data set is taken as the preferred data set.

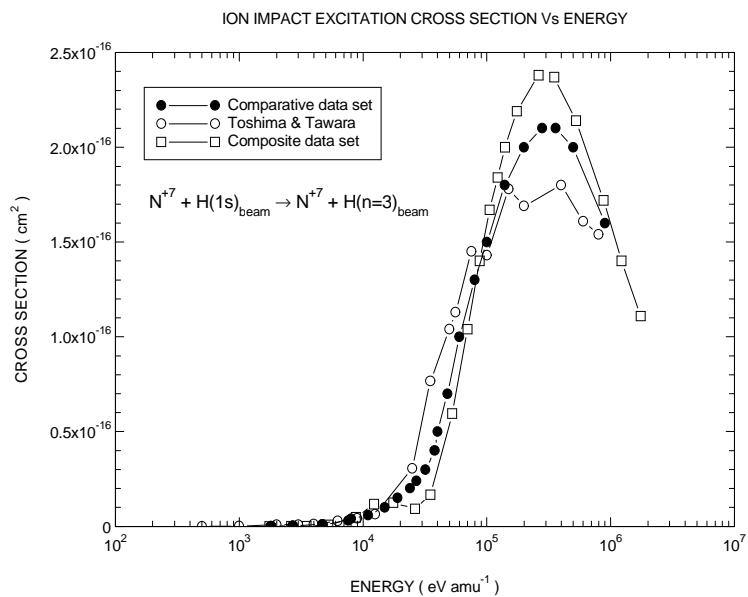


Figure 39.0 A plot of the ion impact excitation cross section Vs energy . The comparative data set is taken as the preferred data.

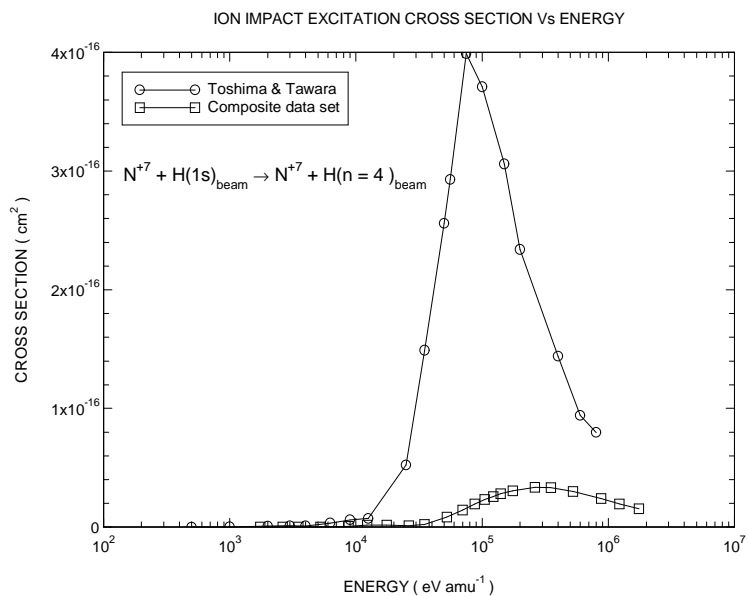


Figure 40.0 A plot of the ion impact excitation cross section Vs energy . The composite data set is taken as the preferred data. The calculation of Toshima & Tawara[91] only include states up to $n = 4$, therefore some over-estimation is present particular for the $n = 4$ shell .

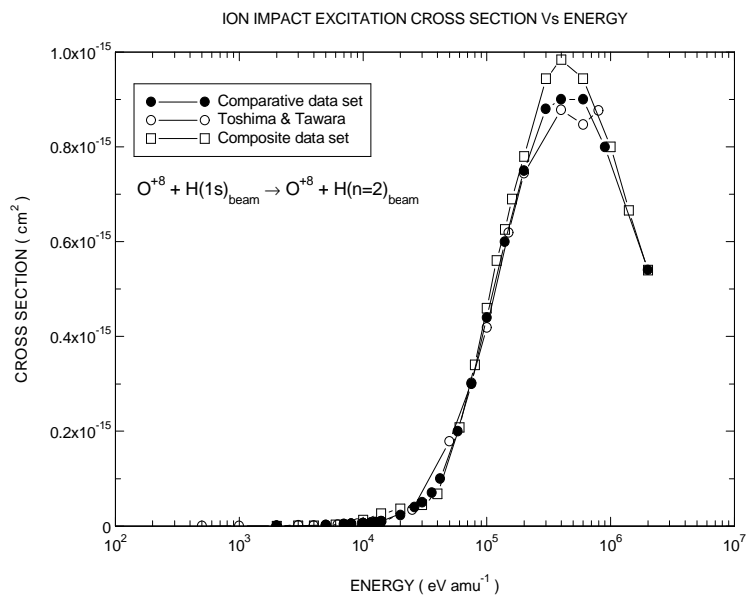


Figure 41.0 A plot of the ion impact excitation cross section Vs energy . The comparative data set is taken as the preferred data for this particular process.

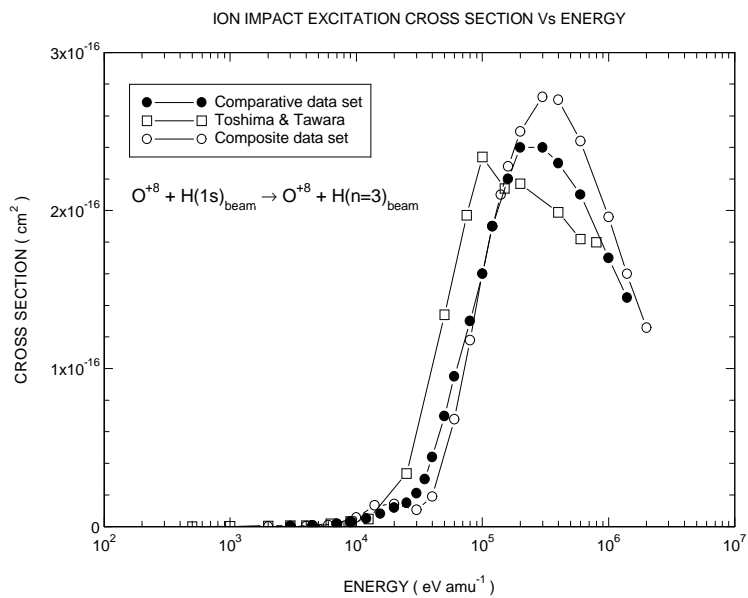


Figure 42.0 A plot of the ion impact excitation cross section Vs energy . The comparative data set is taken as the preferred data.

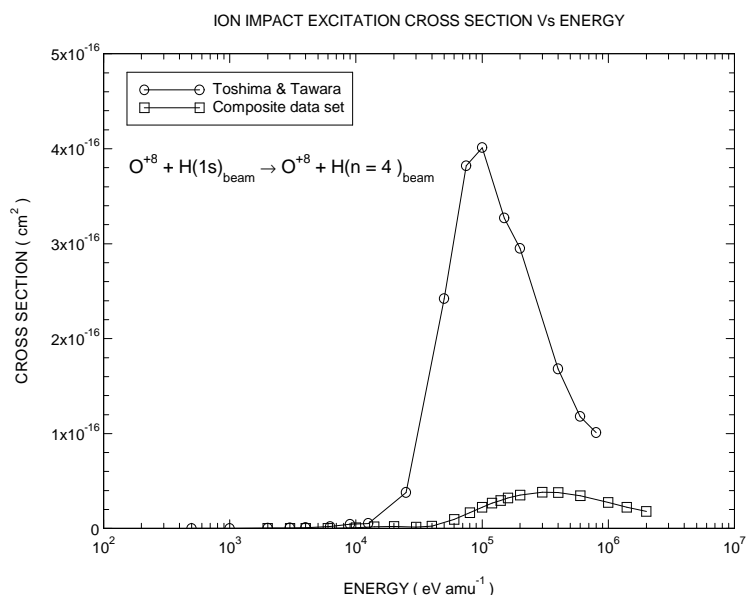


Figure 43.0 A plot of the ion impact excitation cross section Vs energy . The calculation of Toshima & Tawara[91] only include states up to $n = 4$, therefore some over-estimation is present particular for the $n = 4$ shell .

1.4 Review of ion impact ionisation from excited states of H

The database contains data for ion impact ionisation from excited states of the neutral beam particles as described by equation 1.4, where Z_0 is the nuclear charge of the impurity and n is the principal quantum number.



The data which was used in all cases is a general data set which is scaled according to the value of Z_0 and n . New data by Janev & Smith[90], for $Z_0 = 1$ and $n = 2, 3, 4$ & 5 was compared to the results of using the general scaled data. The results can be seen in figures 44.0, 45.0, 46.0 and 47.0 . In all cases the data of Janev & Smith[90] is taken as the preferred data. An interesting point to note is the fairly large difference between the data of Janev & Smith[90] and the general scaled data in figure 45.0 . Ionisation from excited states by impurity ion impact is one of the least precisely known processes and so the more substantial deviations evident here are expected

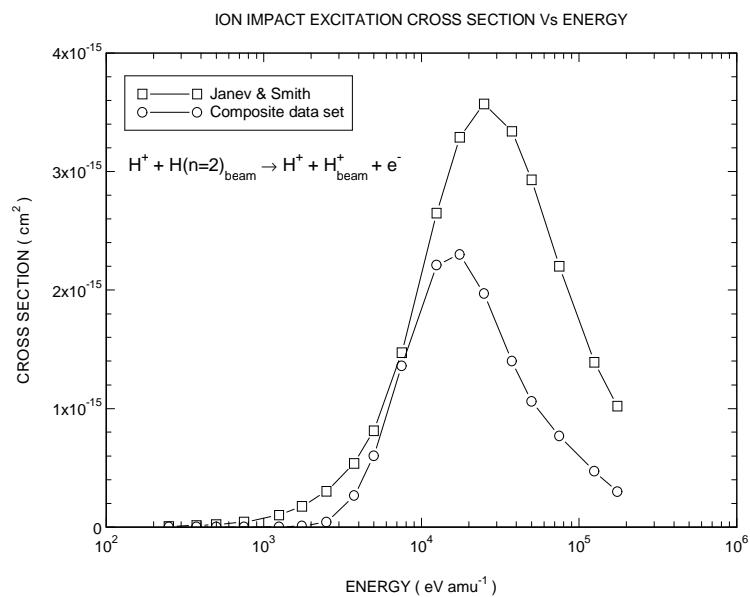


Figure 44.0 A plot of the ion impact ionisation cross section Vs energy . The data reported by Janev & Smith[90] is taken as the preferred data.

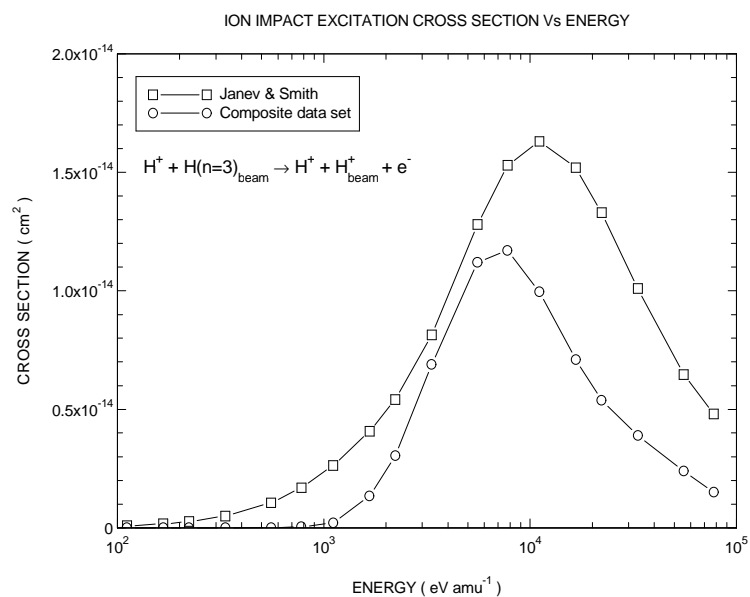


Figure 45.0 A plot of the ion impact ionisation cross section Vs energy . The data of Janev & Smith is taken as the preferred data. Interesting point to note is the significant difference between both data sets.

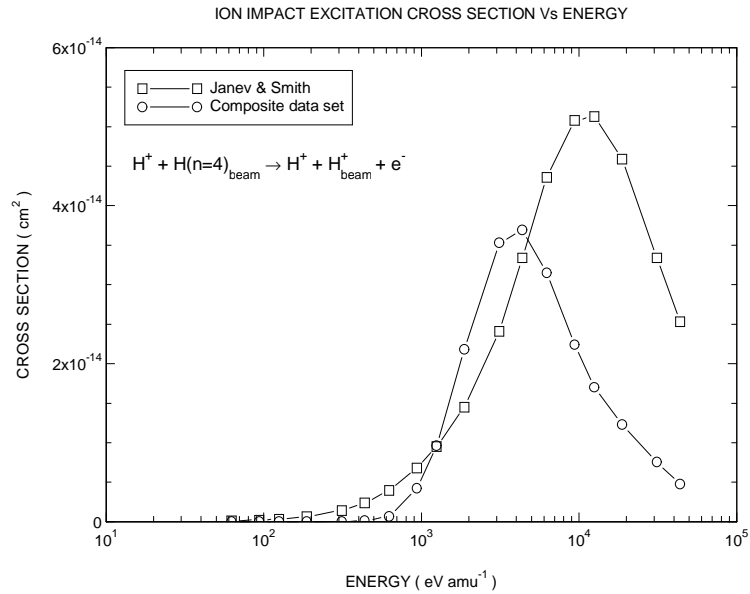


Figure 46.0 A plot of the ion impact ionisation cross section Vs energy . The data reported by Janev & Smith[90] is taken as the preferred data.

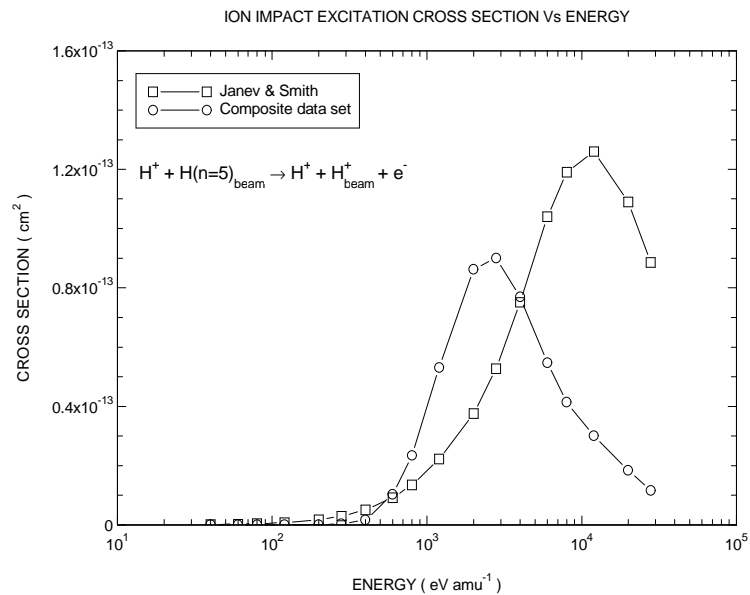


Figure 47.0 A plot of the ion impact ionisation cross section Vs energy . The data reported by Janev & Smith[90] is taken as the preferred data set.

1.5 Review of charge exchange data from excited states of H

The data base also contains data for charge exchange from excited states of the neutral beam particles as described by equation 1.5 .

$$X^{+Z^0} + H(n)_{beam} \rightarrow X^{+Z^0-1} + H_{beam}^+ \quad 1.5$$

Where all the symbols have there usual meaning. At the present, general scaled data is employed for this process and a survey of the literature failed to improve the situation.

References

- [1] Isler, R., 1984, Nuc. Fus., **24**, pp 1599-1678.
- [2] Tawara, H., 1995, National Institute of Fusion Science, NIFS-DATA series, NIFS-DATA-25, Nagoya, Japan.
- [3] Wesson, J., 'Tokamaks', 1987, Clarendon Press, Oxford.
- [4] Pitcher, C. S., Stangeby, P. C., 1997, Plasma. Phys. Control. Fusion, **39** pp 779-930.
- [5] Coffey, I., et. al., 1995, Proc. Conf., 11th Colloquium on UV and X-ray spectroscopy of astrophysical and laboratory plasmas, pp 431-435.
- [6] Terry, J. L., et. al., 1998, Proc. Conf., 11th APS Topical conference, Atomic processes in plasmas, pp 43-57.
- [7] Meigs, A. G., 1998, *private communication*.
- [8] von Hellermann, M.G., et. al., 1994, JET Joint Undertaking preprint, JET-P(94)58.
- [9] Morsi, H. W., et. al., 1995, Plasma. Phys. Control. Fusion, **37**, pp 1407-1431.
- [10] O'Mullane, M., 1996, Ph.D thesis, University of Cork.
- [11] Andrew, Y., et. al., 1998, JET Joint Undertaking conference proceedings, JET-CP(98)03.
- [12] Schweer, B., et. al., 1992, J. Nuc. Mat., **196-198**, pp 174-178.
- [13] Takiyama, K., et. al., 1995, J. Nuc. Mat., **220-222**, pp 205-211.
- [14] Hintz, E., Schweer, B., 1995, Plasma. Phys. Control. Fusion, **37**, pp A87-A101.
- [15] Kislyakov, A. I., Krupnik, L. I., 1981, Sov. J. Plasma. Phys., **7**, pp 478-498.
- [16] von Hellermann, M. G., Summers, H. P., 1993, Atomic and Plasma-material. Interaction processes in controlled thermonuclear fusion, Janev R. K., Drawin, B. V. (editors).
- [17] Fonck, F. J., et. al., 1990, Rev. Sci. Instrum., **61**, pp 3496-3500.
- [18] Isler, R. C., 1994, Plasma. Phys. Control. Fusion, **36**, pp 171-208.
- [19] Spence, J., 1987, Ph.D thesis, University of Strathclyde.
- [20] Mandl, W., 1992, Ph.D thesis, JET Joint Undertaking internal report, JET-IR(92)05.

- [21] Wolle, B., 1997, Max-Planck-institute for plasma physics, IPP internal report, IPP III/222, pp 1-94.
- [22] Maas, A., 1995, Ph.D thesis, JET Joint Undertaking.
- [23] Summers, H. P., et. al., 1991, JET Joint Undertaking preprint, JET-P(91)48 .
- [24] Pohlmeier, B. A., et. al., 1996, J. Phys. B., **29**, pp 221-229.
- [25] Bertolini, E., 1998, JET Joint Undertaking preprint, JET-P(98)54.
- [26] Summers, H. P., 1994, JET Joint Undertaking internal report, JET-IR(94)06.
- [27] Summers, H. P., 1995, ADAS FORTRAN library User manual, University of Strathclyde.
- [28] Spitzer, L., 1956, 'Physics of fully ionised gases', Interscience, New York.
- [29] Brooks, D. H., 1997, Ph.D thesis, University of Strathclyde.
- [30] von Hellermann, M. G., Summers, H. P., 1992, Rev. Sci. Instr. **63**, pp 5132-5139.
- [31] Kimura, M., Lane, N. F., 1986, Phys. Rev. A., **34**, pp 4421-4423.
- [32] Bates, D. R., Kingston, A. E., McWhirter, R. W. P., 1962, Proc. Royal. Soc. London, **267 A**, pp 297-312.
- [33] Riviere, A. C., 1971, Nuc. Fus., **11**, pp 363-369.
- [34] Penningsfeld, F. P., 1986, Max-Planck-institute for plasma physics, IPP internal report, IPP 4/229, pp 1-18.
- [35] Boley, C.D., Janev, R.K., Post, D.E., 1984, Phys. Rev. Lett., **52**, pp 534-537.
- [36] Summers, H.P., 1998, *private communication*.
- [37] Burgess, A. Summers, H. P., 1976, Mon. Not. R. astr. Soc., **174**, pp 345-391.
- [38] Korotkov, A. A., Samsonov, 1989, M. S., A.F Ioffe Physico-technical Institute, I351.
- [39] Janev, R. K., Boley, C. D., Post, D. E., 1989, Nucl. Fus., **29**, pp 2125-2140.
- [40] Levinton, F. M., 1986, Rev. Sci. Instr., **57**, pp 1834-1836.
- [41] Korotkov, A. A., 1992, Nuc. Fus., **3**, pp 79-86.
- [42] Korotkov, A. A., Janev, R. K., 1996, Phys. Plasmas, **3**, pp 1512-1523.
- [43] Summers, H. P., 1977, Mon. Not. R. astr. Soc., **178**, pp101-122.
- [44] Van Regemorter, H., 1962, J. Astrophys., **136**, pp 906-915.
- [45] Percival, I., Richards, D., 1978, Mon. Not. R. astr. Soc., **183**, pp 329-334.

- [46] Burgess, A., 1964, Proc. Symp. Atomic collision processes in plasmas, Culham, A.E.R.E. Rep. 4818, pp 63-71.
- [47] Lodge, J. G., Percival, I. C., Richards, D., 1976, J. Phys. B., **9**, pp 239-254.
- [48] Vainshtein, L., et. al., 1962, Soviet Physics JETP, **16**, pp 370-374.
- [49] Percival, I. C., Richards, D., 1975, Adv. At. Mol. Phys., **11**, pp 1-82.
- [50] Sampson, D. D., Goett, S. J., Clark, R.E.H., 1983, Atomic data and nuclear data tables, **29**, pp 467-534..
- [51] Golden, L. B., et. al., 1981, Astro. J. Supple. Series., **45**, pp 603-612.
- [52] Clark, R.E.H., et. al., 1982, Astro. J. Supple. Series., **49**, pp 545-554.
- [53] Callaway, J., 1994, Atomic data and nuclear data tables, **57**, pp 9-20.
- [54] Summers, H. P., 1996, Atomic data Status, ADAS manual. University of Strathclyde.
- [55] Bell, K. L., et. al., 1982, Culham laboratory internal report, CLM-R216, pp 1-120.
- [56] de Heer, F. J., et. al., 1995, Atomic and Plasma Mater. Inter. Data for Fus., **6**, pp 7-26.
- [57] Fujimoto, T., 1978, Institute of plasma physics, IPPJ internal report, IPPJ-AM-9, Nagoya University, Japan.
- [58] Summers, H. P., Anderson, H., Martin, R., 1998, ADAS users manual, Beam stopping and emission, University of Strathclyde.
- [59] von Hellermann, M. G., 1996, *private communication*.
- [60] Seraydarian, R.P., et. al., 1988, Rev. Sci. Instr., **59**, pp 1530-1532.
- [61] Levinton, F. M., et. al., 1989, Phys. Rev. Lett., **63**, pp 2060-2063.
- [62] Boileau, A., et. al., 1989, J. Phys. B., **22**, L145-L152.
- [63] Wroblewski, D., et. al., 1990, Rev. Sci. Instr., **61**, pp 3552-3556.
- [64] Wroblewski, D., Lao, L. L., 1992, Rev. Sci. Instr., **63**, pp 5140-5147.
- [65] Levinton, F. M., 1992, Rev. Sci. Instr., **63**, pp 5157-5160.
- [66] Wolf R, 1993, Ph.D thesis, JET Joint Undertaking internal report, JET-IR(93)08.
- [67] Fonck, R. J., 1990, Rev. Sci. Instr., **61**, pp 3487-3495.
- [68] Durst, D., et. al., 1992, Sci. Instr., **63**, pp 4907-4912 .

- [69] von Hellermann, M. G., et. al., 1990, Rev. Sci. Instr., **61**, pp 3479-3486.
- [70] von Hellermann, M. G., et. al., 1995, JET Joint Undertaking preprint, JET-P(95)63.
- [71] International Atomic Energy Authority, 1991, ITER Documentation series, No. 25.
- [72] Mandl, W., et. al., 1993, Plasma. Phys. Control. Fusion, **35**, pp 1373-1394.
- [73] Duessing, G., et. al., 1987, Fus. Tech., **11**, pp 163 - 202.
- [74] English, M., 1996, JET Joint Undertaking internal documentation.
- [75] Howman, A., 1997, *private communication*.
- [76] Sobelman, I.I., 1979, 'Atomic Spectra and radiative transitions', Springer Verlag.
- [77] Christiansen, J. P., 1987, Journal of computational physics, **73**, pp 85-104.
- [78] JET data Handbook, 1997, JET Joint Undertaking.
- [79] NAG Documentation, Numerical algorithms group Ltd., Banbury road, Oxford, UK.
- [80] Fiest, J. P., 1996, Diploma thesis, Gernhard-Mercator-University.
- [81] Hemsworth, S. H., 1987, JET Joint Undertaking internal note, RSH-NBP.
- [82] Satzmann, H., et. al., 1989, JET Joint Undertaking internal report, JET-IR(89)07.
- [83] van Rooij, G. J., 1994, Diploma thesis, University of technology, Eindhoven.
- [84] Marcus, F. B., et. al., 1990, JET Joint Undertaking internal report, JET-IR(90)01.
- [85] Hoekstra, R., et. al., 1997, Proc. Conf. ICAMDATA-first international conference, Gaithersburg, Maryland, pp 37-54.
- [86] Burgess, A. Tully, J.A., 1992, Astron. Astrophys, **254**, pp 436-453.
- [87] Shah, M. B., Gilbody, H. B., 1981, J. Phys. B., **4**, pp 2361-2377.
- [88] Shah, M. B., Elliot, D.S., Gilbody, H. B., 1987, J. Phys. B., **20**, pp 3501-3514.
- [89] Ryufuku, H., 1982, Phys. Rev. A., **29**, pp 720-736.
- [90] Janev, R.K., Smith, J.J., 1993, Atomic and Plasma Mater. Inter. Data for Fus., **4**, pp 1-180.
- [91] Toshima, N., Tawara, H., 1995, National Institute of Fusion Science,

NIFS-DATA series, NIFS-DATA-26, Nagoya, Japan.

- [92] Phaneuf, R. A., et. al., 1987, Atomic data for fusion, **5**, ORNL-6090, Oak ridge national laboratory, Hunter, H.T. (editor).
- [93] M^c Clure, G. W., 1966, Phys. Rev. A, **148**, pp 47-54.
- [94] Greenland, P. T., 1984, Culham laboratory internal report, AERE - R11281, pp 1-65.
- [95] Frieling, G.J., 1992, J. Phys. B., **25**, pp 1245-1255.
- [96] Ryufuku, H., 1982, Japan Atomic Energy Research Institute, JAERI internal report, JAERI-M-82-031, pp 1- 127.
- [97] Busnengo, H.F., et. al., 1996, Physica Scripta, **T62**, pp 88-94.
- [98] Park, J.J., et. al., 1976, Phys. Rev. A., **14**, pp 608-614.
- [99] Fritsch, W., Lin, C.D., 1982, Phys. Rev A., **26**, pp 762-769.
- [100] Fritsch, W., Lin, C.D., 1983, Phys. Rev A., **27**, pp 3361-3364.
- [101] Shakeshaft, R., 1978, Phys. Rev. A., **18**, pp 1930-1934.
- [102] Ludde, H. J., Driezler, R. M., 1982, J. Phys. B., **15**, 2703-2711 .
- [103] Theodosian, C. E., 1980, Phys. Rev. A., **22**, pp 2556-2571.
- [104] Janev, R. K., Krstic, P. S., 1992, Phys. Rev. A., **46**, pp 5554-5573.
- [105] Ermolaev, A. M., 1990, J. Phys. B., **23**, pp L45-L50.
- [106] Fritsch, W., 1989, *private communication to Summers*.
- [107] Fritsch, W., Lin, C.D., 1991, Physics Reports, **202**, pp 1 - 97.